Les fils photoniques : une géométrie innovante pour la réalisation de sources de lumière quantique brillantes

Nitin Singh Malik

UNIVERSITÉ DE GRENOBLE

THÈSE

Pour obtenir le grade de

DOCTEUR DE L'UNIVERSITÉ DE GRENOBLE

Spécialité : **PHYSIQUE/ PHYSIQUE DE MATIERE CONDENSE & RAYONNEMENT**

Arrêté ministériel : 7 août 2006

Présentée par

Nitin Singh MALIK

Thèse dirigée par **Jean-Michel GERARD** et
co-encadrée par **Julien CLAUDON**

préparée au sein de **l'équipe mixte CEA-CNRS « NanoPhysique et SemiConducteurs », Service de Physique des Matériaux et Microstructures, INAC, CEA Grenoble**
dans **l'École Doctorale de Physique de Grenoble**

Les fils photoniques : une géométrie innovante pour la réalisation de sources de lumière quantique brillantes

Thèse soutenue publiquement le **21 novembre 2011**,
devant le jury composé de :

Laurent SAMINADAYAR
Professeur Université Joseph Fourier (Président)
Isabelle SAGNES
Directeur de Recherche CNRS (Rapporteur)
Guillaume CASSABOIS
Professeur Université Montpellier 2 (Rapporteur)
Christian SEASSAL
Directeur de Recherche CNRS (Examinateur)
Jean-Michel GERARD
Eq. Directeur de Recherche, CEA Grenoble (Directeur)
Julien CLAUDON
Eq. Chargé de Recherche, CEA Grenoble (Co-encadrant)

Acknowledgements

At the time of writing my dissertation, I am feeling just like walking this journey through time again. That was the last week of February but around three years ago when I was applied for this position in Joint Group of CEA-CNRS, NPSC ‹‹ Nanophysique et Semiconducteurs ›› Grenoble FRANCE, indeed almost half a world away from my home country. In the last week of September in that year, I started my research work in the Group NPSC you will see here is this dissertation. At NPSC, I have been fortunate enough to be surrounded by many kind people to offer help and useful guidance to complete my research there, so first I owe a debt of deep gratitude to the many people who contributed to my maturity as researcher and analytical thinker at NPSC.

First and foremost, I would like to express my deepest gratitude and indebtedness to my Director of thesis Jean-Michel Gérard and my Supervisor Julien Claudon, who offered me this opportunity to work in this group and guided me throughout my research. In spite of his busy schedule, Jean-Michel always made time for individual meetings to discuss about the progress and problem of projects and always gave his invaluable guidance and suggestions.

I would also like to thank Prof. Henri Mariette, Director of the group NPSC, to give opportunity me to work in this group and support me throughout my dissertation.

Again a special thank goes to my supervisor Julien Claudon, a truly incredible research advisor and mentor and above all a nice human being, for the great support and invaluable guidance he has provided me throughout my dissertation. I would say that never once did he act like my boss nor did he ever treat me like a PhD student. Although we worked together most of the time of my dissertation but he never looked over my shoulder to make sure I was working properly or not, yet he was always one door away whenever I needed him for advice (some time for coffee too !). He is role model for me. He expertly guided me to success in many projects I worked on, and I have benefited from his intelligence, critical thinking, creativity and rigorous approach to science. I also thank him for his generous support in other aspects, particularly when I had some health problem. It was his really great effort that gave me courage to think positive and to finish my work in such conditions.

I would also like to convey many many thanks to the members of the jury: Guillaume Cassasbois, Isabelle Sagnes, Laurent Saminadayar and Christian Seassal for refereeing my thesis and accepting to serve in the jury. Their

valuable and constructive comments helped me to improve manuscript to its present shape.

If I ever felt honored to be dependent on the work of so many co-workers involved in growth and optical characterization of the devices, it is because of my colleagues Emmanuel Dupuy, Joël Bleuse, Maela Bazin, Matheiu Munsch, Megan Creasey and Périne Jaffernnou. My thanks also go to other fellows in the NPSC who have been a help: Catherine, Edith, Eva, Gabriel, Herve, Jean, Jean-Phillipe, Joël Eymery, Kuntheak, Lionel, Marléne, Régis, Rudeesan, Vincent, Yann and Yoann. It was a real pleasure to work in such an open, healthy and collaborative environment.

I would also like to acknowledge financial support from the Nanosciences fondation. I would like to thank the technical team of PTA clean room to help me during my research.

A special thanks to Carmelo and Cecile, for their great help dealing with travel and administration matters efficiently during my dissertation.

To Prof. Sujeet Chaudhary, I will never be able to thank you enough for allowing me to work in your lab at IIT Delhi when I was in my M.Tech. You have been the mentor of my improvement from a below average student of science to a graduate research student. The opportunity you provided me and the value of the experience and your support that I received is difficult to put into words, nonetheless, thank you for everything. Huge thanks goes to Prof. Inderjeet Singh, the one who taught physics to me in a wonderful way and motivated me to do research in physics.

I cannot imagine my years at NPSC without two friends, Prem and Sandeep. They are wonderful friends, and they have painted a rich fabric of memories that I will never forget. I have shared an office with Sandeep for two years of my thesis. Because of his presence I never felt I am far from my country. I want to give a special thanks to Veeresh with whom I shared the apartment. A lot of people have also been helping me and pushing me forward during all these years of my research, so special thanks to my friends: Abhinav, Agnieszka, Alexander, Alisher, Amit, Aparna, Bijandra, Gajender, Irina, Pankaj, Pawan, Madhav , Manan, Robert, Sanjay, Tapas, Teju, Xiaojun and Yulia.

Before I finish, I would like to express my deepest gratitude to my parents as well as my brother, my sisters. They have always supported me, trusted me and allowed me for the challenge of studying abroad. I have always felt their warm and strong support during my research. How could it be possible for me to go this far without your support, encouragement and patience? I love you all. I

would like also like to thank Priya, who provided the moral support as a best friend and sister so critical in keeping me on track, in both the best and worst phase of my life. Her words (as like a grandmother) of encouragement helped me traveled the journey of my research. I dedicate this dissertation to my late grandfather. I was not able to visit him when he was badly ill, and hope the accomplishment of this dissertation could fulfill his last wish. May he rest in peace.

Nitin Singh Malik

Contents

Chapter-1

Introduction

1.1 General Introduction and Motivation

1.1.1 On-demand single photon sources

Ideally, an on-demand single-photon source is a device, able to emit a light pulse containing exactly one photon in an optical channel of interest after a trigger pulse (electrical or optical) (see Figure 1.1). Such a device would enable many applications in the field of quantum information technology [1,-8]. The first important one is quantum key distribution, which provides a way for unconditional secure optical communication between two parties [5, 6]. A possible application to linear optical quantum computing arises, providing that the source emits indistinguishable photons [7]. This demanding criterion imposes that the photons are emitted in the same quantum states (well defined frequency, temporal profile, same spatial mode and polarization). In that case, photon interferences can be exploited to implement quantum algorithms. This is however very demanding and makes this goal a long term objective. A single-photon source, emitting a faint light flux with a low photon noise (zero for an ideal source), might also find applications in metrology [3]. In that case, indistinguishability is not required.

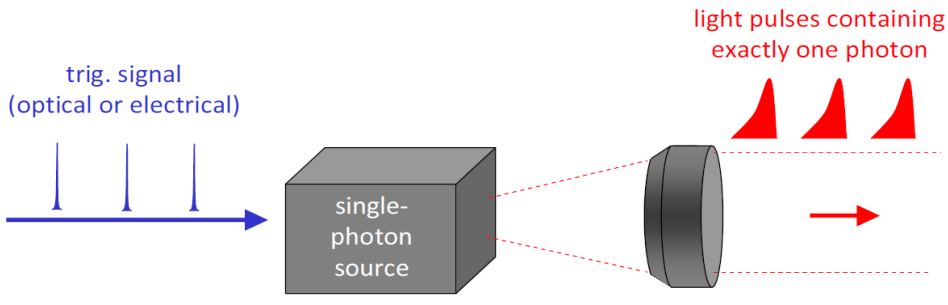

Figure 1.1: An Ideal Single Photon Source.

For all these applications, we have at least two key figures of merit:

- The purity of single-photon emission: the emitted light pulses should contain exactly one photon (and not more). A deviation from this ideal case is captured by the second order intensity correlation function g^2 (further details will be given in Chapter 4).

- The efficiency of the source: In this thesis, we will consider emission into free-space: the optical channel of interest is the collecting cone of the first lens of the optical setup (a microscope objective). The efficiency of the source is then defined as the probability to collect a photon in the microscope objective after a trigger pulse. With this definition, the efficiency is independent on the setup transmission losses and the quantum efficiency of the detectors.

In this thesis, we will show how to realize a bright single-photon source using a solid-state single-photon emitter (a semiconductor quantum dot) inserted in a photonic structure optimised to achieve high collection efficiency. Our strategy is in fact a two step one. The quantum dot is integrated in a photonic structure providing a well controlled electromagnetic environment, to funnel a large fraction of its spontaneous emission into an optical mode of interest. In a second step, the collection of the photon is optimized through a specific photonic engineering. In this chapter, we present quantum dots and the various approaches to control their spontaneous emission, with a special emphasis on the realization of semiconductor single-photon sources.

1.1.2 On-demand single photon emission

In the last decade, considerable efforts have been made to develop single-photon sources [9], and a distinction can be established between approximate and ‘true’ single photon sources.

Approximate single-photon sources

The easiest and most straightforward way to produce a regulated single-photon stream is to attenuate a pulsed laser [10]. This approach has been used to implement quantum cryptography schemes [11, 12]. Well above the lasing threshold, the photons emitted by the laser follow a Poissonian statistics (they are emitted independently from each other). This statistics is preserved when the laser beam is attenuated using neutral filters.

Let us consider a strongly attenuated beam, for which the average photon number per pulse is smaller than unity. In that case, if the probability to emit one photon is p (1), the probability to emit two photon is $p(2) = p(1)^2/2$, which is

shown in Figure 1.2. This gives rise to a potentially important security leakage known as photon number splitting attack [15]. To avoid multi-photon pulses, p(1) has to be made very small (below 10%), leading to a degraded source efficiency. Thus, there is always a trade off between the efficiency and the purity of the single-photon emission.

Alternatively, photon pairs can be obtained by spontaneous parametric down conversion, using a laser beam impinging on a non linear crystal [13, 14]. In that case, a 'signal' and 'idler' photons are emitted simultaneously. One of the photon (*e.g.* the idler) can be used as a 'marker' of the emission of the other. However, the emission statistics of the pairs is still Poissonian, putting the same limit on the source efficiency.

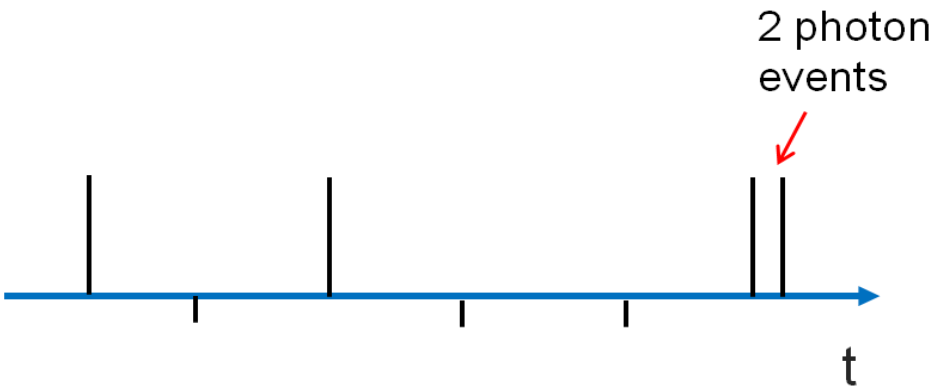

Figure 1.2: Photon stream in case of single photon source based on attenuated laser approach.

'True' single photon source: Solid-state quantum emitters

A quantum emitter (like an atom) provides a model system for single-photon emission. Indeed, a two-level fermionic system can only emit a single photon after excitation (because of the Pauli Exclusion Principle). If the excitation is continuous, photons are emitted one by one (antibunched light) when one considers timescales typically shorter than the mean radiative decay of the emitter. The first experiments demonstrating single-photon emission were conducted on atoms; in 1977, Kimble et al. demonstrated light antibunching of the resonance fluorescence from sodium atoms [16]. Since then, other experiments have been carried out on atoms [17], single ion [18, 19]. Because they are considered as more practical, solid-state single-photon emitters have attracted a lot of interest. These present a discrete energy spectrum, with the advantage to occupy a fixed location in space, since they are embedded inside a solid-state matrix. One can cite molecules [20, 21], colour centres in diamond

[22-24], semiconductor nanocrystals [25] and other semiconductor quantum dots [26-31].

Among these, semiconductor self-assembled quantum dots feature several appealing properties. A semiconductor quantum dot (QD) is a nanometer sized cluster, which typically contains 10^4-10^5 atoms of a semiconductor material, embedded in a matrix of another semiconductor material with a larger band gap [32, 33]. Inside such a QD, the charge carriers (electrons and holes) are confined in the three directions of space, leading to quantized energy levels. As a result, a few discrete bound energy eigenstates with limited degeneracy are available for occupation by carriers. Therefore semiconductor quantum dots (QDs) possess optical properties similar to the one of atoms and are thus often referred to as “artificial atoms”. Moreover, they are photostable neither bleaching nor blinking, feature spectrally-narrow optical emission at cryogenic temperature and present high oscillator strength. In addition, they can be embedded in photonic structures (microcavities and waveguides), and can be excited electrically, using doped and contacted structures. The following section presents their properties with more details.

1.2 Semiconductor quantum dots as single-photon emitters

In this thesis, we use self-assembled InAs/GaAs quantum dots as single-photon emitters. They have demonstrated excellent single-photon emission [29, 30]; therefore we focus on the properties of this system in the following.

1.2.1 Growth of self-assembled quantum dots

We focus on InAs/GaAs quantum dots that are grown by molecular beam epitaxy, using a strain-induced self-assembly method (“Stranski-Krastanov” growth mode). The InAs crystal has a lattice parameter 7% larger than the one of GaAs. For the first monolayer of deposited InAs, the growth mode is 2D and coherent with the GaAs substrate. When the thickness of the InAs layer is further increased, a transition occurs (~1.5 -2.0 ML which depends upon the growth conditions). The strain accumulated in the InAs layer is elastically relaxed through the generation of 3D InAs islands. In order to make them optically active, the dots are finally capped with a GaAs layer. The resulting quantum dots “live” on the top of thin 2D InAs layer which is known as the “wetting layer”. The self-assembly leads to a ‘double’ randomness: the nucleation position of the dots is

random, and they feature a size distribution, leading to a certain spectral distribution linked to the different confinement energies. Figure 1.3 (a) shows an Atomic Force Microscopic (AFM) image of quantum dots grown under optimized conditions and clearly shows the random nature of the growth of quantum dots. Figure 1.3 (b) shows a transmission electron microscopy (TEM) image of caped QDs which shows the formation of three dimension confinement structures. The surface density of the dots, as well as the average size of the dot can be controlled to some extent by the growth parameters (temperature, growth rate, growth interruptions, etc…).

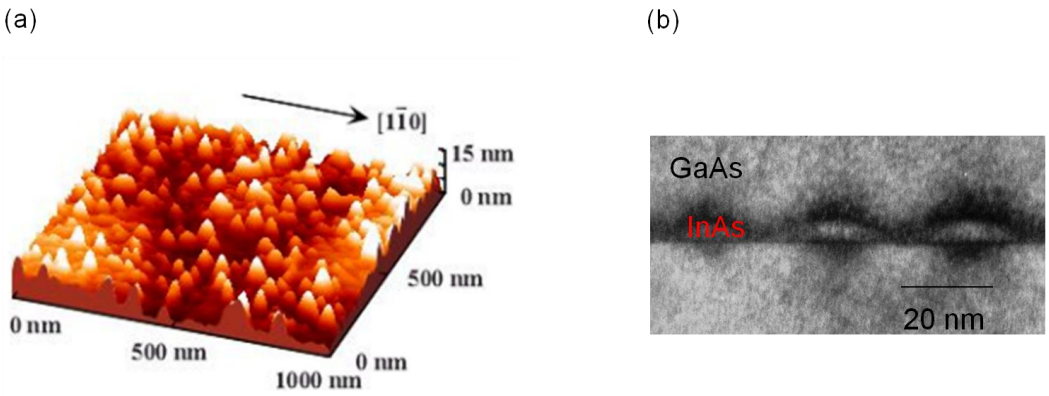

Figure 1.3: Quantum dot formation: a) AFM image of the uncapped QDs, (b) TEM image of the cross section of QD structures.

1.2.2 A single quantum dot as a single photon emitter

Discrete energy spectrum:

A schematic of the different energy states of a quantum dot along the growth direction is shown in the Figure 1.4. This figure illustrates that the three dimension confinement in a quantum dot which gives rise to the discrete energy states as like the atom. It shows the first single-particle confined levels: s (no orbital degeneracy) and p (double orbital degeneracy) in the conduction and valence bands. The wetting layer, which is a 2D well with some thickness fluctuation, introduces a continuum of electronic states with a blurred cut-off (corresponding states shown in grey color).

Some excitonic complexes confined in a QD:

A dot can capture electrons and holes. An electron-hole pair trapped in the QD, usually called exciton, can recombine radiatively. In general any number of

charges can be trapped inside the QD leading to various confined excitonic complexes. Figure 1.5 shows a number of possible excitonic states of a single quantum dot.

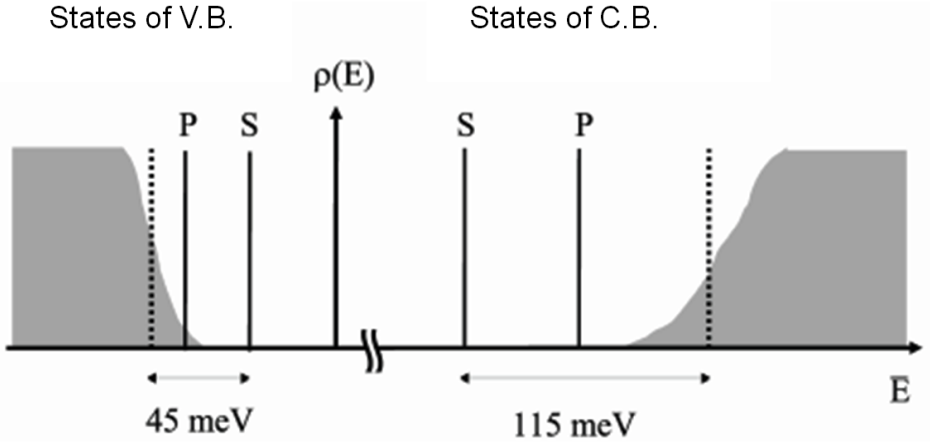

Figure 1.4: Density of states associated with an InAs QD supported by a wetting layer (QD diameter = 20 nm, height = 1.5 nm, mean thickness of the wetting layer=1.7 ML) [34]

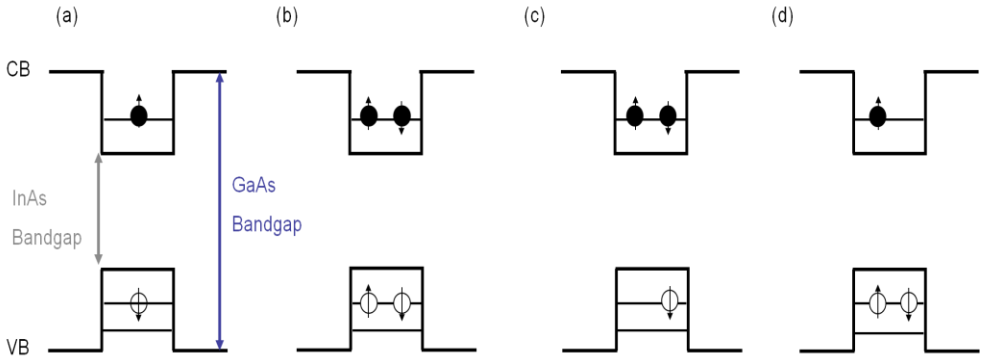

Figure 1.5: Schematic band diagrams of a single quantum dot possible exciton states; (a) exciton (X_1), (b) biexciton (X_2), (c) negatively charge exciton (X_1-), (d) positively charge exciton (X_1+).

Radiative cascade and on-demand single-photon emission:

We consider here an excitation by a short laser pulse (shorter than the radiative dynamics of the system). This pulse is tuned on an energy exceeding the GaAs bandgap: it thus excites electrons into conduction band, leaving holes in the valence band [29, 30]. These charge carriers are captured by the 2D wetting layer very rapidly (a few ps) before being captured in the excited states of

a quantum dot. They then relax via the emission of LO phonons to the lowest unoccupied states of the quantum dots within a few 10 ps [35]. At this stage, the only decay channel is an interband recombination of electrons and holes through the emission of photons [36]. To achieve the brightest single-photon emission, it is desirable to pump efficiently the dot that is to say to inject at least one exciton in the QD per excitation pulse. In first approximation, exciton trapping in the QD can be supposed to be Poisonnian due to the randomness of pumping and capture events. In that case the probability to trap two or more excitons is not negligible. Fortunately, this is not a limitation to use the dot as single-photon emitter, providing a proper spectral filtering is conducted. As shown the in Figure 1.6, when a QD is occupied with more than one electron-hole pairs, the combination of spatial confinement and Coulomb interaction (direct and exchange terms) leads to spectrally different emission energies for each excitonic complex (i.e. $\omega_{X1} \neq \omega_{X2} \neq \omega_{X3}$) [26, 37]. During the progressive recombination of these, single photons with *different* energies are thus emitted. In particular, the fundamental transition, corresponding to the recombination of a single exciton (X_1) can be isolated by spectral filtering to generate single photons [27]. Since carriers can be also injected in the GaAs barrier with electrodes and a properly doped structure, this excitation scheme has been readily applied to the realization of single-photon LED [31]. This non-resonant excitation scheme is also thus much more convenient than the resonant electrical excitation presented in Ref. [38].

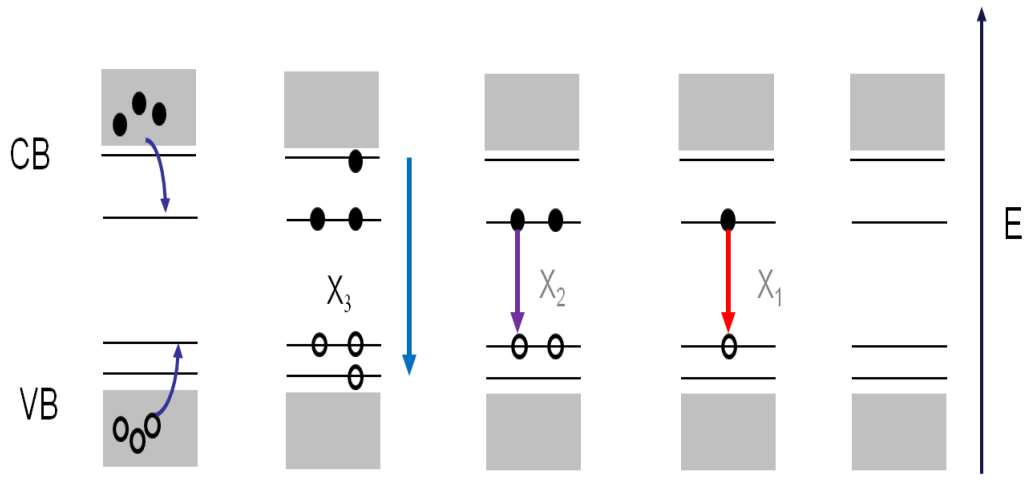

Figure 1.6: Schematic diagrams of radiative cascade of a single quantum dot and possible exciton states in case of non-resonant excitation approach. Dark black circles and white circles represent the electrons and holes respectively.

Feasibility of the above-mentioned procedure

To collect single-photon emission from a QD, the most critical point is to separate spectrally the exciton (X) from the biexciton (XX) emission. The full width at half maximum (FWHM) of the associated transitions should be smaller than the X-XX spectral separation, on the order of 1-2 meV in InGaAs QDs. This condition is easily meet at cryogenic temperature, where the excitonic line typically displays a FWHM of a few 10 μeV (or below) under non-resonant excitation [39]. When the temperature increases, dephasing processes associated with the coupling to the bulk matrix (in particular acoustic phonons) broaden the lines and set a maximum operation temperature [40, 41]. In addition, for a temperature range 50-100K or higher (for InAs QDs), the onset of thermally activated non-radiative processes spoil the radiative yield of the emitter.

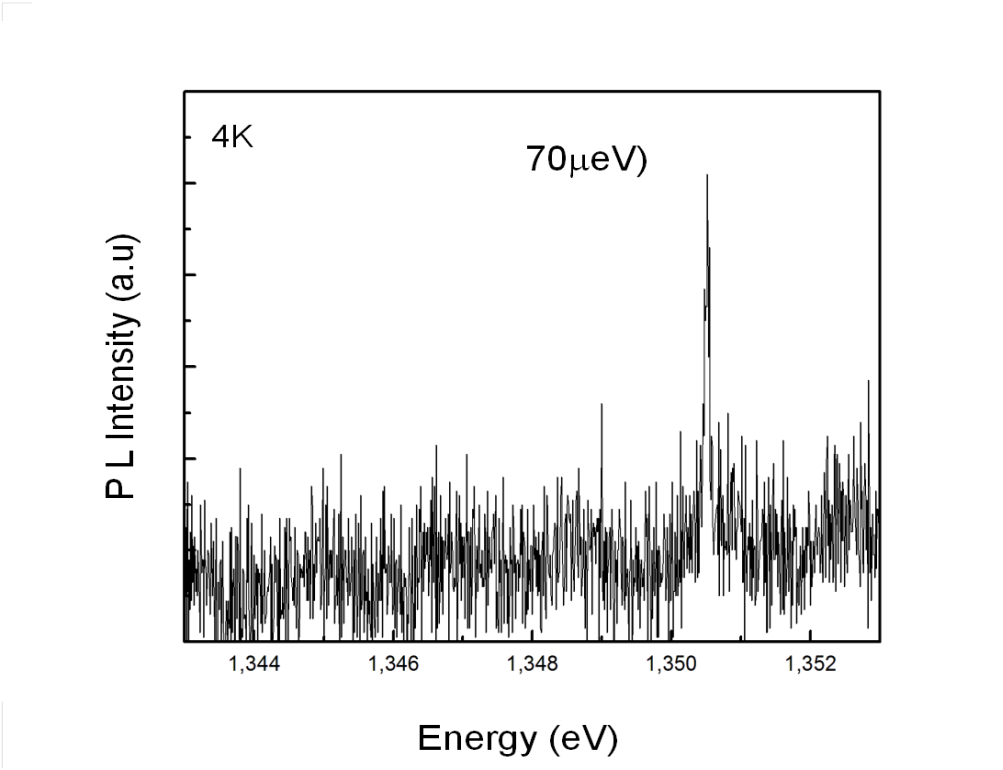

Figure 1.7: Micro-photoluminescence spectrum of a single quantum dot.

Figure 1.7 shows the high resolution μ-PL spectra of a single quantum dot that show a narrow emission line with FWHM~ 70μeV. Ideally it must show the narrow peak as like the delta function of electronic density of states. This deviation comes from homogenous broadening. The homogenous level broadening is an intrinsic QD property since it is result of carrier lifetime, carrier-phonon [42] and carrier-carrier interaction [43].

1.2.3 Improving the collection efficiency

A quantum dot is much smaller than the wavelength of the emitted light. Roughly, it thus emits light in all the directions. Moreover, it is embedded in a high index matrix: due to a total internal reflection at the semiconductor-air interface, a very small fraction of the light can be extracted (typically 1%) [45]. To improve the collection efficiency, various solutions have been proposed and developed so far: as discussed below, they can be classified in two categories:

Solutions from geometrical optics:

The first class of solutions is based on geometric optics. A review of several methods can be found in [44, 45]. One can cite mesa supported by a gold mirror, and solid immersion lenses that help to improve the outcoupling efficiency. Experimentally, the obtained efficiencies are in the 10% range [46].

Spontaneous emission control:

Another radically different approach uses a two steps strategy, which is illustrated in Figure 1.8. First, by embedding the emitter into a well chosen photonic structure, we control the spontaneous emission of the emitter, to funnel a large fraction β of its SE into an optical mode of interest. Second, the collection of the photons present in the optical mode is optimized, using a specific engineering of the photonic structure.

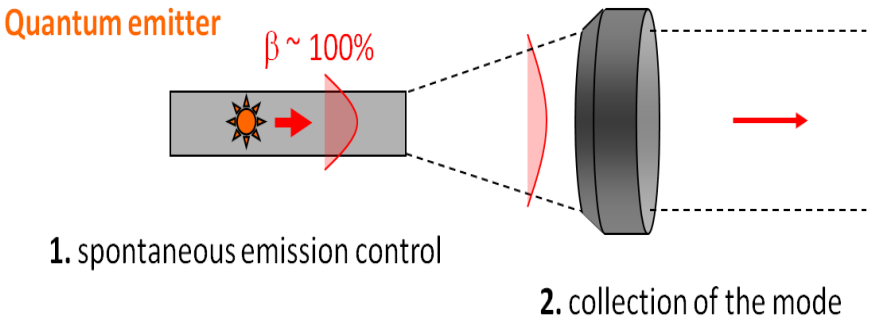

Figure 1.8: Spontaneous emission control strategy for the efficient single photon source.

The fraction β of SE funnelled into the mode of interest reads:

$$\beta = \frac{\Gamma_M}{\Gamma_{tot}} = \frac{\Gamma_M}{\Gamma_M + \gamma}, \quad (1.1)$$

with Γ_M the SE rate into the target mode, Γ_{tot} the total SE rate, equal to $\Gamma_M+\gamma$; γ is the SE rate into the continuum of the other modes, named after 'radiative' or 'leaky' modes. Achieving a high β thus requires $\Gamma_M>>\gamma$, which can be obtained with an enhancement of Γ_M or an inhibition of γ (or a combination of the two). The next section presents the physical effects that can be exploited to control the SE rates.

1.3 Various approaches to control spontaneous emission

This section presents various tool and approaches to control SE and discusses the associated state-of-the-art. Note also that we will discuss mostly SE control in the context of single-photon sources. It has however a broader interest, *e.g*. the development of low threshold nano-lasers [47, 48] or the realization of quantum optics experiments with a 1D atom (a two-level) [49].

1.3.1 How to control spontaneous emission rates?

Spontaneous emission is a fundamental process of light-matter interaction by which an emitter undergoes a transition from an excited energy state to a lower energy state and simultaneously emits a photon. Such a process is associated with the zero-point fluctuations of the electromagnetic fields, which destabilizes the excited states of the emitter. For simplicity, we consider here a two level emitter with a fundamental level |g> and an excited state |e>. The energy separation between these levels is $\hbar\omega_{eg}$. This emitter is also supposed to be point-like, so that we retain only the dipolar term in the interaction with the electromagnetic field. The spontaneous emission Γ rate is given by the Fermi golden rule [28]:

$$\Gamma = \frac{2\pi}{\hbar^2}\left|\langle e|-\mathbf{d}.\mathbf{E}|g\rangle\right|^2.\rho(\omega_{eg}), \quad (1.2)$$

Here, $\rho(\omega_{eg})$ is the spectral density of photonic modes seen by the emitter, at the emitter angular frequency ω_{eg}; **E** is the electrical field at the location of the emitter and **d** is the dipole operator. It is clear from this expression that Γ depends on the oscillator strength of the atomic transition, but is also highly dependent on the electromagnetic environment of the emitter (through **E** and $\rho(\omega_{eg})$). In the

following, we will briefly summarize the physical effects that offer a control over **E** and ρ (ω_{eg}).

1.3.1.1 Influence of the density of photonic states

Dimensionality of the photonic structure:

To achieve single mode emission, a first, natural idea is to use a localized optical mode, confined in a 0D photonic structure (as in microcavity). Ideally, the confinement in the 3 directions of space gives rise to a discrete energy spectrum, associated with resonant modes. However, after a certain time, which is proportional to the quality factor (Q-factor) of the mode, the photons escape from the cavity. Thus, we have to describe a localized mode coupled to a 3D reservoir of optical modes. In the weak coupling regime (characteristic emitter-mode coupling time >> photon escape time), one can show that the cavity mode is described as a quasi-continuum whose spectral density ρ_{0D} follows a Lorentzian profile. As pictured in Figure 1.9 (a), its line width at half maximum is inversely proportional to the resonance Q-factor. Because this quasi-continuum describes 1 mode, spectral integration leads to 1. The maximum density of states that can be experienced by a monochromatic emitter is thus proportional to Q.

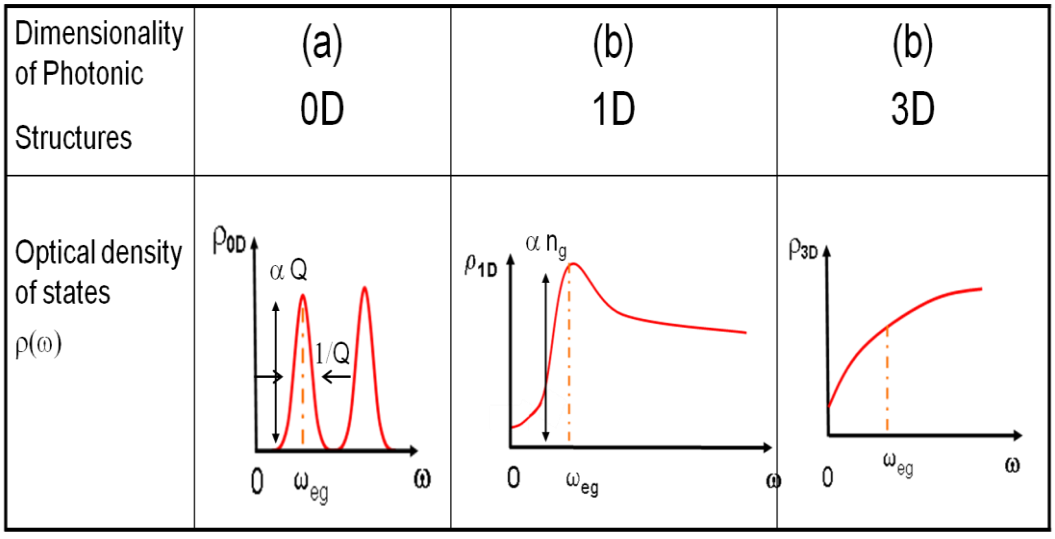

Figure 1.9: Strategy of SE control of an emitter through the engineering of the optical density of states by changing the dimension of the surrounding photonic structures.

By inserting the emitter inside a waveguide, one can also couple the emitter to a 1D continuum of modes with a spectral density ρ_{1D}. A typical profile is shown in Figure 1.9 (b). Such a distribution can also feature peaks, associated with low group velocity v_g. In that case, the maximum density of states experienced by a monochromatic emitter is proportional to the group index '$n_g=c/v_g$' (c is the speed of light in vacuum). To conclude, in both approaches one can control the density of photonic modes seen by emitter in comparison to the 3D bulk material (shown in Figure 1.9 (c)) by changing the dimensionality of the photonic structures.

Photonic bandgap structures:

This approach is inspired from the theoretical work of Yablonovitch [47]. In 1987, he invented photonic crystals, in which a periodic structurization of the dielectric function opens a photonic bandgap, that is to say a frequency range for which no optical mode exists. As discussed later on, the motivation was to suppress the SE into the continuum of 'useless' optical mode. Note that, strictly speaking, a complete photonic bandgap can only exist in an infinite 3D photonic crystal. An excited emitter placed inside a photonic crystal with an emission frequency in this bandgap will not be able to decay radiatively. Inhibition in the optical domain has been demonstrated in 3D- photonic crystal based on Titania inverse opals [50]. It was later realized that strong inhibition of the SE rate of an emitter can also be obtained in photonic crystals membranes, without creating a full photonic bandgap [51. 52].

1.3.1.2 Controlling the amplitude of the zero-point fluctuations

As seen in the Fermi golden rule, the SE rate into a given mode is also proportional to the square of the zero-point fluctuations of the electrical field at the location of the emitter. Increasing or suppressing these fluctuations is also a powerful route to control the SE rates

Increasing the SE rate through a spatial confinement of the mode:

The principle is illustrated in Figure 1.10: for a given mode, a confinement in one or several directions increases the amplitude of the field at the location of the emitter. For example, for a 0D optical mode confined in a microcavity, the amplitude of the zero-point fluctuations associated with the mode scales as $1/\sqrt{V}$, where V is the mode volume (precise definition in the next section) [28].

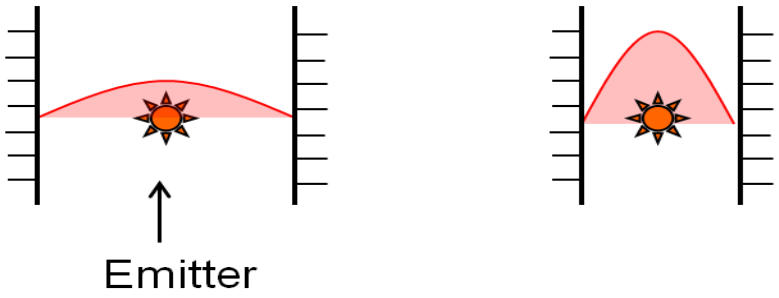

Figure 1.10: SE control approach based on the confinement effect.

Decreasing the SE rate using screening effects:

On another hand, it is also interesting to reduce the zero-point fluctuations of the field to suppress the coupling to the continuum of 'useless' modes. The structures that will be studied in this thesis are dielectric cylinders, made of a high refractive index material (GaAs, n=3.45). As illustrated in Figure 1.11, a dielectric screening effect reduces to a large extent the field inside the wire, for polarizations perpendicular to the wire axis. Briefly, the incident electric field polarizes the wire, leading to the appearance of surface charges which in turn generate a field opposite to the incident one. If the refractive index contrast between the wire and its surroundings is high enough, the total field inside the wire is considerably reduced.

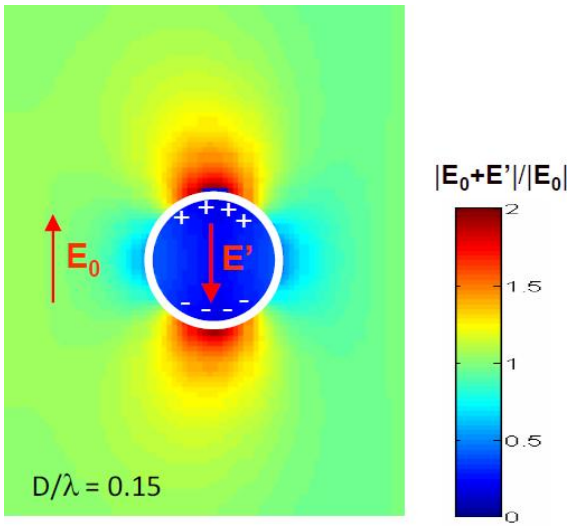

Figure 1.11: Illustration of the dielectric screening effect in a photonic nanowire. The plot is a map of the total electrical field amplitude. The white solid line represents the circumference of the wire.

As a remark, one can also mention that a finite photonic bandgap structure does not lead to a 'true' photonic bandgap. The action of Bragg reflection can be understood as a screening of the mode incident on the structure.

1.3.2 Two major strategies to control SE

In this section, we examine two strategies to obtain single-mode emission. The first one is resonant; it uses a resonant optical microcavity and has been inspired by atomic physics. The second approach, which has been used in this thesis, uses a waveguide and provides a broadband operation range.

1.3.2.1 Resonant SE control: the Purcell effect

In 1946 E.M. Purcell [53] proposed that the emitter's spontaneous rate could be dramatically enhanced when it is inserted in a resonant cavity; the so-called Purcell effect leads to a selective enhancement of Γ_M, the SE rate into the cavity mode. Choosing the SE rate Γ_{3D} of an emitter embedded in bulk GaAs as a reference, the maximum magnitude of this effect is captured by the Purcell factor $F= \Gamma_M/\Gamma_{3D}$. F is calculated for a maximum coupling to the cavity mode (on-resonance monochromatic emitter, emitter located on a maximum of the electrical field, linear dipole of the transition aligned along the electrical field). In these conditions,

$$F = \frac{3}{4\pi^2}\frac{Q}{V}\left(\frac{\lambda}{n}\right)^3, \qquad (1.3)$$

with λ the emission wavelength in vacuum, Q the quality factor of the mode and V the mode volume. Achieving a high Purcell factor thus requires a cavity able to store the photons over long times (high Q) and to confine the electromagnetic field over small volumes (small V).

In the early 1990s, the progress of the growth of QD (artificial atoms), and the simultaneous development of processing at sub-micron scale has triggered the development of cavity-emitter systems in semiconductors. Several geometries have been proposed and developed; among the best candidates one can cite: micropillar [27, 54-56], VCSEL-like cavities [57, 58], microdisk [30, 59] and 0D defect in photonic crystal membranes [60-64]. These structures are presented in Figure 1.12 (a) and (b). In micropillar, VCSEL-like and microdisk cavities, the coupling to the continuum of 'radiative' modes is not affected significantly (i.e.$\gamma \sim \Gamma_{3D}$). In addition to Purcell effect, 0D defect in photonic crystal membranes also offer a suppression of the emission into other modes ($\gamma << \Gamma_{3D}$).

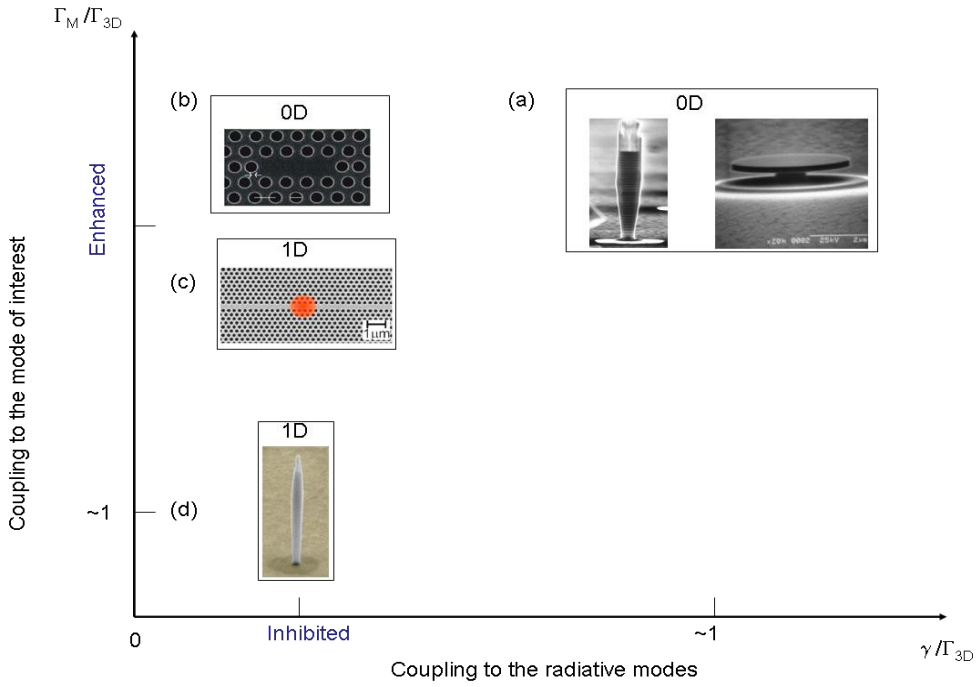

Figure 1.12: Various approaches to control the spontaneous emission, (a) Micropillar [56] and Microdisk [30], (b) Photonic nanocavity [61], (c) Photonic crystal waveguide [76] and (d) Photonic nanowire. Here Figure (a) and (b) represent the 0D photonic system while Figure (c) and (d) represents 1D photonic system.

Purcell-based single-photon sources:

To realize a bright single-photon source with a collection of light in the far-field, or to couple the emission to a monomode optical fiber, the control over the far-field radiation pattern of the cavity is also very important. To this respect, VCSEL-like or micropillar cavities, whose fundamental optical mode features a Gaussian structure [64], are the most advanced to date. By using this strategy, the first optically pumped solid state single-mode single-photon source has been demonstrated [55, 65, 66].as well electrical pumped SPS [75]. This approach has also been realized the situation when a single emitter is strongly coupled to the single optical mode of cavity under optical [67, 68] and electrical pumping [69]. In terms of global efficiency, photonic crystal structures are less advanced [70, 71], because of the difficulty to control the far-field emission pattern. Several solutions have been proposed, such as the efficient on-chip coupling to a waveguide [72] or near-field tunnelling to a monomode fiber [73]. One can also engineer the PhC

slab nanocavity geometry (by shifting holes or changing holes sizes etc), which can funnel the cavity mode into free space with reduce divergence angle. In principle unidirectional emission can be achieved by placing a mirror beneath the slab cavity [74]. Various single photon source based on this approach is shown in the Figure 1.13.

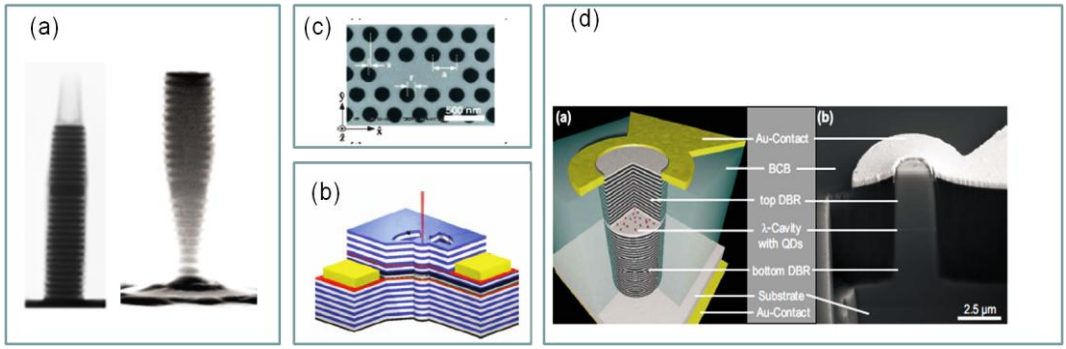

Figure 1.13: Purcell effect based single photon sources with, (a) Micropillar cavity [65,66], (b) Oxide aperture cavity [54], (c) Photonic crystal nanocavity [62], all of three are optically pumped and (d) Electrically pumped single photon source [75].

1.3.2.2. Limits of a resonant approach

The Purcell effect is a resonant effect; it is therefore limited to the narrow operation bandwidth of the cavity. For a cavity with Q>1000 operating with a resonance in the 1 µm wavelength range, the operation bandwidth of the system is below 1 nm. Such a resonant effect implies several constraints. The first one is practical: given the inhomogeneous distribution (50 nm) of self-assembled InAs QD, and the temperature tuning range of 1 nm, only a small fraction of the QDs will spectrally match the cavity. Moreover, this strategy is restricted to monochromatic emitters (with respect to the cavity linewidth): it will not be efficient for spectrally-broad emitters. For the realization of sources of entangled-photon pairs using a QD, one has to collect simultaneously the exciton and bi-exiton transition of a QD (1-3 nm of detuning in a typical InAs/GaAs QD). In the context of single-photon emission, non-resonant cavity feeding effect can spoil the purity of single-photon emission (for a strong, non-resonant excitation); these non-trivial effects will be discussed later on in the manuscript.

A supplementary drawback is the sensitivity of the radiation pattern of high-Q microcavities. It has been reported that the radiation pattern of high-Q

micropillars is partially spoiled by extrinsic loss mechanisms such as scattering by sidewall roughness [45]. Therefore the maximum efficiency of the source is limited to 40% for optically pumped QD-micropillar [54, 55, 65]. These considerations are general: after more than a decade of intense research, the practical realization of single photon source relying on the use of a micro / nano - resonator and offering extraction efficiencies close to 100% remains a challenge.

All these considerations motivate the quest for *non-resonant approaches* to control spontaneous emission. We describe two examples in the following.

1.3.2.3. First examples of SE control in a waveguide

To obtain a non resonant SE control, a possible idea consists in increasing the dimensionality of the photonic structure from 0D to 1D; in other word, to use a waveguide to control the SE of an embedded emitter.

Waveguide in photonic bandgap structures:

A convincing experiment has been performed on a waveguide defined in a photonic crystal membrane (see Figure 1.14) [76], following a theoretical proposal [77, 78]. In this structure, the good coupling to the guided mode is ensured by a tight lateral confinement of this mode. The coupling to the 3D continuum of 'leaky' modes is suppressed thanks to a photonic bandgap effect. These two effects are clearly shown in Figure 1.12 (c). In photonic crystal waveguides a large β-factor in excess of 95% has been theoretically predicted for the two in-plane QD dipole orientations over a 40 nm bandwidth [79], β-factors of up to 0.89 over a 20 nm bandwidth have been experimentally inferred for InAs QDs embedded into GaAs photonic crystal waveguide[76].

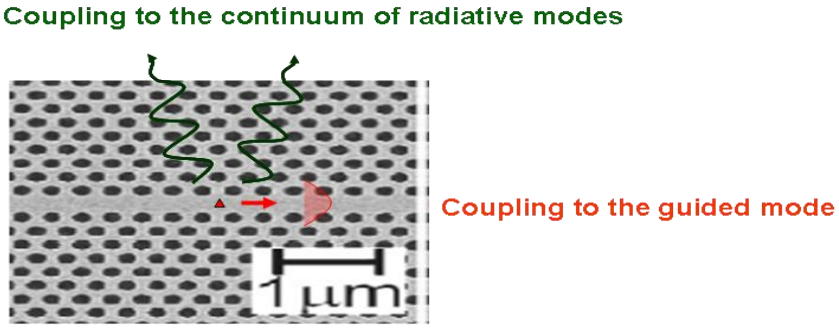

Figure 1.14: Spontaneous emission control mechanisms of photonic crystal waveguide [76].

As a remark, it is possible to further increase the coupling to the guided mode by playing with the dispersion relation of this mode. In the slow light regime (low group velocity v_g), the light-matter coupling is increased (the SE rate scales as 1/vg) [80]. However, this strategy restricts the operation bandwidth of the system.

Plasmonic waveguides:

Plasmonic waveguides offer another route for broadband SE control [81]. The coupling of an emitter to a metal nanowire, illustrated in Figure 1.15, has been demonstrated in Ref. [82]. This approach requires positioning the emitter very close to the metal surface (a few 10 nm), which can lead to the onset of non-radiative decay channels and quench the radiative efficiency of the emitter. In addition, the propagation of plasmons is lossy.

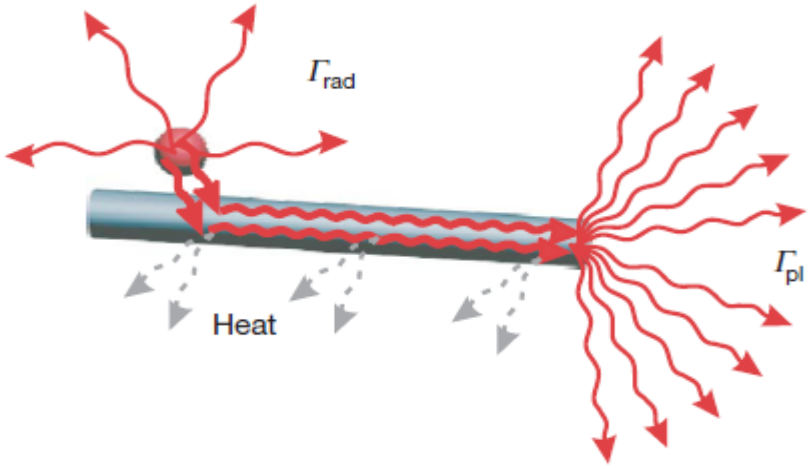

Figure 1.15: Spontaneous emission control in plasmonics waveguides [82].

1.4 This thesis: fiber-like photonic nanowires to realize efficient sources of quantum light

In this thesis, we demonstrate a new 1D photonic system to control SE: a fiber-like, vertical photonic nanowire (see Figure 1.16). This structure offers a unique combination of high-β, low losses, and controlled far-field pattern, provided that a proper engineering of the wire ends is conducted.

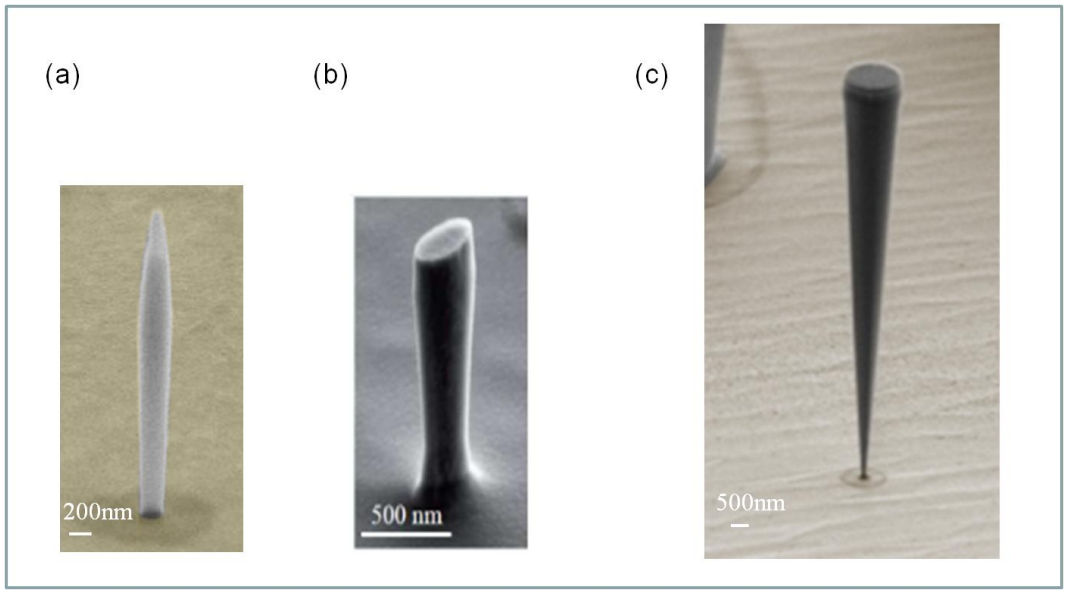

Figure 1.16: Photonic nanowire system with different shapes, (a) Regular taper photonic nanowire, (b) Elliptical photonic nanowire, and (c) Inverted taper based photonic wire.

1.4.1 Fiber-like photonic nanowires

More precisely, a dielectric photonic wire is a waveguide made of a high refractive index material, surrounded by a cladding with a low refractive index. They were first introduced in the context of planar ring microlasers [83]. We consider here a vertical, cylindrical photonic nanowire, a configuration more adapted to efficient light collection in the far-field. In our case, the wire is made of GaAs (n=3.45 at 950 nm) and is surrounded by air or vacuum (n=1). The wire embeds a single layer of self-assembled InAs QDs (typical emission wavelength in vacuum around 950 nm). The high refractive index contrast between the wire and the cladding has two important consequences. It first allows confining the guided mode very tightly, which ensures a good coupling to the embedded emitter. Second, a dielectric screening effect suppresses to a large extent the coupling to the 3D continuum of 'radiative' modes. This results in an efficient SE control, with β-factors exceeding 90% over a bandwidth larger than 100 nm at 950 nm.

Next, one has to collect efficiently the guided photons with a microscope objective located above the wire. For this goal, the two ends of the wire are carefully engineered. The photons emitted downward are reflected back into the guided mode with an integrated mirror, made of gold and silica. The upper wire

end features a conical tip, designed to deconfine progressively the guided mode into the cladding, in order to obtain a more directive far-field emission pattern.

The main experimental results described in this manuscript are:
- **The detailed investigation of SE in photonic nanowires**, in particular the demonstration of the inhibition of the SE into the continuum of 'radiative' modes
- **The realization of a bright single-photon source**, featuring a record single-photon emission efficiency (72% into the first collecting lens), combined with a pure single-photon emission.
- **The realization of a new generation of trumpet-like photonic wires**, that should bring the out-coupling efficiency closer to 100% (experiments are in progress).
- **The realization and study of photonic wires featuring an elliptical section**. In this geometry, the electromagnetic environment seen by an embedded emitter is dominated by a single mode, with a linear polarization oriented along the ellipse major axis.

1.4.2 Outline of the thesis

The thesis will cover all the aspects associated with the above-mentioned realizations: design, micro fabrication and optics experiments. After this introductory chapter, the thesis is organized as follows:

Chapters 2 describes the design of two high efficiency single-photon sources based on quantum dots embedded into photonic nanowires. In the first part of chapter, we analyse the mechanisms of spontaneous emission control in photonic nanowires and optimize the geometry to achieve a high β-factor. Then we optimize far field to increase the extraction efficiency by engineering the nanowire ends. We introduce a high reflectivity bottom mirror (combination of gold and silica) to reflect the photon emitted towards the substrate. To reduce the far field divergence we introduce two possibilities: regular tapering of the top facet and inverted taper photonic wires. These two geometries provide high efficiency single-photon emission.

Chapter 3 describes the fabrication of these two photonic nanowire structures. It begins with the description of the design details and epitaxial sample details for both structures. Then we discuss flip chip process to realize the high reflectivity composite bottom mirror for both structures. Afterward we discuss the fabrication

of the regular taper structures including the mask requirements and optimization of the etching. In the last part of the chapter we describe the fabrication process of the second geometry, specially discuss the etching mask and etching condition to realize this highly anisotropic structure.

Chapter 4 describes the optical performances of regular taper device. First we probe the SE control process of the photonic nanowire. We experimentally show that this structure provides moderate coupling of emitter to the fundamental guided mode. Then we demonstrate that the coupling to the radiative modes is strongly inhibited thanks to the dielectric screening effect. This geometry provides a broadband SE control. In the second part of the chapter, we demonstrate the performance of the device in context of single photon emission. We show that this structure provides the highly pure and highly efficient single photon emission in comparison to state-of-the-art cavity-based devices.

Chapter 5 introduces photonic nanowires with an elliptical cross section, which provide an electromagnetic environment dominated by a single guided mode, with a linear polarization oriented along the ellipse major axis. The first section presents the theoretical analysis and the optimization of the SE coupling factor β. Afterward we describe the fabrication process. In the last part of this chapter, we represent the optical characterization of this device. This structure provides the broadband and efficient polarization control which leads to the truly single mode spontaneous emission.

Chapter 6 concludes this thesis with a summary of the results and their relevance to the field of quantum information processing.

1.5 Contribution to the experimental work

During my PhD, I was mostly involved in the microfabrication in clean room for the optimization of the fabrication of the devices. The developments I conducted are fully developed in Chapter 3 and 5; they are briefly summarized below:

- *Flip-chip process*, to obtain a GaAs membrane on the top of a high reflectivity mirror (combination of gold and silica). This was the first critical step of our device fabrication, and has been used for numerous other projects.

- *E-beam lithography* (mask design using L-EDIT and operation of the JEOL 6300 FS e-beam system)
- *Optimization of the dry etching* (etching parameters and hard mask): this step, which defines the shape of the structures, is critical. We were able to realize photonic wires with a conical top taper, trumpet like structures and finally wires with a well-controlled elliptical cross-section. The main challenge was to control the shape of the wire while preserving smooth sidewalls.

Co-workers acknowledgment:

The work presented in this manuscript has been done under the supervision of Julien Claudon and Jean-Michel Gérard. It has required the joint efforts of people with complementary expertises. The simulation of the structures for design optimization has been performed by Yuntian Chen, Niels Gregersen and Jesper Mork (DTU Fotonik, Lyngby, Denmark) and Inbal Friedler, Ivan Maksymov, Jean-Paul Hugonin, Christophe Sauvan and Philippe Lalanne (Institut d'Optique, Orsay, France).

The experimental work has been entirely conducted in the team 'NanoPhysics and SemiConductors'.

- *Growth by molecular beam epitaxy of GaAs layer with embedded self-assembled InAs QDs*: Maela Bazin, Périne Jaffrennou and Emmanuel Dupuy.
- *Nanofabrication, clean room processing:* Julien Claudon and myself
- *Optics experiments:* Joël Bleuse, Mathieu Munsch and Megan Creasey

Besides the realizations presented in this thesis, I was also involved into other projects: they are listed below:

Electrically pumped single-photon source based on a photonic nanowire:

This project is the natural prolongation of the work presented in this thesis. The realization of this single-photon LED is relatively complex: I was involved in the definition of a suitable process flow and its optimization. We have performed 4 steps e-beam lithography alignment with an alignment accuracy of about 20 nm and the optimization of the n- and p-type contact recipes for GaAs. The first device (no bottom mirror) is almost ready for the experiment.

Coupling of InAs/GaAs quantum dots (QD) to whispering gallery mode (WGM) supported by a high-Q microtoroid cavity:

This project was my initial PhD project: the motivation was to couple a nice artificial atom to the ultra-high Q modes that are supported by a fused silica microtoroid. I was involved in the optimization of the fabrication of semiconductor QDs mesa, the device assembling and optical characterization. The mesas were realized using a top-down approach (e-beam lithography and etching). The fused silica microtoroids were provided by Jean-Baptiste Jager (SP2M/SINAPS). We realized the device by assembling the microtoroid and mesa on the same chip with the help of Focussed Ion Beam (FIB) equipped with a manipulation tip (with Violaine Salvador (SP2M/LEMMA) and Marlène Terrier (SP2M/NPSC)) which is shown in Figure 1.17. In optical characterization, this device demonstrated a coupling between the QD and WGM of microtoroid, with relatively low optical Q-factors, in the 1000 range.

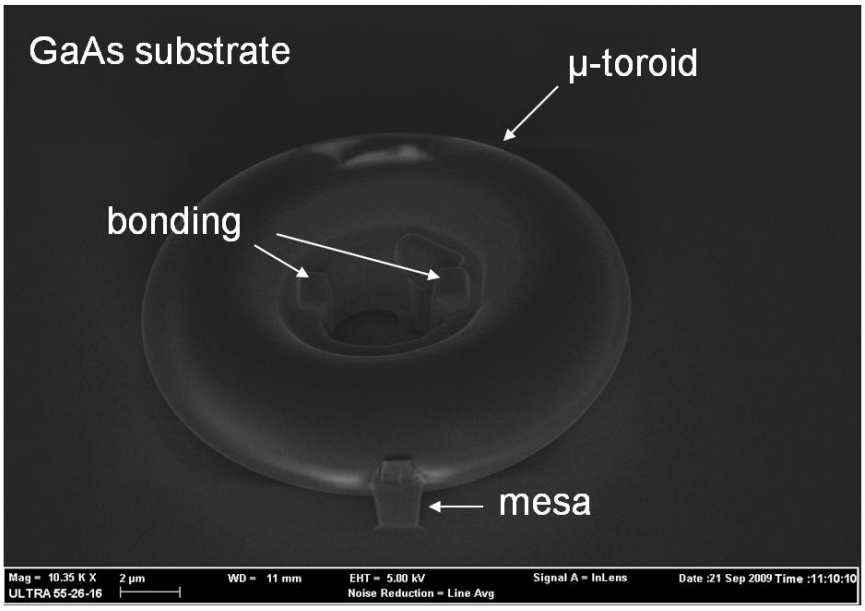

Figure 1.17: SEM image of quantum dots mesa and microtoroid assembly realized on the same chip by FIB manipulation.

Whispering gallery mode lasing in a micropillar cavity (room temperature operation with electrical pumping):

This laser is a first step toward the realization of a compact and innovative THz radiation source, which exploits the non-linear generation of THz, through the frequency difference of two near infrared WGMs. The epitaxial samples were provided by Wurzburg University, and I conducted the fabrication (single e-beam lithography step to define the top contact and the etching mask + participation to

the optimization of the etching). The laser has demonstrated lasing at 300K, under electrical pumping (wavelength around 920 nm). Figure 1.18 shows the SEM image of the realized device with the electrical contacts scheme and we drilled the annular trenches with FIB to reduce the number of QDs uncoupled to WGM of pillars that leads to the reduction of lasing threshold.

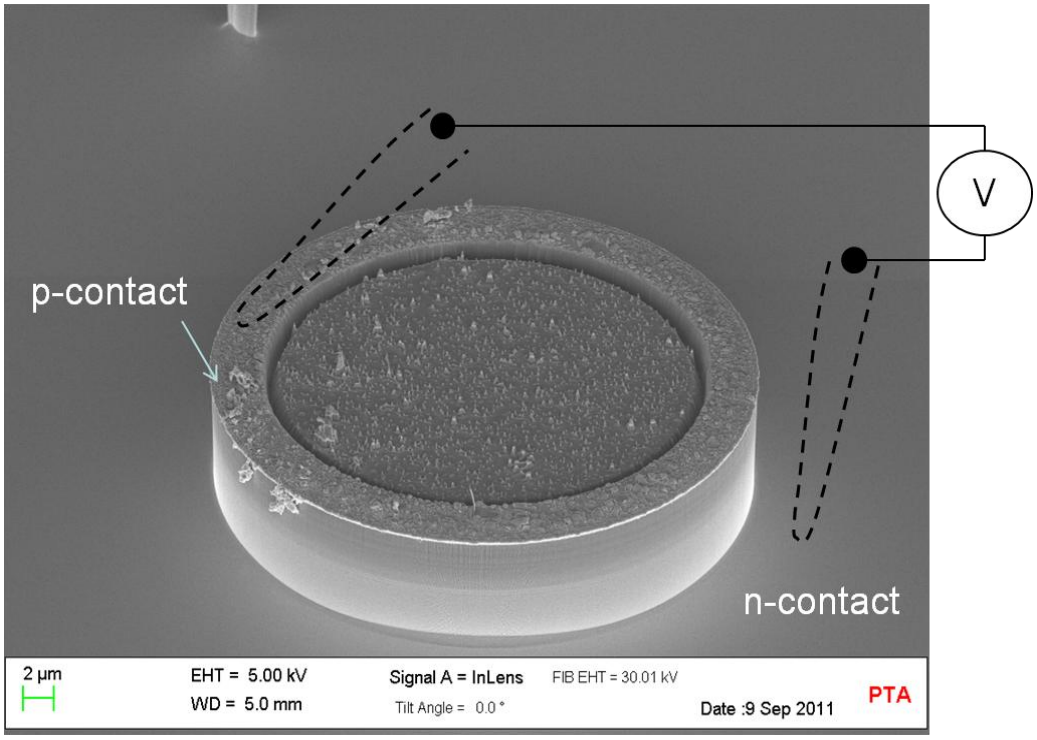

Figure 1.18: SEM image of Whispering gallery mode laser based on micropillar cavity and the electrical contacts scheme of device.

Coherent X-ray diffraction imagining of single InAs monolayer / InAs QDs embedded in GaAs nanowire:

This project, in collaboration with Francesca Mastropietro, Vincent Favre Nicolin (SP2M/NRS) and Joel Emery (SP2M/NPSC), targets the localisation of single heterostructures (InAs QD or QW), using coherent X-ray diffraction (experiment performed at the SYNCHROTRON, Grenoble). To this end, a key requirement is to isolate the signal of the wire from the one of the background most probably from the substrate. We thus exploited the know-how developed in the context of photonic wire single-photon sources, to define wires on a Silicon (Si) substrate by using 3 µm thick Silicon nitride intermediate layers. Figure 1.19

shows the SEM images of nanowires defined on the top of Silicon nitride layer lying on the Si-substrate.

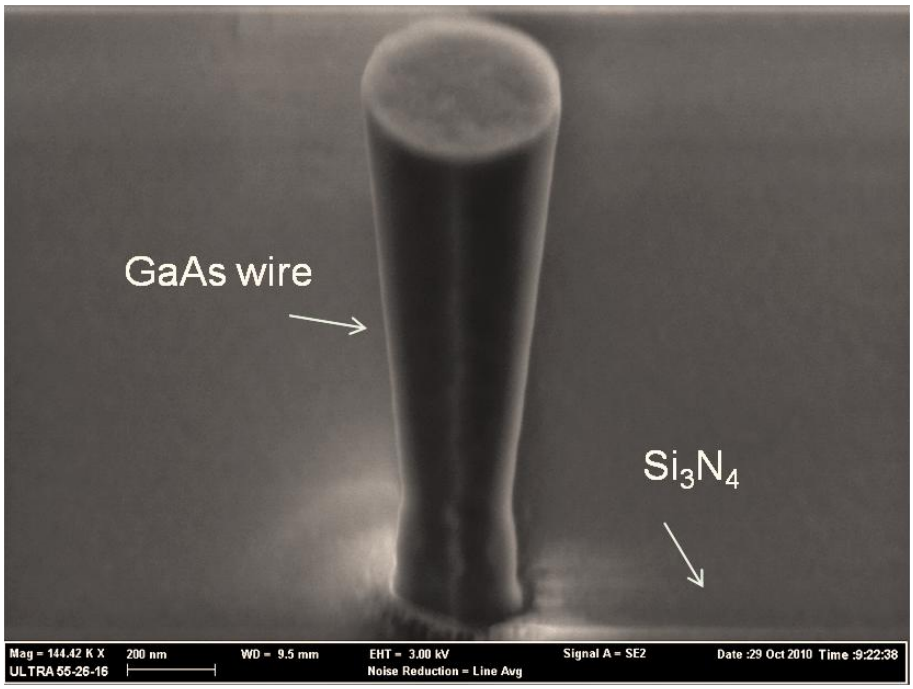

Figure 1.19: SEM image of the GaAs nanowire with embedded InAs monolayer/InAs QDs lying on the top of Si_3N_4 layer.

References

1. A. Ekert D. Bouwmeester and A. Zeilinger, "*The Physics of Quantum Information."* Springer Verlag, (Berlin), (2000).
2. I. L. Chuang and M.A. Nielsen, "*Quantum Computation and Quantum Information*," Cambridge University Press, (2000).
3. A. Shields, "*Semiconductor quantum light sources*," Nature Photonics **1**, 215 (2007).
4. E. Knill, R. Laflamme, and G. J. Milburn, "*A scheme for efficient quantum computation with linear optics*," Nature **409**, 46-52 (2001).
5. N. Gisin, G.G Ribordy, W. Tittel, and H. Zbinden, "*Quantum cryptography*," Rev. of Mod. Phys. **74**(1), 145 (2002).
6. E. Waks, K. Inoue, C. Santori, D. Fattal, J. Vuckovic, G.S. Solomon, and Y. Yamamoto, "*Secure communication: Quantum cryptography with a photon turnstile*, " Nature **420**, 762 (2002).
7. P. Kok, W.J .Munro, K. Nemoto, T.C. Ralph, J. P. Dowling, and G.J. Milburn, "*Linear optical quantum computing with photonic qubits*," Rev. Of Mod. Phys. **79** (1), 135 (2007).

8. H. J. Briegel, W. Dur, J.I. Cirac, and P. Zoller, "*Quantum repeaters: The role of imperfect local operations in quantum communication*," Phys. Rev. Lett. **81**, 5932 (1998).
9. B. Lounis and M. Orrit, "*Single-photon sources*," Rep. Prog. Phys. **68**, 1129 (2005).
10. A. Muller, T. Herzog, B. Huttner, W. Tittel, H. Zbinden, and N. Gisin, "*Plug and play systems for quantum cryptography*," Appl. Phys. Lett. **70**, 793 (1997).
11. W. T. Buttler, R. J. Hughes, P. G. Kwiat, et al., "*Free-space quantum-key distribution*," Phys. Rev. A **57**, 2379 (1998).
12. G. Brassard, N. Lutkenhaus, T. Mor, and B. C., *Sanders*, "*Limitations on practical quantum cryptography*," Phys. Rev. Lett. **85**, 1330 (2000).
13. S. A. Castelletto and R. E. Scholten, "*Heralded single photon sources: a route towards quantum communication technology and photon standards*," Eur. Phys. J. Appl. Phys. **41**, 181 (2008).
14. C. K. Hong and L. Mandel, "*Experimental realization of a localized one photon state*," Phys. Rev. Lett. **56**, 58 (1986).
15. G. Brassard, N. L¨utkenhaus, T. Mor, and B. C. Sanders, "*Limitations on practical quantum cryptography*," Phys. Rev. Lett. **85**, 1330 (2000).
16. H. J. Kimble, M. Dagenais, and L. Mandel, "*Photon antibunching in resonance fluorescence,*" Phys. Rev. Lett. **39**, 691 (1977).
17. A. Kuhn, M. Hennrich, and G. Rempe, "*Deterministic single-Photon source for distributed quantum networking*," Phys. Rev. Lett. **89**, 067901 (2002).
18. M. Keller, B. Lange, K. Hayasaka, W. Lange, and H. Walther, "*Continuous generation of single photons with controlled waveform in an ion-trap cavity system*," Nature **431**, 1075 (2004).
19. F. Diedrich and H. Walther, "*Nonclassical radiation of a single stored ion. Phys. Rev. Lett.*," **58(3),** 203 (1987).
20. T. Basche, E. W. Moerner, M. Orrit, and H. Talon, "*Photon antibunching in the fluorescence of a single dye molecule trapped in a solid*," Phys. Rev. Lett. **69,** 1516 (1992).
21. B. Lounis and W. E. Moerner, "*Single photons on demand from a single molecule at room temperature*," Nature **407**, 491 (2000).
22. R. Brouri, A. Beveratos, J. P. Poizat, and P. Grangier, "*Photon antibunching in the fluorescence of individual color centers in diamond*," Opt. Lett. **25**, **1294** (2000).
23. C. Kurtsiefer, S. Mayer, P. Zarda, and H.Weinfurter, "*Stable solid-state source of single photons*," Phys. Rev. Lett. **85**, 290 (2000).
24. D. A. Simpson, E. Ampem-Lassen, B. C. Gibson, S. Trpkovski, F. M. Hossain, S. T. Huntington, A. D. Greentree, L. C. L. Hollenberg and S. Prawer, " *A highly efficient two level diamond based single photon source,*' Appl. Phys. Lett. **94**, 203107 (2009).
25. P. Michler, A. Imamoglu, M. D. Mason, P. J. Carson, G. F. Strouse, and S. Buratto, "*Quantum correlation among photons from a single quantum dot at room temperature*," Nature, **406**, 968 (2000).

26. A. J. Bennett, D. C. Unitt, P. Atkinson, D. A. Ritchie, and A. J. Shields, "*High performance single photon sources from photolithographically defined pillar microcavities*," Opt. Exp. **13**, 50 (2005).
27. J.-M. Gérard, and B. Gayral, "*Strong Purcell effect for InAs quantum boxes in three-dimensional solid-state microcavities*," J. Lightwave of Technology **17**, 2089 (1999).
28. J.-M. Gérard, "*Solid-State Cavity-Quantum Electrodynamics with Self-Assembled Quantum Dots,*" *Single quantum dots: Fundamentals, applications and new concepts* **90**, 269 (2003).
29. C. Santori, M. Pelton, G. Solomon, Y. Dale, and Y. Yamamoto, "*Triggered single photons from a quantum dot*," Phys. Rev. Lett. **86**, 1502 (2001).
30. P. Michler, A. Kiraz, C. Becher, W.V. Schoenfeld, P.M. Petroff, L.D. Zhang, E. Hu, and A. Imamoglu, "*A quantum dot single-photon turnstile device*," Science **290**, 2282 (2000).
31. Z. L. Yuan, B. E. Kardynal, R. M. Stevenson, A. J. Shields, C. J. Lobo, K. Cooper, N. S. Beattie, D. A. Ritchie, and M. Pepper, "*Electrically driven single-photon source*," Science **295**, 102(2002).
32. D. Bimberg, M. Grundmann, and M.M. Ledenstov, "*Quantum Dot Heterostructures*," Wiley, Chichester, (1999).
33. Y. Masumoto, T. Takagahara, "*Semiconductor quantum dots: physics, spectroscopy and applications*," Springer, (2002).
34. G. Cassabois, *"Origines et limites du modèle de l'atome artificiel pour une boîte quantique de semiconducteurs*," HDR Thesis, Universite Paris VI (2006).
35. B. Ohnesorge, M. Albrecht, J. Oshinowo, A. Forchel, and Y. Arakawa, "*Rapid carrier relaxation in self-assembled* $In_xGa_{1-x}As/GaAs$ *quantum* dots," Phys. Rev. B **54**, 11532 (1996).
36. Y. Masumoto, T. Takagahara, "*Semiconductor quantum dots: physics, spectroscopy and applications*," Springer, (2002).
37. P. Michler, editor, "*Single Quantum Dots: Fundamentals, Applications and New Concepts*," Springer-Verlag, Berlin, (2003).
38. O. Benson, C. Santori, M. Pelton and Y. Yamamoto, "*Regulated and Entangled Photons from a Single Quantum Dot*," Phys. Rev. Lett. **84**, 2513 (2000).
39. C. Kammerer, C. Voisin, G. Cassabois, C. Delalande, Ph. Roussignoal, F. Klopf, J. P. Reithmaier, A. Forchel and J.-M. Gérard, "Line narrowing in single semiconductor quantum dots: Toward the control of environment effects," Phys. Rev. B **66**, 041306(R) (2002).
40. I. Favero, A. Bertelot, G. Cassabois, C. Voisin, C. Delalande, Ph. Roussignol, R. Ferreira and J.-M. Gérard, "*Temperature dependence of the zero-phonon linewidth in quantum dots : An effect of fluctuating environment*," Phys. Rev. B **75**, 073308 (2007).
41. L. Besomes, K. Kheng, L. Marsal and H. Mariette, "*Acoustic photon broadening mechanism in single quantum dot emission*," Phys. Rev. B **63**, 155307 (2007).

42. K. Leosson, B. Birkedal, I. Magnusdottir, W. Langbein, and J. M. Hvam, "*Homogeneous linewidth of self-assembled III-V quantum dots observed in single-dot photoluminescence*", Physica E **17**, 1 (2003).
43. A. V. Uskov, I. Magnusdottir, B. Tromborg, J. Mørk, and R. Lang, "*Line broadening caused by Coulomb carrier-carrier correlations and dynamics of carrier capture and emission in quantum dots*", Appl. Phys. Lett. **79**, 1679 (2001).
44. V .Zwiller, T. Aichele, and O. Benson, "*Quantum optics with single quantum dot devices*," New J. of Phys. **6**, 96 (2004).
45. W. L. Barnes, G. Bjork, J.-M. Gérard, P. Jonsson, J. A. E. Wasey, P. T. Worthing and V. Zwiller, "*Solid-state single photon sources: light collection strategies*," Eur. Phys. J. D **18**, 197 (2002).
46. V. Zwiller and G. Bjork, *"Improved light extraction from emitters in high refractive index materials using solid immersion lenses*," J. Appl. Phys. **92**, 660 (2002).
47. E. Yablonovitch, "*Inhibited spontaneous emission in solid-state physics and electronics*," Phys. Rev. Lett. **58**, 2059 (1987).
48. B. Ellis, M. A. Mayer, G. Shambat, T. Sarmiento, J. Harris, E. E. Haller, and J. Vuckovic, "*Ultralow-threshold electrically pumped quantum dot photonic-crystal nanocavity laser*," Nature Photonics **5**,297 (2011).
49. Q. Turchette, R. Thompson, and H. Kimble, "*One dimensional atoms*" Appl. Phys. B **60**, S1 (1995).
50. P. Lodahl, A. Floris van Driel, I. S. Nikolaev, A. Irman, K. Overgaag, D. Vanmaekelbergh and W. L. Vos, "*Controlling the dynamics of spontaneous emission from quantum dots by photonic crystals*," Nature **430**, 654 (2004).
51. S. M. Barnett and R. Loudon, "*Sum Rule for the Modified Spontaneous Emission Rates*, Phys. Rev. Lett. **77**, 2444 (1996).
52. S. Noda, M. Fujita and T. Asano, "*Spontaneous emission control by photonic crystals and nanocavities*," Nature Photonics **1**, 449 (2007).
53. E.M. Purcell, "*Spontaneous emission Probabilities at radio frequency*, " Phys. Rev **69**, 681 (1946).
54. S. Strauf, N. G. Stoltz, M. T. Rakher, L. A. Coldren, P. M. Petroff, and D. Bouwmeester, "*High-frequency single-photon source with polarization control*," Nature Photonics **1**, 704 (2007).
55. E. Moreau, I. Robert, L. Manin, V. Thierry-Mieg, J.-M. Gérard and I. Abram, "*A single-mode solid-state source of single photons based on isolated quantum dots in a micropillar*," Physica E **13**, 418 (2002).
56. J.-M. Gérard, B. Sermage, B. Gayral, B. Legrand, E. Costard and V. Thierry-Mieg, "*Enhanced spontaneous emission by quantum boxes in a monolithic optical microcavity*," Phys. Rev. Lett. **81**, 1110 (1998).
57. H. Saito, K. Nishi, I. Ogura, S. Sugou, and Y. Sugimoto, "*Room-temperature lasing operation of a quantum dot vertical-cavity surface-emitting laser*," Appl. Phys. Lett. **69**, 3140 (1996).
58. M. Karsaian, and D. Botez, "*Single-lobed far-field radiation pattern from surface-emitting complex-coupled distributed-feedback diode lasers*," Appl. Phys. Lett. **67**, 2783 (1995).

59. B. Gayral, J. M. Gérard, A. Lemaıtre, C. Dupuis, L. Manin, and J. L. Pelouard, "*High-Q wet-etched GaAs microdisks containing InAs quantum boxes*," Appl. Phys. Lett. **75**, 1908 (1999).
60. A. Kress, F. Hofbauer, N. Reinelt, M. Kaniber, H. J. Krenner, R. Meyer, G. Bohm, and J. J. Finley, "*Manipulation of the spontaneous emission dynamics of quantum dots in two-dimensional photonic crystals*," Phys. Rev. B **71**, 241304(R) (2005).
61. D. Englund , D. Fattal, E. Waks, G. Solomon, B. Zhang, T. Nakaoka, Y. Arakawa, Y. Yamamoto, and J.Vuckovic, "*Controlling the spontaneous emission rate of single quantum dots in a two-dimensional photonic crystal*," Phys. Rev. Lett. **95**, 013904 (2005).
62. W. H. Chang, W.Y. Chen, H.S. Chang, T. P. Hsieh, J. I. Chyi, and T. M. Hsu, "*Efficient single-photon sources based on low-density quantum dots in photonic-crystal nanocavities*," Phys. Rev. Lett. **96**, 117401(2006).
63. M. Fujita, S. Takahashi, Y. Tanaka, T. Asano and S. Noda, "*Simultaneous Inhibition and Redistribution of Spontaneous Light Emisson in Photonic Crystals*, Science **308**, 1296 (2005).
64. H. Rigneault, J. Broudic, B. Gayral and J.-M. Gérard, "*Far-field radiation from quantum boxes located in pillar microcavities,"* Opt. Lett. **26**, 1595 (2001).
65. M. Pelton, C. Santori, J. Vuc˘kovic´, B. Zhang, G. S. Solomon, J. Plant, and Y. Yamamoto, " *Efficient Source of Single Photons: A Single Quantum Dot in a Micropost Microcavity*, " Phys. Rev. Lett. **89,** 233602(2002).
66. E. Moreau, I. Robert, J. M. Gérard , I. Abram, L. Manin, and V. Thierry-Mieg," *Single-mode solid-state single photon source based on isolated quantum dots in pillar microcavities*," Appl. Phys. Lett. **79**, 2865 (2001).
67. J. P. Reithmaier, G. Se¸k, A. Lo¨ffler, C. Hofmann, S. Kuhn, S. Reitzenstein, L. V. Keldysh, V. D. Kulakovskii, T. L. Reinecke and A. Forchel," *Strong coupling in a single quantum dot–semiconductor microcavity system,"* Nature **432**,197 (2004).
68. L. C. Andreani, G. Panzarini, and J.M. Gérard, "*Strong-coupling regime for quantum boxes in pillar microcavities: Theory,"* Phys. Rev. B **60**, 13276 (1999).
69. C. Kistner, K. Morgener, S. Reitzenstein, C. Schneider, S. Höfling, L. Worschech, A. Forchel, P. Yao, and S. Hughes, "Strong *coupling in a quantum dot micropillar system under electrical current injection*," Appl. Phys. Lett. **96**, 221102 (2011).
70. S. Laurent, S. Varoutsis, L. Le Gratiet, A. Lemaître, I. Sagnes, F. Raineri, A. Levenson, I. Robert-Philip, and I. Abram, "*Indistinguishable single photons from a single-quantum dot in a two-dimensional photonic crystal cavity*," Appl. Phys. Lett. **87**,163107 (2005).
71. M. Kaniber, A. Laucht, T. Hurlimann, M. bichler, R. Meyer, M.C. Amann and J. J. Finely, "*Highly efficient single-photon emission from single quantum dots within a two-dimensional photonic band-gap*," Phys. Rev. B **77**, 073312 (2002).

72. D. Englund, A. Faraon, B. Y. Zhang, Y. Yamamoto, J. Vuckovic, "*Generation and transfer of single photons on a photonic crystal chip*," Opt. Exp. **15**, 5550 (2007).
73. C. Grillet, C. Monat, C. L. C. Smith, B. J. Eggleton, D. J. Moss, S. Frederik, D. Dalacu, P. J. Poole, J. Lapointe, G. Aers, and R. L. Williams, "*Nanowire coupling to photonic crystal nanocavities for single photon sources*," Opt. Express **15**, 1267 (2007).
74. S. H. Kim, S. K. Kim and Y. H. Lee, "*Vertical beaming of wavelength scale photonic crystal resonators*," Phys. Rev. B **73**, 235117 (2006).
75. T. Heindel, C. Schneider, M. Lermer, S.H. Kwon, T. Braun,S. Reitzenstein, S. Höfling, M. Kamp, and A. Forchel, "*Electrically driven quantum dot-micropillar single photon source with 34% overall efficiency*," Appl. Phys. Lett. **96**, 011107 (2010).
76. T. Lund-Handsen, S. Stobbe, B. Julsgaard, H. Thyrrestrup, T. Sünner, M. Kamp, A. Forchel, and P. Lodahl, "*Experimental realization of highly-efficient broadband coupling of single quantum dots to a photonic crystal waveguide,*" Phys. Rev. Lett. **101**, 113903 (2008).
77. V. S. C Manga Rao and S. Hughes, "*Single quantum-dot spontaneous emission in a finite-size photonic crystal waveguide: Proposal for an efficient "on chip" single photon gun,"* Phys. Rev. Lett. **99**, 193901 (2007).
78. G. Lecamp, P. Lalanne, and J. P. Hugonin, "*Very large spontaneous emission β-factors in photonic crystal waveguides*," Phys. Rev. Lett. **99**, 023902 (2007).
79. V. S. C Manga Rao and S. Hughes, "*Single quantum-dot Purcell factor and β-factor in photonic crystal waveguide*," Phys. Rev. B **75**, 205437 (2007).
80. Y. A. Vlasov, M O'Boyle, H.F. Hamann and S. J. McNab, "*Active control of slow light on a chip with photonic crystals waveguides*," Nature **438**, 65 (2005).
81. D. E. Chang, A. S. Sørensen, P. R. Hemmer and M. D. Lukin, "*Quantum optics with surface plasmons*," Phys. Rev. Lett. **97**, 053002 (2006).
82. A. V. Akimov, A. Mukherjee, C. L. Yu, D. E. Chang, A. S. Zibrov, P. R. Hemmer, H. Park and M. D. Lukin, "*Generation of single optical plasmons in metallic nanowires coupled to quantum dots*," Nature **450**, 402 (2007).
83. J. P. Zhang, D. Y. Chu, S. L. Wu, S. T. Ho, W. G. Bi, C. W. Tu, and R. C. Tiberio," *Photonic-wire laser*" Phys. Rev. Lett. **75**, 2678 (1995).

Chapter 2

Design of High Efficiency Single Photon Sources Based on Photonic Nanowire

---

Design can be art. Design can be aesthetics. Design is so simple, that's why it is so complicated. - ***Paul Rand***

The goal of this chapter is to introduce the reader to the main underlying physical ideas which are behind the design optimization and operation of the optically pumped single photon source. This theoretical chapter provides the elements to design an efficient single photon source based on a QD inserted in a dielectric photonic nanowire. We provide the basic light-matter interactions and optical properties of the single photon sources, which are enabled by inserting single quantum dots inside the photonic nanowires. The chapter is divided into two main sections. The first one details the mechanisms of spontaneous emission control in a photonic nanowire. In particular, we show that for an optimal wire diameter, all the emission of the embedded QD can be funnelled into the fundamental guided mode. The second section describes how the collection of the guided photons can be brought close to unity with a proper engineering of the wire ends.

2.1 Control of spontaneous emission in an infinite photonic nanowire

This section deals with the control of the spontaneous emission of an emitter embedded inside an infinite photonic nanowire. The wire is made of GaAs (n=3.45) and features a circular section with a diameter *D*. In all the section, we assume, emission wavelength of the emitter is λ=950 nm, which is a typical value for the fundamental optical transition of self-assembled InAs QDs. Depending on the wire diameter, the emitter is coupled to one or several families of guided modes. In parallel, it is also coupled to a continuum of free-space modes that are called 'radiative' modes in the following, which are shown in Figure 2.1. In this section, we first analyse the emission rate into the guided modes and the coupling to the radiative modes. We then show how to maximize the fraction of spontaneous emission coupled to the fundamental guided mode, the so-called β -factor.

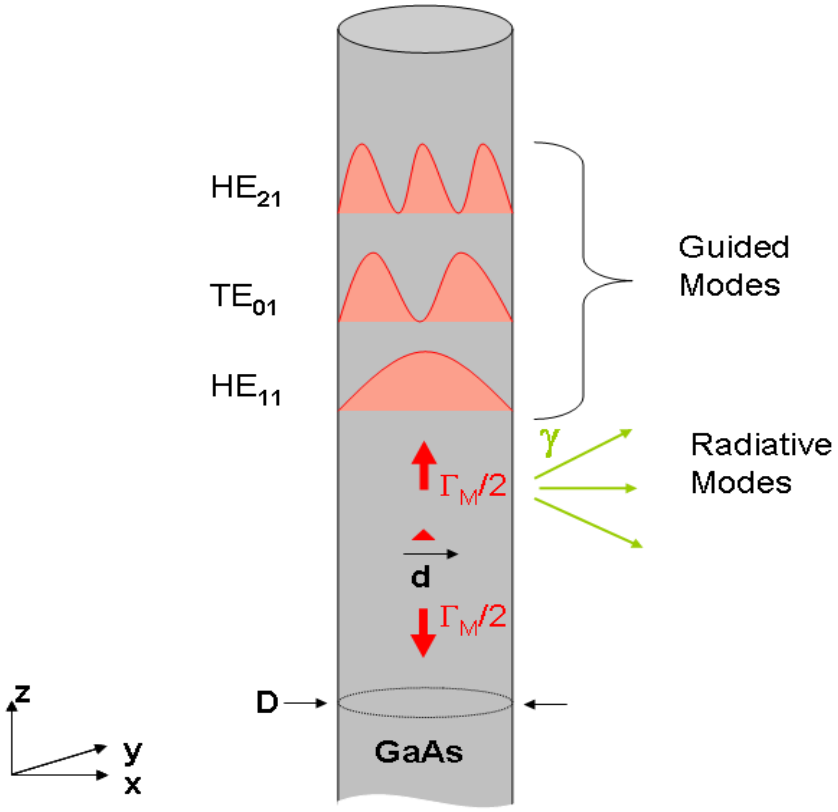

Figure 2.1: Various decay channels for an emitter embedded into a photonic wire.

2.1.1 Coupling to the guided mode(s)

In this section we discuss the coupling of an emitter to guided modes of the photonic wire.

2.1.1.1 Guided modes supported by a photonic nanowire

We first consider optical modes that are guided by the nanowire: the structure provides a confinement of the optical field in the two lateral dimensions (x and y) and the mode propagates freely in the third direction (z) as shown in Figure 2.1. In General, the electrical field associated to these modes has the following structure

$$\mathbf{E}(r,t) \propto \mathbf{f}(x,y)e^{i(\beta z-\omega t)}, \qquad (2.1)$$

In this expression, the function **f**(x, y) describes the spatial structure of the guided mode; it is normalized such as its maximum amplitude is 1 and β is the propagation constant in the z-direction. A full calculation of the modes guided by a dielectric cylinder can be found in the PhD thesis of Bruno Gayral [1]. We also use in this paragraph the program that he has developed to find the dispersion relation $\omega = \omega(\beta)$ of these modes.

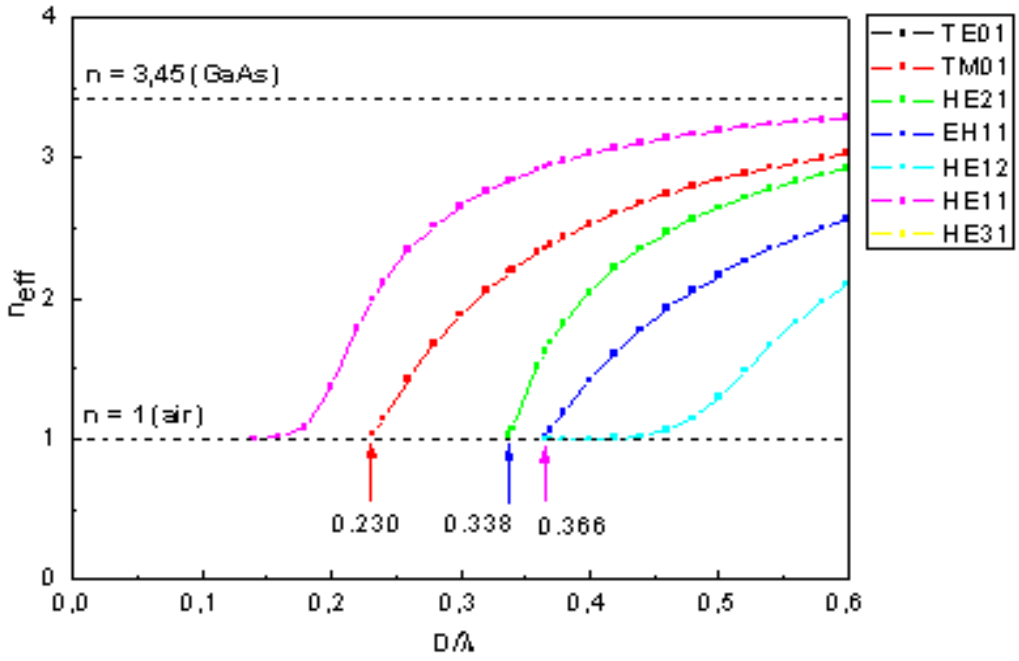

Figure 2.2: Effective index n_{eff} of the first guided modes in a GaAs wire.

Figure 2.2 displays the effective index n_{eff} as a function of reduced diameter (D/λ) for the first guided modes (HE_{mn}, EH_{mn}, TE_{mn} and TM_{mn}) that are supported by the structure. The dielectric wire always supports a fundamental guided mode HE_{11}. In the small diameters range ($D<0.18\lambda$), its effective index is very close to 1, indicating that the mode is completely deconfined in the air surrounding the wire. Above $D=0.18\lambda$, n_{eff} increases at a fast pace with D, indicating that the mode is progressively well confined in the GaAs. For $D>0.230\lambda$, two new families of guided modes appear (TE_{01} and TM_{01}). However, they feature zero amplitude on the wire axis and can be neglected for a dot located at this position. The second family of modes with a non-zero component on the wire axis is HE_{21}: it appears in the structure for $D>0.338\lambda$. As D is further increased, the number of guided modes increases, and their effective indices tend toward 3.45, the refractive index of GaAs.

2.1.1.2 Generalized Purcell factor of a guided mode

We now consider the coupling between an excited two-level emitter and a 1D continuum of modes which are supported by photonic wire (see Figure 2.3 (b)). We respectively denote $|g\rangle$ and $|e\rangle$ the ground state and the excited state of the emitter. ω_{eg} is the Bohr frequency associated to the e - g transition. This emitter is also supposed to be punctual (very small as compared to the optical wavelength), in order that the multipolar interaction terms with an order exceeding 2 can be neglected. In these conditions, the interaction Hamiltonian between the emitter and the field is $H = -\mathbf{d}.\mathbf{E}(\mathbf{r}_{em})$. Here, $\mathbf{d}$ is the dipole operator of the emitter and $\mathbf{E}(\mathbf{r}_{em})$ is the electrical field operator at the location of the emitter (under the rotating wave approximation). In the following, we note respectively $|0\rangle$ and $|1\rangle$ the field states corresponding to the vacuum and a population of 1 photon. The decay rate Γ_M into the 1D mode family M is given by the Fermi golden rule:

$$\Gamma_M = \frac{2\pi}{\hbar^2}\left|\langle e,0|-\mathbf{d}.\mathbf{E}(\mathbf{r}_{em})|g,1\rangle\right|^2 \rho_M(\omega_{eg}), \qquad (2.2)$$

In this expression, ρ_M is the spectral density of states associated to the 1D continuum of modes. To proceed further, we consider a calculation volume with height 'L_z', as shown in Figure 2.3 (a). We adopt the periodic boundary condition such as $\mathbf{E}(x, y, z + L_z) = \mathbf{E}(x, y, z)$. The lateral extension 'L' is large enough so that the field is completely damped at the lateral boundaries. Due to the

symmetry of the problem under translation along z, we can calculate Γ_M for any z, in particular for z=0. At z=0, the field operator takes the form:

$$\mathbf{E}(r_{em}) = \sqrt{\frac{\hbar\omega}{2\varepsilon_0 n^2 L_z S_{eff}}}\left[a\mathbf{f}^*(x,y) + a^+\mathbf{f}(x,y)\right], \tag{2.3}$$

where a and a^+ are the annihilation and creation operators of the optical field respectively, and **f** is the spatial function that has been introduced previously. ε_0 is the dielectric permittivity of vacuum and n is the refractive index of the wire (The L_z term, which is arbitrary, will disappear in the final expression of Γ_M).The effective surface area of the mode, which characterizes the transverse confinement of the field, is given by:

$$S_{eff} = \frac{1}{n^2}\iint n^2(x,y)\left|\mathbf{f}(x,y)\right|^2 dxdy\,,$$

$$= \frac{\iint n^2(x,y)\left|\mathbf{E}(x,y,z)\right|^2 dxdy}{max(n^2\left|\mathbf{E}\right|^2)}\,, \tag{2.4}$$

The spectral density of states can be written as

$$\rho_M(\omega) = 2\times\frac{L_z}{2\pi}\times\frac{1}{v_g}\,, \tag{2.5}$$

Here v_g is the group velocity of the mode, given by $v_g = \frac{d\omega}{d\beta}$. The factor of 2 accounts for the upward and downward propagating modes.

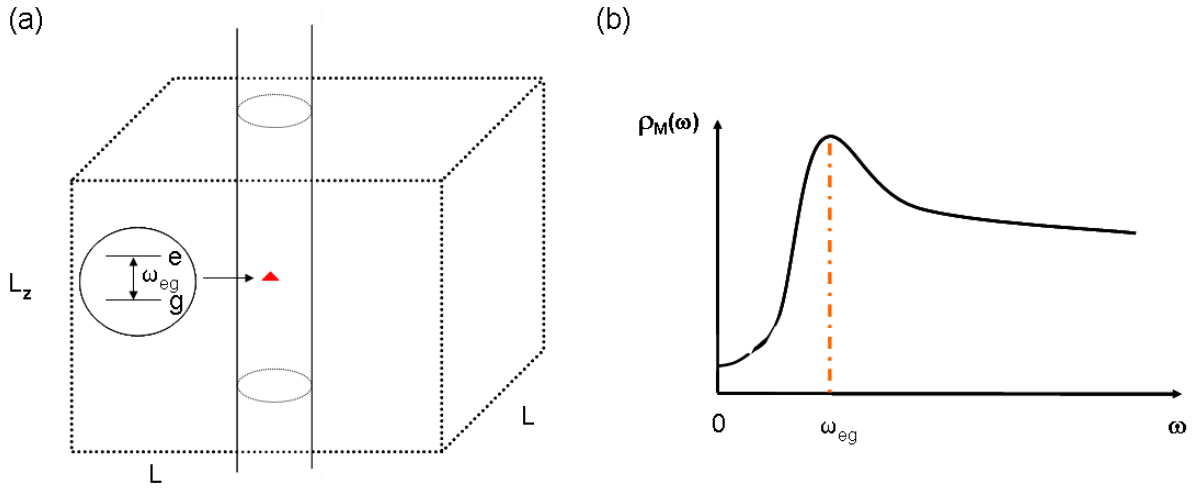

Figure 2.3: (a) Schematic of the system, Emitter inside the 1D photonic nanowire waveguide system (b) Optical density of state for 1D photonic nanowire.

For an emitter localized on a maximum of the field with a dipole aligned along the local electrical field, Γ_M takes the maximum value, given by

$$\Gamma_M = \frac{\left|\mathbf{d_{eg}}\right|^2 \omega_{eg}}{\hbar \varepsilon_0 n^2 S_{eff} v_g}, \tag{2.6}$$

Here $\mathbf{d}_{eg}$ = <e|**d**|g> is the matrix element of the dipole operator. As a reference, we introduce the emission rate Γ_{3D} of the same emitter located inside bulk GaAs. In that case, the spectral density of states is given by

$$\rho_{3D}(\omega) = \frac{\omega^2 V n^3}{\pi^2 c^3}, \tag{2.7}$$

where $V = L_z L^2$ is the volume of the calculation volume, which disappears in the final expression of Γ_{3D} that can be written as

$$\Gamma_{3D} = \frac{\left|\mathbf{d_{eg}}\right|^2 \omega_{eg}^{\ 3} n}{3\pi\hbar\varepsilon_0 c^3}, \tag{2.8}$$

By introducing λ, the wavelength of the emitter in vacuum, the generalized Purcell factor $F_M = \Gamma_M/\Gamma_{3D}$ associated to the mode can be expressed as

$$F_M = \frac{3}{4\pi} \times \frac{(\lambda/n)^2}{S_{eff}} \times \frac{n_g}{n}, \tag{2.9}$$

The generalized Purcell factor represents the degree of enhancement of the spontaneous emission of the emitter which is coupled to the guided mode. It is clear from this expression that this Purcell factor depends only on the waveguide properties and constitutes a figure of merit of the waveguide. This factor is inversely proportional to the effective mode area (S_{eff}) which directly characterizes the mode lateral confinement. F_M is also proportional to the group index n_g, which is proportional to the local density of state associated to a 1D continuum. The expression (2.9) shows that to reach a large Purcell factor for an emitter of fixed emission frequency, it is therefore necessary to design a waveguide with a small effective mode area and a large group index. This expression is valid for any family of guided modes. In the following, we focus on the fundamental guided mode HE_{11}.

2.1.1.3 Generalized Purcell factor of the fundamental guided mode

Figure 2.4(a) shows the evolution of the effective mode area for the fundamental guided mode HE_{11} as a function of normalized diameter (D/λ). In the small diameter range, the mode is deconfined in the air surrounding the wire, leading to very large S_{eff}. When $D/\lambda > 0.18$, the effective area decreases

drastically, as the mode starts to be well confined in GaAs wire. An optimal confinement is reached around $D/\lambda = 0.25$, and above this value S_{eff} increases again. In the large diameter range, the mode is well confined in GaAs, and its lateral extension increases with the diameter of the wire.

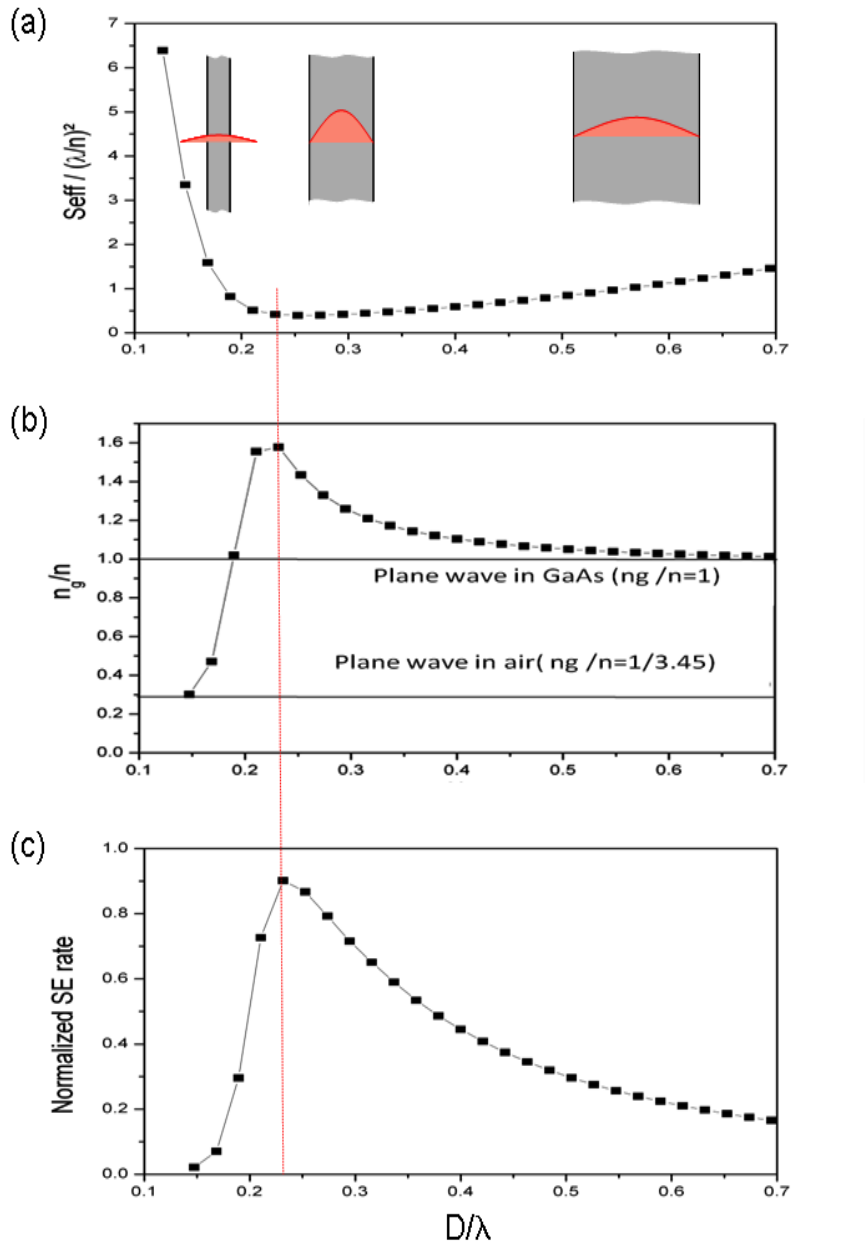

Figure 2.4 : Evolution of various parameters of guided mode HE_{11} of photonic nanowire as a function of normalized diameter (D/λ) (a) effective mode area S_{eff}, (b) ratio of the group index to GaAs index (n_g/n) and (c) Normalised spontaneous emission rate (Γ_M/Γ_{3D}), where red line indicates the cut off of the higher modes.

Figure 2.4(b) shows the evolution of the effective index ratio (n_g/n) for the fundamental guided mode HE_{11} as a function of (D/λ). In the low diameter range, n_g=1: the mode is very close to a plane wave propagating in air. In the large diameter limit, n_g tends toward n: the mode is very close to a plane wave propagating in GaAs. In between, around D/λ =0.24, one observes that the group velocity of the guided mode is slightly slowing down, with n_g/n reaching a maximum value close to 1.6. The evolution of Γ_M/Γ_{3D}, shown in Figure 2.4(c) is closely related to the evolution of S_{eff} and n_g/n. Γ_M/Γ_{3D} reaches a maximum value of 0.9 for D/λ =0.25, which is the signature of a good coupling to the guided mode.

2.1.1.4 Link with the decay rate of a quantum dot

Up to now, for the calculation of SE Γ_M, we have considered the ideal case of a linear dipole, located on the maximum of the electrical field, and aligned on its direction. In this section, we make the link to the decay rate (into the guided mode) of an InAs quantum dot.

We first examine the case of an on-axis QD. If we consider the neutral exciton, it features two bright optical transitions, which are orthogonal and perpendicular to the growth axis. For the interesting diameter range, the maximum amplitude of the electrical field is attained on the wire axis. At this location, it displays only one non-zero component, that is furthermore perpendicular to the wire axis. Thus, we have a good alignment between the field and the dipole component if the wire axis coincides with the growth axis. Moreover, by symmetry, there are in fact two degenerate HE_{11} mode families, with orthogonal linear polarizations. For the experiments (non-resonant optical pumping), one can consider that the two dipole components are excited each with equal 0.5 probabilities. The decay rate of the quantum dot is thus 0.5 Γ_M + 0.5 Γ_M = Γ_M. The degeneracy of the mode and the one of the optical transition compensate each other.

With our fabrication process, the location of the dot is random, the dots are thus in general off-axis. For off-axis quantum dots, the decay rate directly follows the mode profile, which is approximately Gaussian inside the wire. Its evolution is shown in Figure 2.5. For an off-axis emitter the Purcell factor is function of position r due to the spatial dependence of the electric field and given by

$$F(r) = \overline{\Gamma}_M(r) = F_M(r=0) \cdot \frac{|\mathbf{E}(\mathbf{r})|^2}{\max\left[|\mathbf{E}(\mathbf{r})|^2\right]}, \qquad (2.10)$$

In order to investigate this effect, we consider the cylindrical co-ordinates (r, ϕ, z) system in the calculation and modelled the quantum dot as two equally populated dipoles (r, ϕ) that are orthogonal to each other (radial and orthoradial) and perpendicular to the wire axis. The displacement of the QD is denoted by amount x (see Figure 2.5). After neglecting the axial dipole component, we performed the calculation the SE rate into HE_{11} mode Γ_M by varying the QD position inside the wire of diameter around 220 nm, which is shown in the Figure 2.5. We can clearly see from the plot of Γ_M in Figure 2.5, when the QD is located at the centre of the wire, the coupling to the radial and orthoradial modes (r, ϕ polarised mode) is maximum and isotropic. As we go toward off axis positions, the coupling to the radial and orthoradial modes reduce anisotropically.

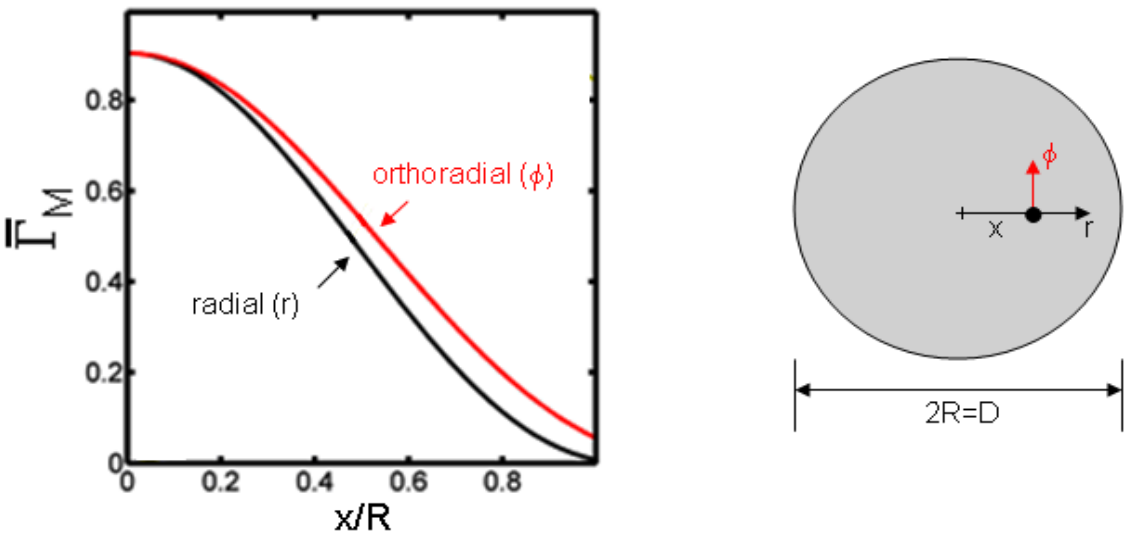

Figure 2.5: Effect of QD position variation on the coupling to the guided mode HE_{11} of the photonic nanowire with diameter 220nm.

2.1.2 Coupling to the radiative modes and dielectric screening

In the monomode waveguide regime, the emitter embedded into the photonic nanowire is also coupled to a 3D continuum of so-called radiative modes. We will see in this section that these radiative modes are very efficiently screened by the wire. This dielectric screening effect does not affect the density of state seen by the emitter, but leads to a strong damping of the zero-point fluctuations associated to each mode. We will first examine the small diameter limit ($D/\lambda << 1$): in that case, the propagation of the optical field can be neglected

and we are left with a simple analytical, electrostatic-like problem. We will then examine numerical results, obtained for the finite diameter range, which is relevant for spontaneous emission control.

2.1.2.1 Some basics of electrostatic in a dielectric material

In this paragraph, we briefly remind some basic properties of a dielectric material: they will be useful for the calculation of the screening effect. Dielectrics are electrical insulating materials, in which all the electrons are bound to the nuclei and can't flow. When a dielectric is placed in an externally applied electric field $\mathbf{E}_o$, electric charges do not flow through the material as in the conductor but the medium will adapt to this perturbation by dynamically changing the equilibrium position of the electric charges which causes a small separation of the centres of negative and the positive charges so that each infinitesimal element of the volume behaves as an electric dipole. The electric dipole moment per unit volume is called the polarization **P**; it is related to the *total* electrical field **E** by the relation

$$\mathbf{P} = \varepsilon_0 \chi_e \mathbf{E}\,, \tag{2.11}$$

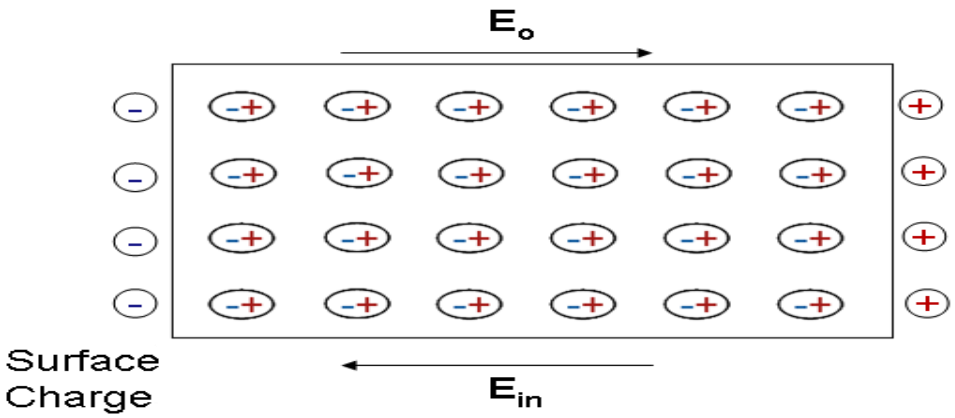

Figure 2.6: Polarization induced by an externally applied electrical field.

Note that, in general, **E** is equal to sum of the external applied field $\mathbf{E}_o$ and a depolarization field $\mathbf{E}_{in}$ associated to the response of the material: $\mathbf{E} = \mathbf{E}_o + \mathbf{E}_{in}$ (see Figure 2.6). χ_e is the dielectric susceptibility of the material: it fully characterizes the response of the material to an electric field. It is related to the dielectric constant ε by the relation

$$\varepsilon = \varepsilon_0 (1 + \chi_e)\,, \tag{2.12}$$

If losses are neglected, we have the relation,

$$\varepsilon = \varepsilon_o \cdot n^2, \tag{2.13}$$

In order to investigate the screening effect, the only thing that needs to be calculated is then total electric field inside the dielectric when it is placed an external electric field which will be done in next section for the cylindrical photonic wire case.

2.1.2.2 Screening in a 'thin' dielectric cylinder

To calculate the response of a wire to an incident optical field is in general a difficult problem that cannot be solved analytically. To investigate the physics behind dielectric screening, we first study the response of a 'thin' cylinder, with D<<λ. In that case, we are left with an analytical problem of electrostatics. There are two possibilities for the incident electric field polarization, as shown in Figure 2.7: longitudinal polarization (parallel to the axis) and in-plane polarization (perpendicular to the wire axis). They lead to very different results.

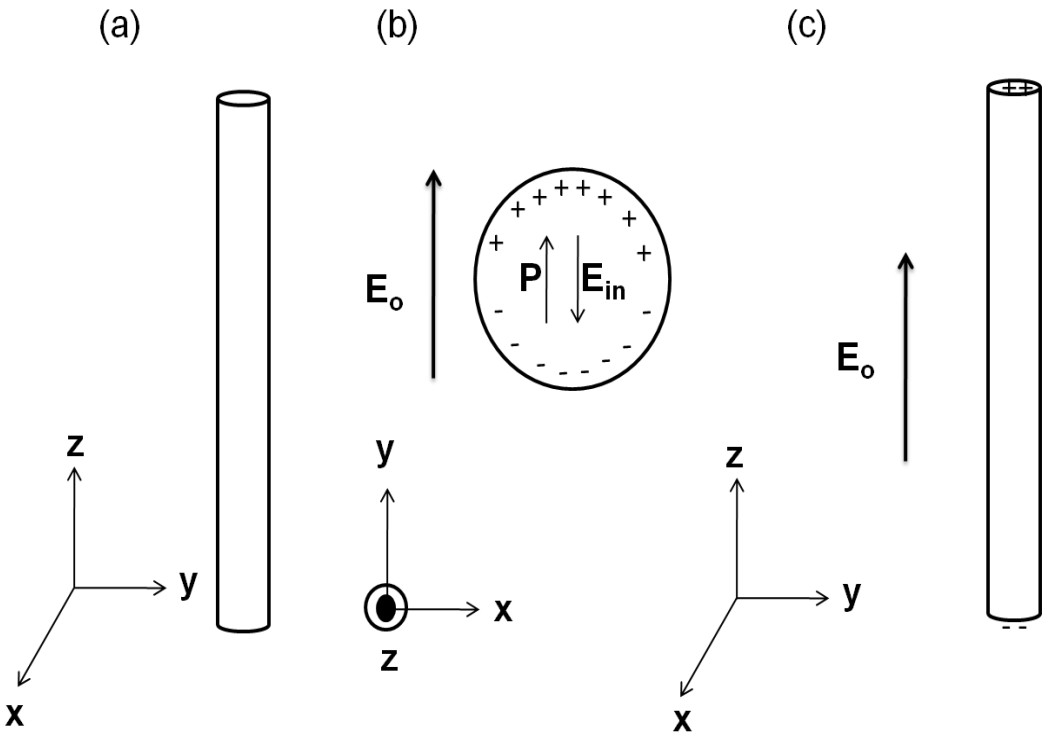

Figure 2.7: Photonic nanowire in electric field of different polarizations (a) Drawing of the thin dielectric photonic nanowire, (b) In case of in-plane polarization electric field, (b) In case of longitudinal polarization electric field.

In-plane polarization:

We first consider the case of an incident electric field with in-plane polarization. The external field $\mathbf{E}_0$ generates a homogenous polarization **P** inside the structure. This polarization generates surface charges hat in turn generate a depolarization field $\mathbf{E}_{in}$ inside the wire. As shown in the Appendix A, with a simple model and using the Gauss formula, one can obtain

$$\mathbf{E_{in}} = -\frac{\mathbf{P}}{2\varepsilon_o}, \tag{2.14}$$

The depolarization field is constant inside the wire. After using the equations (2.11) and (2.14), we can deduce the depolarization electric field as a function of applied external field

$$\mathbf{E_{in}} = -\frac{(\varepsilon - \varepsilon_o)}{(\varepsilon + \varepsilon_o)}\mathbf{E_o}, \tag{2.15}$$

$\mathbf{E}_{in}$ opposes the applied external field; for a material with a high dielectric permittivity ($\varepsilon >> \varepsilon_0$), one can already see that $\mathbf{E}_{in} \sim -\mathbf{E}_0$: the dielectric screens nearly perfectly the external field. Using $\varepsilon = \varepsilon_o \cdot n^2$, the total electric field inside the dielectric wire can be written as

$$\mathbf{E} = \frac{2}{n^2 + 1}\mathbf{E_o}, \tag{2.16}$$

If $n^2 >> 1$, the electric field E becomes very close to 0. Using the refractive index of GaAs (n = 3.45) the amplitude of the field is damped by a factor exceeding 6.

We now use the Fermi golden rule to calculate the emission rate γ in the continuum of radiative modes, for an emitter with a linear, in-plane dipole moment. One obtains

$$\gamma \propto \left(\frac{2}{n^2 + 1}\right)^2 \rho_{3D}^{vac}, \tag{2.17}$$

Here ρ_{3D}^{vac} the density of states of the 3D continuum of modes in vacuum. We now normalize this result to Γ_{3D}, the emission rate into bulk GaAs. Since $\Gamma_{3D} \propto n \times \rho_{3D}^{vac}$, one can get

$$\bar{\gamma} = \frac{\gamma}{\Gamma_{3D}} = \frac{4}{n(n^2 + 1)^2}, \tag{2.18}$$

For GaAs, the normalized decay rate is $\bar{\gamma} = 1/144$, which clearly shows that a very thin photonic nanowire made of a high index material, provides a very efficient screening of the radiative modes. This leads to a huge inhibition of the SE into these modes.

Longitudinal polarization

In that case, the polarization of the material leads to surface charges on the wires top and bottom facets. Putting these to infinity makes $\mathbf{E}_{in}$ tend toward 0: there is no screening in that case. For an emitter with a longitudinal dipole in an infinitely long photonic wire, the normalized SE rate into the radiative mode is $\bar{\gamma} = n^{-1}$.

Influence of the cladding material on the screening: In-plane polarization

When the dielectric cylinder (refractive index 'n') is surrounded by a cladding material with refractive index 'n_c', one can easily calculate the reduction of the internal field relative to the external field $\mathbf{E_o}$ by using the above method

$$\mathbf{E} = \frac{2}{(n/n_c)^2 + 1}\mathbf{E_o}, \tag{2.19}$$

The normalized SE rate in such a cladding material is given by

$$\bar{\gamma} = \frac{4}{n/n_c\left((n/n_c)^2 + 1\right)^2}, \tag{2.20}$$

This expression provides information about the effect of the surrounding environment on the spontaneous emission rate of the emitter embedded into the thin cylindrical wire. We see that the screening (the associated SE inhibition) are decreasing as the refractive index contrast between the cladding and the wire is decreasing as shown in Figure 2.8.

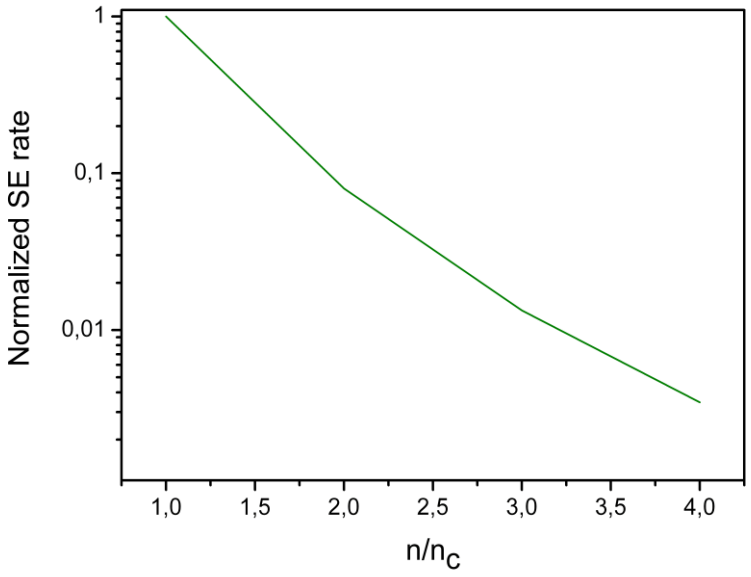

Figure 2.8: Evolution of normalized SE rate (with respect to SE into bulk) $\bar{\gamma}$ into radiative mode as a function of refractive index contrast (n/n_c).

2.1.2.3 Dielectric screening in other geometries

In the similar way one can calculate the screening effect in various geometries of different dimensionality, always in the small dimension regime. The Table 2.1 summarizes the results in the case of a slab, a cylinder and a sphere. We assume all geometries are made from same material of refractive index 'n' immersed in air. Globally, one observes screening in the directions where the structure presents small dimensions.

Geometry	Thin Slab	Thin Wire	Small Sphere
	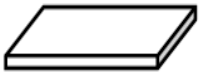		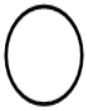
Screen direction (s)		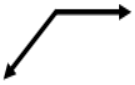	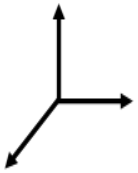
Normalized SE rate in Screen direction $\bar{\gamma}$	$\frac{1}{n^5} \sim \frac{1}{489}$	$\frac{4}{n(n^2+1)^2} \sim \frac{1}{144}$	$\frac{9}{n(n^2+2)^2} \sim \frac{1}{64}$
Unscreen direction (s)	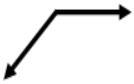		.....
Normalized SE rate in unscreen direction $\bar{\gamma}$	$\frac{1}{n} \sim \frac{1}{3.5}$	$\frac{1}{n} \sim \frac{1}{3.5}$	.....

Table 2.1: Comparison of the dielectric screening effect of the incident electric field E_o and inhibition of the SE into radiative modes for the case of thin dielectric slab, thin dielectric cylinder and small dielectric sphere.

2.1.2.4 Dielectric screening in a 'thick' cylinder

We now come back to cylindrical structures with a finite diameter. They also demonstrate a significant screening of the radiative modes. However the simple picture of the previous dielectric screening is no longer valid: both the magnitude and the spatial dependence of the screening are modified. In order to investigate this important property, we first numerically investigate the screening of a single plane wave whose wave vector **k** and electric field polarization $\mathbf{E}_0$ are perpendicular to the wire axis (z-axis). The corresponding field maps are presented in Figure 2.9 for three critical diameters. They have been calculated in the group of Philippe Lalanne. The electric field amplitude inside the structure increases progressively for the diameter D/λ range from 0.05 to 0.19, but remains approximately uniform. When the diameter D/ λ is larger than 0.19, the field amplitude becomes position dependent inside the photonic wire and the screening effect remains maximum in the vicinity of the wire axis.

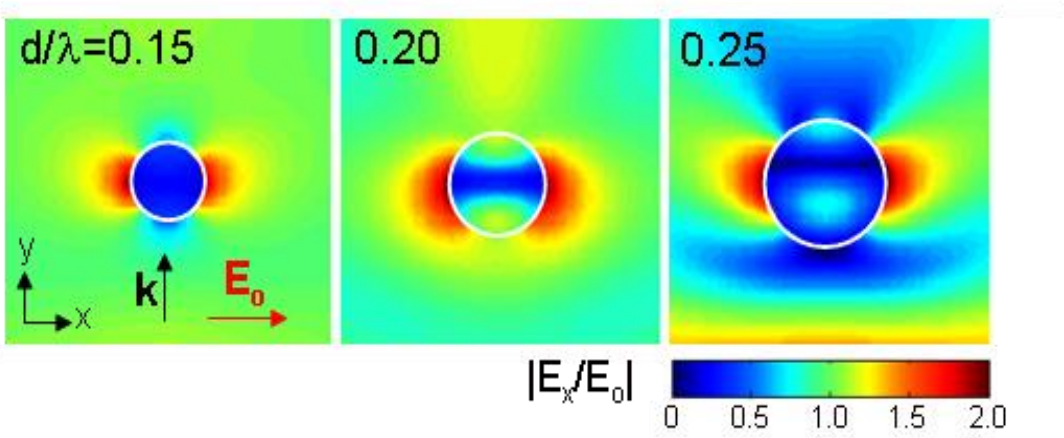

Figure 2.9: Screening of the incident plane wave by photonic nanowires for the various diameters. The figures are the colour map of the ratio of the amplitude of the electrical field inside the wire along x-axis $\mathbf{E}_x$ normalized to the amplitude of the incident field $\mathbf{E}_0$.

The evolution of the normalized SE rate $\bar{\gamma}$ for an on-axis emitter as a function of D/λ, is shown in Figure 2.10 by red dashed curve. Note that here, $\bar{\gamma}$ also contains the contribution of the other guided modes. For D/λ<0.338, $\bar{\gamma}$ only contains the contribution of the radiative modes. This curve clearly shows that the SE into the radiative modes is strongly inhibited over a large diameter range

($\bar{\gamma}$ < 0.075 for D/λ< 0.29). The sharp rise above 0.338 is associated to a supplementary guided mode with a contribution on the wire axis.

2.1.3 Spontaneous emission control and β-factor

A key design parameter for single photon sources is the fraction of photons that are emitted into the desired mode (here the fundamental, Gaussian-like mode). This quantity, often referred as the β factor, can be written in terms of the decay rate into the target guided mode (Γ_M) and the total decay rate of the emitter (Γ_{Tot})

$$\beta = \frac{\Gamma_M}{\Gamma_{Tot}} = \frac{\Gamma_M}{\Gamma_M + \gamma}, \tag{2.21}$$

where the total decay rate is given by $\Gamma_{Tot} = \Gamma_M + \gamma$. Here, γ is the decay rate into all the other modes (the radiation modes and other possible guided modes).

2.1.3.1 On-axis emitter case

In this paragraph we consider an on-axis emitter, with an in-plane dipole moment. Figure 2.10 represents the main emission properties of the QD located on the nanowire axis as the function of the normalized diameter D/λ. All the SE rates are normalized with respect to the emission of same QD placed in the bulk GaAs matrix. The emitted photons that are directly coupled into the upward and backward fundamental guided mode HE_{11} is denoted by blue-solid curve. The emission into other radiation modes γ, is denoted by red-dashed curve and the total emission (Γ_M+γ) including the modes of interest is represented with the green-dotted line curve. The β-factor is shown as a light blue dashed curve.

The evolution of Γ_M and γ has been extensively commented in the previous paragraph: we focus here on the β-factor. The fraction β of SE coupled to the fundamental guided mode HE_{11} reaches 95% for D=0.24λ. This high value, results from a good coupling to the fundamental guided mode HE_{11} combined to a very strong inhibition of SE in the other electromagnetic modes. Moreover, β exceeds 90% for a wide range of diameters, from 0.20λ to 0.29λ. Such a tolerance in term of diameter and wavelength relaxes fabrication constraints. Since λ=950 nm, we thus have to work with a GaAs wire having a diameter in the range of 200-300 nm. More importantly, this tolerance also indicates a broadband SE control that is expected for a 1D photonic system. Such a broadband SE control has several key advantages, when compared to the traditional cavity-based approach:

- It relaxes the need of a spectral emitter-cavity tuning, which is very important from a practical point of view, given the spectral inhomogeneous broadening of self-assembled quantum dots (50 nm).

- It allows the use of spectrally broad emitters (QD at higher temperatures, colour-center in diamond).

- It allows the good collection of several transitions that are detuned, like the X and XX transitions in a QD. This is a critical point when one wants to realize an efficient source of entangled photon pairs. Although this is beyond the scope of the present manuscript, this is clearly a very interesting perspective of this work.

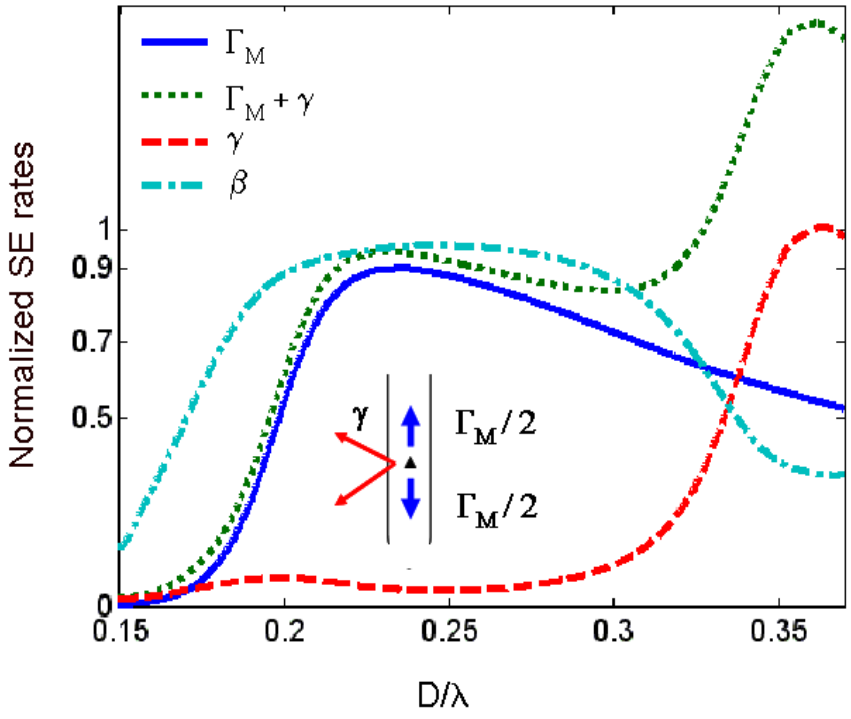

Figure 2.10: Normalized spontaneous emission rates of a radial dipole embedded in an infinite cylindrical GaAs nanowire and located on the wire axis. Blue-solid curve: emission Γ_M into the HE_{11} fundamental mode. Dashed-red curve: emission rate γ into the other modes including the radiative modes. Dotted-green curve: total emission rate, $\Gamma_M+\gamma$. Dashed-dotted curve: $\beta=\Gamma_M / (\Gamma_M+\gamma)$ for the HE_{11} fundamental mode (Ref. [2]).

2.1.3.2 Influence of the spatial position of the emitter

Given our technological choice for the realization of the structure, the position of the emitter in the wire section will be random. In this paragraph, we examine the β-factor for off-axis quantum dots. The quantum dot is modelled as two equally populated dipoles, that are orthogonal to each other (radial and orthoradial) and perpendicular to the wire axis. When the distance 'x 'of the QD to the axis increases, calculations show that:

- The coupling to HE_{11} decreases (see Figure 2.5) and becomes slightly anisotropic (different coupling rate between the radial and orthoradial dipoles).

- For $D/\lambda > 0.23$, off-axis quantum dots are also coupled to the second guided mode in the structure.

- The screening effect decreases and becomes very anisotropic (the radial dipoles remains well screened, whereas the orthoradial one is significantly coupled to radiative modes).

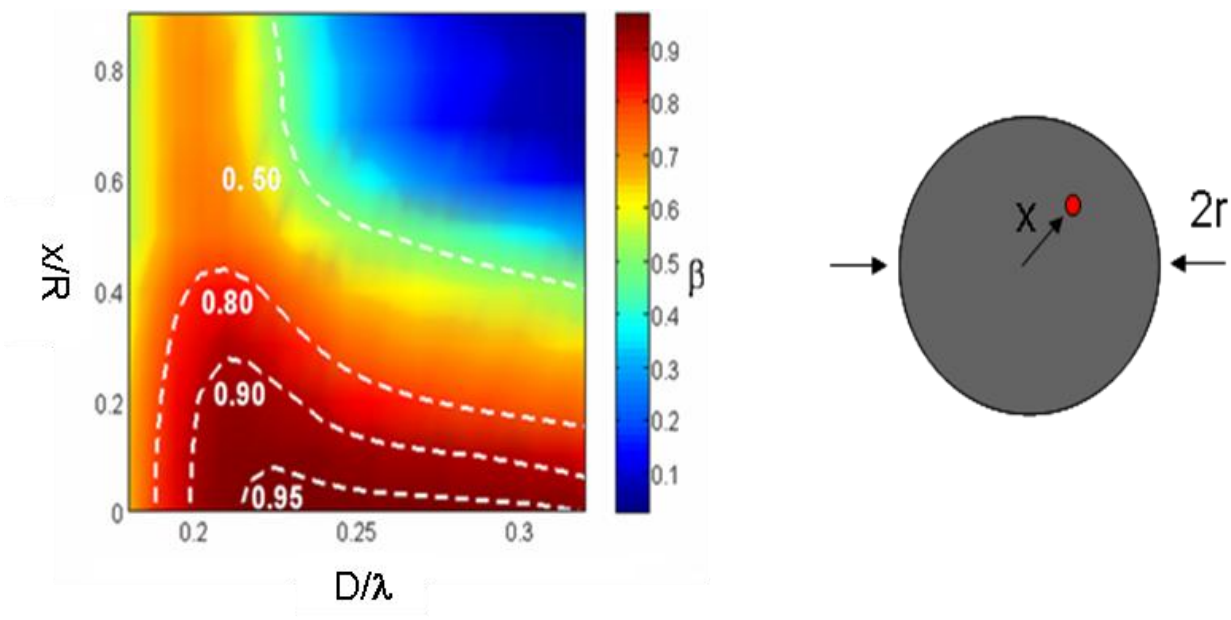

Figure 2.11: Fully vectorial calculation of β factor as a function of emitter position (x/r) and the photonic nanowire normalized diameter (D/λ).

The group of Philippe Lalanne performed the calculation of β for various diameters range and for various reduced position of the emitter x/R (where R is the radius of the wire): the results are shown in Figure 2.11. The emitter position is varied from *x* = 0 to x = 7R/8 and the SE rate is obtained by averaging the SE rates associated to radial and orthoradial polarizations. This calculation was performed for a wire with an integrated bottom mirror, which increases slightly the β factor as compared to the infinite wire. It is clear from this figure, for the diameter $D/\lambda \sim 0.21$, the β factor varies from 0.95 to 0.8 as the x/r varies from 0 to 0.4. For this diameter nanowire, one randomly located QD out of 14 experiences $\beta > 0.9$, and one QD out of 5 experiences $\beta > 0.8$. This indicates that the spatial distribution of the QDs inside the wire is not a serious limitation to achieve high β's.

2.2 Optimization of far-field radiation pattern

In this section we discuss the various issues to optimize the far field of a photonic nanowire to increase the collection efficiency.

2.2.1 Collection issues

As we have seen in the previous section, an infinite photonic nanowire provides a single mode emission (high β) over a broadband wavelength range. To realize a real single-photon source, one has to collect these guided photons, in a wire which has of course a finite length. In this case, two main problems come into the picture because of the two end facets of the finite length wire: they are illustrated in Figure 2.12. First, when an emitter embedded in photonic nanowire emits photons, there are equal probability for the emitted photons to couple to the forward and downward propagating fundamental modes. Hence half of the generated photons which propagate towards the substrate are lost there. Second, far-field emission diagrams for a standard cylindrical wire were presented in [3]; which shows that the photons reaching the top facet are strongly scattered over large angles. These two problems severely limit the collection efficiency.

In this next subsection, we first present a simple Fabry-Perot (FP) model that captures the physical parameters which govern the efficiency of the SPS. Afterward, we show that the collection of the guided photons can be brought close to one with a proper bottom mirror and a tapering of the top facet of the photonic nanowire.

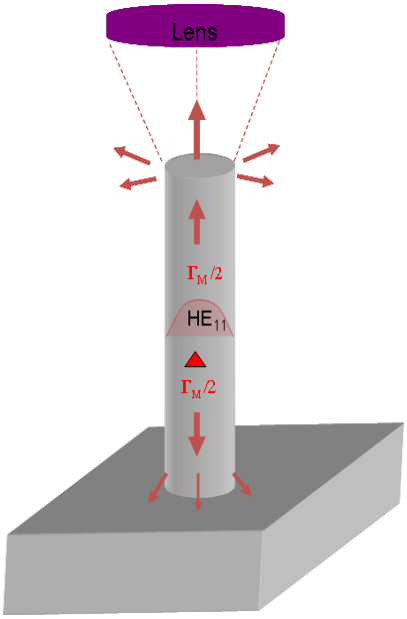

Figure 2.12: A finite length photonic nanowire: limitation factors to reach high efficiency

2.2.2 Fabry- Perot model

The model that we present here has been developed in the group of Philippe Lalanne, and can be found with extensive details in Ref. [2]. The motivation is here to provide a simple analytical model that gives guidelines for the design of the full source. Despites its simplicity, this model has been checked to give accurate results trough a comparison with a full-vectorial calculation.

When an infinite nanowire turns into finite length then the material discontinuity of the nanowire and the adjacent back-ground at the two facets (wire-air and wire-substrate interface) of the nanowire can reflect the light, and the two facets can act as two mirrors [4]. In that case, the structure is in fact a cavity, where multiple interferences lead to a frequency-selective effect. Since we want to take advantage of the broadband β-factor of semiconductor nanowires (Figure 2.10), we limit the discussion to a semi-open geometry, where the reflectivity of the upper facet has been suppressed (we will see later on how to achieve this in practice). As sketched in Figure 2.13, we consider the emitter is placed at the centre of the nanowire, at a height L/2 from the bottom end. The

unknown modal amplitudes of the HE_{11} mode are denoted by A^+ and A^- for the forward and the backward directions respectively. These amplitudes are given by

$$A^+ = A_s\left[1 + r_b \exp(i\phi)\right], \tag{2.22}$$

$$A^- = A_s, \tag{2.23}$$

where $r_b = R_b^{1/2}\exp(i\phi_b)$ is the bottom reflection coefficient, $\phi = (2\pi/\lambda)n_{eff}L$ is the propagation phase of the HE_{11} mode over the length L and A_s is the amplitude discontinuity induced by the dipole source. It is directly related to the SE rate into the fundamental guided mode of the infinite wire by $A_s = (\Gamma_M/2)^{1/2}$.

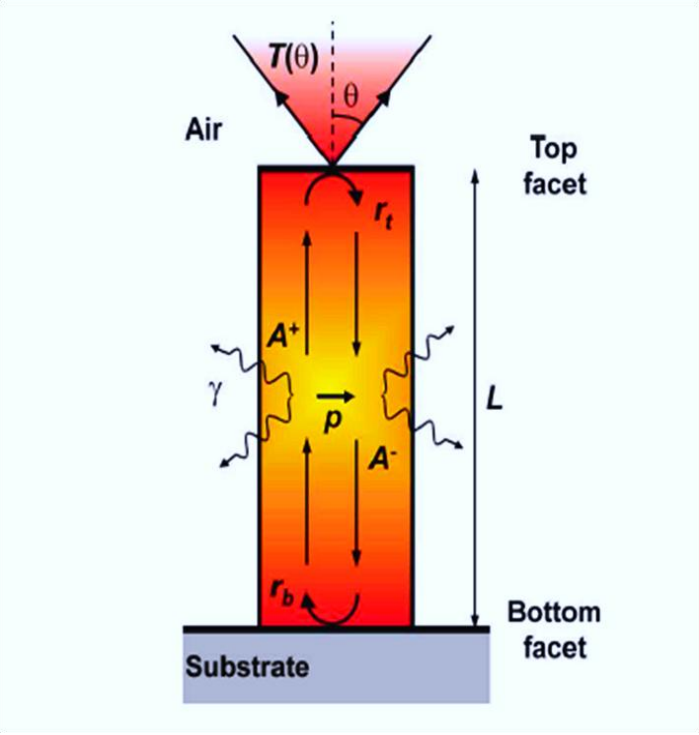

Figure 2.13: Fabry-Perot model for the emission of the dipole **p** in a nanowire of length 'L'. The amplitudes of the forward and downward- propagating HE_{11} guided mode are given by $\mathbf{A^+}$ and $\mathbf{A^-}$ respectively; the reflection coefficients of the top and bottom facets are denoted by r_t and r_b. The emission rate in the continuum of radiation modes is denoted by γ. The transmitted intensity, $T(\theta)$, represents the fraction of the incident energy carried by the forward mode that is scattered by the top facet into a cone defined by the angle θ [2].

Modification of the coupling to the guided mode

The main assumption of this model is to suppose that the SE rate γ into the radiation modes is not affected by the wire ends. It is the same as in case of infinitely-long nanowire. The bottom facet only affects the guided mode. Due to interference between the fields emitted upward and the one reflected back by the bottom mirror, the SE rate into HE_{11} is multiplied by a factor of $[1+|r_b|\cos(\phi+\phi_b)]$. Of course, to take advantage of this interference effect, the position of the emitter will be set on one of the maximum of the standing wave pattern existing between the bottom mirror and the emitter. The total SE rate then given by

$$\Gamma_{Tot} = \Gamma_M (1+|r_b|) + \gamma , \tag{2.24}$$

where Γ_M is the SE rate in HE_{11} calculated for an infinite wire.

Global efficiency of the source

The extraction efficiency $\eta(\theta)$ of the finite-length nanowire is defined as the fraction of emitted photons that are collected above the top facet in a cone with a solid angle 2π [1-cos (θ)] (see Figure 2.13). If T (θ) represents the fraction of photons transmitted into that cone when the top facet is illuminated by the upward-propagating HE_{11} mode. According to the FP model, the number of photons collected into this cone is equal to $T(\theta)|A^+|^2$. The extraction efficiency of the source is given by

$$\eta(\theta) = T(\theta)\frac{|A^+|^2}{\Gamma_{Tot}} , \tag{2.25}$$

For an emitter located on one of the antinodes of the electric field, the extraction efficiency takes the simple form

$$\eta(\theta) = \frac{1}{2}T(\theta)\frac{\beta(1+|r_b|)^2}{(1+\beta|r_b|)} , \tag{2.26}$$

This expression clearly shows that the efficiency depends only on three parameters:

- The β–factor of an infinite wire
- The reflection of the fundamental mode on the bottom facet 'r_b',
- Its transmission through the top facet 'T (θ)'

In the previous section, we have already seen how to optimize β. We first consider the ideal situation that is achieved when one engineers a bottom facet

with a high reflectivity, $R_b \sim 1$ and a top facet with a large transmission $T(\theta) \sim 1$. The maximum achievable extraction efficiency is given by

$$\eta_{max} = \frac{2\beta}{\beta + 1}, \tag{2.27}$$

In the ideal situation, the efficiency is only limited by the β-factor of the infinite photonic nanowire. We have shown in the section 2.1.3.1 that a QD placed at the axis of semiconductor nanowire with diameter D ~ 0.22λ, exhibits a large β-factor (β> 90%) over a broad wavelength range. This 0.9 β-value gives an upper bound of the extraction efficiency $\eta_{max} \sim 95\%$. In the following, we will examine different physical realization of a broadband bottom mirror with a high modal reflection. We will also see that a proper tapering of the top facet allows us to bring T (θ) close to 1.

2.2.3 Bottom Mirror

In order to realize a high efficiency SPS, it is necessary to efficiently redirect the photons emitted towards the substrate. Hence, a bottom mirror with a high reflection coefficient of the fundamental mode HE_{11} is a primary requirement. Moreover, we need a broadband reflectivity, to maintain the broadband operation of the source. Mirrors come in two basic varieties: metallic mirrors with dissipative losses of few percent, and a dielectric Bragg mirrors that are more complex but with possibly very low losses. In this paragraph, we examine how to adapt these strategies, which are well known to reflect plane wave, to reflect efficiently the very confined HE_{11} mode.

2.2.3.1 Bragg mirror

We have two possibilities; those are sketched in Figure 2.14: either we have a planar bottom mirror, or we use a mirror that is etched with the nanowire.

Planar Bragg mirror

This situation has been studied by Niels Gregersen (see Figure 2.14 (a)); the reflectivity curve of such a mirror with different number of pairs is shown in Figure 2.15. The reflectivity of a planar GaAs-AlAs Bragg mirror drops to very low values for diameters below 280 nm; therefore they are not useful for photonic nanowires. In fact, light is strongly scattered when it crosses the bottom facet: it is transmitted to the substrate with high angles. Since GaAs-AlAs Bragg mirrors have a limited angular acceptance (~ 20°) therefore a lot of the incoming light is not reflected back.

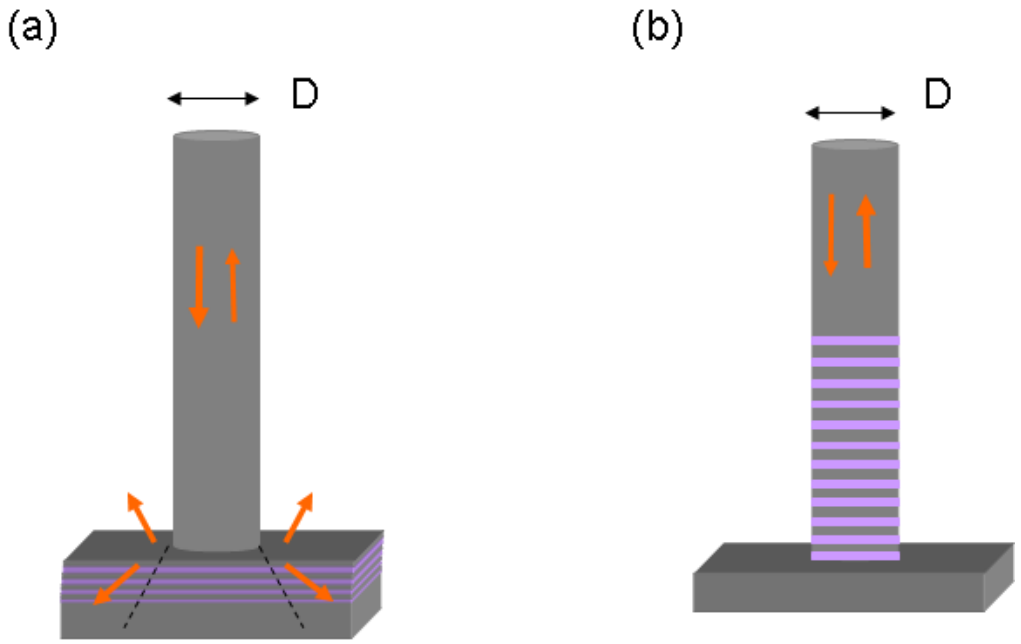

Figure 2.14: Schematic of two possibilities of Bragg mirror, (a) Planar Bragg mirror, and (b) Etched Bragg mirror.

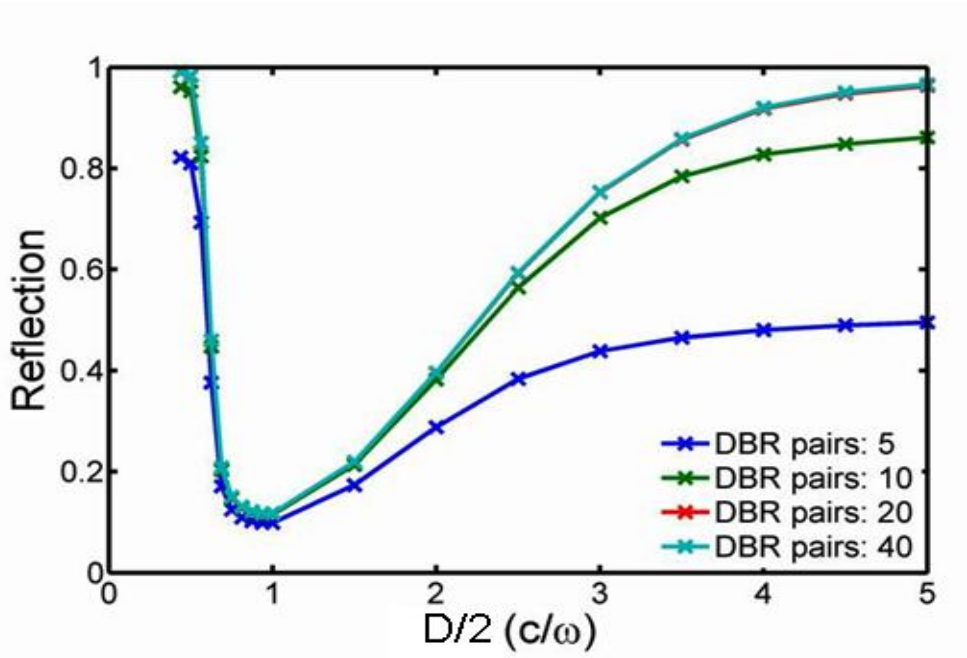

Figure 2.15: Reflection of planar Bragg mirror with different number of pairs as function of dimension of photonic wire.

Etched Bragg mirror

Dielectric Bragg mirrors embedded into the wire [see inset of Figure 2.16 or 2.14 (b)] was suggested by Chen et al [5] in the context of nanowire lasers and they have shown theoretically the possibility to obtain a reflectivity greater than 90%. According to the calculations of Friedler et al [6], Figure 2.16 shows the reflectance of GaAs/AlAs ($n = 3.45/2.95$) Bragg mirrors composed of N =16 and 32 pairs as a function of normalized diameter D/λ. For the calculation of the reflection coefficient for the guided mode, we assume the fixed wavelength (λ= 950 nm), and the thickness of each layer of mirror is assumed to be quarter wave thick ($\lambda/[4n_{eff}]$) for every Diameter (D), which implies that as D varies, the layer thickness also vary. n_{eff} is the effective index of the HE_{11} mode of the wire diameter D made from the corresponding layer material.

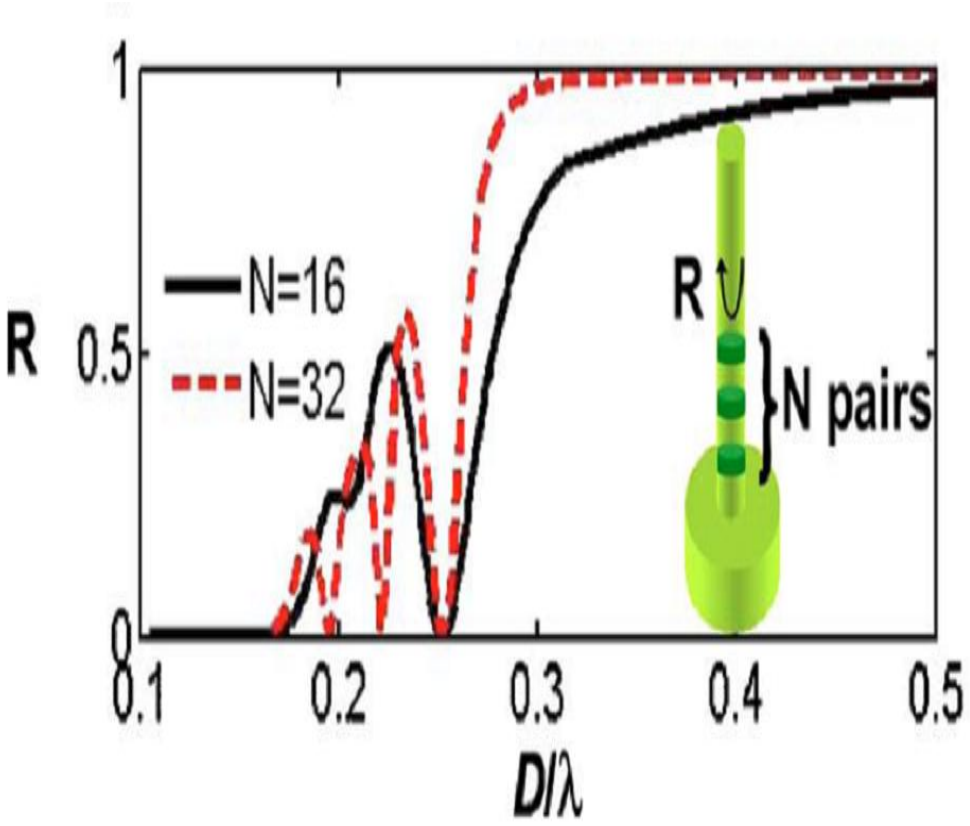

Figure 2.16: HE_{11} modal reflectance R of a GaAs cylindrical nanowire with N-pair GaAs /AlAs (n = 3.45/2.95) Bragg mirror composed of N=16 pairs (solid curve) and N=32 pairs (dashed red curve) as a function of the normalized diameter D/λfor λ=0.95μm.

In the interesting diameter range (D < 0.3λ), the reflectivity of the Bragg-mirror varies dramatically with the wire diameter, its remains small in the small diameter range due to the strong diffraction effects in the DBR leadings to poor reflectivity. This mirror gives poor reflectivity for the optimal diameter D = 0.22λ (which is given by the highest value of β-factor in an infinite wire, see section 2.1.3.1), the reflectivity is nearly zero for D = 0.25λ and for N=16 and 32. This is due to the very weak HE_{11} modal reflectance at GaAs/AlAs interface for this diameter. In addition, due to the weak refractive index contrast for small D's, a large number of DBR pairs are required for achieving a moderate reflectivity which is not feasible for the fabrication.

2.2.3.2 Metallic mirror

Metallic mirrors are interesting because of their broadband reflectivity and easy fabrication. For example, silver or gold presents a good reflectivity in the near infrared. We consider the case when nanowire bottom facets are connected to a planar metallic mirror [see inset in Figure 2.17 (a)]. According to the calculation of Friedler et al [6], the evolution of the modal reflectivity as a function of normalized diameter is shown in Figure 2.17 (a). The solid blue curve of this figure clearly shows that metallic mirror provides good reflectivity for small and large diameter nanowire where the guided mode behaves like a plane wave. However it is not a case for diameters close to the optimal value D ~0.22λ (the one that are interesting to reach a large β), since then the guided mode is strongly confined. The modal reflectivity of HE_{11} exhibits a pronounced dip, R=0.3% for D=0.19λ. There is a self-focussing effect in the gold layer where 15% of the incident energy is absorbed (see Figure 2.17 (b)). The remaining light is reflected upward, in free-space modes. At present, we do not have a clear microscopic picture of the phenomena, even if we suspect it might be related to the excitation of surface Plasmon's.

Fortunately, a good modal reflectivity can be restored by adding a thin dielectric layer (silicon dioxide $n = 1.5$) between the nanowire bottom end and metal mirror. Figure 2.17 (a) shows the modal reflectance over a broad range of diameter with the different thickness of the dielectric adlayer ($t = 0 - 15\text{nm}$). As shown in the Figure 2.17 (a), using an 11nm thick SiO_2 spacer ensures a modal reflectivity higher than 90% for all diameters of interest. We will use for the final design of the source this type of planar metal-dielectric mirrors. They offer a good compromise between the high modal reflectivity, the spectral tolerance and the tolerance with the wire diameter

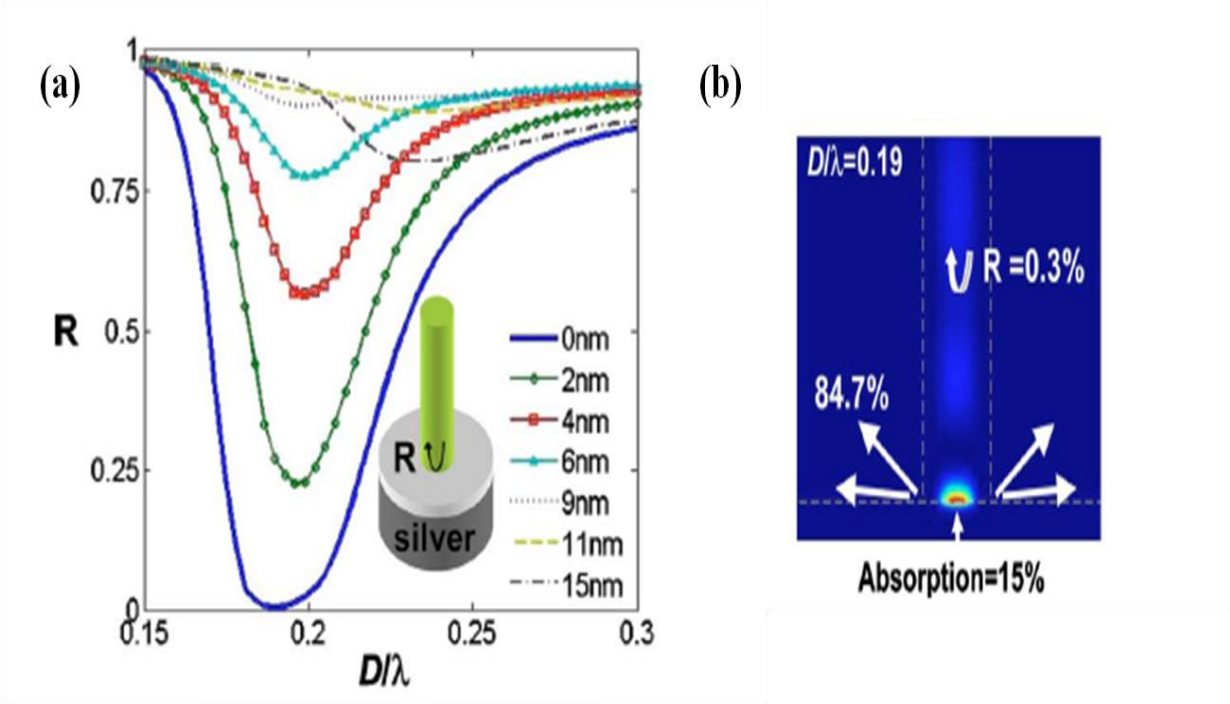

Figure 2.17: Metal mirror performance (a) HE_{11} modal reflectance R of a planar metal mirror either pure metal ($t = 0$, solid curve) or coated with a thin dielectric adlayer ($n = 1.5$) of various thickness t (b) Self-focusing effect for $D/\lambda = 0.19$, at the nanowire-metal interface, where 15% of the incident HE_{11} energy is absorbed.

2.2.4 Tapering of the top facet of the wire

The choice of the upper facet geometry is governed by two objectives:

- cancel the modal reflectivity associated to HE_{11}.
- redirect the emission along the wire axis, to allow for the efficient collection of light with a standard microscope objective.

To achieve this last goal, one has to increase the lateral extension of the mode, to make its far-field emission more directives. We will see we can do it with two geometries: a decrease of the wire diameter (‘regular’ taper) or an increase of this diameter (‘inverted’ taper). In any case, to preserve a Gaussian far-field, the taper has to ensure an adiabatic transition along the wire, so that the photon remains in the HE_{11} mode.

2.2.4.1 Regular Taper

We first consider a conical taper shaped tip in which diameter decreases with the height, sketched in Figure 2.18 (a) (shown by black line). In such a structure, the effective index of the guided mode gradually decreases with the

reduction of the diameter. Hence the HE_{11} guided mode, well confined at the bottom of the tip, becomes less and less confined as the wire diameter decreases to its top diameter where it's completely deconfined in the air. This adiabatic expansion of the guided mode gives two beneficial effects. First this expansion of the mode waist minimizes back reflection at the top facet and second, it reduces the beam divergence in air. Figure 2.18 (a) and (b) show the field profile of the non tapered standard nanowire and ideal taper which clearly indicates that tapered tip reduce the far field divergence.

Figure 2.19 (b) illustrates the total transmission into free space as well as the relative collection efficiency γ for 0.5 and 0.8 numerical aperture (NA) [7]. For large opening angles, the collection efficiency is not improved by the taper because the transition through the tapering is not adiabatic: the light is emitted into free-space modes that do not correspond to HE_{11}. To maintain the adiabaticity of the transition, a small opening angle is mandatory; we observe that as opening angle α decreases, γ increases dramatically, reaching 87% for $\alpha = 1°$. In addition, when the diameter reaches 150 nm, the mode is completely deconfined in the air and the upper part of this taper can be truncated while preserving its characteristics (reduction of beam divergence and same transmission value shown in Figure 2.18 (c) and 2.19 (c)). This can be of practical interest since it relaxes fabrication constraint.

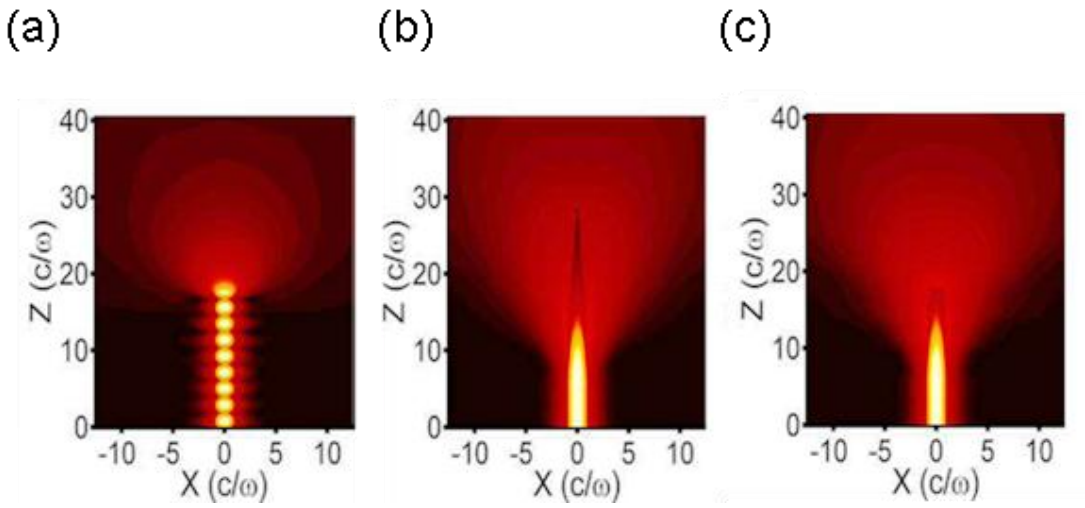

Figure 2.18: Field profile E for (a) nanowire without taper (b) conical taper, and (c) Truncated taper for opening angle α=5°.

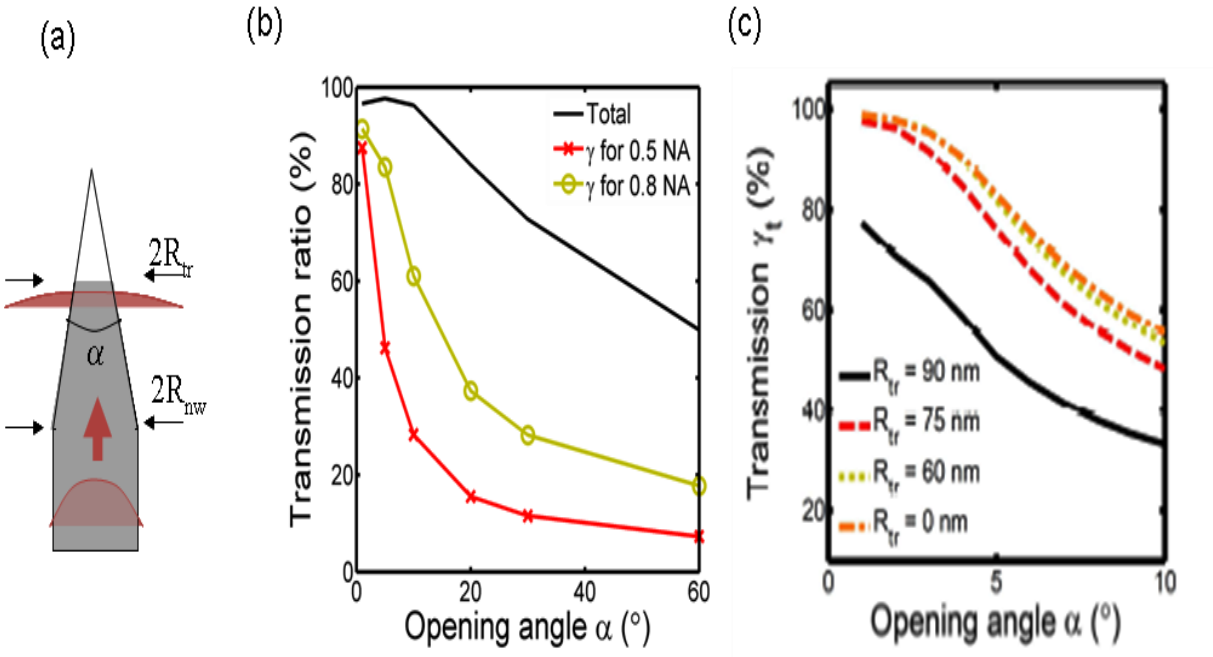

Figure 2.19: (a) Sketch of conical taper tip (b) modal transmission and the relative collection efficiency γ for 0.5 and 0.8 NA lenses as a function of opening angle α for ideal sharp tip (c) relative collection efficiency γ for a 0.8 NA lens as a function of α for truncated tip for various values of R_{tr} with $2R_{nw} = 0.22\lambda$, where R_{nw} and R_{tr} are radius of nanowire and truncated tip section respectively .

2.2.4.2 Inverted Taper

In the second approach, the diameter of the wire increases slowly with the height, so that the effective mode index also gradually increases as well as the mode area (see Figure 2.20 (a)). As a consequence the mode is optimally confined at the bottom of the wire and it's progressively less and less confined as the diameter increases [8]. In contrast to the regular taper approach in which mode is deconfined in the air, in case of inverted taper mode adiabatically expands inside the wire.

The first task is then to estimate the minimum diameter of the top facet to guarantee a good collection in a given numerical aperture. Calculations, done by Niels Gregersen, show that a top facet with a 1.5 µm-diameter guarantees a nearly perfect collection for NA=0.8. Using a lower NA=0.5 imposes a top diameter around 2.5 µm. For these diameters, the HE_{11} mode is really close to a

plane wave. It is therefore possible to suppress the reflectivity of the top facet with a standard anti-reflection coating.

The second point is to estimate the adiabaticity condition. The transmission coefficient of the fundamental guided mode HE_{11} as function of sidewall angle θ for the various value of R_{top} is shown in the Figure 2.20 (b). The modal transmission is around 95 % for a 10° tapering angle and top facet diameter is higher than 1.5 µm. The good surprise here is that the condition of the tapering angle is less stringent than the one for regular tapers.

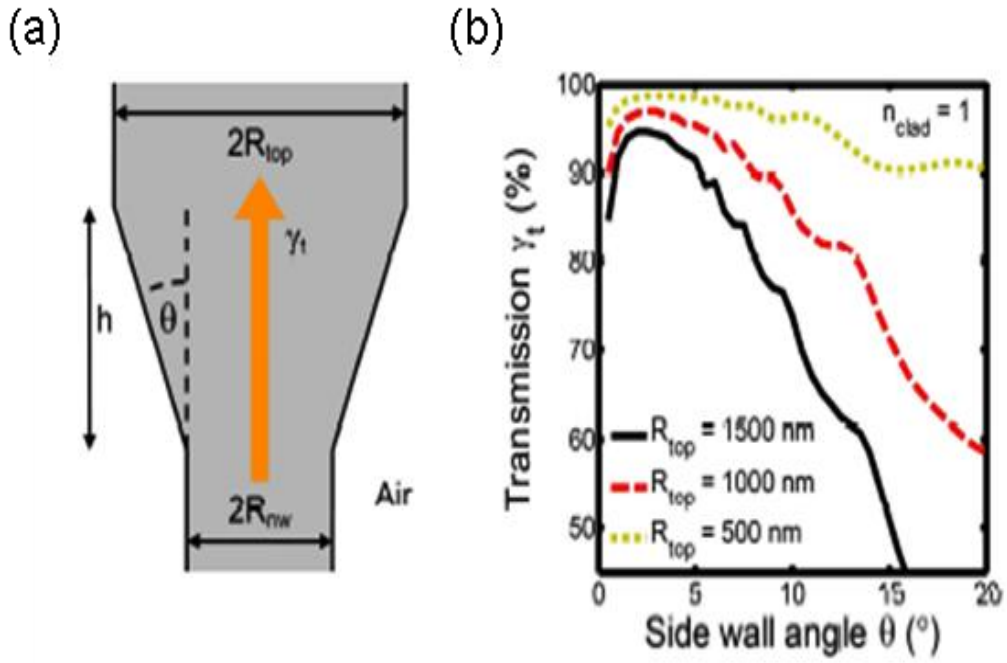

Figure 2.20: (a) Schematic of the inverted taper (b) transmission of the fundamental mode HE_{11} as function of sidewall angle θ for various values of R_{top} with air cladding.

2.3 Two possible designs and their performance

In this last section, we present two designs that have been realized during the PhD; they are sketched in Figure 2.21. For the bottom mirror, we have retained a gold and silica combination mirror solution, which offers the best combination between reflectivity, broadband operation and tolerance versus the wire diameter. In the two designs, the emitter is located on the first longitudinal antinodes of the structure (110 nm above the silica layer). This provides us the

maximum tolerance with respect to the wire diameter (a change of the diameter changes the effective index of HE_{11}, which in turn stretches the standing wave pattern). Both devices feature optimum diameter photonic nanowire section at the bottom with diameter about 200nm to ensure high β-factor. Concerning the choice of the taper, regular tapers present the advantage of compactness: a total tapering height of about 1 µm is sufficient to achieve satisfying collection efficiency. Therefore, it was the first kind of sample realized during the thesis. Inverted tapers are structures that are more difficult to fabricate: to increase the diameter of the wire from 200 nm to 1.5 µm, for a taper angle of 10°, requires a structure with a height exceeding 10 µm. However, this strategy provides higher modal transmission and a superior control over the far-field. In addition, it is well adapted to the implementation of electrical contact [8]. It is therefore very promising and has been realized in the end of the PhD.

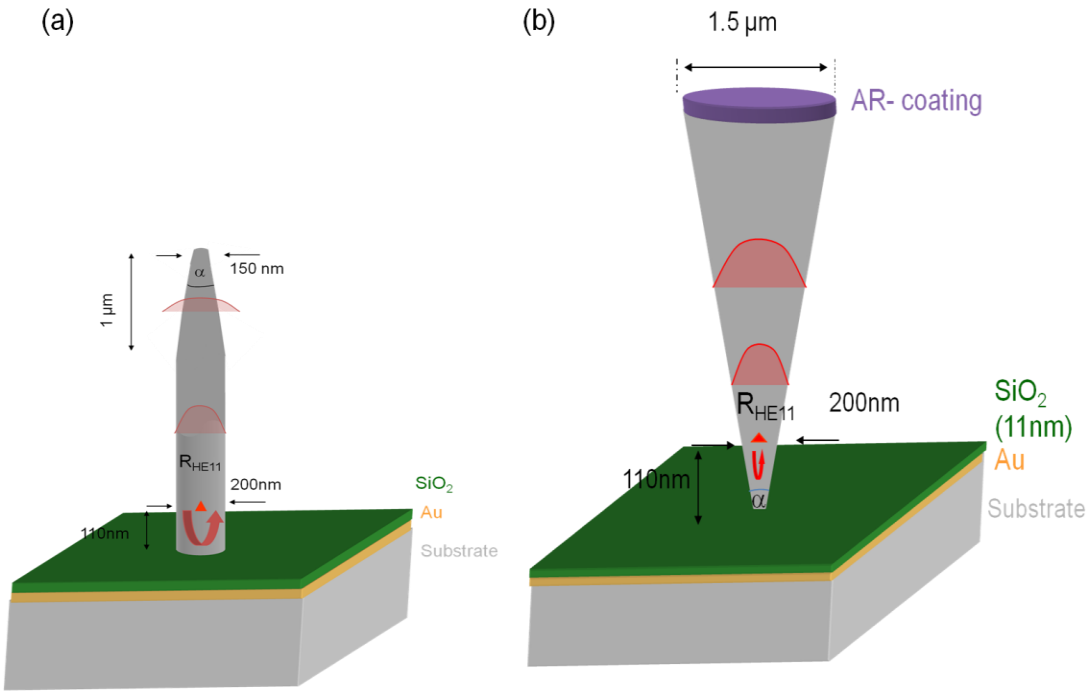

Figure 2.21: Two designs of single photon sources, (a) Regular taper based and (b) Inverted taper based design.

The performance of these two devices is summarized in the Table 2.2. Details of the calculation can be found in the references [2, 8]. This is clear from the table that both devices provide the same β-factor and high modal reflectivity of the bottom mirror. The inverted taper geometry provides the high efficiency single

photon emission due to the better adiabatic mode transformation and high modal transmission of the top facet.

Geometry	Design 1 (Regular Taper)	Design 2 (Inverted Taper)
β-factor	95%	95%
Modal Reflection of Mirror	90%	90%
Modal Transmission in NA=0.8	97% (α=2°) 80% (α=5°)	95%(α=10°) 97 %(α=5°)
Global ε for NA=0.8	90% (α=2°) 74% (α=5°)	88%(α=10°) 90%(α=5°)

Table 2.2: Comparison of the performance of two designs of Single Photon Source.

2.4 Conclusion

To conclude this chapter, we have shown that photonic wires provide a broadband and very efficient SE control, in stark contrast with the cavity-based approach. In addition, the β-factor is not very sensitive to the spatial position of the emitter. This double tolerance is of crucial importance from a practical point of view. In a photonic wire which features a bottom mirror, nearly 1 dot out of 14 exhibits β>90%, whereas the fraction of well-coupled dot in a cavity is in general on the order of 1/1000. Beside, this non–resonant approach offer novel opportunities for the development of single-photon sources based on non-

monochromatic single photon emitter, such as a colour centres on diamond at room temperature or semiconductor QDs at moderate temperature (T> 100K).

In addition, we have seen how to control the collection of the guided photon, in order to reach a global efficiency approaching 1 in a NA=0.8 collection cone. In chapter 3, we describe the fabrication of the two proposed structures (regular and inverted taper). We detail the measured performance of the regular geometry in chapter 4.

References

1. B. Gayral, “Controlling *spontaneous emission dynamics in semiconductor microcavities; an experimental approach*,” Ann. Phys. Fr **26**, N°2 (2001).
2. I. Friedler, C. Sauvan, J. P. Hugonin, P. Lalanne, J. Claudon, and J. M. Gérard, “*Solid-state single photon sources: the nanowire antenna*,” Opt. Exp. **17**, 2095 (2009).
3. A. V. Maslov and C. Z. Ning, “*Far-field emission of a semiconductor nanowire laser*,” Opt. Lett. **29**, 572 (2004).
4. A. V. Maslov and C. Z. Ning, “*Reflection of guided modes in a semiconductor nanowire laser*,'' Appl. Phys. Lett. **83**, 1237(2003).
5. L. Chen and E. Towe, “*Nanowire lasers with distributed-Bragg-reflector mirrors*,” Appl. Phys. Lett **89**, 053125 (2006).
6. I. Friedler, P. Lalanne, J. P. Hugonin, J. Claudon, J. M. Gérard, A. Beveratos and I. Robert-Philip, “*Efficient photonic mirrors for semiconductor nanowires*,” Opt. Lett. **33**, 2635 (2008).
7. N. Gregersen, T. R. Nielsen, J. Claudon, J. M. Gérard, and J. Mørk, “*Controlling the emission profile of a nanowire with a conical taper*,” Opt. Lett. **33**, 1693 (2008).
8. N. Gregersen, T. R. Nielsen, J. Mørk, J. Claudon, and J.-M. Gérard, “*Designs for high-efficiency electrically pumped photonic nanowire single-photon sources*,” Opt. Exp. **18**, 21204 (2010).

Chapter 3

Fabrication of high efficiency single photon sources in the photonic wire geometry

---

Technology has to be invented or adopted. - ***Jared Diamond***

The technological development of the fabrication process was one of the main works of this thesis. In this chapter, the fabrication process and the discussion of the results of two high efficiency optically pumped single photon sources (SPS) based on photonic nanowire geometry with embedded quantum dots, will be described. First, the design of the two single photon sources will be presented in this chapter and then the planar MBE structure will be discussed in context of single photon source requirements. Next, we will present some intermediate various fabrication steps like, the realization of high performance modal mirror, and then a flip-chip process to get quantum dots membrane on the metal mirror surface will be discussed. Finally a section of this chapter will be dedicated to the optimization of electron beam (e-beam lithography) and reactive ion etching (RIE) process, which are the key steps in view of a control of the final geometry. We will put strongly emphasis on the optimization of the flip-chip process and the etching process, which have been the most challenging technological developments within this PhD work.

3.1 Introduction

Fabrication of high efficiency single photon sources (SPS) has been a major interest of research in the last decades, and has been recognized as a major challenge in the context of quantum information processing, quantum cryptography and low light flux metrology [1-3]. The technology of real single photon devices is still in its infancy, although the physical basis for single photon emission from single QDs seems well developed so far [4-6]. A practical approach to realize a high efficiency real single photon source has to be demonstrated. As predicted in the chapter 2, the control of spontaneous emission rate of an emitter inserted in photonic nanowire with carefully tailored ends, can be used to get the high efficiency single photon source [7]. On the basis of theoretical predication, we have developed a high efficiency single photon sources based on the emission of InAs QDs embedded in GaAs photonic nanowire. Although the nanofabrication process is very challenging, we could demonstrate a successful fabrication of photonic nanowires with embedded quantum dots. The development of fabrication technology of the photonic nanowires represents the much of work done in the context of this thesis, and results obtained in quantum optics presented in later chapters could obviously not have been obtained without this strong prior technological effort.

3.2 Single Photon Source Designs

We designed an optically pumped single mode single photon source based on the emission of quantum dot embedded in semiconductor nanowire. In this section, I will present the two single-photon device designs which we have fabricated in the course of this thesis, before starting any fabrication steps. The first design is shown in Figure 3.1. It features a nanowire made from high refractive index semiconductor material (GaAs) with an optimum diameter in the range of 200 -250 nm to ensure high β and height of 2.5 µm. It features a broadband modal mirror at the bottom and an upper end with a needle-like tip (regular taper). The taper is designed to deconfine the guided mode in the surroundings of the wire. A self assembled InAs/GaAs QDs layer is located 80 nm above the mirror: the dots are located on the first antinode of the standing wave pattern for $D/\lambda = 0.25$ [7].

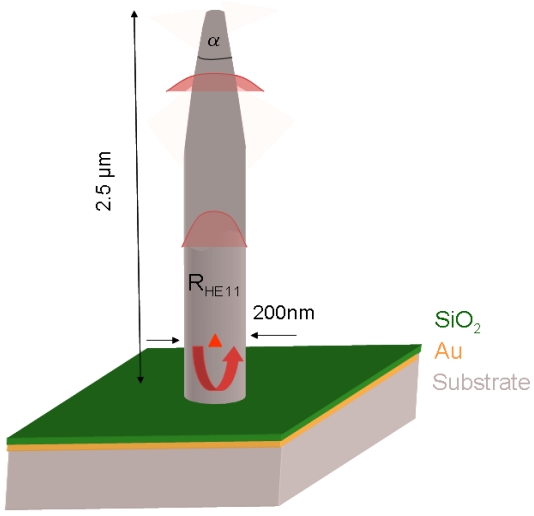

Figure 3.1: First design of Single-photon source device, an InAs QD (red triangle) is embedded in a GaAs photonic nanowire. The far field emission collection is optimized with an integrated modal mirror and smooth regular tapering of the top facet of nanowire.

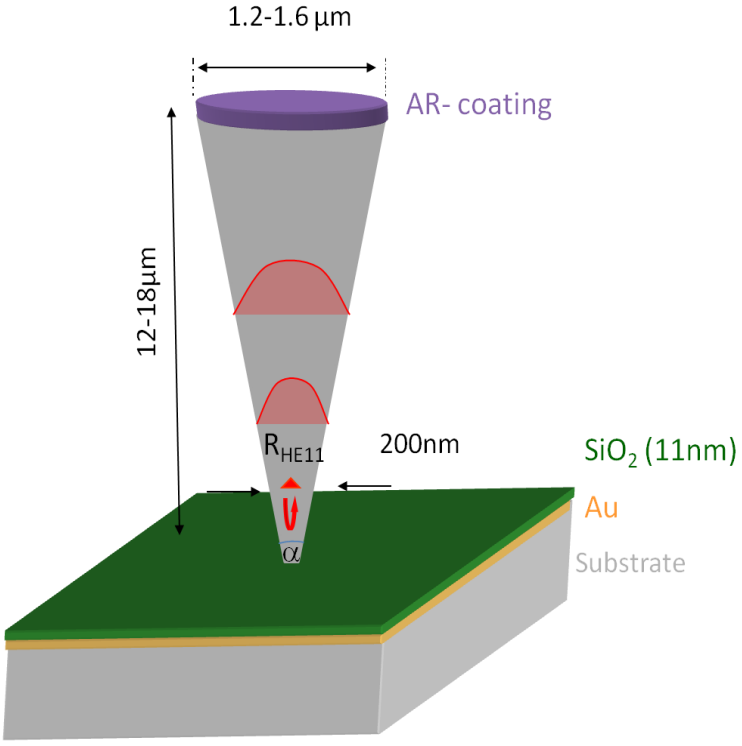

Figure 3.2: Second design of Single-photon source device, with an InAs QD (red triangle) is embedded in a GaAs photonic nanowire section. The far field emission collection is optimized with an integrated modal mirror and with smooth inverted taper design.

The second geometry is sketched in Figure 3.2. The bottom part of the structure is the same as in design 1, except for the QD location (110 nm above the silica layer). In these conditions, the dots are located on the first antinodes of the standing wave pattern for $D/\lambda=0.22$. The upper section of the wire features a trumpet-like taper; the guided mode remains confined inside the structure, but the lateral size of the mode increases progressively. The height of the taper structure is in the range of 12-18 µm. The top facet diameters (typically 1.5 µm) ensure a nearly perfect out coupling to the standard microscope objective with N.A. =0.75 [8]. Fresnel reflection at the GaAs-Air interface is suppressed by a standard anti-reflection coating (Si_3N_4, n= 2). This large top facet is also very attractive in view of future electrical injection, as it opens simpler strategies for contacting the wire's top end.

In conclusion, there are three main components for both devices: (1) nanowire section with embedded QDs for the spontaneous emission control, (2) high reflectivity modal mirror at the bottom to reflect the photons emitted downward back into fundamental guided mode, and (3) the taper section (regular and inverted taper) to adiabatically deconfine the mode to increase the collection efficiency. In order to optimize the fabrication of the device, one has to take care of all three sections.

3.3 Fabrication of single photon sources

In this section, we will describe the various steps of the fabrication of the photonic nanowire with regular and inverted tapers. Since there is no way in semiconductor growth technology to grow QDs on metal, the implementation of the bottom mirror implies a flip-chip step (wafer bonding and layer transfer technology) [9,10]. The various steps of the full fabrication process are the following: we start from a planar sample grown by molecular beam epitaxy. After this, the mirror (gold and silica) is deposited, and the sample is flip-chip glued on a host substrate. After removal of the growth substrate, the wires are defined using a top-down approach (e-beam lithography and dry plasma etching). All steps of the process are described in details in the next sections. Some of them are common to both structures; they are described only once in the next sections.

3.3.1 Starting point: planar epitaxial structures

The samples were fabricated from high quality planar heterostructures which were grown by molecular beam epitaxy (MBE) on a semi-insulating (001)

GaAs wafer (By M. Bazin, P. Jaffrennou or M. Ducruet at NPSC). Their structures are shown in Figure 3.3. A 500 nm thick GaAs buffer layer is first grown on the GaAs wafer, followed by the 500 nm thick $Al_{0.8}Ga_{0.2}As$ sacrificial layer which will acts as an etch stop layer later in the process flow. Afterward, for the first source design, we grow 2.5 µm-thick GaAs layer, with a layer of self-assembled InAs QDs located 80 nm below the top surface. The nanowires will be defined in this GaAs layer. For the second source design, the GaAs layer is 12-16 µm thick, and the layer of self-assembled InAs QDs is located 110 nm below the surface. The self-assembled InAs QDs are grown in the Stranski-Krastanov growth mode, this is one of the most well developed methods to form semiconductor QDs [11,12].

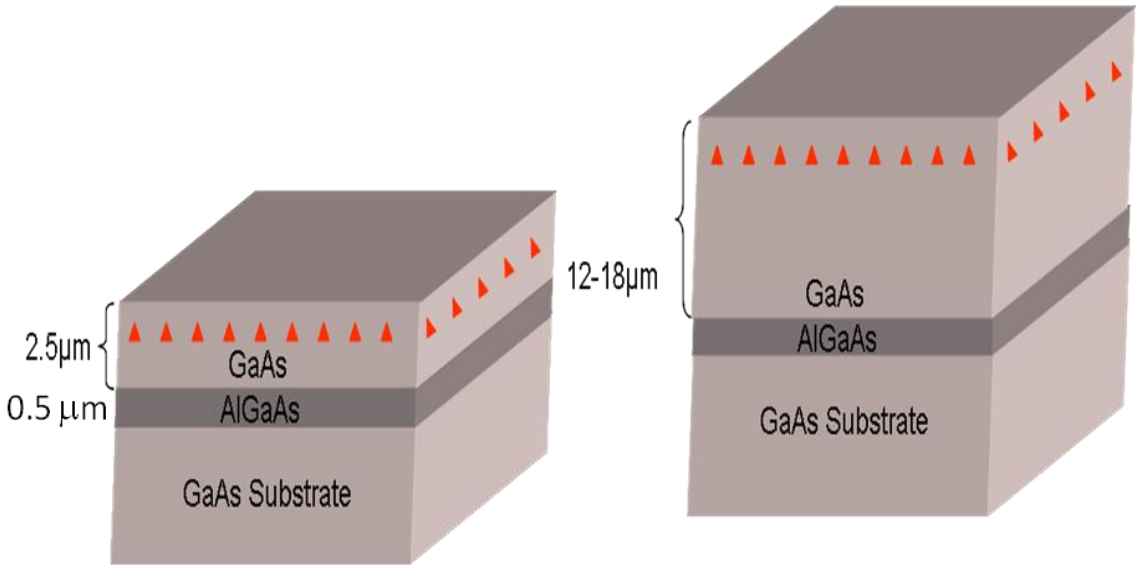

Figure 3.3: The epitaxial structures used for photonic wire fabrication, left schematic for the first design and right for the second design of SPS, where the QD (shown by red triangle) is located at 80 nm and 110 nm below from the surface in left and right structures.

We have seen that to achieve a good SE control, the wire diameter is typically of 200 nm. To be compatible with spectral separation of the X lines, the number of dots in the wires should be in the range of 1-10. This leads to areal dot density of 30-300µm^{-2} (3x10^{9} - 3x10^{10} cm^{-2}). Typically, the ensemble luminescence peaks at 920 nm, with a 50 nm inhomogeneous broadening. The fundamental optical transition, which involves heavy holes, features a dipole components perpendicular to the growth axis.

3.3.2 Deposition of Bottom Mirror

After the growth of the epitaxial structure, the high reflectivity mirror is deposited on the surface of epitaxial samples. This mirror is a combination of gold (Au) metal and a thin dielectric silicon dioxide (SiO_2) layer. Since the quality of deposited material is just replica of the surface quality of the sample, one has to conduct a proper cleaning and surface treatment before making any deposition. After cutting the epitaxial wafer in the proper pieces (typically 5mm x 5mm) in view of subsequent processing, we clean the sample surface properly with acetone, methanol and isopropyl alcohol (IPA) and then heat to dry off the solvent. This procedure removes the large particles and chips that are eventually deposited on the surface of wafer due to cleaving or dicing steps. Afterward we deposit 11nm of SiO_2 by e-beam evaporation. The very precise calibration of this thickness has been obtained by studying several samples by ellipsometry.

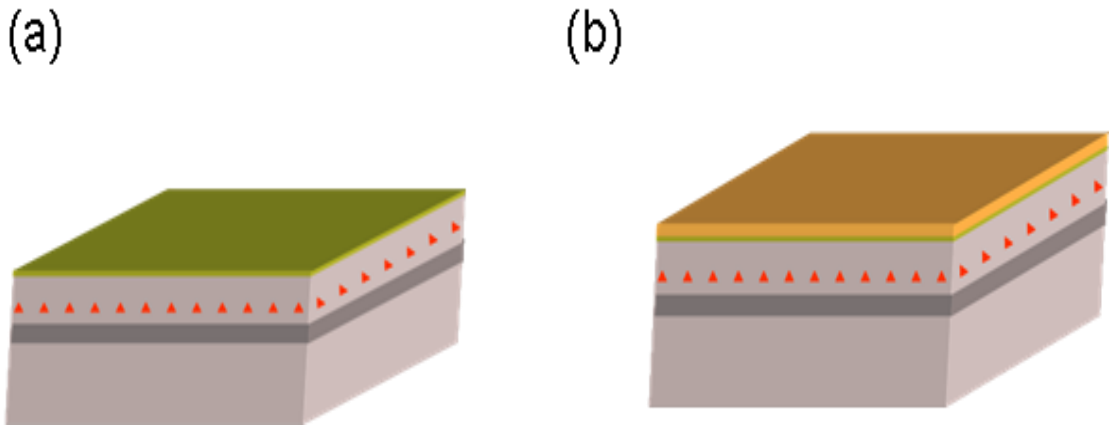

Figure 3.4: Realization of bottom Mirror, (a) SiO_2 deposition (b) With SiO_2 and Au deposition.

After depositing the SiO_2, we deposit a 250 nm-thick Au layer using RF magnetron sputtering (done at PTA). Before deposition, hydrocarbon contaminants were cleaned off from the substrate surface by baking the sample at 100°C for 1-2 minutes on hotplate. As gold has a poor adherence to the silicon dioxide, we first deposit 3 nm of Ti as a sticking layer before depositing the gold layer. Since we have to make flip chip in next step so we deposited mirror with nearly zero stress by choosing the proper deposition parameters of sputtering (see Figure 3.4) [13].

3.3.3 Flip Chip Process

The optimization of the flip-chip process was one of the most time consuming step of the entire fabrication process. In this section we will describe the associated steps of this process, sketched in Figure 3.5.

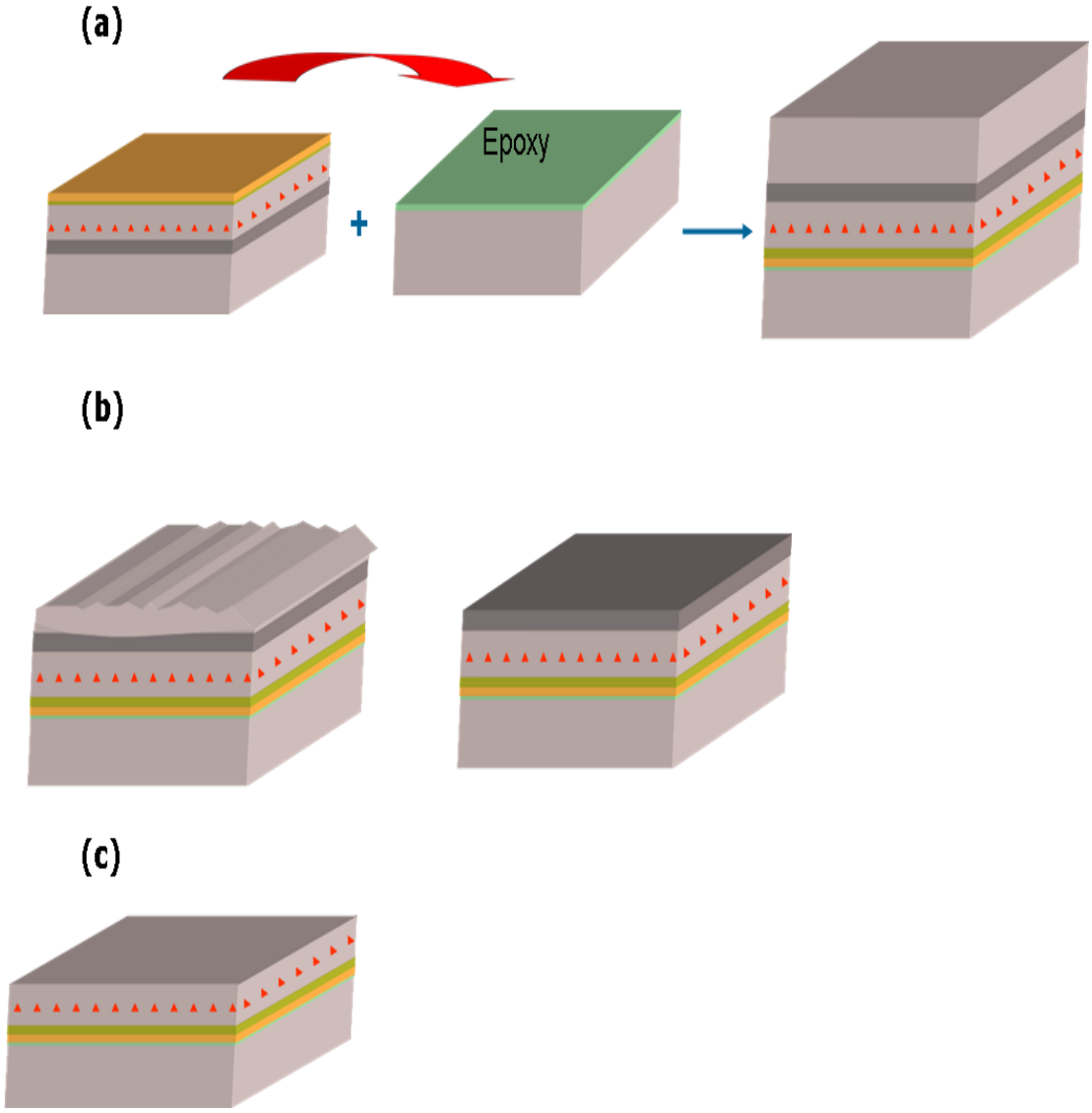

Figure 3.5: Overview of the flip chip process, (a) Bonding of the wafer (b) Removal of growth substrate by mechanical grinding (left figure) and chemical etching (right figure), (c) Etching of the sacrificial layer.

3.3.3.1 Wafer Bonding

Wafer bonding is the first step of the flip chip process. Generally speaking, bonding is the process to join of the two pieces of the same or different type materials together. Bonding of the wafers can be classified into following two categories: (1) Direct bonding in which the wafers are directly bonded, without using any intermediate layer, (2) Indirect bonding for which an interlayer is implemented. In principle, most of the materials can bond together if they have flat, smooth and clean surfaces. The choice of specific bonding process depends on the nature of the initial substrates and their tolerance to temperature as well as on the target application.

Our approach:

In this work, we use adhesive bonding (indirect bonding): an intermediate polymer adhesive layer is used to form bonding between two different wafers. Most of the time adhesives are typically composed of polymer i.e. macromolecules that are formed by cross linking of many simpler molecules known as monomers. In general, polymer has tendency to spread and interact on the surface of the wafer material. The interfacial bonding formation follows a well defined sequence, first wetting occurs (i.e. a molecular contact between the adhesive and adherent is established at the interface by a flow process, followed by absorption (the formation of the adhesive bonding across the interface) and in the last step cross linking occurs [14, 15].

We use here epoxy glue (M-Bond 610) which is a heat curable solvent-based thermosetting polymer. In order to use it for wafer bonding, M-Bond can be spin or spray coated onto one of the two wafers to be bonded. During bonding, Epoxy has the property to reach a viscous state and its ability to flow can be used for surface planarization. The advantages of the adhesive wafer bonding include the insensitivity to the surface topography, a low temperatures annealing and the ability to join different types of wafers. The bonding process is also cheap and requirements for the surface smoothness are low. We optimized this process carefully to get high quality membrane after bonding. At the beginning of the PhD, the fabrication yield was on the order of 1 out of 10. It is now about 9 out of 10. Typically, the bonded epitaxial samples are 5 x 5 mm. The various steps of the bonding process for the wafer are detailed in the next subsections

Surface preparation:

The required quality of the surfaces (cleanliness and planarity) to be bonded is partially relaxed thanks to the adhesive bonding. But it is nevertheless

always good practice to clean the sample surface before the bonding. To this end, we flow a jet of Acetone, Methanol and IPA on the GaAs host wafer and the epitaxial sample with mirror. After cleaning, the wafers are rinsed in DI water; blown dry by a clean nitrogen jet. The wafers are then heated at 100°C for short time (typically 1 min) to dry off the remaining solvent from surface of the wafers.

Gluing of the wafers and attachment:

After cleaning, we then apply a small bead of epoxy (M-bond 610) on the surface of host wafer. Afterward the mirror side of epitaxial wafer is brought in contact with the host GaAs wafer. The top wafer is floating above the host substrate. To remove the air bubbles trapped at the bonding interface, we apply an external pressure with the help of tweezers onto the surface of the top chip. To reduce the surface contamination, the time between the last step of cleaning and contacting the wafers must be as short as possible. Up to this point, the process is reversible and the wafers can be separated from each other and uncured epoxy can be cleaned with acetone.

Curing of the epoxy with heat:

In the next step of wafer bonding, the room temperature bonded wafers have to undergo a heat treatment, which is required to strengthen the bonds across the interface. Following the data sheet provided by the epoxy company [16], the epoxy is cured at a temperature of 150°C during 2h while applying a pressure (70-480 kN/m^2) with the help of metal dice. After this a postcure baking at 240°C is conducted during 2h.

3.3.3.2 Growth Substrate Removal

After the wafer bonding step of flip chip process, the next step is to remove the growth wafer. To this end, we use a process which is the combination of the mechanical etching and chemical etching.

Mechanical etching

We first remove the growth substrate by mechanically grinding using abrasive discs (which act as an abrasive slurry of chemical mechanical polishing (CMP) in presence of water) with different roughness. We start with higher roughness abrasive discs then we reduce the roughness of the discs with the thinning of the growth wafer. We stop mechanical etching before 30-35 microns

above the QDs layer to reduce the damage by mechanical etching. The process flow for this step is given below:

1. Gluing on the cylindrical metal dice
    - Check the planarity of the metal dice (maximum 20µm of height difference over the surface is tolerable)
    - Gluing the sample on the dice surface with a white wax which is soluble in acetone (at temperature 180°C on hot plate).
    - Cool down with a weight on the surface and check the planarity of the glued sample (maximum 20µm of height different over the surface is tolerable)
    - If sample surface is dirty with wax, clean the sample surface with acetone.

2. Mechanical Etching (30-35µm before the QDs membrane)
    - Measure carefully the reference height of the sample
    - Several polishing steps, with careful height checks
        - High roughness abrasive disc (p 800): from 0 to -200µm
        - Intermediate roughness abrasive disc (p1200): from -200µm to -350µm
        - Low roughness abrasive disc (p2400): from -350µm, typically 30-35µm above the membrane.

In the last step of mechanical etching process, we remove the sample by heating at 180°C on hot plate.

Chemical Etching:

After the mechanical etching, the remaining part of the growth substrate is removed by using wet chemical etching (to avoid damaging the epitaxial membrane). We use a GaAs etchant that has a high selectivity to the $Al_{0.8}Ga_{0.2}As$ stop layer, namely a solution of citric acid and hydrogen peroxide (H_2O_2). H_2O_2 oxidizes the semiconductor and the organic acid dissolves the GaAs oxide. This solution combines a reasonable GaAs etch rate (typically 1.5 µm/min at 35°C) with a high selectivity to $Al_{0.8}Ga_{0.2}As$ (>100) [17]. When the AlGaAs layer is exposed to etchant, Al_XO_y is formed, which is not dissolved by the organic acid, leading to the high selectivity. The process flow of this step is given below.

1. Gluing of the sample for etching

- Glue the sample on the microscopic glass slide with the help of white wax at 180°C, pay attention to keep some wax on the sample circumference to avoid the etching of the host substrate
- Remove exceeding wax; if necessary clean the sample surface with acetone.
-

2. Chemical Etching
   - A 40gm of citric acid is dissolved in 40ml of DI water
   - Heat this solution at 35°C with stirring for some time until solution temperature is stable.
   - Add 16ml of H_2O_2 (30% in water) in solution just before the etching, wait for 5 min for the homogenization of the solution.
   - Put the sample glass slide in the solution.
   - At the end of etching we get the mirror flat AlGaAs surface.

In the last step of this process, we remove the sample by heating at 180°C on hot plate. One could use acetone to remove the sample but it would require long time.

3.3.3.3 Etching of sacrificial layer

Once the complete removal of GaAs growth substrate is done, next step is removal of the sacrificial layer. It is recommended to protect the sacrificial $Al_{0.8}Ga_{0.2}As$ layer from interacting with air between this etching process and the preceding wet etching process. Ideally, this step should be done immediately before the air exposed sacrificial layer is oxidized. We used wet chemical etching based on hydrofluoric (HF) acid to remove sacrificial layer. The HF chemical etchant is known to have excellent etch selectivity of AlGaAs over GaAs, so GaAs layer is not affected in this process [18, 19]. To perform this process, we first clean the sample surface with acetone, ethanol and IPA to remove all the dust and remaining white wax, afterward we blow the dry nitrogen on the sample to dry off the solvent. In the second step of the process, etching is performed in 50% HF acid for 1-2 minutes (one can use lower concentration to get a lower etch rate). After the etching we rinse sample in baths of DI water, followed by the same cleaning step which we already discussed in this process. This cleaning ends the flip-chip step.

3.3.4 Fabrication of Regular Tapered Photonic Nanowire

In this work, the photonic nanowires (PNWs) are defined through a top down approach. In particular, we use e-beam lithography and plasma dry etching

(two steps). The last etching step, which defines the shape of the wire directly control the performance of the device. The process flow is summarized in Figure 3.6; the various steps are described in this section.

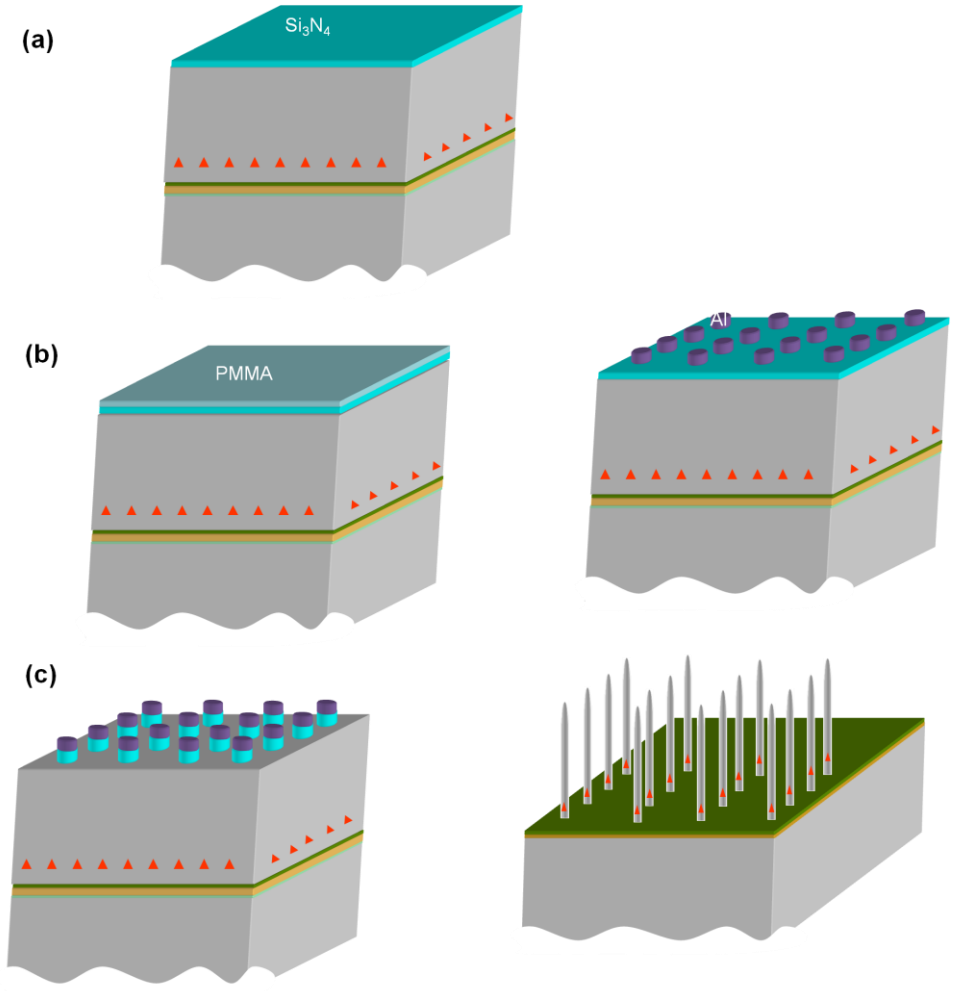

Figure 3.6: Schematic of process flow of nanofabrication, (a) Deposition of Hard Mask (Si_3N_4), (b) Ebeam lithography and lift off of Al-metal, (c) Etching of the hard mask (left figure) and Etching of the GaAs (right figure).

3.3.4.1 Hard Mask Deposition

We have to etch 2.5 µm of GaAs, thus we have to use a hard etching mask. Dielectric thin films, such as Si_3N_4 or SiO_2, can be used as masking materials for semiconductor etching to provide the high quality etching profile [20, 21]. We use here a 400nm-thick Si_3N_4 layer, deposited by plasma enhanced chemical vapour deposition (PECVD). Before deposition, the sample is cleaned

(acetone, isopropyl alcohol and methanol, dry N_2 jet). A surface treatment is used to deoxidize and passivate the surface by a sulfide solution '$(NH_4)_2S$'; this chemical treatment helps increasing the adhesion of the Si_3N_4 on the surface of GaAs. Afterward Si_3N_4 is deposited by PECVD with gas mixture of N_2 and SiH_4 by using RF power plasma excitation. We will discuss later why we used this mask for our process.

3.3.4.2 Defining an Al mask using Electron Beam lithography (EBL)

The next step of the nanofabrication of SPS devices consisted of patterning the sample surface using high-resolution electron beam lithography (EBL). EBL uses a focused beam of high energy electrons (100kV in our case) to expose an electron sensitive resist coated on the wafer [22]. The exposed resist is then selectively removed with a dedicated chemical.

The EBL system available at PTA (JEOL 6300 FS) is very performant. It features a typical 20nm spot size associated with very well calibrated writing fields. The beam is deflected by electric and magnetic fields to write individuals pixels. Since the scanning fields can only deflect the electron beam to a certain degree, large patterns are sub-divided into smaller ones, either squares with 62.5 or 500 micrometer side, which are written individually and stitched together to form the entire pattern. A laser–interferometer controlled stage is used to move from field to field (20 nm stitching accuracy). In addition, we use typical 1nA beam current, leading to high writing speeds. The lithography masks are designed with the L-edit software (Tanner EDA). For the photonic nanowire structure with regular taper, the design pattern consists of circles with diameter starting form 1µm down to 50nm with 20nm step which provides a way for a systematic study in term of etching and optics. In addition, arrows and coordinates are present, to help optics experiments.

Specifically, we used a positive e-beam resist: PMMA- 4%. It was spin coated on the sample (4000 rpm for 40 seconds), which gave a resist thickness of approximately 280 nm. The sample was then baked on a hot plate at 180°C for 5 minutes to evaporate the solvents. The sample was then ready for exposing the desired pattern, with typical doses in the 1000-3000 $\mu C/cm^2$ range. The proper dose depends on the size of the structure and of possible proximity effects. These doses have been optimized with tests. After the e-beam exposure, the resist was then developed in 1:3 methyl-isobutyl-ketones (MIBK): isopropyl-alcohol (IPA) for 30 seconds, and rinsed in IPA for 35 seconds and finally blown with dry N_2 gas.

The next step is the deposition of a mask layer, using a standard lift-off procedure. E-beam evaporation is used to deposit the thin layer of Al-metal, approximately 40 nm thick. After deposition, the sample is put in a solvent, usually acetone, to remove the unexposed resist and the metal on top of it. This lift-off step leaves Al metal disc corresponding to nanowire pattern. These metal discs will serve as an etch mask for the Si_3N_4 etching. As last step, a short oxygen plasma etching is done in a reactive ion etcher to remove possible traces of PMMA. The general principle of the sample fabrication of this step is shown in Figure 3.7.

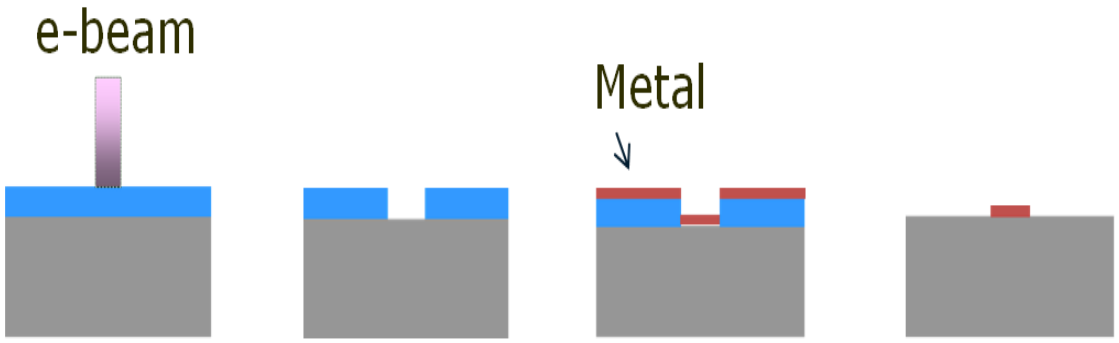

Figure 3.7: Schematic description of the EBL process with lift-off process. An electron sensitive resist is exposed to a high energy electron beam (left images). The exposed resist areas are dissolved in a suitable developer and metal is deposited on top of the remaining resist structure (two central images). As a last step the sample is put in a strong solvent that removes all resist as well as the metal deposited on top of the resist.

3.3.4.3 Defining the wires with Reactive Ion Etching (RIE)

After the definition of the Al mask, the next step is the etching to transfer the pattern. In microfabrication, etching is a process whereby a pattern from a surface mask is transferred to a sample by removing material that is not protected by mask [22]. This step, which defines the wire shape, controls the performance of the wire single-photon sources. Because of the high aspect ratio of our structure, a controlled dry etch process was the most appropriate. In this thesis, we used reactive ion etching (RIE). More advanced techniques also exist like inductively coupled plasma (ICP) [23], electron cyclotron resonance (ECR) [24]. However, such machines were not available, and RIE, which presents the advantage of robustness, gave very good results.

3.3.4.3.1 A short introduction of RIE

We use a RIE system of the standard “parallel plate” variety, which is sketched in Figure 3.8. In the parallel plate geometry, the sample to be etched sits on an electrode and gases flow into an evacuated chamber. Radio frequency power is applied to the lower electrode plate which produces an oscillating electric field inside the chamber. This field creates the plasma by the ionization of the gases. The reactions in the plasma are quite complex and include dissociation, atomic or molecular ionization, atomic and molecular excitation [22, 25]. Moreover, since the electrons are much lighter than the massive ions, electrons are much more mobile and hence collide towards the electrode. The lower electrode is dc electrically isolated from the rest of the grounded chamber and acquires a net negative charge. This results in a DC bias voltage (typically a few hundred volts) that accelerates the positive ions towards the sample. This bias voltage is controlled by system parameters (applied RF power and chamber pressure).

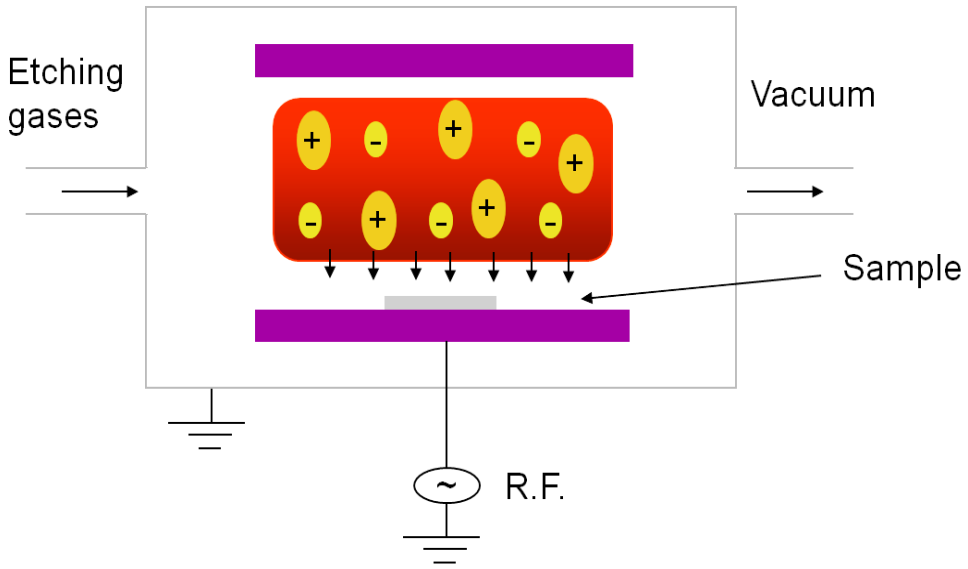

Figure 3.8: Schematic drawing of the reactive ion etching system

RIE is, in general, complex, but one can nevertheless identify 3 main processes:

- **Physical etching** occurs when ions in the plasma are accelerated by the electric field, strike the sample surface, and sputter off surface atoms by momentum transfer process. Therefore this component will induce ion

bombardment and is not very selective. This etching component tends to be anisotropic.

- **Chemical etching** involves reactive neutral species, as well as free radicals from the plasma, striking and interacting with the surface of the wafer via a chemical reaction. The by product of the reaction is typically a volatile species, which will vaporize and expose more of the wafer to be etched. The chemical aspect enables selective etching (as in wet chemical etching). Chemical etching also reduces the surface roughness. This etching component tends to be isotropic.

- **Sidewall passivation** may also occur during the etching process. This can occur due to etch by products, mask erosion and trace of the gases. This provides passivation of the etched sidewalls from the lateral etching and is very important to achieve vertical sidewalls.

Globally, the final etching profile results from the competition between these 3 processes. In turn, they are controlled by varying the gases combination and a careful tuning of the etching parameters (RF power, chamber pressure, and temperature etc).

3.3.4.3.2 General etching strategy

In this paragraph, we give the general strategy to obtain a tapered wire which is shown in the Figure 3.9. Further details will be given in the following sections. At the beginning of the etching, we have an Al metal disc on top of the Si_3N_4 layer. First, we etch the Si_3N_4 layer with a SF_6 based RIE using Al as hard mask. The etching conditions are chosen to provide a significant chemical component, leading to a conical structure in Si_3N_4, below the Al disc, which is shown in the Figure 3.9 (a). Then we etch the GaAs with a $SiCl_4$-Ar gases based RIE using two layers mask (Al and Si_3N_4) The conditions are chosen to provide an anisotropic etching (vertical sidewalls), and 3 main stages can be identified. In the beginning, the Al disc protects the structure, leading to a vertical etching of GaAs as shown in the Figure 3.9 (b). However, Al is progressively etched away by the chlorine chemistry and it disappears at some point (Figure 3.9 (c)). The etching mask is now the conical Si_3N_4 structure, and the etching starts to transfer the shape of the top mask to the GaAs as shown in Figure 3.9 (d). Note that, due to the difference in the etching rates, the opening angle of the cone is reduced,

leads to the desired taper structure which is shown in Figure 3.9 (e). The next sections provide some details on the process optimization.

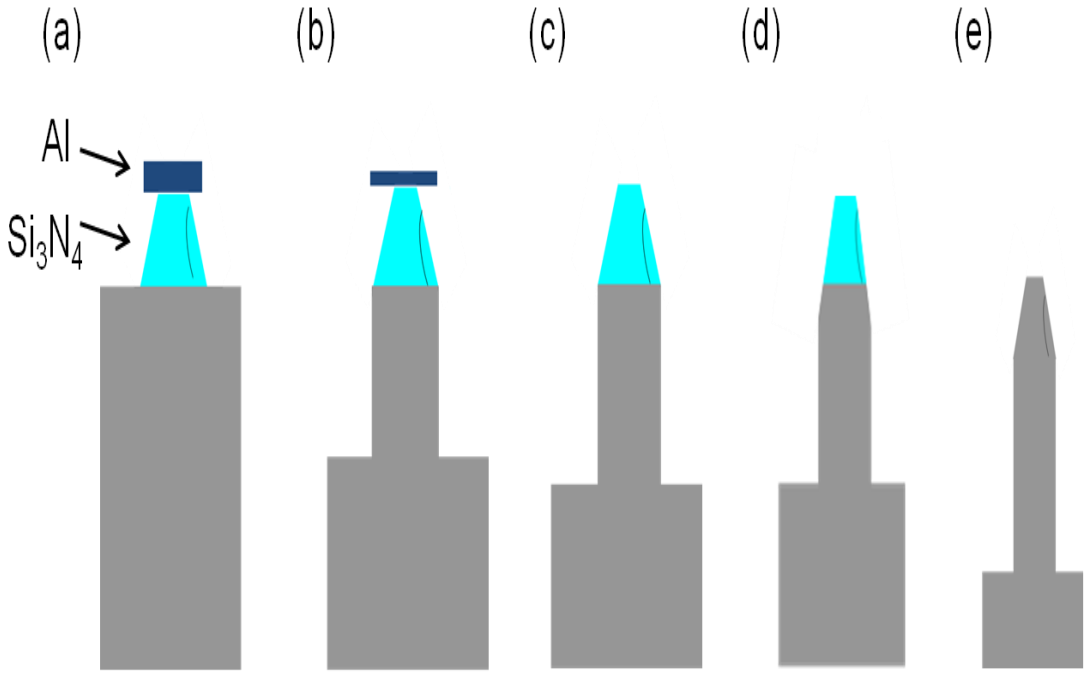

Figure 3.9: Schematic of the mechanism involved in to RIE of regular taper photonic nanowires: (a) Initial structures, (b) etching with Al as a mask, (c) Si_3N_4 mask profile after the complete etching of Al mask layer, (d) etching of angular sidewall in GaAs through Si_3N_4 mask, and (e) defining the angle of taper in GaAs after the complete removal of mask.

3.3.4.3.3 RIE of the Si_3N_4 hard mask

This process is performed using a fluorine-based chemistry (SF_6), a well known method to etch Si_3N_4 [26]. Three basic etching mechanisms for the Si_3N_4 exist under this chemistry: 1) fluorine (F) radicals reach the substrate, where they react with Si_3N_4 to form SiF_4 and N_2, both of them are volatile species and are pumped away (chemical etching), 2) F ions impinge on the substrate and knock away a Si ion (mechanical etching), and 3) F ions impinge on the substrate, chemically bind with the Si (ion assisted etching i.e. when ions don't have sufficient energy to make physical etching but have sufficient energy to induce a chemical reaction to occur). The Al mask is robust against SF_6 chemistry (Al metal creates AlF_3 in fluorine based etching which is non –volatile) [27]). The erosion of Al mask is thus negligible during this etching step.

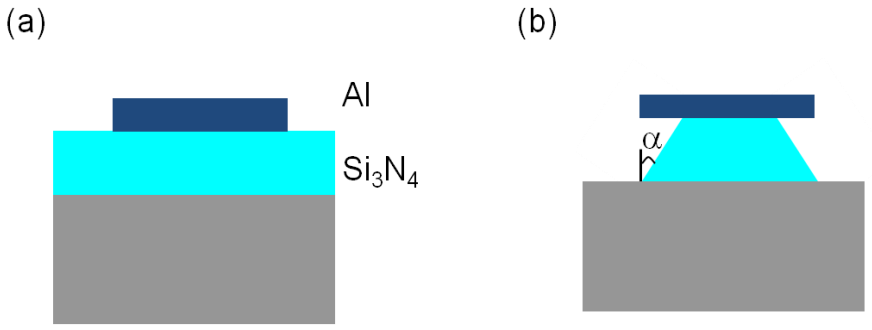

Figure 3.10: a) Initial profile of the masking layer; b) Etched profile of the masking layer.

To define a conical mask as shown in the Figure 3.10 (b), we start from the profile as Figure 3.10 (a)) and we use a highly chemical RIE. It defines some undercut below the mask with a well defined sidewall angle. In simple terms, the vertical etching rate R_{VF} involves mechanical and chemical etching, while the horizontal etching rate R_{HF} is purely related to chemical processes. The resulting slope of the mask is given by

$$\tan\alpha = \frac{R_{HF}}{R_{VF}}, \tag{3.1}$$

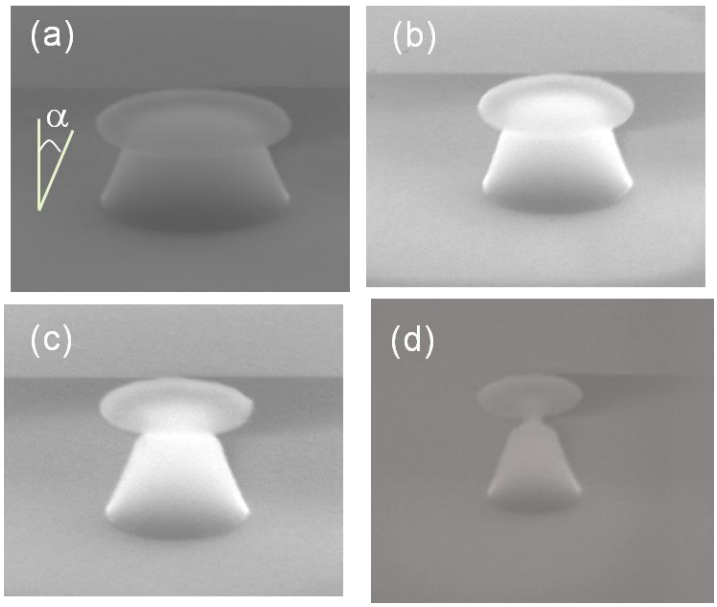

Figure 3.11: SEM images for the evolution of angular side walls of the mask with nominal bottom diameter (nm), a) 680, b) 590, c) 380, and d) 270.

Fortunately, a process developed prior to this thesis already gave satisfying results. The parameters are the following: RF power = **60**W, chamber pressure = 10 mTorr, SF_6 gas flow = **25** sccm. A post-etch SEM image of the Si_3N_4 mask of various dimensions is shown in Figure 3.11; the sidewall angle doesn't depend on the post diameter and is around 18°.

3.3.4.3.4 RIE of GaAs: definition of the nanowire

The last step of the nanofabrication is the transfer of the hard mask pattern into GaAs, to define the desired nanowires. This process is performed using a chlorine-based chemistry ($SiCl_4$ - Ar gases mixture) which is well known to etch GaAs [28-30] by using two layers (Al and Si_3N_4) etching mask. $SiCl_4$ injected into the RIE chamber and ionized to create a mixture of chlorine and silicon ions. These ions are then accelerated down to the GaAs substrate where the chlorine ions combine with the Ga, thus forming volatile etch products that are pumped away. By contrast, Ar ions provide a purely physical etching component. For these etch processes, there is no dedicated passivation gas being injected. However Si ions and oxygen traces in the etching chamber recombine to deposit a passivation layer of silicon dioxide on the sidewalls. This passivation layer stops the chemical lateral etching and is critical to achieve smooth and vertical sidewalls.

Globally, the etching recipe must satisfy 3 constraints:

- provide vertical and smooth sidewalls
- be compatible with the transfer of the shape of the conical Si_3N_4 mask
- provide a neat connection to the bottom planar mirror.

Vertical etching of GaAs – optimization of the process:

In order to optimize the etching of the structures, the first constraint was to achieve vertical sidewalls and the second was to maintain the tapering at the top facet in RIE of GaAs with this two layers mask. In general, there is a trade off between the directionality and the selectivity of the etching in the RIE. The balance of these factors depend upon which reaction mechanisms dominate on the etching (chemical or physical etching), which in turn is determined by the energy of the ions striking on the surface and by the concentration of the reactive gases. To optimize this we conducted various test. We use anisotropic etching to obtain vertical sidewalls in the first step of the etching. We have worked on optimizing the process parameters to minimize the degree of undercutting while

maintaining sufficient selectivity. In the following we discuss the optimization of this step.

Starting point (too chemical): Our starting point was the following: chamber pressure = 15mT, gases flow rates: $SiCl_4$ = **6** sccm and Ar = **75** sccm, RF power = **40**W. Figure 3.12 (a) and (b) show SEM image of nanowires with top diameter 370 nm and 250 nm etched with this process. One can clearly see from the Figure 3.12 (b), there is a slight under etching due to dominating chemical nature of this etching process. Due to this under etching, the nanowires in the diameter range of our interest are fallen down. Moreover, the conical tip formation in diameter range of interest is insufficient.

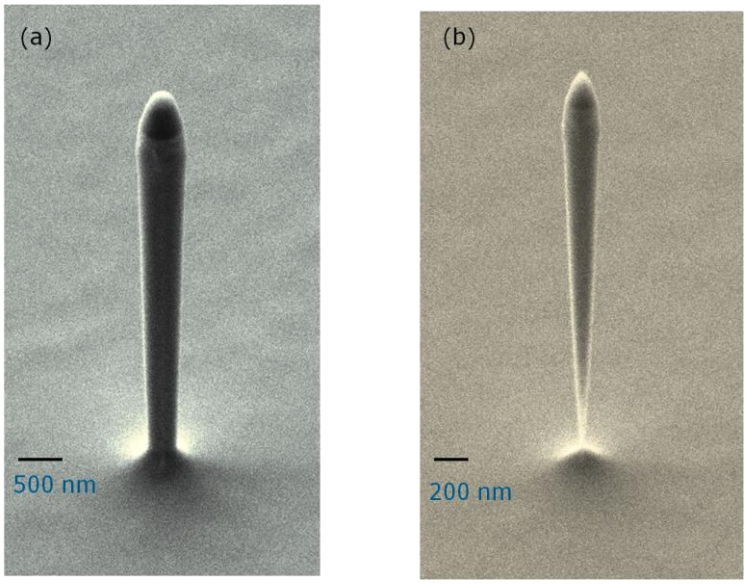

Figure 3.12: SEM images of nanowires etched with chemical components dominating RIE with top diameter 370 nm (a) and 250 nm (b).

It was thus necessary to increase the mechanical component of the process. 20 different tests were realized, principally increasing the RF power (to increase the dc bias), decreasing the chamber pressure and decreasing the $SiCl_4$ relative concentration. We detail in the following only a few representative examples.

A second example (too physical): A more physical etching is provided by the following settings: chamber pressure = 15mT, gases flow rates: $SiCl_4$ = **1.5** sccm and Ar = **75** sccm, RF power = **80**W. Figure 3.13 (a) and (b) show SEM image of

nanowires with diameters of 320 nm and 215 nm. The sidewalls are perfectly vertical. The biggest wire shows a tapered upper tip, but in the diameter range of interest (200nm), the top facet of nanowire is damaged due to excessive mask erosion (Figure 3.13 (b)).

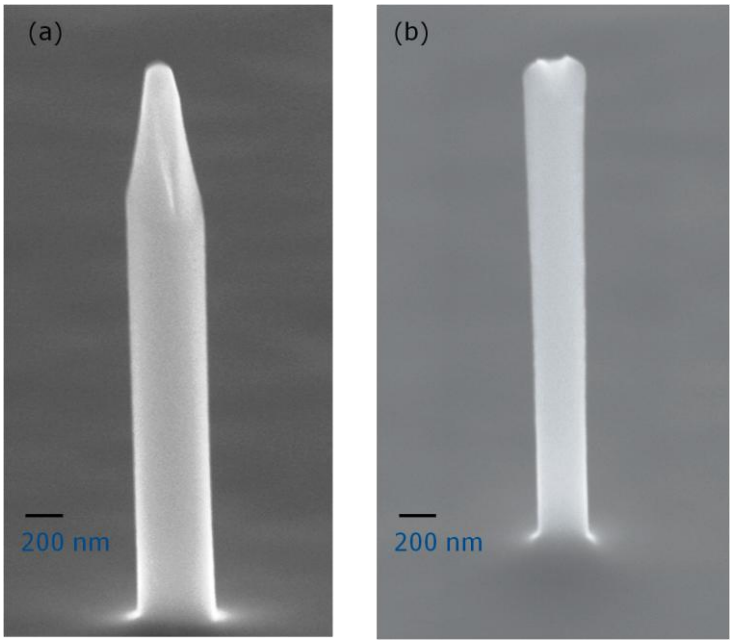

Figure 3.13: SEM images of nanowires etched with physical components dominating RIE with top diameter 318 nm (a) and 215 nm (b).

Final process: Satisfying etching was obtained from the following combination of parameters: chamber pressure = 15mT, gases flow: SiCl4 = **3** sccm and Ar = **75** sccm, RF power = **80** W. Figure 3.14 shows the SEM images of the nanowire of diameter 230 nm etched with this process. It clearly shows the etching of vertical sidewalls and the formation of taper tip at the upper end of the nanowire. For these parameters, the RIE etch rate was estimated to be 125-150 nm/min. In the beginning of the etching, the Al acts as a mask and provides vertical etching profile in the beginning. The Al mask survives around one third of the duration of the complete etching. After the complete erosion of this mask, the Si_3N_4 posts with angular sidewalls play the role of etching mask. In this step, the physical part of the etching facilitates the vertical etching of GaAs nanowire and the chemical part provides smoothing to sidewalls. The nanowire patterns are then etched to a depth of 2.5 micron via RIE. In the following section we discuss the mechanism to define the taper in detail.

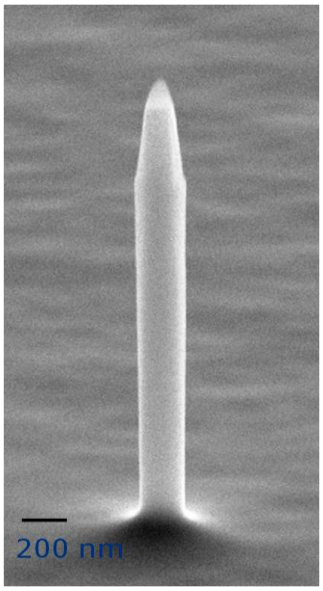

Figure 3.14: SEM image of nanowire of diameter 230 nm etched with balance RIE process using 3 sccm of $SiCl_4$.

Mechanism of the taper formation

In fact, thanks to the etching rate difference between the GaAs and the Si_3N_4, there is a sharpening of the wire tip during the shape transfer in the second step of RIE due to progressively unmasking of the GaAs. The mechanism is illustrated in 3.15. For simplicity, we assume that the etching is purely vertical. The etching rates of Si_3N_4 and GaAs in Cl-based RIE are respectively denoted R_{SiN} and R_{GaAs}. Therefore, during a time interval t, the etching mask is vertically etched of $t.R_{SiN}$ and the circumference of the GaAs wire is etched of $t.R_{GaAs}$. Simple geometry leads to:

$$\tan\alpha_{GaAs} / \tan\alpha_{SiN} = R_{SiN} / R_{GaAs}, \quad (3.2)$$

where α_{SiN} and α_{GaAs} are respectively the sidewall angles of the mask and the GaAs wire. It is clear from the equation 3.2 that the final slope in the GaAs is the function of initial slope of the Si_3N_4 mask and the selectivity. The higher the selectivity, the sharper is the transferred taper. If the process is too physical that is to say low selectivity, the taper angle is not decreased enough (see Figure 3.13). In our case the top mask is completely consumed at the end of the etching in the range of interested diameter of the photonic wire which leads to the sharp taper. This process is clearly shown in the Figure 3.16.

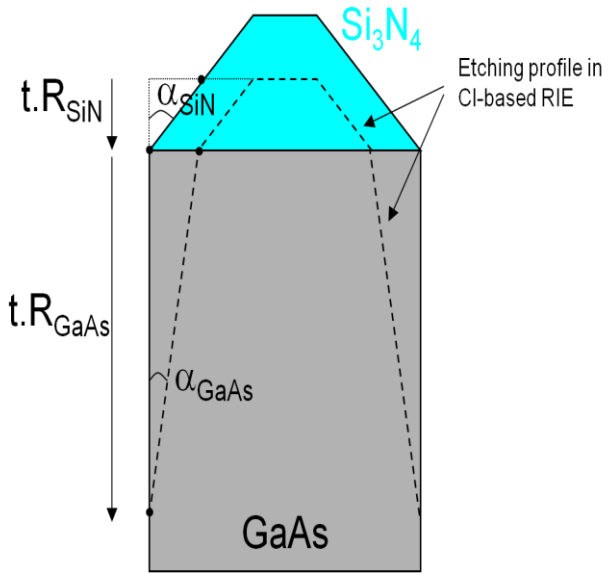

Figure 3.15: Mechanism of taper formation, where the dashed lines shows the etching profile of Si_3N_4 and GaAs in Chlorine based etching.

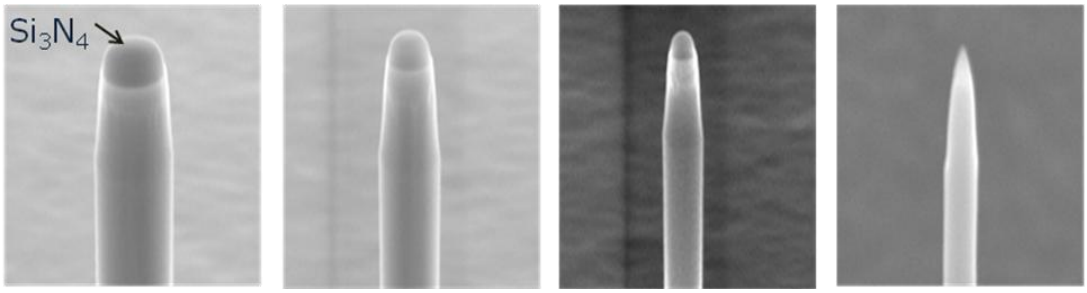

Figure 3.16: SEM images for the taper tip formation process for nanowire with decreasing diameters.

Etching stop:

The end of etching is determined using an laser interferometric detection. In the case of an etch stop layer made of gold, the interference signal is very clear. To eliminate the GaAs pedestal which is often surrounding the wire at the bottom facet, an over etching of 3 min is conducted. Figure 3.17 (a) shows an array of photonic wires, with decreasing diameters from 800 nm to 100 nm with 20 nm steps. Figure 3.17 (b) is a SEM tilted view of a wire corresponding to a nominal mask diameter of 280 nm with a very smooth sidewalls. The GaAs wire is 2.5 µm high, with a diameter of about 200 nm at the location of the dots which ensures an efficient SE control. The final dimensions and profiles of the GaAs

photonic nanowires were determined by the initial diameter of the Si_3N_4 etch mask and the etching conditions. It features a clean geometry, with a smooth conical top taper and a clean connection to the bottom mirror. The total tapering angle has been estimated to about 5°, which provides a modal transmission exceeding 78% into a numerical aperture of 0.75. The observed slight under etching of the sidewall is not a problem for experiments.

(a) (b)

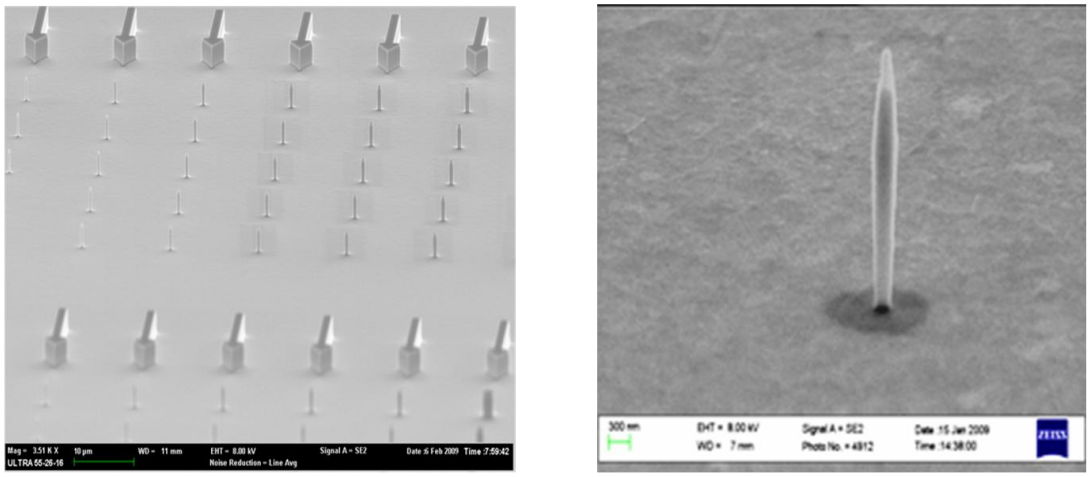

Figure 3.17: (a) SEM view of an array of nanowires on modal mirror (Au+ SiO2), with decreasing diameters by 20 nm steps. (b) SEM tilted view of a nanowire having a nominal mask diameter of 280 nm with real post etched diameter around 210 nm. This diameter leads reproducibly to the best SPS efficiencies.

3.3.5 Fabrication of trumpet like photonic nanowires

In this section, we will describe the nanofabrication process of the single photon source based on the photonic nanowire with inverted taper section. We also use a top down approach and the first process steps (flip chip) are similar to the fabrication of the regular taper nanowires. The process flow, after the flip-chip, is illustrated in Figure 3.18. In this process, first a dielectric anti-reflection (AR) coating is deposited on the structure and then Ni etching disc masks are defined by ebeam lithography and liftoff process. Afterward the AR coating is etched in a RIE system (fluorine chemistry) and the wires are finally defined by a chlorine based RIE step. In the last step, the etching mask is removed by wet chemistry.

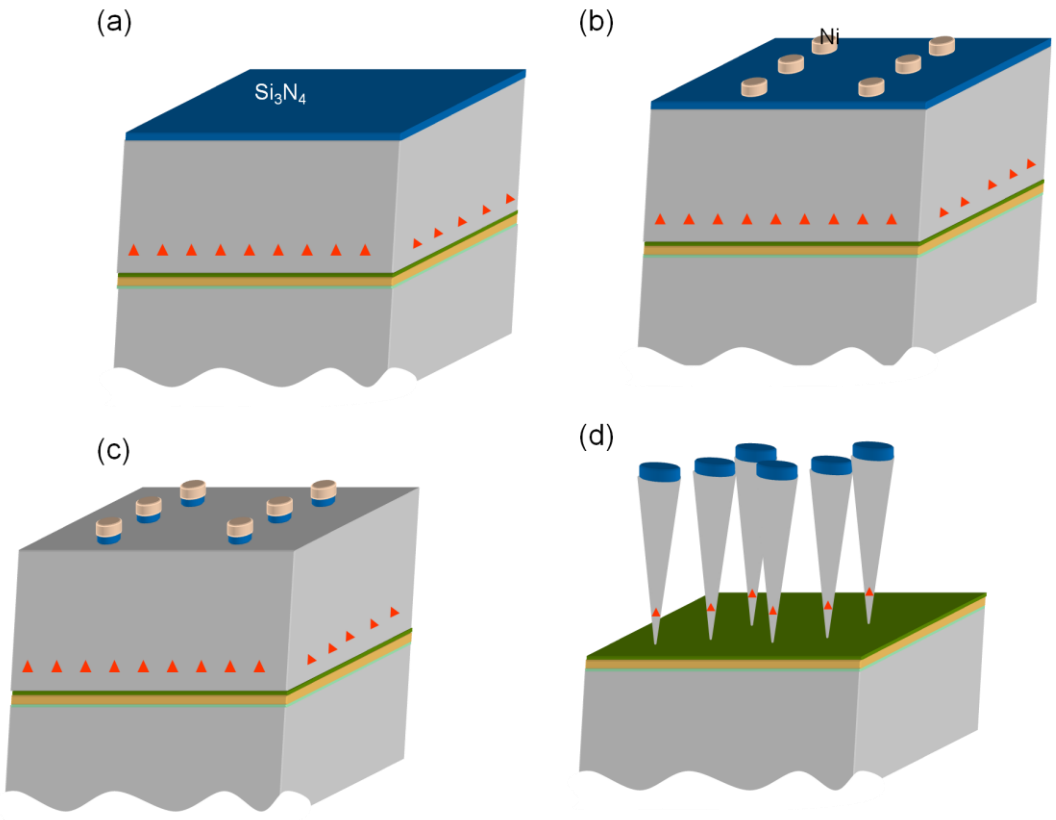

Figure 3.18: Process flow of the Ni-metal hard mask approach to fabricate inverted taper, (a) Deposition of AR-coating (Si_3N_4), (b) e-beam and lift-off process for the Ni-metal mask, (c) RIE of the AR-coating and (d) RIE of the inverted taper in GaAs.

3.3.5.1 Deposition of Anti-reflecting coating

After the flip chip process, a silicon nitride anti-reflection (Si_3N_4-AR) coating was deposited on the top of the QDs membrane surface by PECVD, which is required to reduce the reflection at the top facets of the wire. Before the Si_3N_4 on the flip chip sample, the samples are cleaned in the sequence of acetone, isopropyl alcohol and methanol. The surface is then deoxidized and passivated by a wet ammonium sulfide treatment to increase the adhesion of the Si_3N_4 on the surface of GaAs and then silicon nitride was deposited by PECVD. The Si_3N_4 film has a refractive index of about 2 at the wavelength λ of 935nm. For a single layer AR coating, a quarter-wavelength thick Si_3N_4 is chosen in order to minimize the normal incidence reflection. For applications operating at the wave length of 935 nm, the target Si_3N_4 thickness is calculated to be $\lambda/4n$ = 116 nm, which is deposited on the top surface of the sample. After the AR-coating, the sample is ready for the next step.

3.3.5.2 Choice and definition of the etching mask

We have to perform a very deep etching of GaAs (typically 15 µm). We have thus chosen to use a Ni hard mask, with a thickness of 150 nm. This mask is very robust against the chlorine etching [28- 31], much more than the equivalent thickness of Si_3N_4. Moreover, it can be removed with nitric acid, without deteriorating the GaAs structure. Prior to this, we have also made test with a 1 µm-thick Si_3N_4 layer, but this mask was not hard enough to make such deep etching of GaAs. Figure 3.19 shows the SEM image of the inverted taper structure etched with this approach and failure of this mask.

To define the top Ni mask, we use single step electron beam lithography. The patterns consist of circle from 3 µm down to 500 nm with a 20nm step. After the spin coating and baking of the resist, we perform e-beam exposure and then the development of the resist, a 150 nm thick Ni metal was evaporated on the sample, followed by an acetone liftoff process. It leaves several identical arrays of Ni discs, with various diameters. These Ni metal discs act as a hard mask for the etching of GaAs in the subsequent etching steps.

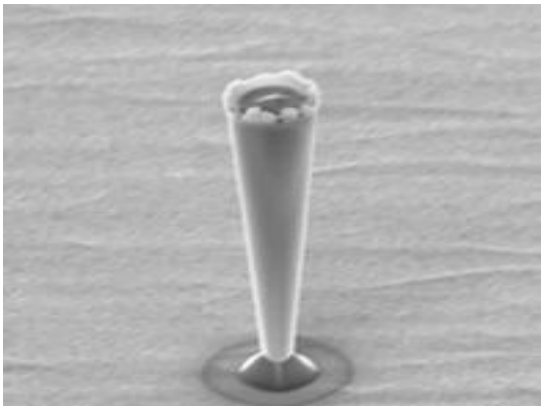

Figure 3.19: SEM image of a pillar etched by using Si3N4 as a hard mask.

3.3.5.3 Reactive Ion Etching: Pattern Transfer Process

In this section, we will describe the reactive ion etching process to transfer the pattern into GaAs. Our process optimization work was focused on achieving a dry etching process to provide the inverted taper section with high quality sidewalls. The RIE steps consist of the two steps which we describe below in details.

3.3.5.3.1 RIE of AR-coating

The next step of the fabrication is to transfer the pattern from the Ni layer to the silicon nitride AR-coating. We use the same fluorine-chemistry (SF_6) in the RIE that the one used for the regular taper structures (same process parameters). Given the small height of the layer (116 nm), and the large top facet diameter, the Si_3N_4 under etching can be neglected in that case that. Figure 3.20 shows the SEM image of a wire whose top facet is covered by Si_3N_4.

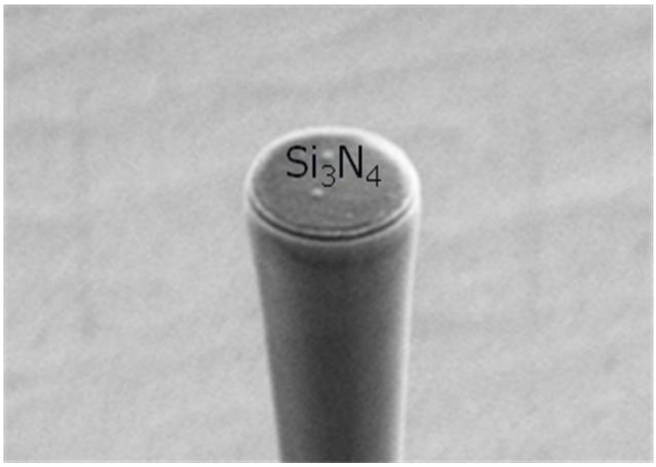

Figure 3.20: SEM image of the etching profile of Si_3N_4, the top Ni-mask we have removed in this picture.

3.3.5.3.2 Defining trumpet-like tapers

The last step of the nanofabrication is to transfer the wire pattern in to the GaAs. This process is carried out in the RIE system, using a chlorine-based chemistry (Ar and $SiCl_4$ gas mixture). The main challenge is here to fabricate high aspect ratio structures with smooth sidewalls. Compared to the process used for regular tapers, we use a more chemical recipe, for two reasons:

- Given the long etching time (1-2h), we want to preserve the Ni mask. As discussed before, chemical etching is more selective than physical etching.
- A significant under etching is desirable (otherwise an unrealistically long structure is required to achieve a 1.5 µm top facet diameter with 200 nm bottom diameters).

We thus use a lower RF power and an increased $SiCl_4$ relative concentration. After some tests, we have finally retained the following recipe: chamber pressure = 15mT, gases flow: $SiCl_4$ = **12** sccm and Ar = **75** sccm, RF

power = **40** W. Figure 3.21 shows an SEM image of an inverted taper wire etched in a GaAs test sample (without bottom mirror). The etching depth was around 12 µm; the bottom and top diameters of the last surviving pillar are 240 nm and 1.8µm with the side walls angle is around 5° (total tapering angle of 10°). For a given bottom diameter, the top facet diameter is determined by the sidewall angle. Note that the structure features a pedestal; it is removed in the final sample with a proper over etching (time estimated according to the height measured on the SEM picture).

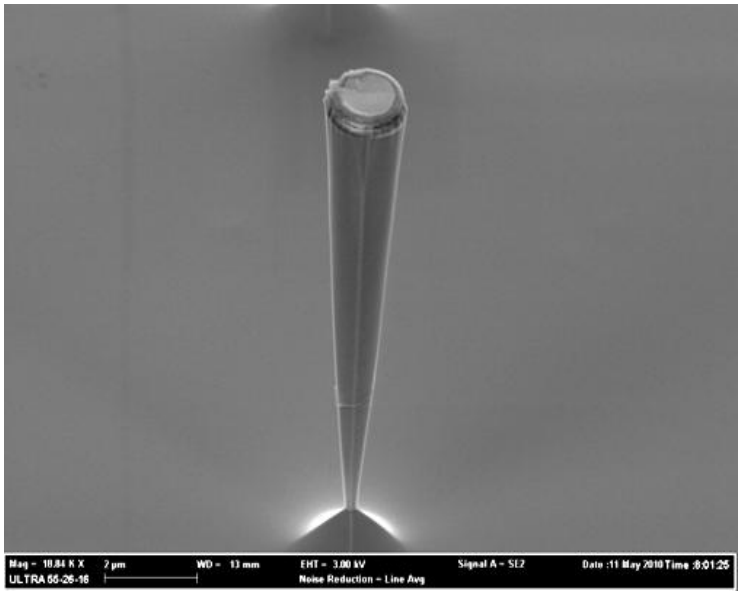

Figure 3.21: SEM image of an inverted taper pillar etched with 12 sccm of $SiCl_4$ by using Ni metal as a hard mask.

Figure 3.22 shows the SEM images of the inverted taper structures (real sample with bottom mirror) etched with same etching recipe, which features the nice taper with smooth and high quality sidewalls and a clean connection between the mirror and the bottom end of the wires. The etching depth is around 12µm with bottom and top facets diameters 200 nm and 1.5 µm respectively and the total taper angle is around 7°. Figure 3.23 shows, we fabricated high aspect ratio inverted taper with a bottom diameter as low as 90 nm with Ni metal etching mask, which highlights the quality of our etching process and very fine control of it. The final step is the removal of the remaining of the Ni hard mask. This is done using a wet etching solution of nitric acid (66%) diluted 10 times in deionised

water (for 1 min 30 s). The result is shown in Figure 3.24, showing the clean top facet.

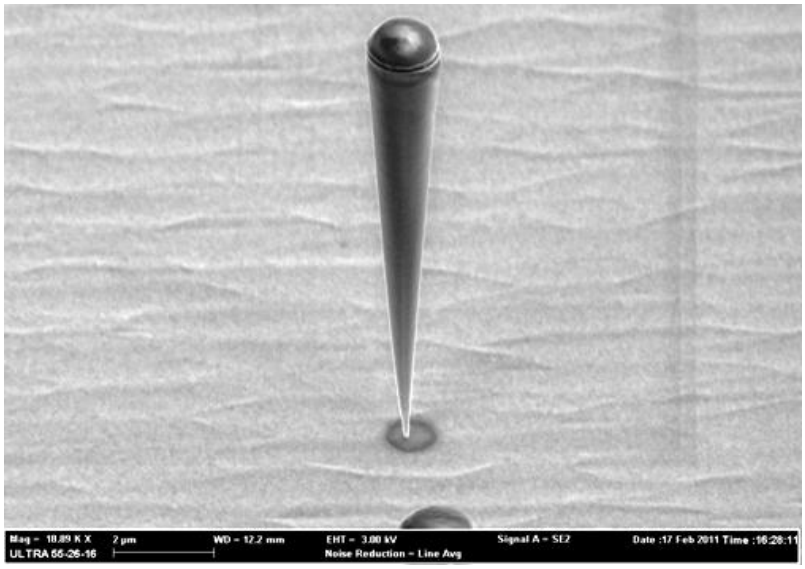

Figure 3.22: SEM image of an inverted taper etched with Ni metal as a hard mask. The etch height was around 12µm. The bottom and top facets diameters are 200nm and 1.5µm.

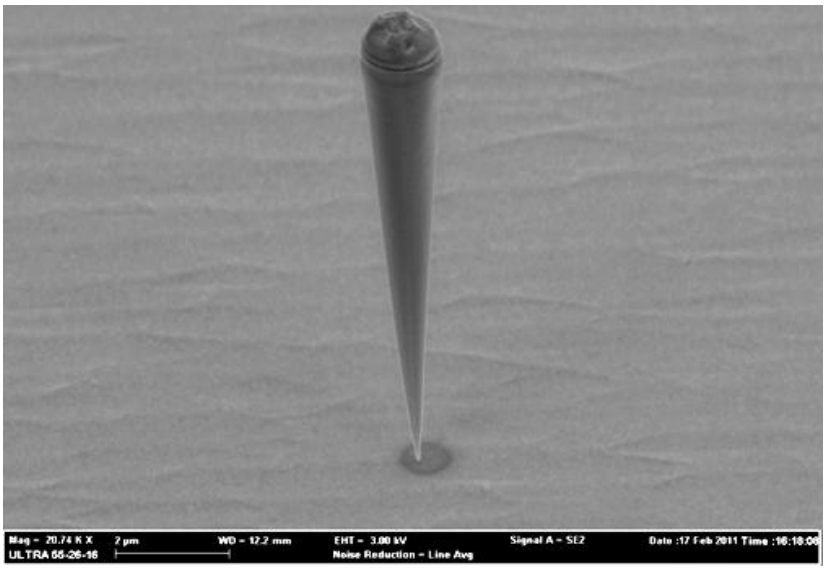

Figure 3.23: SEM image of an inverted taper etched with Ni metal as a hard mask. The etch height was around 12µm. The bottom and top facets diameters are 86nm and 1.45µm.

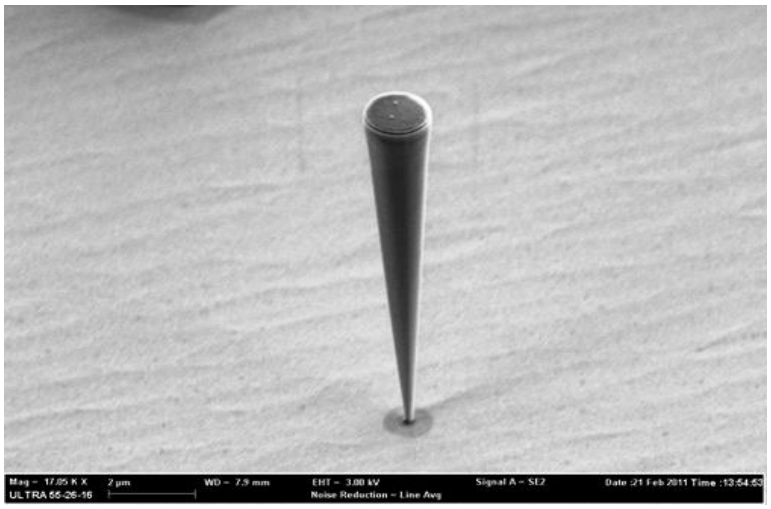

Figure 3.24: SEM image of an inverted taper after removing Ni metal hard mask. The etch height was around 12µm. The bottom and top facets diameters are 200nm and 1.5µm. It features a clean top facets and smooth side walls.

The top facet diameter, of the order of 1.5µm, is already sufficient to ensure a nearly perfect coupling to a standard microscopic objective in the far field. In principle one can use this process to get much larger top facet of the wire. Figures 3.25 shows SEM image of GaAs wire realized with the same process. The top and bottom facet diameters are around 1.7 µm and 216 nm with taper height around 16.5.

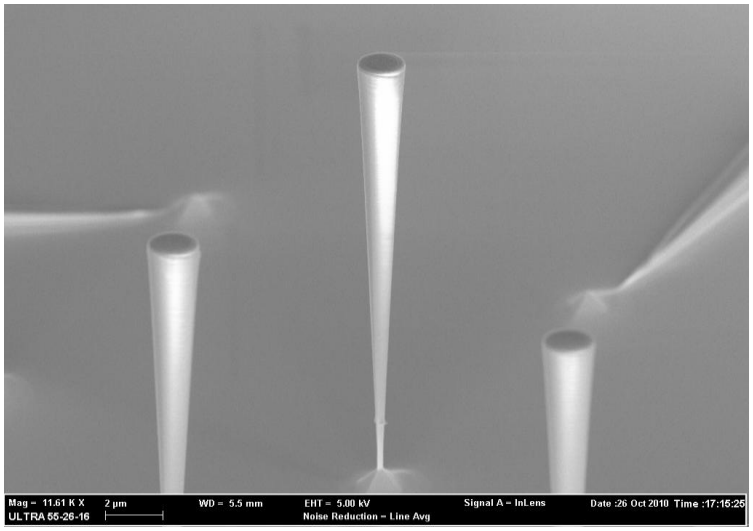

Figure 3.25: SEM image of an inverted taper etched with Ni metal as a hard mask. The etch height was around 16.5 µm. The bottom and top facets diameters are about 216nm and 1.7 µm.

3.4 Conclusion

The fabrication of these high efficiency single photon sources is a complex task which involves a large number of technological steps as described in this chapter. The choice of the etching mask has a strong influence on the other technological steps. To conclude this chapter, a new process for the realization of the high reflectivity modal mirror for the photonics nanowire structure is developed. We have demonstrated a new process to fabricate a photonic nanowire based single photon source which features a regular taper with conical tip. It uses two layers mask (with Al and Si_3N_4) and two steps RIE process. Very good control over the sidewall profile and the tip profile has been achieved.

On the other hand, we have also demonstrated a new optimized process for the fabrication of the inverted taper structures with extremely high aspect ratios. In order to fabricate the high aspect ratio inverted taper, we have developed a new hard mask by using Ni metal. This mask is strong enough to hold for the deep etching of the semiconductor and rather easy to remove selectively at the end. For the both fabrication processes, the etch profile has been optimized to get the desire slope, by playing with the settings of the ion energy (control by the DC bias), chlorine/argon ratio and the chamber pressure. We have also demonstrated that these etch processes can also be used to fabricate structures on the top of a planar gold mirror, with a neat connection by careful optimization of the process. Both realized structures are very attractive for the single photon source applications as theoretically predicted in chapter 2. The optical performance of the device will be presented in the next chapter.

References

1. E. Knill, R. Laflamme, and G. J. Milburn, "*A scheme for efficient quantum computation with linear optics*," Nature **409**, 46 (2001).
2. E. Waks, K. Inoue, C. Santori, D. Fattal, J. Vuckovic, G. S. Solomon, and Y. Yamamoto, "*Secure communication: Quantum cryptography with a photon turnstile*," Nature **420**, 762 (2002).
3. A. Shields, "*Semiconductor quantum light sources*," Nature Photonics **1**, 215 (2007).
4. J.-M. Gérard, and B. Gayral, "*Strong Purcell effect for InAs quantum boxes in three-dimensional solid-state microcavities*," J. Lightwave of Technology **17**, 2089 (1999).
5. J.-M.Gérard, "*Solid-State Cavity-Quantum Electrodynamics with Self-Assembled Quantum Dots,*" *Single quantum dots: Fundamentals, applications and new concepts* **90**, 269 (2003).

6. W.L.Barnes, G.Bjork, J.M. Gérard, P.Jonsson, J.A.E.Wasey, P.T.Worthing and V.Zwiller, "*Solid-state single photon sources: light collection strategies*," Eur. Phys. J. D **18**, 197 (2002).
7. I. Friedler, C. Sauvan, J. P. Hugonin, P. Lalanne, J. Claudon, and J. M. Gérard, "*Solid-state single photon sources: the nanowire antenna*," Opt. Exp. **17**, 2095 (2009).
8. N. Gregersen, T. R. Nielsen, J. Mørk, J. Claudon, and J.-M. Gérard, "*Designs for high-efficiency electrically pumped photonic nanowire single-photon sources*," Opt. Exp. **18**, 21204 (2010).
9. C.A.Wang, D.A. Shiau, P.G. Murphy, P.W. O'Brien, R.K. Huang, M.K. Connors, A.C. Anderson, D. Donetsky and G. Bleneky *et al*., "*Wafer Bonding and Epitaxial Transfer of GaSb-Based Epitaxy to GaAs for Monolithic Interconnection of Thermophotovoltaic Devices," J. Electron. Mater* **33***,* 213 (2004).
10. A. Ersen, I. Schnitzer, E.Yablonovitch and T.Gmitter,"*Direct bonding of GaAs films on silicon circuits by epitaxial liftoff***,**" Solid State Elec. **36**, 1731 (1993).
11. Y. Masumoto, T. Takagahara, "*Semiconductor quantum dots: physics, spectroscopy and applications* ," Springer, 2002.
12. P. Michler, Editor, "*Single Quantum Dots: Fundamentals, Applications,and New Concepts,"* Springer-Verlag, 2003.
13. Y. N. Picard, D. P. Adams, O. B. Spahn, S. M. Yalisove, D. J. Dagel, and J. Sobczak, **"***Low Stress, High Reflectivity Thin Films for MEMS Mirrors,"* Mat. Res. Soc. Symp. Proc. **729**, 3111 (2002).
14. W. P. Eaton, S. H. Risbud, and R. L. Smith, "*Silicon wafer to wafer bonding at* T< *200°C with polymethylmethacrylate,"* Appl. Phys. Lett, **65**, 439 (1994).
15. S. Weichel, R. de Reus and M. Lindahl,"*Silicon-to-silicon wafer bonding using evaporated glass,"* Sensors&Actuators A **70,** 179 (1998).
16. http://www.datasheetcatalog.org/datasheet/vishay/bond610.pdf
17. J.-H Kim, D. H. Lim, and G. M. Yang, *"Selective etcing of AlGaAs/GaAs structures using the solutions of citric acid /H_2O_2 and de-ionized H2O/buffered oxide etch,"* J. Vac. Sci. Technol. B, **16**, 558 (1998).
18. E. Yablonovitch, T. Gmitter, J. P. Harbison, and R. Bhat, "*Extreme selectivity in the lift-off of epitaxial GaAs films,"* Appl. Phys. Lett. **54**, 2222 (1987).
19. X. S. Wu, L. A. Coldren, and J. L. Merz, "*Selective etching characteristics of HF for $Al_xGa_{1-x}As$/GaAs,"* Electronics Letters **21**, 558 (1985).
20. A. Behfar-Rad, S. S. Wong, J. M. Ballantyne, B. A. Soltz, and C. M. Harding, "*Rectangular and L-shaped GaAs/AlGaAs lasers with very high quality etched facets*," Appl. Phys. Lett. **54**, 493 (1989).
21. T. Rivera, A. Izrae , R. Azoulay , R. Kuszelewicz, J.F. Bresse, J.L. Oudar, and F.R. Ladan., "*Fabrication of all-optical quantum well bistable microresonators by reactive ion etching,"* J. Vac. Sci. Technol. B **13,** 268 (1995).
22. Stephen A. Campbell, "*The Science and Engineering of Microelectronic Fabrication,*" Oxford University Press (2001).
23. D.C. Hays, H. Cho, K.B. Jung , Y.B. Hahn, C.R. Abernathy, S.J. Pearton ,F. Ren and W.S. Hobson, "*Selective dry etching using inductively coupled*

plasmas Part I. GaAs/AlGaAs and GaAs/InGaP," Appl. Sur. Sci. **147**, 125 (1999).
24. Y. W. Chen, B. S. Ooi, G. I. Ng, K. Radhakrishnan, and C. L. Tan, "*Dry via hole etching of GaAs using high-density Cl_2/Ar plasma*," J. Vac. Sci. Technol. B **18**, 2509 (2000).
25. A. G. Baca and C. I. H. Ashby editor, "*Dry etching of GaAs and related alloys,*" Fabrication of GaAs Devices Chapter 5, The institution of Electrical Engineers, 147 (2005).
26. F. R. de Almeida, R. Katsuhiro, and H.S. Maciel, "*Reactive ion etching of PECVD silicon nitride in SF_6 plasma*," J. of Nuclear Mat. **200**, 371 (1993).
27. E.Cook and Bernanrd Siegel, "*Reactions of SF6 with exploding metals*," J. Inorg. And Nuc. Chem. **29**, 2739 (1967).
28. S. Varoutsis, S. Laurent, I. Sagnes, A. Lemaitre, L. Ferlazzo, C. Meriadec, G. Patriarche, I. Robert-Philip and I. Abram, "*Reactive-ion etching of high-Q and submicron-diameter* GaAs/AlAs micropillar cavities," J. Vac. Sci.Technol. B **23**, 2499 (2005).
29. M. B. Stern, P. F. Liao, "*Reactive ion etching of GaAs and $SiCl_4$*," J. Vac. Sci. Technol. B **1**, 1053 (1983).
30. D. Lauvernier , S. Garidel, C. Legrand and J.-P. Vilcot, "*Realization of sub-micron patterns on GaAs using a HSQ etching mask*," Microelec. Eng. **77**,210 (2005).
31. M. W. Geis, G. A. Lincoln, N. Efremow and W.J. Piacentini, "*A novel anisotropic dry etching technique*," J. Vac. Sci. Technol 19, 1390 (1981).

Chapter 4

Optical performance of the cylindrical photonic nanowire

*Theory guides. Experiment decides.-**J. Wolfgang von Goethe***

In this chapter, we investigate the optical performances of cylindrical GaAs photonic nanowires embedding InAs QDs. To optimize the out coupling to the far-field, the sample features a bottom mirror and a tapered upper tip, as described in Chapter 2 and 3. First, we study the control of emission dynamics of single quantum dots (QDs) embedded in photonic nanowire, using time-resolved micro-photoluminescence measurements. Working with wires of different diameter allows us, to probe separately the coupling to the radiative modes and the coupling to the guided mode. In the second section, we study the performance of the single photon source (SPS) under pulsed optical pumping. We present measurements of the source efficiency and measurements of the photon statistics. Compared to the state-of the art, our photonic nanowire-based SPS offer significant improvements that are discussed in the end of the chapter.

4.1 Control of Spontaneous Emission of Quantum Dot by photonic nanowire

In this section, we discuss the direct experimental investigation of spontaneous emission dynamics of single InAs quantum dot embedded into a GaAs photonic nanowire. After describing the sample, we present the principle of time-resolved micro-photoluminescence measurements. Then we discuss the strategy to probe separately the coupling to the radiative and guided modes and present the experimental results.

4.1.1 The Sample

The sample investigated in this chapter is shown in Figure 4.1 (optical micrograph and SEM image). It has been fabricated following the process as described in the chapter 3. The wires, that feature a circular section, are made of GaAs and contain a single layer of self-assembled InAs QDs. In order to optimize the collection of light in far field, the bottom facet is terminated by a modal mirror. A conical taper is implemented at the top facet in order to reduce the divergence of the output beam. To allow for systematic studies, we fabricated a series of photonic wires with diameter varying by a fine 20-nm step. The diameter of the wires studied in this chapter has been measured by scanning electron microscopy with ± 10nm accuracy.

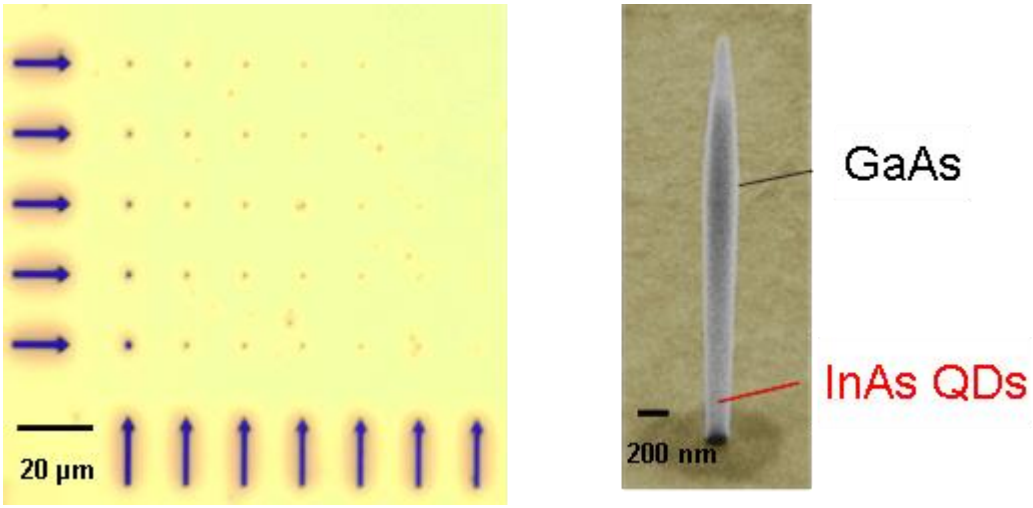

Figure 4.1: (a) Optical micrograph of the array of photonic nanowire, (b) Scanning mircograph of the photonic nanowire.

4.1.2 Photoluminescence spectra

In order to investigate the emission property of the emitter embedded into a photonic wire, the first step is to measure the photoluminescence (PL) spectra of individual photonic nanowire, at cryogenic temperature. This was done on the setup developed by Joël Bleuse; a simplified sketch of the experimental apparatus can be found in Figure 4.2. The sample is placed on the cold finger of a He-flow cryostat with an optical access. All the experiments described in this chapter, are carried out at cryogenic temperature (5K). The injection of electrons and holes in the quantum dots is provided by a pulsed Ti: Sapphire laser tuned at 820 nm, having 200-fs pulsed length with a repetition rate of 76 MHz. The laser beam is focused down to a 1.5 µm diameter spot on the sample with the help of high resolution microscopic objective (NA = 0.75), which also collects the luminescence signal. The collected luminescence signal is then spectrally filtered by a 310-mm focal length monochromator, before reaching a silicon avalanche photodiode (APDs) which was installed on the output of the monochromator. To acquire a spectrum, one scans the wavelength that is selected by the monochromator, while simultaneously recording the magnitude of the APD counts. As discussed later on in this chapter, the same setup will be used for time resolved measurement and intensity-correlation measurement.

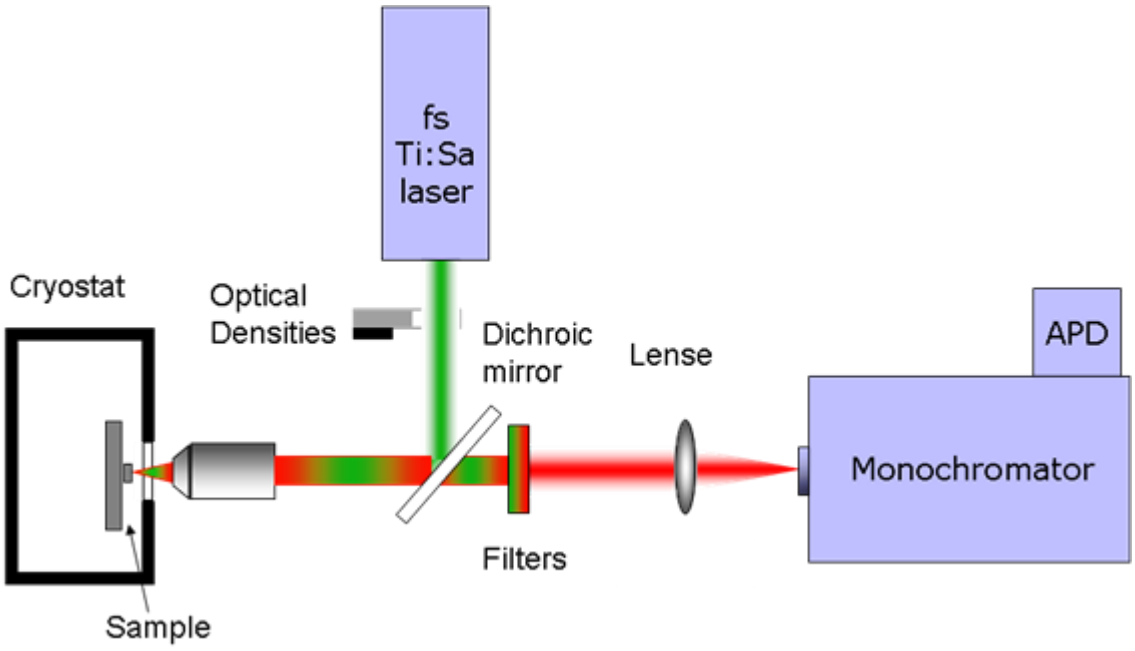

Figure 4.2: Sketch of the experimental optical set up.

Two photoluminescence spectra recorded on two photonic nanowires with diameters D= 160 nm and 260nm are shown in Figure 4.3. They feature sharp, isolated lines associated to several quantum dots. The spectral dispersion is directly linked to the size dispersion of self-assembled InAs QDs [1]. From the number of lines measured at low excitation power, one can estimate the number of optically active quantum dots located in the wire with a certain diameter. Due to the low areal density of QD layer which is ~ 300 μm^{-2} for our self-assembled QDs, a 200-nm-diameter wire typically contains 10 randomly located QDs

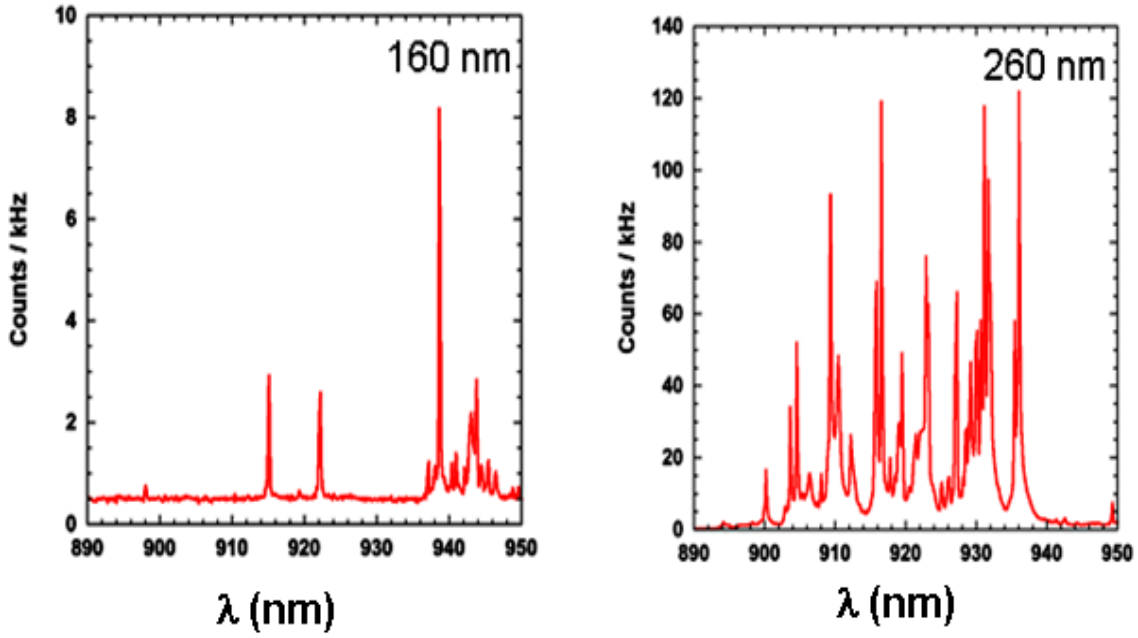

Figure 4.3: Photoluminescence spectra of the quantum dots emission embedded into photonic nanowires with a diameter of 160 nm and 260 nm, displaying discrete lines corresponding to the single quantum dot emission.

4.1.3 How to investigate SE control in a photonic nanowire?

In this section, we will discuss the criteria for the selection of suitable photonic nanowire to explore the SE dynamics of the quantum dots embedded into the photonic nanowire. As discussed in Chapter 2, SE control mechanism in a photonic nanowire relies on a good coupling to the fundamental HE_{11} guided mode combined with a pronounced inhibition of the SE into the continuum of radiative modes. In the following, we note Γ_M the emission rate into the HE_{11}

mode and γ the emission rate into the radiative modes. To provide results that are not dependent on the emitter oscillator strength, we normalize these rates by Γ_{3D} , the emission rate of the emitter embedded into bulk GaAs. The normalized rates will appear with an upper bar (e.g. $\overline{\Gamma}_M$ and $\overline{\gamma}$).

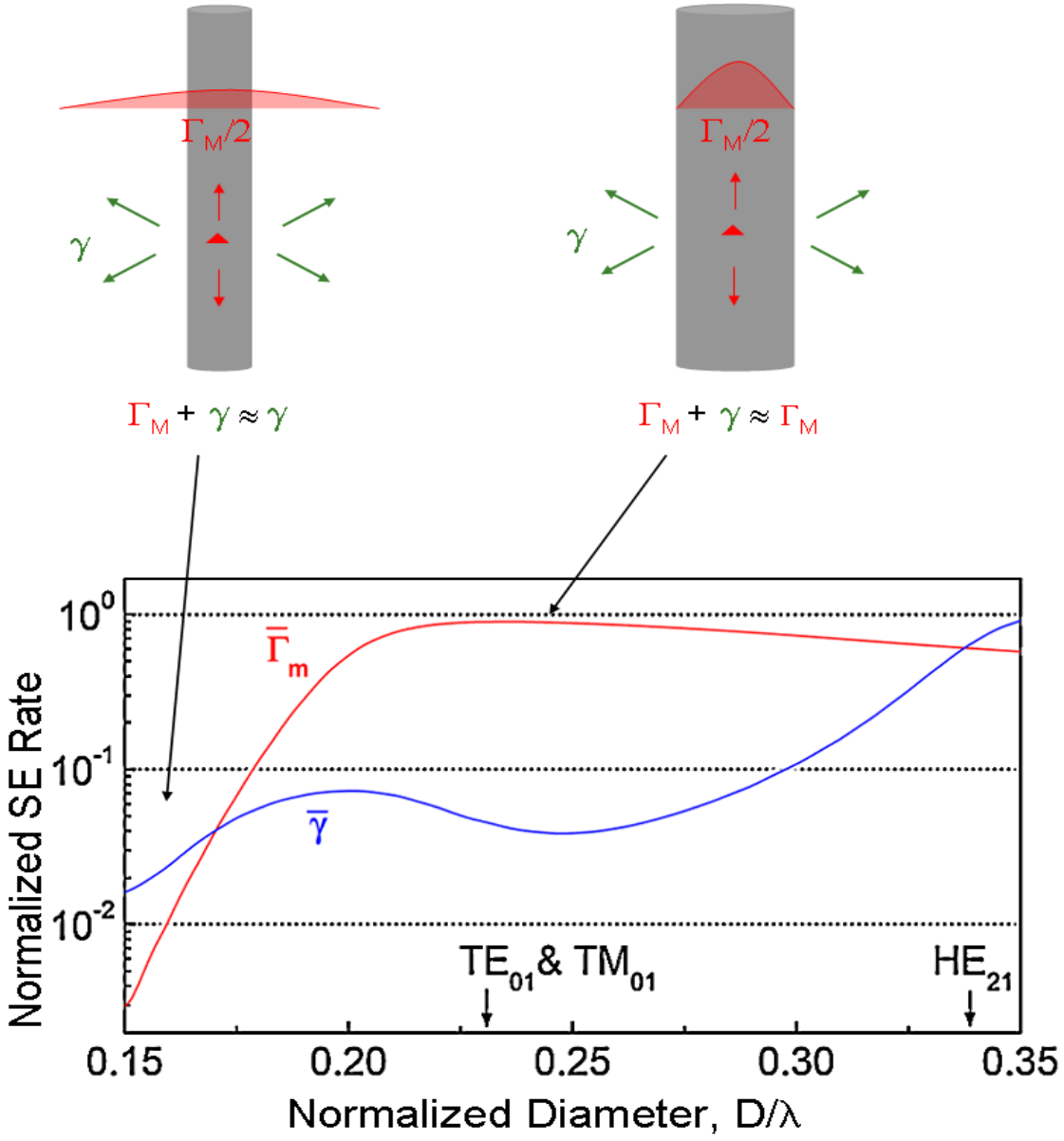

Figure 4.4: Principle to probe the coupling to the radiative modes and guided mode: Evolution of the normalized SE rates into the fundamental guided mode HE_{11}, $\overline{\Gamma}_M$, and into the other modes, $\overline{\gamma}$, as a function of normalized diameter of D/λ. The arrows indicate the cut-off of higher order guided modes.

In an optical microcavity, it is relatively convenient to probe the coupling to the mode of interest with a detuning of the dot induced by a change of temperature. When the emitter is on resonance, its decay rate is $\Gamma_M + \gamma$. In case of off-resonance, the Purcell effect disappears, and the decay rate reduces to γ. Unfortunately, such a straightforward procedure is not possible in a 1D photonic system that inherently features a relatively wavelength-insensitive behaviour. In fact, it is possible to circumvent this difficulty by studying wires with well chosen diameters. The idea behind our approach to explore SE in photonic wires is shown in the upper part of Figure 4.4. To support the discussion, lower part of the Figure 4.4 presents $\overline{\Gamma}_M$ and $\overline{\gamma}$ as a function of D/λ, the reduced diameter of the structure. The calculation is performed for a punctual emitter located on the axis of an infinite wire, with a dipole moment orthogonal to this axis. The HE_{11} mode is optimally confined for $D / \lambda = 0.24$, leading to $\overline{\Gamma}_M = 0.9$. When the diameter is decreased, this mode starts to deconfine and the coupling to this mode vanishes rapidly. Starting from the optimal value, decreasing D by 80 nm reduces $\overline{\Gamma}_M$ by nearly 3 orders of magnitude. For a diameter $D/\lambda < 0.17$, the coupling to the radiative modes dominates largely the spontaneous emission process. Thus, the coupling to the radiative modes can be investigated in these 'small' wires. On the other hand, the coupling to HE_{11} can be studied for bigger structures (D / λ around 0.24), for which the coupling to guided mode dominates the SE process.

4.1.4 Dielectric screening and (strong) inhibition of SE into the radiative modes

In this subsection, we present the quantitative measurements of the coupling of the emitter to the radiative modes and demonstrate the inhibition of SE into these modes. As discussed above, the key idea to probe the coupling to the radiative modes is to utilize the fast deconfinement of the HE_{11} mode as D/λ is reduced. We thus perform time-resolved PL experiments on small photonic wires ($D/\lambda < 0.17$). The setup is the same the one used for μ-PL measurements. Carriers are injected in the GaAs barrier with a short laser pulse (200-fs). They relax in the QDs in a few tens of picoseconds (ps), and light is emitted by the structure [2, 3]. The temporal resolution of the setup, associated to the time jitter of the APD, is 250 ps. The measurements are conducted at low excitation power, in order to study single excitonic transitions that are spectrally filtered by the monochromator.

Figure 4.5 shows the TR-PL decay of two dots (named as QD3 and QD4) embedded in a photonic nanowire with D/λ ~ 0.13. The emission wavelength of QD3 and 4 are 937.5nm and 926.57nm respectively. To serve as a reference, the TR-PL decay curve of an ensemble of QDs embedded into the as grown sample is also shown (black curve, ref.). The decay curves of the QD3 and QD4 in this figure show the strong reduction of the SE rates which indicates a marked inhibition of the SE.

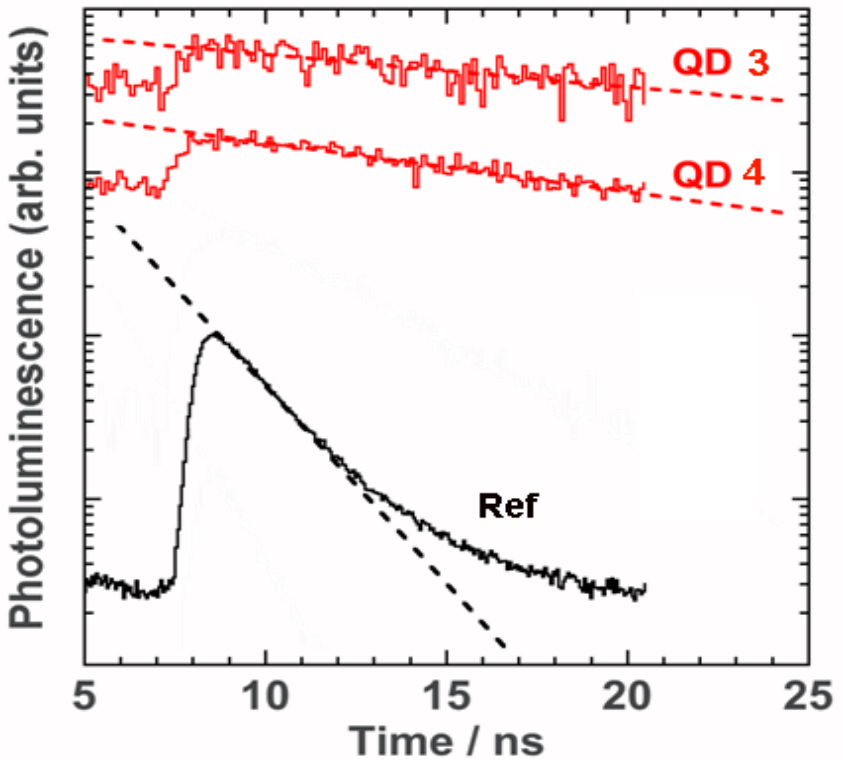

Figure 4.5: Inhibition of the SE: Time resolved PL decay curve from two QDs corresponding to the X-transition of the dot (named as QD3 and QD4) embedded in the photonic wire with D/ λ ~ 0.13. The TRPL decay curve corresponding to the as-grown reference sample is shown by black curve.

For a quantitative analysis, the data are fitted to a mono-exponential decay α exp (- Γt) and convolved with the measured instrument response of the setup (including the dark count level of the detector). For QD3 (resp. QD4), the decay rate is Γ = 0.045 ns^{-1} (resp. 0.068 ns^{-1}). The decay rate of the ensemble of QDs present in the as grown sample is Γ = 0.59 ns^{-1}. At this stage, it is important

to note that the presence of the GaAs-air interface modifies significantly the emission rate of the QD, compared to the situation of bulk GaAs. This interference effect has been studied by J. Johansen et al. and used to evaluate the radiative efficiency of the QDs, are shown in Figure 4.6 [4]. We use their results to evaluate the SE rate in bulk GaAs, knowing that the dots are located 80 nm below the surface in our case. Finally, one obtains after correction Γ_{3D} = 0.71 ns^{-1}, which constitutes our reference in the following.

The decay rate of QD3 (resp. QD4) is inhibited by a factor $\overline{\Gamma}^{-1} = 16$ (resp. 10) compared to a quantum dot in bulk GaAs. This strong inhibition of spontaneous emission shows the efficiency of the dielectric screening effect in photonic nanowire. In fact, similar performances have only been achieved in 2D-photonic crystals, which are much more complex structures where SE inhibition relies on a different mechanism (namely the opening of a forbidden photonic band gap) [5].

Finally, the measured SE decay rate contains also a possible non-radiative decay part. For the smallest wires, the total decay rate is larger than the theoretical recombination SE rate in this regime. In principle, one could measure even much higher inhibition factor in this structure provided non-radiative losses are reduced. We will see later on in the chapter that this effect can be utilized to measure the quantum efficiency of the emitter.

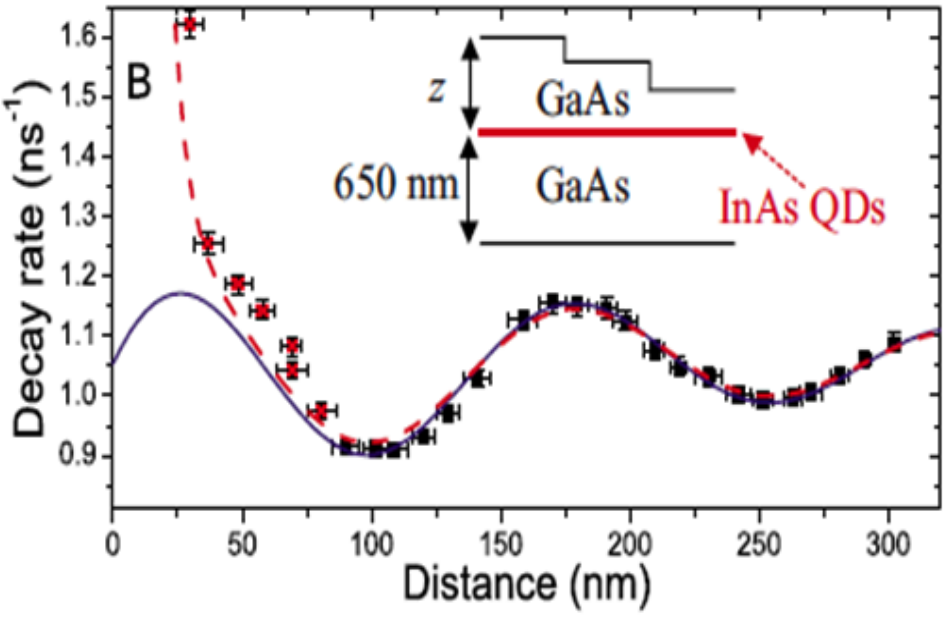

Figure 4.6: SE decay rate of QDs as a function of distance z to the GaAs-air interface [4].

4.1.5 Coupling to guided mode and (moderate) enhancement of SE

In order to investigate the coupling to HE_{11}, we now focus on nanowires with a larger diameter ($D / \lambda \sim 0.25$), for which HE_{11} is optimally confined. Figure 4.7 shows the TRPL decay of the two dots (named as QD1 and QD2) embedded in such a nanowire. Their emission wavelengths are 943.8 nm and 934.9 nm respectively. QD1 exhibits a faster decay than the reference ensemble, with a rate of Γ = 1.1 ns^{-1}. The corresponding SE enhancement factor, $\overline{\Gamma}_M$ = 1.54, is close to the theoretical maximum value of 1.65 [6], expected for an on-axis emitter. According to the simple Fabry-Perot model developed in chapter 2, the reflection from the modal mirror located at the bottom end of wire only modifies $\overline{\Gamma}_M$ by a factor of $(1+|r_m|)$, where $|r_m|$ is the modal reflectivity of the mirror and leaves $\overline{\gamma}$ unchanged. Therefore, this moderately enhanced rate also provides an evidence of the high modal reflectivity of the integrated bottom mirror.

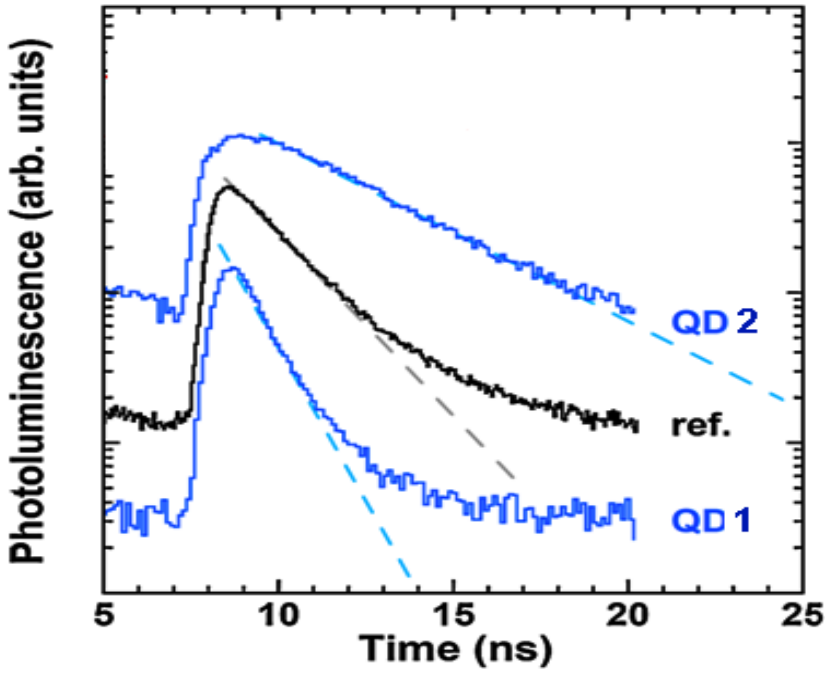

Figure 4.7: Enhancement of the SE in photonic wires: Time resolved PL decay curve from two QDs corresponding to the X-transition of the dot (named as QD1 and QD2) embedded in the photonic wire with $D/\lambda \sim 0.25$. The TRPL decay curve corresponding to the as-grown reference sample is shown by black curve. The dashed lines are guide for the eye.

The other dot displays a decay slower than the reference (and QD1), with a rate Γ =0.27 ns^{-1}. This is attributed to a spatial mismatch between the antinodes of guided mode electric field and quantum dots location. As the emitter – photonic wire axis distance increases, $\overline{\Gamma}_M$ decreases, at a faster rate than the $\bar{\gamma}$ increases (see section 2.1.1.4 and 2.1.2.4). As a result, some quantum dots, such as QD2, exhibit a normalized SE rate as low as $\overline{\Gamma}_M$ = 0.39.

4.1.6 Global picture of spontaneous emission in photonic nanowires

In order to provide a comprehensive picture of SE control in photonic wire, a complete set of measured normalized SE decay rates $\overline{\Gamma}$ of 60 QDs embedded in wires with various diameters is plotted in Figure 4.8. The measured SE decay rates are plotted as a function of normalized diameter D / λ, where λ is the free space emission wavelength of the emitter. All the data are modelled according to the mono exponential decay dynamics of exciton (X) and are fitted by single exponential decay functions. In order to support the analysis, we have calculated the maximum and minimum $\overline{\Gamma}$ by varying the lateral position of the emitter in the wire, shown with the solid curves. This calculation was performed by the group of Phillipe Lalanne. In this calculation, the emitter position is varied from *x* = 0 to *x* =7R/8, where R is the radius of the nanowire and the SE rate is obtained by averaging the SE rates associated to radial and orthoradial polarizations.

Two regimes can be easily distinguished in this plot. The first one is associated with reduced diameters above D / λ = 0.16, QD1 and QD2 belong to this regime. In this regime, the coupling to HE_{11} is significant, and some dots, located near the wire axis, exhibit a moderate enhancement of the SE rate. The strong variations of $\overline{\Gamma}$ from 0.3 to 1.6, are attributed to the spatial variations of $\overline{\Gamma}_M$ and $\bar{\gamma}$. In the other regime, D / λ is below 0.16, QD3 and QD4 belong to this limit. In this regime, the coupling to HE_{11} is not significant, and the SE is strongly inhibited, as a result of the dielectric screening effect. The SE rates are quite uniform in this regime, because $\bar{\gamma}$ presents relatively limited spatial variations in the small diameter limit (see Figure 2.9 of chapter 2). Globally, we obtain a good agreement between theory and experiment for various quantum dots embedded in nanowires with various diameters. This demonstrates a rather good understanding of SE dynamics in photonic nanowires. Moreover, the above demonstration of a very strong inhibition of SE into the radiative modes, as well

as moderate enhancement of SE into the guided mode, confirm the potential of photonic nanowires to achieve $\beta > 0.9$ for on-axis emitters.

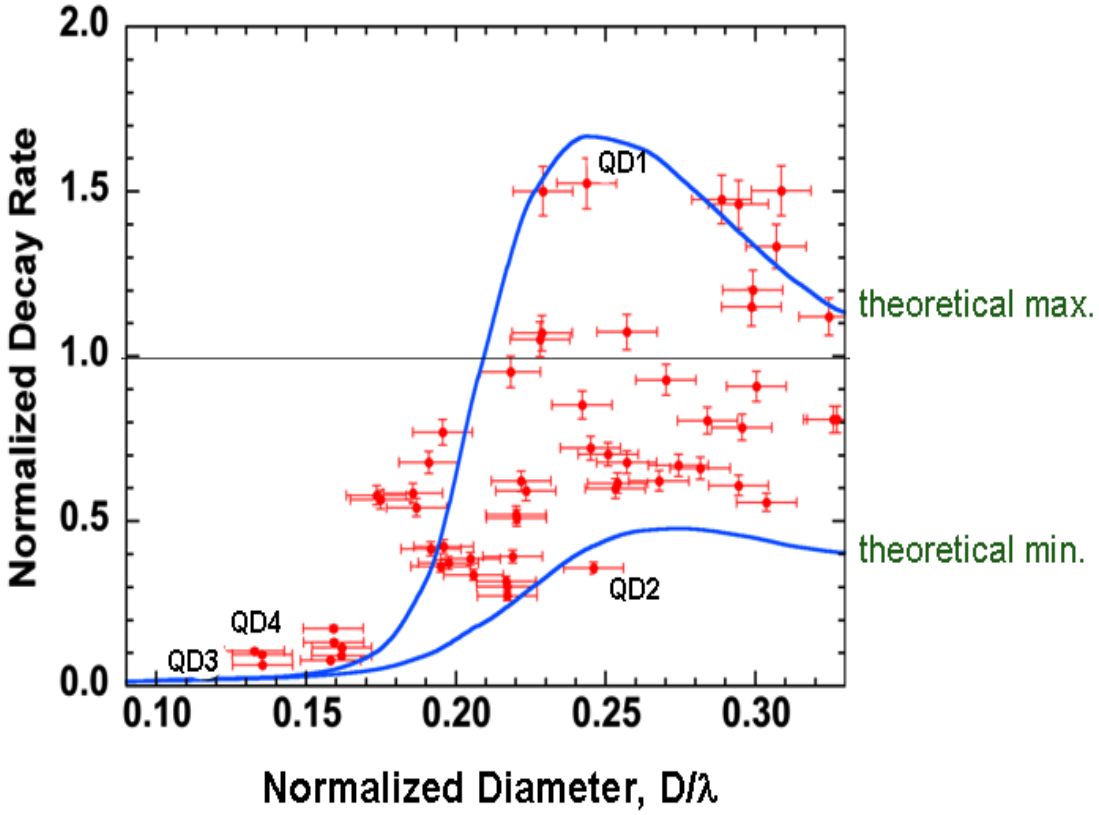

Figure 4.8: Measured SE decay rates of 60 single QDs embedded in photonic nanowires with various diameter as a function of normalized diameter D/λ. All the data points (red dots) are modelled using a single exponential decay model. The data is bounded by the calculated maximum and minimum total SE rates (solid blue lines), obtained by varying the lateral position of the emitter in the wire.

4.1.7 Measuring the quantum efficiency of the emitter with a 'small' photonic wire

Inspecting Figure 4.8, one notices that QD3 and QD4 exhibit a faster decay rate that the calculated radiative one. This is attributed to a weak non-radiative decay channel, revealed by the marked SE inhibition that occurs for small wires. In fact, photonic wires provide a tool to measure the quantum efficiency η of the emitter. The decay rate that is measured in time resolved

experiments is the total decay rate Γ_{tot} which consists of a radiative and non-radiative decay rates part and is given by:

$$\Gamma_{tot} = \Gamma_{rad} + \Gamma_{nrad}, \quad (4.1)$$

Γ_{rad} is known from calculations, thus Γ_{nrad} can be deduced from the measurement. The quantum efficiency of the emitter is:

$$\eta = \frac{\Gamma_{rad}}{\Gamma_{rad} + \Gamma_{nrad}}, \quad (4.2)$$

Experimentally we measured, the total decay rate $\Gamma_{tot} = 45$ μs^{-1} for QD3 (68 μs^{-1} for QD4), which is larger than the theoretical radiative value of 23 μs^{-1}. This point indicates that we have a nonradiative recombination channel, with a rate of 22 μs^{-1} (45 μs^{-1}). In order to determine the quantum efficiency of the emitter QD3(QD4), we consider that the nonradiative decay channel is same in the as grown reference sample. Using the 0.71 ns^{-1} reference decay rate in bulk GaAs, one obtains $\eta = 0.97$ (0.94). This analysis confirms the high radiative yield of QDs and shows that η is preserved in nanowires with diameter around 200 nm for which the radiative rate is similar to the one of bulk GaAs. For wires with $D/\lambda < 0.13$, no significant signal was found. This is likely due to the fast increase of surface nonradiative recombination as the distance to the surface is reduced [4], combined with the fast decrease of the radiative rate as the diameter of the wire is reduced. For these very small wires, the relaxation process is expected to be dominated by non-radiative processes.

4.1.8 Discussion of SE control

In conclusion of this section, we have experimentally demonstrated for the first time that spontaneous emission of the emitter embedded into the photonic nanowire can be controlled very efficiently by photonic nanowire. For a diameter corresponding to the optimal confinement of the guided mode, quantum dots couple to a guided mode of the photonic wire and an increase of the SE rate by a factor of 1.5 was found. In the lower diameter, photonic nanowires provide a very strong inhibition with a factor of 16 of the SE into the continuum of radiative modes. The observed enhancement and inhibition of the SE are in excellent agreement with the calculated value

In the optimum diameter range, the moderate enhancement of SE due to the coupling to the guided mode combined with strong inhibition into radiative modes leads to a very efficient funnelling of the SE into the guided modes and

provides $\beta > 0.9$. Due to the broadband high value of β-factor, these structures are thus appealing candidates for the realization of efficient single photon sources. The next major challenge for using photonic wire waveguide based single photon source is the outcoupling of the emitted photon. This issue already theoretically addressed in the chapter 2 and in the context of single photon source, the experimental performance of the device will be presented in the next section.

4.2 On-demand single-photon emission from a QD inserted in a photonic nanowire

In this section, we operate the device as an on-demand single-photon source, which is pumped optically by a pulsed laser. Because a wire contains several QD with various sizes, and each QD possesses several transitions, a spectral filtering is required to obtain a single photon after an excitation pulse [7, 8]. In practice, the sample is located in the setup that is used for μ-PL measurement (see Figure 4.2). For most applications of SPS, like quantum cryptography or metrology, we have two essential figures of merit:

1. The purity of single-photon, that is determined from the measurement of the intensity correlation function $g^2(t)$.
2. The efficiency of the source, that we define as the probability to emit a photon into the collecting cone of the first lens of the optical setup (such a definition is intrinsic to the source, and does not depend on the transmission of the setup).

These sections presents the measurements of these two figures of merit and compare them to the state-of-the art of single-photon sources, which have been so far represented by cavity-based devices.

4.2.1 Micro-photoluminescence spectrum

The first step in investigating the single-photon emission is the measurement of photoluminescence (PL) from the nanowire. Figure 4.9 (a) shows the PL-spectra of the photonic wire of diameter 210 nm in the range of 911-919 nm wavelength range. The measurement were performed at 5K, under non-resonant (at 820 nm), and pulsed optical pumping (200-fs pulse duration with a repetition rate of f = 76MHz), for 4 increasing pumping power. First of all, the spectra are very clean, with a very low background. Because the wires are

located on a gold mirror, the semiconductor volume that could contain parasitic emitters is very small. At high pumping power, the spectrum exhibit two bright lines at 915.2 nm and 914.1nm. These peaks are attributed to a neutral exciton (X) and a biexciton (XX) of a single QD.

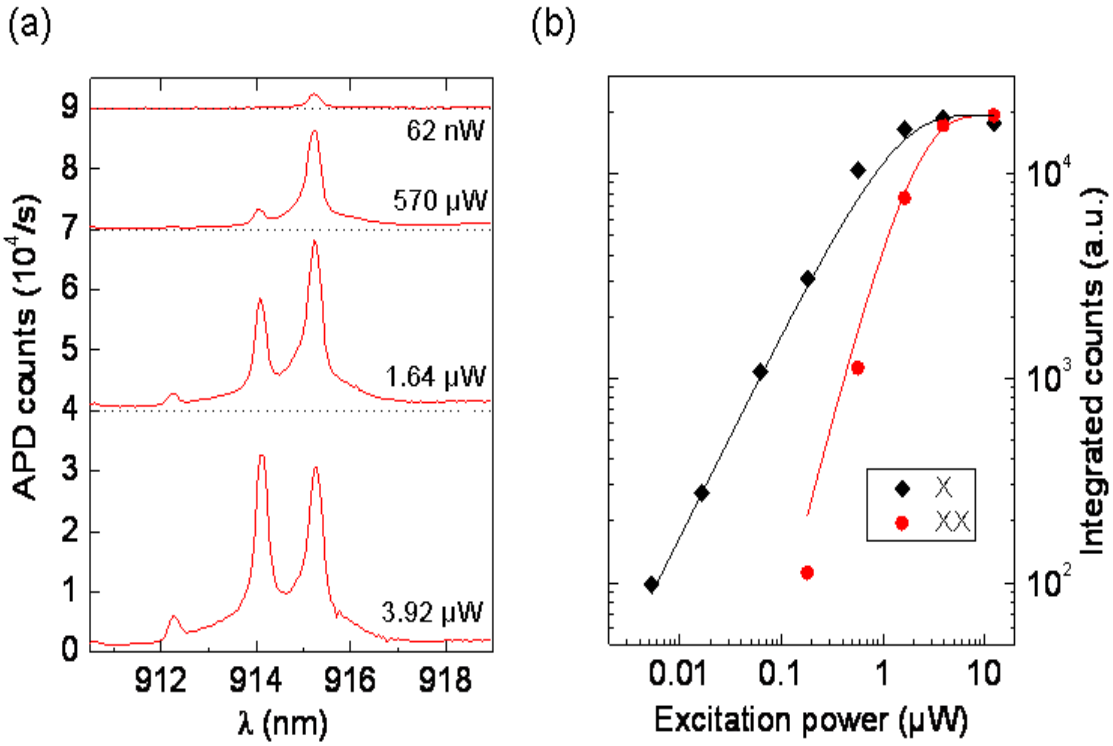

Figure 4.9 Micro photoluminescence spectra of the photonic nanowire, (a) Evolution of the luminescence with the pumping power, (b) Integrated intensity as function of pumping power corresponding to the excition (X) and bi-exciton (XX). The solid lines represent the model to confirm the origin of these lines.

This identification is supported by the analysis of the spectrally integrated intensity of the two lines, respectively denoted I_X and I_{XX}. I_X and I_{XX} versus pumping power are plotted in Figure 4.9 (b). In this figure, the solid curves are calculated from the standard model that the probability of creating *n* excitons in a QD follows a Poissonian statistics. In order to calculate this, we consider the case of excitons and further assume that the capture of an electron-hole pair is a random process as well as neglect the coulomb interaction of the charges [8]. For such condition, the numbers of pairs created in the QDs follow Poissonian statics and are given by

$$P(n) = \frac{\langle n \rangle^n}{n!} \exp\left(-\langle n \rangle\right) = \frac{1}{n!}\left(\frac{P}{P_O}\right)^n \exp\left(-\frac{P}{P_0}\right), \quad (4.3)$$

where P (n) is the probability to having n exciton in the QD and $\langle n \rangle$ is the average number of electron-hole pairs created by each laser pulse which has linear dependence upon the excitation power. Therefore the probability to inject at least 1 exciton in the QD is given by

$$P(n \geq 1) = 1 - P(0), \quad (4.4)$$

And the probability to inject at least 2 excitons is given by

$$P(n \geq 1) = 1 - P(0) - P(1), \quad (4.5)$$

Denoting I_O saturation intensity and P_o is the saturation excitation power, one can obtain

$$I_X(P) = I_O\left(1 - \exp\left(-\frac{P}{P_O}\right)\right), \quad (4.6)$$

$$I_{XX}(P) = I_O\left(1 - \exp\left(-\frac{P}{P_O}\right) - \frac{P}{P_O}\exp\left(-\frac{P}{P_O}\right)\right), \quad (4.7)$$

The fit of the data leads to a saturation power P_o = 1.05 μW. In a low power excitation regime $(P/P_O \to 0)$, $I_X(P) \propto \frac{P}{P_O}$ and $I_{XX}(P) \propto \left(\frac{P}{P_O}\right)^2$, which can be seen in Figure 4.9 (b). The intensities completely saturate for an excitation power exceeding 4.0 μW; in these conditions, I_X and I_{XX} are approximately equal. This is expected for a single QD with a nearly perfect radiative yield embedded in a source having broadband collection efficiency. In the following, we focus on the excitonic line and examine the purity of single photon emission as well as the efficiency of the source, when the emitter is saturated.

4.2.2 Photon Statistics of single photon source

4.2.2.1 A few words about photon statistics

The photon statistics of a light source characterizes the correlation between the emissions of photons. To characterize these correlations, we introduce the normalized second-order intensity correlation function $g^{(2)}(\tau)$ which represents the conditional probability of detecting a photon at the time (t+ τ) while the first photon is detected at time t. Classically, the second order auto-correlation for an optical field can be defined as:

$$g^{(2)}(\tau) = \frac{\langle I(t)I(t+\tau)\rangle}{\langle I(t)\rangle\langle I(t+\tau)\rangle}, \tag{4.8}$$

where I (t) is the intensity of the light at time t, and the brackets denote an ensemble averaging. For a stationary situation, $g^{(2)}$ does not depend on the time origin t. First of all, one must be careful about the time scale of the intensity fluctuations. In general, one can introduce a characteristic time 'τ_c' of the source. If $\tau >> \tau_c$, then the intensity fluctuations will be completely uncorrelated. On other hand for the case $\tau << \tau_c$, there will be correlations between the fluctuations may exist.

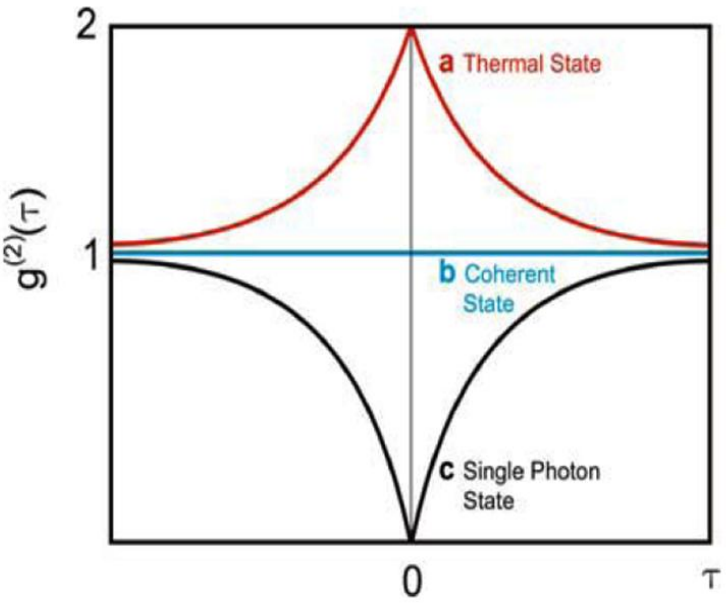

Figure 4.10: Continuous-wave (cw) second order photon correlation functions $g^{(2)}(\tau)$ for (a) thermal, (b) coherent, and (c) a single photon source, respectively.

In general, one can define 3 categories of light sources; the corresponding typical $g^{(2)}(\tau)$ is shown in Figure 4.10.

- ***Bunched light*:** with positive correlations at short τ. For example, the thermal light which is produced by a blackbody belongs to this family. In that case, the positive correlations are caused by the Bosonic nature of photons [10,11].
- ***Poissonian light*:** In that case, the photons are emitted independently from each other. A laser operated well above the lasing threshold produces such a light field (which is also called a coherent field).

- ***Antibunched light*:** with negative correlation between the arrival of photon at short delays. The single-photon source belongs to this family. Here, the negative correlations appear because light is produced by a single transition of a single quantum emitter. Observation of this antibunching was first made by Kimble *et al.* in 1977, using the light emitted by sodium atoms [9].

For a mono mode optical field and τ=0, the intensity correlation function can be written in term of average number of photon in the mode $\langle n \rangle$ and variance in the number of photons in the mode $(\Delta n)^2 = \langle n^2 \rangle - \langle n \rangle^2$ and given as

$$g^{(2)}(0) = 1 + \frac{(\Delta n)^2 - \langle n \rangle}{\langle n \rangle^2}, \tag{4.9}$$

In order to illustrate the properties of the intensity correlation function $g^{(2)}(\tau)$, we consider the 3 different kinds of light sources discussed above:

- In case of a coherent source (stationary laser beam) with Poisson photon statistics $(\Delta n)^2 = \langle n \rangle$ which gives $g^{(2)}(0) = 1$ for all τ.
- In case of classical light source such as thermal light $(\Delta n)^2 = \langle n \rangle^2 + \langle n \rangle$, hence $g^{(2)}(0) = 2$.
- In case of a single-mode number state $\langle n^2 \rangle = \langle n \rangle^2$, hence by definition the variance of the number of photons in the mode is zero so that

$$g^{(2)}(0) = 1 - \frac{1}{\langle n \rangle} \tag{4.10}$$

For a pure single-photon state ($\langle n \rangle = 1$), the value of $g^{(2)}(0)$ takes the minimum value of 0. However a two photon state gives $g^{(2)}(0) = 1/2$ and: for this reason $g^{(2)}(0) < 1/2$ is often used as criteria to define a single photon emission.

Experimentally, our single-photon source is operated in pulsed mode, with a repetition period T. Figure 4.11 shows the typical behaviour of $g^{(2)}(\tau)$ for thermal, coherent and single-photon states. For $\tau \neq 0$, the different peaks do not exhibit any correlations and present equal height and area. The correlations appear for the zero-delay peak (central peak). In case of a coherent source all peak areas are equal, i.e. representing a Poissonian statistics. In case of a thermal source, the area of the central peak is twice the area of the other peaks.

In case of Sub-Poisson statistics the area of central peak at τ=0 is less than the areas of the other peaks. For a perfect single photon source the central peak is absent indicating the generation of only one photon per pulse.

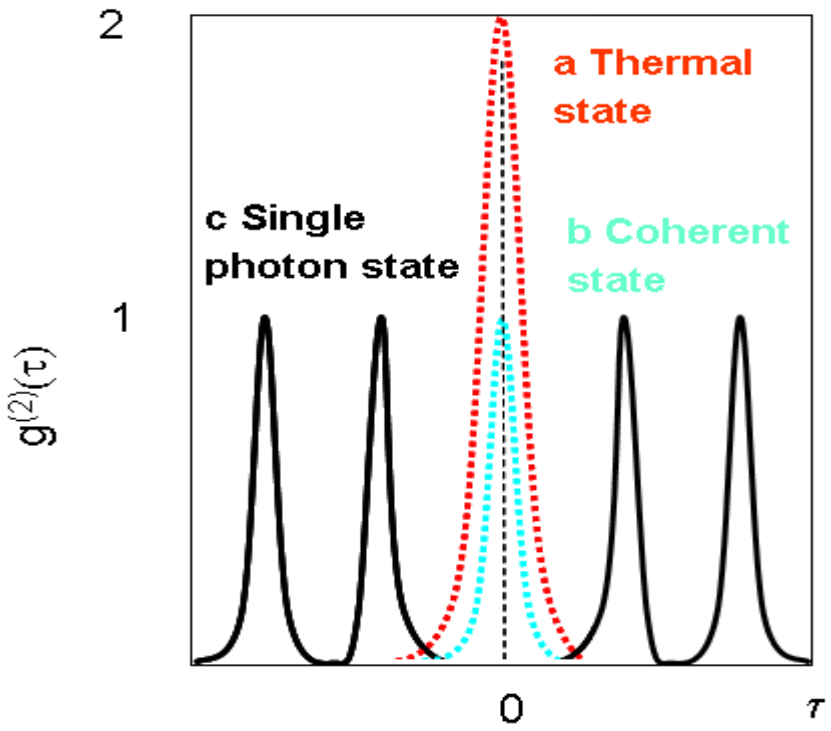

Figure 4.11: Pulsed-wave excitation second order photon correlation functions $g^{(2)}(\tau)$ for (a) thermal, (b) coherent, and (c) a single photon source, respectively.

4.2.2.2 Experimental setup (HBT)

Single-photon detectors typically employed for the detection in optical setup cannot distinguish one or multiple photons and hence the photon statistics cannot be measured directly. To circumvent this difficulty, Hanbury-Brown and Twiss introduced a simple interferometer shown in Figure 4.12, that has become a classical characterization tool for the community of quantum optics [10 -11]. In a HBT setup, the incoming light beam is separated in two by a 50:50 beam splitter. Then the resulting two light beams are focused onto the two single-photon detectors D1 and D2 (silicon APDs in our case). The resulting outputs of these detectors are fed into an electronic counter/timer (time to amplitude converter (TAC)). The pulses from the D1 and D2 provide 'start' and 'stop' pulse respectively to this TAC. The results of the experiments are typically presented as a histogram which displays the number of events that are registered at each

value of the time τ between the start and stop pulses which is equivalent to the second order intensity correlation function $g^{(2)}(\tau)$

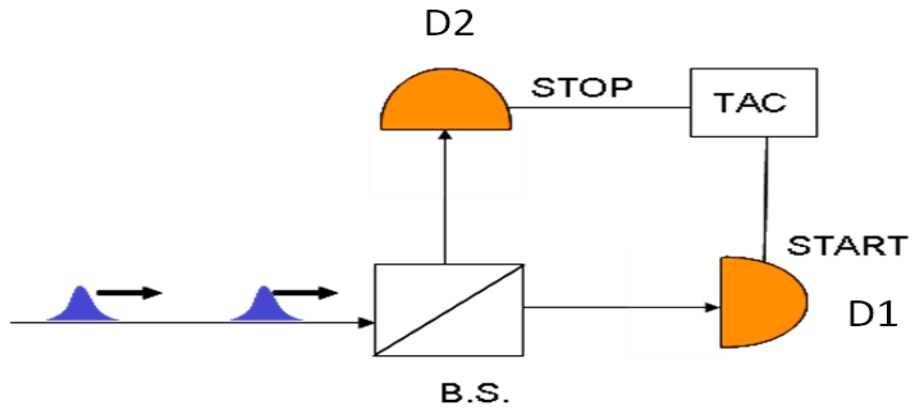

Figure 4.12: Hanbury Brown-Twiss (HBT) experiment with a photon stream incident on the beam splitter of the measurement of second order coherence function $g^{(2)}(\tau)$. The output of the detectors D1 and D2 are fed into the start and stop inputs of an electronic counter/timer.

4.2.3 Purity of Single photon emission

In this section, we present the measurement of intensity correlations for the spectrally filtered X line. The spectral filtering bandwidth was about 0.5 nm and the time bin was set to 120 ps. Figure 4.13 shows the auto correlation function for a pump power of 4 μW which is well above the saturation of the X emission. The side peaks are separated by the laser repetition rate and all have equal areas, while the central peak is nearly absent, which reflect strong suppression of the multi-photon probability.

In order to determine the area of central peak and the decay time of the exciton emission, it is necessary to fit the data. To do this, we used the following correlation function

$$f(t) = A\left[\left(g^{(2)}(0)-1\right)\exp\left(\frac{-|t-t_o|}{\tau}\right)+\frac{\cosh\left(\frac{t-t_o-pT}{\tau}\right)}{\cosh\left(\frac{T}{2\tau}\right)}\right], \qquad (4.11)$$

where t_o is the origin of time ,T is the repetition period of laser, τ is the decay time of the emitter, and p is smallest integer which is greater than $[(t - t_o)/T]$ but less than 1/2. The data is fitted for τ = 2.66 ns.

In the measurements of the figure 4.13, we extract $g^{(2)}(0) < 0.008$ for the exciton. Since the value is well below the 0.5, therefore the X line exhibits the signature of very pure single photon emission. The measurement was performed well above the saturation that corresponds to the maximum source efficiency, which will be measured in the next section. Hence the photonic nanowire based source provides a highly pure single photon emission. We will compare our device performance in term of single photon purity with state of arts cavity based source later in this chapter.

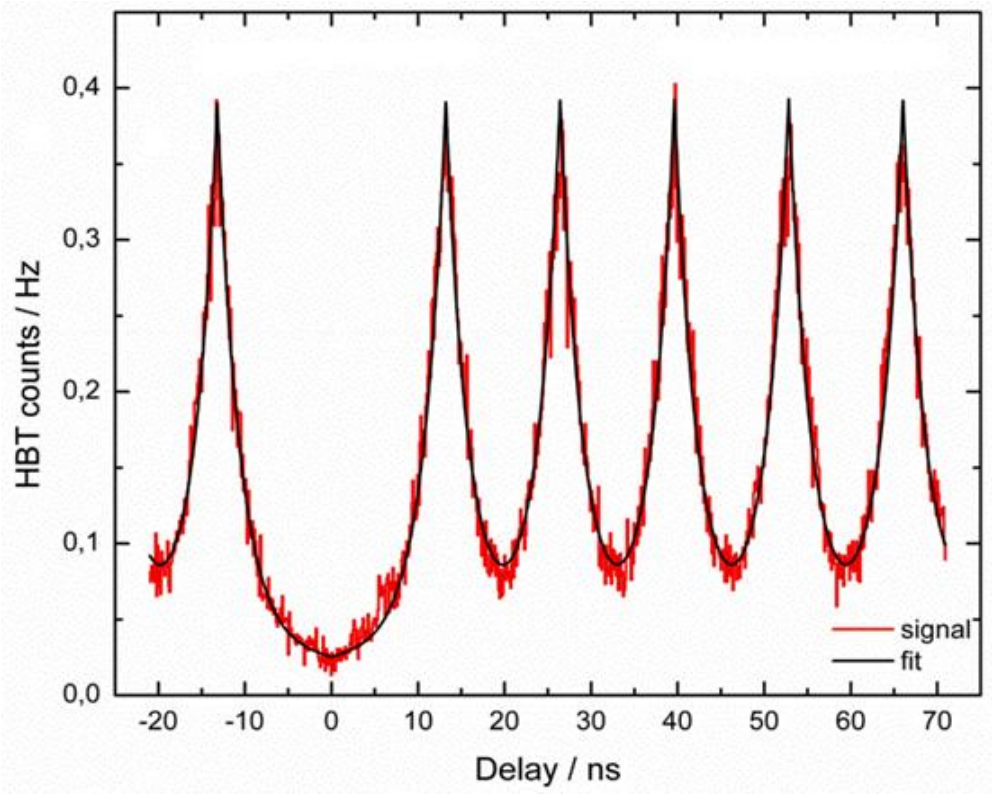

Figure 4.13: Measured autocorrelation trace of the X-transition (red curve) of single quantum dot in a photonic wire well above the saturation (P ~ 4μW) and fit is shown by black lines.

4.2.4 Efficiency of the single-photon source

After the confirmation of the purity of the single-photon emission, the next step is to measure the efficiency ε of the source. It is defined as the probability to collect a photon into the first lens of the optical set-up, after an excitation pulse, and the measurement procedure is described in the following subsections.

4.2.4.1 Determination of the efficiency using the Ti:Sa laser

The maximum efficiency ε can be achieved when the emitter is well pumped, that is to say when the X line of QD is saturated. In that case, the QD emits exactly 1 photon per pulse excitation. Thus, the single photon flux into the first lens is

$$\varphi_x = f \cdot \varepsilon, \tag{4.12}$$

where f is the repetition rate of the laser (we have supposed here that the radiative yield of the QD is 100%). The source efficiency is then determined from the comparison to a source emitting a known photon flux, created using the reflection of the Ti: Sa laser. The laser is tuned on the energy $\hbar\omega$ of the X line and the beam is focused on the gold/silica mirror a few micrometers away from the wire. The reflected power P_{laser} is measured by power meter and the associated photon flux into the first lens is given by

$$\varphi_{laser} = \frac{P_{laser}}{\hbar\omega}, \tag{4.13}$$

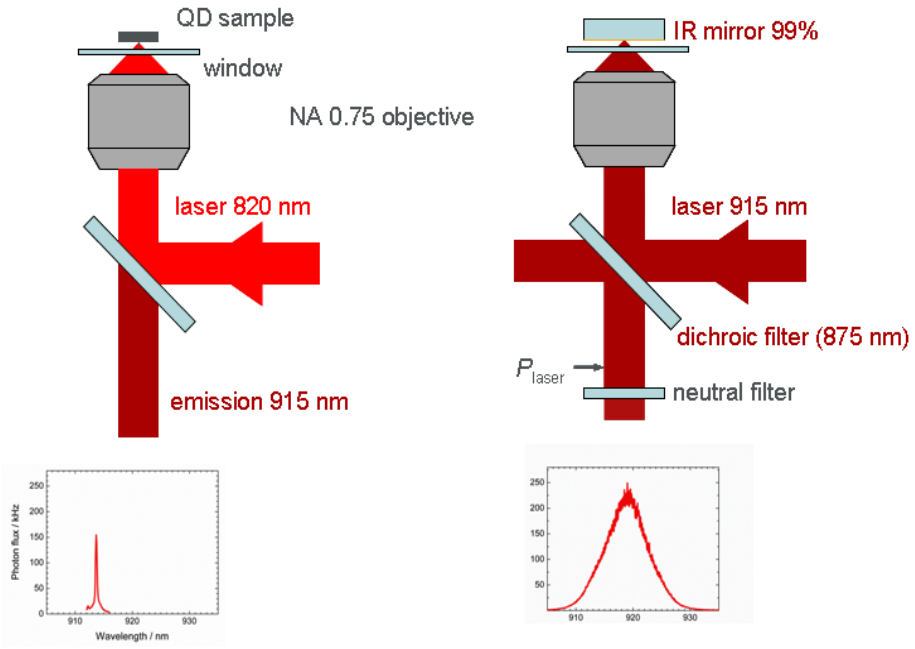

Figure 4.14: Schematic drawing of efficiency calibration method of the source.

Afterward we acquire the spectra of the two sources (laser and the desired source) with the same set-up conditions (see figure 4.14). In order to keep the same order of magnitude for the peak count rates in both cases, we use a

density filter with transmission t = 0.01. The spectrally integrated APD counts rates for both cases are given by

$$I_x = \eta\varphi_x , \tag{4.14}$$

$$I_{laser} = \eta t\varphi_{laser} , \tag{4.15}$$

where η is detection efficiency of the full set-up. Therefore the efficiency of the ε can directly deduced from the ratio of I_x and I_{laser} and is given as

$$\varepsilon = \frac{I_x}{I_{laser}} = \frac{\varphi_x}{t\varphi_{laser}} , \tag{4.16}$$

4.2.4.2 Validation of calibration method

In order to validate the above calibration method, we first measure the efficiency of a source with known photon flux. To do this, we used a reference single photon sample which consists single InAs QD buried 120 nm below the surface of an unprocessed GaAs sample. For such a simple structure, efficiency ε is calculated (by Niels Gregersen) using eigenmode expansion technique, for varying numerical apertures (solid line in Figure 4.15).

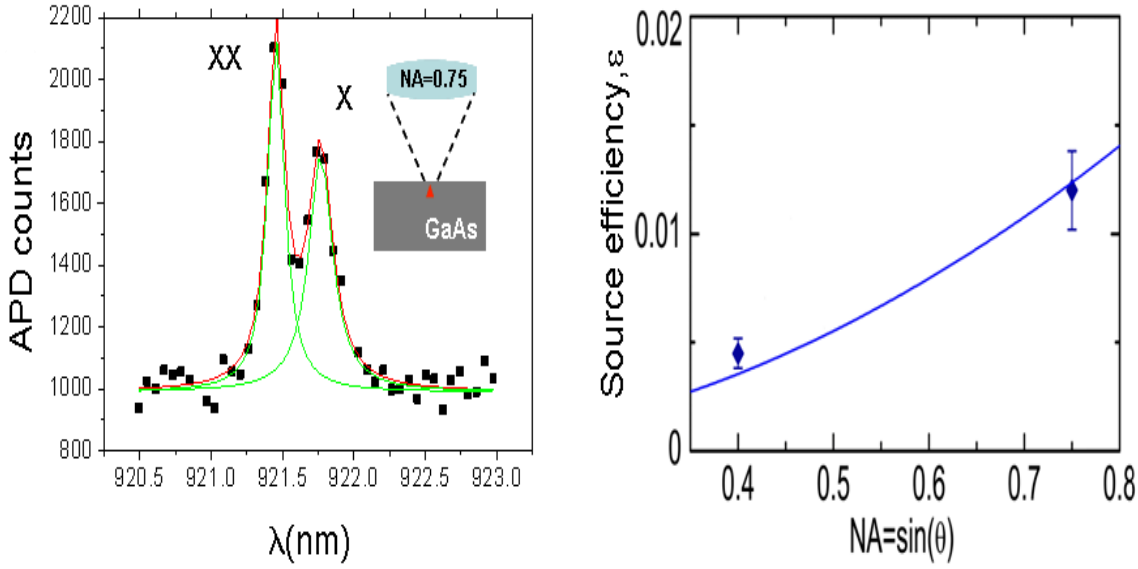

Figure 4.15: Efficiency of the reference source: the micro-PL spectra of a single InAs QD embedded in bulk GaAs is shown in left side. The experimental (blue symbols) and theoretical efficiency (solid line, Calculation done by N. Gregersen) is shown on right side of figure.

We measured the efficiencies at the X saturation with two microscope objective having NA = 0.4 and 0.75, and we have obtain $\varepsilon = (4.5 \pm 0.8) \times 10^{-3}$ and $(1.2 \pm 0.19) \times 10^{-2}$. These values are in close agreement with theoretical predictions and represents the validation of our efficiency calibration approach (see figure 4.15).

4.2.4.3 Efficiency of the Photonic wire

After the validation of the efficiency measurement approach, the same measurements have been performed on the X line of the QD already studied in Figures 4.9 and 4.13. We obtained $\varepsilon = 0.35 \pm 0.05$ (see Figure 4.15) for a numerical aperture NA=0.4, this value is similar to state-of-the-art microcavity based single photon sources, since $\varepsilon = 0.38$ has been reported by S.Strauf et *al*. [12] and 0.44 by E. Moreau et *al*. [13]. However the far field radiation pattern of our photonic nanowire is not fully intercepted by a 0.4 NA collecting cone unlike microcavity based devices.

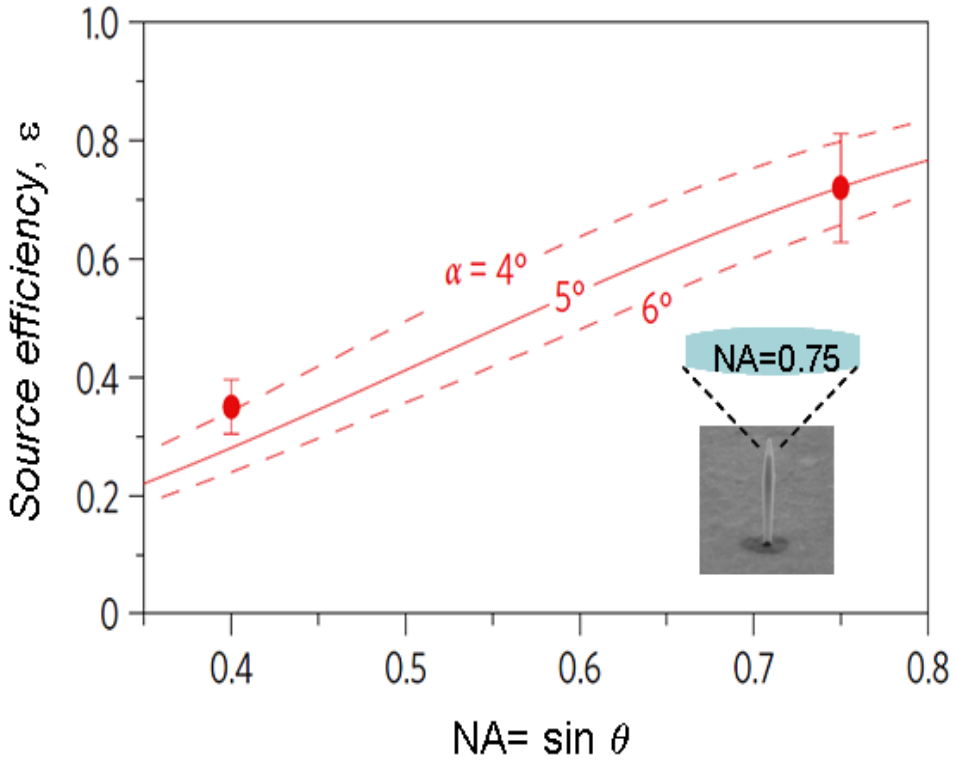

Figure 4.15: Efficiency of the photonic nanowire based single photon source. The measurements (red symbols) were conducted with two microscope objectives (NA=0.4 and 0.75). The three lines are theoretical predictions for three tapering angles α (Calculation was performed by N. Gregersen).

We further used microscopic objective with 0.75 NA which leads to $\varepsilon = 0.72 \pm 0.09$, which corresponds to a 55 MHz single photon flux into the first lens and represents an improvement by a factor of 1.6 compared to microcavity based SPS. In addition, we measured several devices with $\varepsilon > 0.6$, and reproducibly obtained $\varepsilon > 0.5$ on a number of photonic nanowires with diameter ranging from 200 to 260 nm. These results prove the broadband operation of this photonic nanowire geometry for single photon emission. Our data is well fitted with the Fabry-Perot model described in the chapter 2 with a tapering angle α = 5° which leads to the transmission $T_{5°}$ (0.75) =0.77 (solid lines in figure 4.15). The source efficiency is mainly limited by the upper taper geometry. We will discuss possible improvements in the following section.

4.2.5 Discussion

In this section, we come back on the performances of the source, compare them to the state of the art (cavity-based devices), and provide some indications about how to further improve the performance of photonic nanowire single-photon sources.

4.2.5.1 Some practical considerations

Single-photon sources based on QD inserted in a microcavity rely on a resonant approach. The emitter has thus to be spectrally matched with the localized optical mode (within 1 meV, the typical tuning range accessible with temperature variations). Despites a lot of growth efforts, the inhomogeneous linewidth of an ensemble of self-assembled QD still exceeds 10 meV. Therefore, 1 dot out of 100 typical presents the good emission energy. The constraint of spatial matching further degrades the usable dot fraction to a typical 1 out of 1000 [14]. This makes the experiments very ‘painful’ and the device fabrication yield very low. Recently, such a limitation has been resolved using complex in-situ lithography [15].

In a photonic wire, we have seen in the section 2.1.3, that the SE control is very robust (spectral tolerance thanks to the waveguide geometry and spatial tolerance thanks to the marked inhibition of the coupling to the radiative modes). Thus the randomness inherent to self-assembled QDs does not limit seriously the device fabrication yield.

4.2.5.2 Purity of single-photon emission

We have seen that our single-photon source features a very pure single-photon emission, even when the QD is driven to saturation (maximum source efficiency). This property is in general for QD in bulk material. However, the purity of single-photon emission is seriously degraded when the emitter is integrated in a microcavity featuring a high Purcell factor. In cavity-based devices, $g^{(2)}(0)$ increases with power and exhibits a much higher value at the saturation (see figure 4.16).

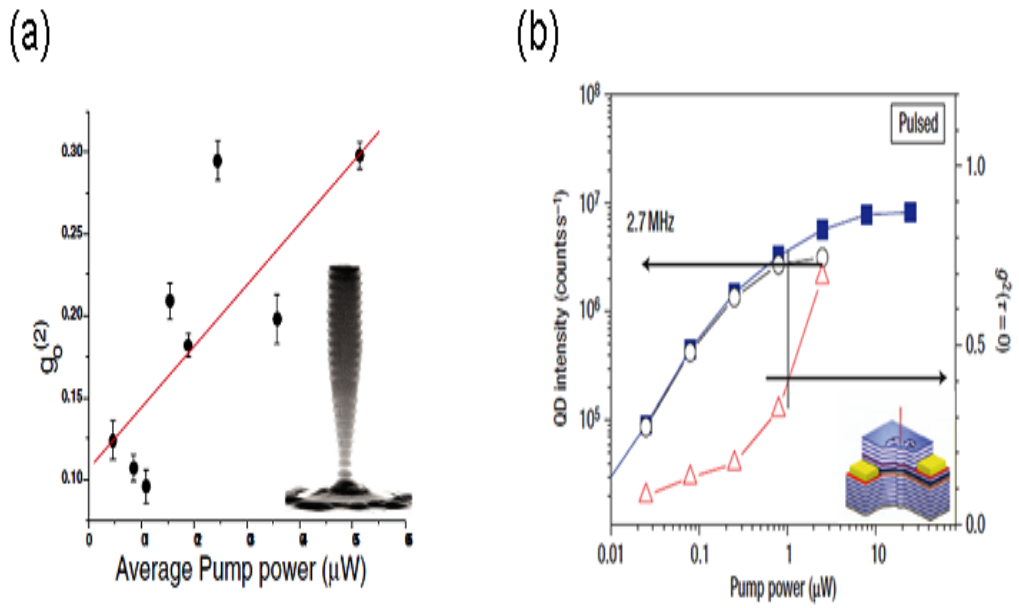

Figure 4.16 : Second order correlation function as function of pumping power for the cavity based devices (a) Micropillar cavity [16], (b) Oxide aperature cavity [12].

This degradation is likely due to a 'non-resonant cavity feeding' process, which results in the non-resonant collection of a detuned, non-monochromatic transitions by the cavity mode. In that case, the cavity mode can be fed by several transitions, which degrades the $g^{(2)}(0)$. In some sense, the cavity is acting oppositely to a spectral filter and collects light from detuned transitions. Due to its mesoscopic nature, a QD features a spectrum which is much richer than the one of an atom. The QD transitions can be broadened by several mechanisms, leading to non-resonant feeding (pure dephasing [17, 18], acoustic phonons broadening [19, 20]). In addition, the hybridization of the QD localized states with

the continuum of the wetting layer generates a continuum of transition [21], also leading to non-resonant feeding. Because SE control in a photonic nanowire is broadband, these very detrimental effects are not present: the nice single-photon emission of a QD is preserved in this system.

4.2.5.3 Source efficiency

In case of cavity based devices, the best reported efficiency is limited to around 40% [12, 13, 16]. In fact, the far-field radiation pattern of a high-Q microcavity is very sensitive to fabrication imperfections [22]. Schematically, the photon stays a long time trapped in the cavity mode and has some significant probability to be scattered in random direction by a residual defect. In that perspective, a photonic nanowire structure is much more robust. In such a waveguide, the photon escapes very quickly from the device.

At present, the source efficiency is mainly limited by the tapering geometry. In principle, a decrease of the tapering angle may bring the efficiency closer to its theoretical limit, ~ 0.95 for a taper having unity transmission [6]. We believe it is difficult to realize with our top-down (etching) approach. However, it might be feasible in a bottom-up approach [23, 24]. Another very promising way to reach high efficiencies, compatible with our top-down approach, is to use an inverted taper [25]. In fact, such structures have been realized in the end of this PhD, their characterization is underway.

4.3 Conclusion

To conclude, we have shown that photonic nanowires provide broadband spontaneous emission control. This structure provides a very strong inhibition of SE into the continuum of radiative modes that ensures a very efficient funnelling of SE into the single guided mode. Moreover, the inhibition of the total SE rate obtained for small wires provides a convenient tool to measure the radiative yield of the embedded emitters. In addition, the photonic nanowire single-photon source demonstrated a record source efficiency of 0.72, combined with highly pure single-photon emission which is great improvement in comparison to the state-of-art cavity based source.

References

1. J.-Y. Marzin, J.-M. Gérard, A. Izrael, D. Barrier and G. Bastard, "*Photoluminescence of Single InAs Quantum Dots Obtained by Self-Organized Growth on GaAs*," Phys. Rev. Lett.**73**, 716 (1994).
2. J. Siegert, S. Marcinkevicius, and Q.X. Zhao, "*Carrier dynamics in modulation-doped InAs/GaAs quantum dots,*" Phys. Rev. B **72**, 0853161 (2005)
3. K. W. Sun, J. W. Chen, B. C. Lee, C. P. Lee and A. M. Kechiantz, "*Carrier capture and relaxation in InAs quantum dots,"* Nanotechnology **16**, 1530 (2005).
4. J. Johansen, S. Stobbe, I. S. Nikolaev, T. Lund-Hansen, P. T. Kristensen, J. M. Hvam, W.L. Vos, and P. Lodahl, "*Size dependence of the wavefunction of self-assembled InAs quantum dots from time-resolved optical measurements,"* Phys. Rev. B **77**, 073303 (2008).
5. S. Noda, M. Fujita and T. Asano, "*Spontaneous emission control by photonic crystals and nanocavities*," Nature Photonics **1**, 449 (2007).
6. I. Friedler, C. Sauvan, J. P. Hugonin, P. Lalanne, J. Claudon, and J. M. Gérard, "*Solid-state single photon sources: the nanowire antenna*," Opt. Exp. **17**, 2095 (2009).
7. J. M. Gérard, and B. Gayral, "*Strong Purcell effect for InAs quantum boxes in three-dimensional solid-state microcavities*," J. Lightwave of Technology **17**, 2089 (1999).
8. M. Grundmann and D. Bimberg, "*Theory of random population of quantum dots,*" Phys. Rev. B **55**, 9740 (1997).
9. H. J. Kimble, M. Dagenais, and L. Mandel, "*Photon antibunching inresonance fluorescence,*" Phys. Rev. Lett. **39,** 691 (1977).
10. R. Hanbury Brow and R. Q. Twiss, "*A new type of interferometer for use in radio astronomy*," Phil. Mag. **45**, 663 (1954).
11. R. Hanbury Brown and R. Q. Twiss, "*Correlation between photons in two coherent beams of light,*" Nature **177**, 27 (1956).
12. S. Strauf, N. G. Stoltz, M. T. Rakher, L. A. Coldren, P. M. Petroff, and D. Bouwmeester, "*High-frequency single-photon source with polarization control*," Nature Photonics **1**, 704 (2007).
13. E. Moreau, I. Robert, L. Manin, V. Thierry-Mieg, J. M. Gérard and I. Abram, "*A single-mode solid-state source of single photons based on isolated quantum dots in a micropillar*," Physica E **13**, 418 (2002).
14. M. Munsch, "*Étude du régime de Purcell pour une boîte quantique unique dans une microcavité semiconductrice*," PhD Thesis UJF Grenoble, (2009).
15. A. Dousse, L. Lanco, J. Suffczyn´ski, E. Semenova, A. Miard, A. Lemaıˆtre, I. Sagnes, C. Roblin, J. Bloch, and P. Senellart, "*Controlled Light-Matter Coupling for a Single Quantum Dot Embedded in a Pillar Microcavity Using Far-Field Optical Lithograpy,*" Phys. Rev. Lett. **101**. 267404 (2008).
16. M. Pelton, C. Santori, J. Vucˇkovic´, B. Zhang, G. S. Solomon, J. Plant, and Y. Yamamoto, "*Efficient Source of Single Photons: A Single Quantum Dot in a Micropost Microcavity*, " Phys. Rev. Lett. **89**, 233602 (2002).

17. A. Auffèves, J.-M. Gérard and J.-P. Poizat, "*Pure emitter dephasing: A resource for advanced soild-state single photon sources,"* Phys. Rev. A **79**, 053838 (2009).
18. J. Suffczyn´ski, A. Dousse, K. Gauthron, A. Lemaıˆtre, I. Sagnes, L. Lanco, J. Bloch, P. Voisin, and P. Senellart, "*Origin of the Optical Emission within the Cavity Mode of Coupled Quantum Dot-Cavity Systems,"* Phys. Rev. Lett. **103**, 027401 (2009).
19. S. Ates, S. M. Ulrich, A. Ulhaq, S. Reitzenstein, A. Lo¨ffler, S. Ho¨fling, A. Forchel and P. Michler, "*Non-resonant dot–cavity coupling and its potential for resonant single-quantum-dot spectroscopy*, " Nature Photonics **3**, 724 (2009).
20. U. Hohenester, "*Cavity quantum electrodynamics with semiconductor quantum dots: The role of phonon-assisted cavity feeding,"* Phys. Rev. B **81**, 155303 (2010).
21. M. Winger, T. Volz, G. Tarel, S. Portolan, A. Badolato, K. J. Hennessy , K.J. Hennessy, E. L. Hu, A. Beveratos, J. Finley, V. Savona and A. Imamohlu, "*Explanation of Photon Correlations in the Far-Off-Resonance Optical Emission from a Quantum-Dot–Cavity System*," Phys. Rev. Lett. **103**, 207403 (2009).
22. W.L. Barnes, G. Bjork, J.M. Gérard, P. Jonsson, J.A.E. Wasey, P.T. Worthing and V. Zwiller, "*Solid-state single photon sources: light collection strategies*," Eur. Phys. J. D **18**, 197 (2002).
23. S. N. Dorenbos, H. Sasakura, M. P. van Kouwen, N. Akopian, S. Adachi, N. Namekata, M. Jo, J. Motohisa, Y. Kobayashi, K. Tomioka, T. Fukui, S. Inoue, H. Kumano, C. M. Natarajan, R. H. Hadfield, T. Zijlstra, T. M. Klapwijk, V. Zwiller, and I. Suemune, "*Position controlled nanowires for infrared single photon emission,"* Appl. Phys. Lett. **97**,171106 (2010).
24. J. Heinrich, A. Huggenberger, T. Heindel, S. Reitzenstein, S. Höfling, L. Worschech,and A. Forchel,"*Single photon emission from positioned GaAs/ AlGaAs Photonic nanowires*," Appl. Phys. Lett. **96**, 211117(2010).
25. N. Gregersen,T. R. Nielsen, J. Mørk, J. Claudon, and J.-M. Gérard, "*Designs for high-efficiency electrically pumped photonic nanowire single-photon sources*," Opt. Exp. **18**, 21204 (2010).

Chapter 5

Control of Photon Polarization by Elliptical Photonic Nanowire

*The only way to get rid of a temptation is to yield to it.-**Oscar Wilde***

In this chapter, we propose a new method to obtain a true single-mode emission (with a well defined, linear polarization), using a photonic nanowire with an elliptical cross-section. First, we present the state-of- art of single mode emission and the motivations to achieve this regime. We then present theoretical results showing that for a moderate aspect ratio, the local density of modes inside the structure is dominated by the contribution of a single guided mode, with a linear polarization. We will also see that the detailed understanding of polarization control requires a fine description of the nature of the embedded emitter. Afterward, we present the fabrication process to realize this novel geometry. In this regard, we will mainly emphasis on the etching mask requirements and etching process optimization to realize this structure. In order to investigate the control of photon polarization experimentally, we have performed polarization-resolved photoluminescence experiments on the elliptical nanowires. In particular, we show that the proportion of photons with the desired polarization among the collected ones can be as high as 95%. Moreover, these high performances are maintained over a broad wavelength range, a key asset of this 1D photonic structure.

5.1 Single-mode emission: motivations and state-of-the-art

5.1.1 Context and motivations

True single-mode emission, that is to say the emission into an optical mode with a well defined spatial structure and polarization, is interesting for the realization of a new generation of advanced optoelectronic devices, and for fundamental quantum optics experiments. As a first example, random polarization is a potential source of polarization noise in a vertical cavity surface emitting lasers [1, 2]. Moreover a true single mode emission can provide high-β microlasers which exhibits ultra-low threshold [3]. In the field of quantum communication, inserting a QD inside an electromagnetic environment dominated by a single mode allows for the realization of efficient sources of polarized single photons, a key component of quantum cryptography [4]. Moreover, if the photons emitted by the QD features a lineshape that is limited by Fourier transform, one can generate indistinguishable photons (same spatial structure, same polarization, and same temporal dependence). Such a device may find applications in linear quantum computing [5, 6]. More generally, the coupling of a single quantum emitter to a single optical mode, often referred as a 1D atom [7], is an ideal system to perform quantum optics experiments.

5.1.2 State-of-the-art: cavity-based devices

In this section, we describe the cavity-based approach to obtain single-mode emission. It relies on the Purcell effect, that is to say the selective acceleration of spontaneous emission into a resonant cavity mode. As a first example, we discuss results obtained on elliptical pillars and we begin by considering a circular pillar. In that case, the fundamental HE_{11} mode is 2-fold degenerated, with 2 orthogonal linear polarizations [8, 9]. Thus, an emitter with an isotropic dipole will be simultaneously coupled to these 2 modes, with the same decay rate. As a consequence, the light emitted by the structure is not polarized. To obtain polarized emission, one has to lift the degeneracy of these 2 modes. To this end, Gayral *et al.* introduced pillars with an elliptical shape [10]. The low energy modes guided by an elliptical waveguide have different effective indexes, and linear polarizations that are aligned on the long and short axis of the ellipse. To build the cavity, Bragg mirrors are added and this shape birefringence then results in different resonance energies for the 2 polarizations. They can be

resolved providing that the energy splitting induced by the elliptical shape is larger than the optical Q-factor. The dashed line in Figure 5.1 shows the µ-PL spectra under strong excitation of an elliptical pillar with major diameter 1.4 µm and minor diameter 0.7 µm. The 2 modes are clearly resolved and the structure can be used to achieve polarized single-photon emission (in that case, the pumping is weaker: solid line). Moreau *et al.* has been demonstrated that the dot on-resonance with a mode then emits light with a linear polarization that is imposed by the resonant mode to which it is coupled [13].

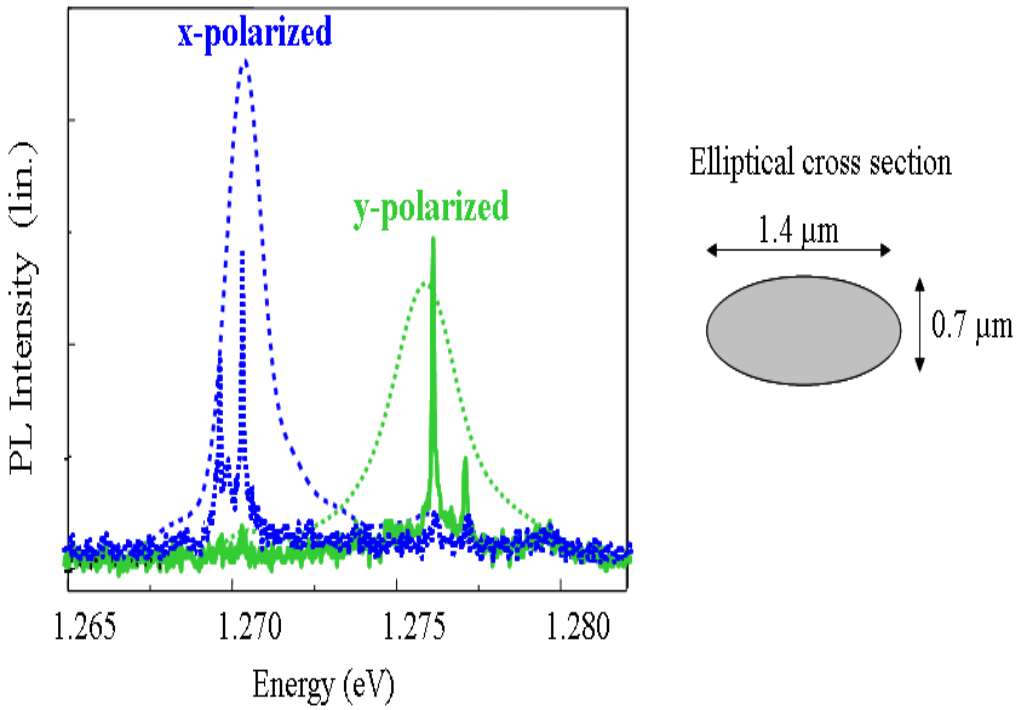

Figure 5.1: Principle of microcavity-based device to get polarization: Lifting the degeneracy of the fundamental guided mode [13].

After Gayral's and Moreau's demonstrations, many research groups have been used this kind of cavity to control the photon polarization [11 -12]. Certain photonic crystal microcavities also feature highly polarised cavity mode [14 -16]. But all these approaches based on the resonance based scheme, require the spatial and spectral matching between the emitter and cavity modes. As we already discussed and demonstrated respectively in the chapter 2 and chapter 4, cylindrical photonic nanowires provide broadband SE control: it is therefore tempting to try to achieve single-mode emission using this geometry.

5.2 Control of photon polarization with photonic wire

In this section, we introduce dielectric elliptical photonic nanowires to funnel efficiently the spontaneous emission of an embedded emitter into a truly single optical guided mode. All the calculations mentioned in this section have been performed by Niels Gregersen (and his colleagues).

5.2.1 The case of circular photonic nanowires

First, we consider infinite wires with a circular cross-section. The nanowire is made of GaAs (refractive index n = 3.45) and surrounded by an air cladding (n =1). In the following we suppose a free space emission wavelength λ= 950nm. The wire always supports two degenerate fundamental guided modes $HE_{11X,Y}$ with orthogonal linear polarization, similarly to the circular micropillar discussed in the last section. The calculated electric field profile of the two components of HE_{11} mode for a photonic nanowire with diameter d=0.22λ, is shown in Figure 5.2. This figure shows that spatial field profile for x and y- polarized mode is as expected the same, but for a rotation of a 90° angle.

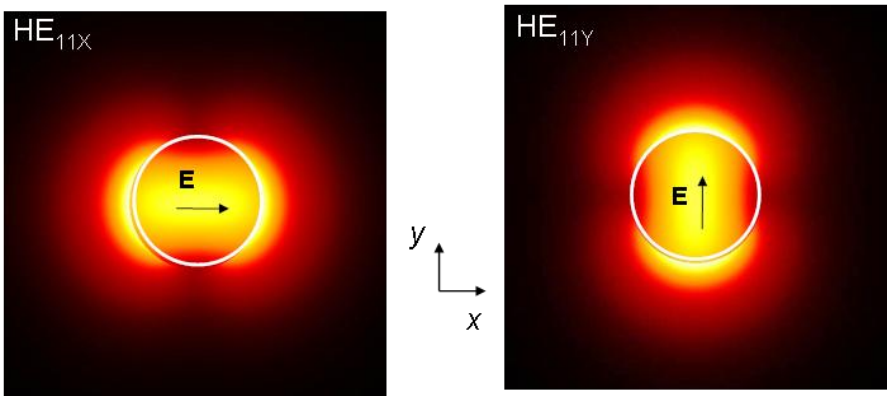

Figure 5.2: Degeneracy of the Fundamental guided mode HE_{11} of circular photonic wire: HE_{11X} and HE_{11Y} have polarizations respectively aligned with the X and Y directions. The plots are colour maps of the total amplitude of the electrical field (yellow=high, black=low).

As a result, single-mode emission from circular wires can only be achieved using a highly polarized emitter, which is not the case of usual semiconductor emitters (e.g. neutral or charged excitons confined in a QD, excitons trapped in a quantum well). In case of an isotropic emitter embedded in this photonic wire,

polarization of the emission is random. To obtain single-mode emission, one has to suppress selectively the coupling to one of the mode: we address this issue in the following section.

5.2.2 Spontaneous emission control in Elliptical photonic nanowires

5.2.2.1 Selective deconfinement of one mode

In order to lift the degeneracy of the fundamental guided mode, we introduce a GaAs photonic nanowire featuring an elliptical cross section. The long and short axis are respectively denoted (ll) and ($\perp$), and the corresponding diameters d_{ll} and $d_{\perp}$. The wire always supports two low energy guided modes M_{ll} and $M_{\perp}$ with linear polarization respectively oriented along (ll) and ($\perp$). To suppress the coupling to one of the mode, we use the effect studied in chapter 2 and chapter 4: the guided mode can be deconfined in air by reducing the diameter of the wire. Adjusting the aspect ratio of ellipse allows us to selectively deconfine $M_{\perp}$, while M_{ll} remain tightly confined in the semiconductor. This effect is illustrated in Figure 5.3, which shows a field map of the two modes for $d_{ll} = \lambda/n$ and $d_{\perp} = 0.50 \times d_{ll}$.

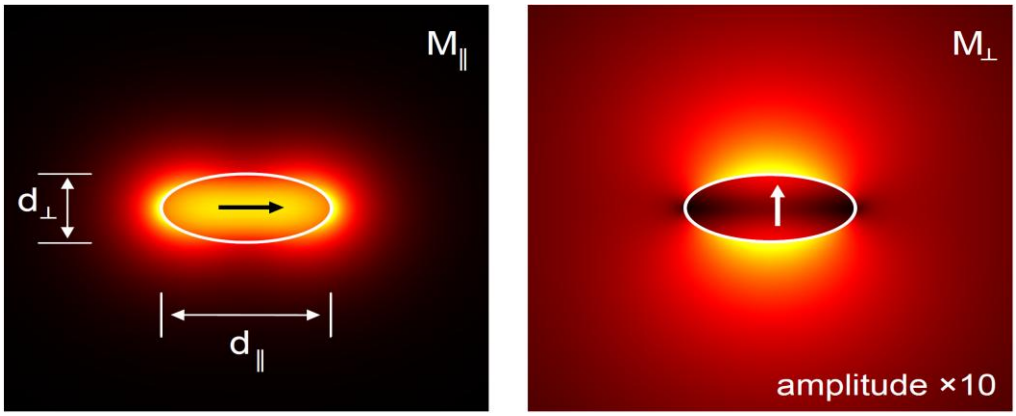

Figure 5.3: Selective deconfinement of the guided mode $M_{\perp}$ in an elliptical wire while M_{ll} remains well confined ($d_{ll} = \lambda/n$ and $d_{\perp} = 0.50 \times d_{ll}$). The plots are colour maps of the total amplitude of the electrical field (yellow=high, black=low). For clarity, the amplitude associated with $M_{\perp}$ has been multiplied by a factor of 10.

Because the deconfinement occurs very rapidly with the dimension reduction, it is possible to achieve a huge anisotropy of the vacuum electromagnetic field inside the photonic wire, even with moderate shape anisotropy.

5.2.2.2 Generalized Purcell factor associated with the guided modes

In this paragraph we investigate the generalized Purcell factors $F_{\parallel}$ and $F_{\perp}$ associated with the modes $M_{\parallel}$ and $M_{\perp}$ respectively. We recall they are calculated as the ratio of the SE rate in the photonic wire over a reference decay rate, which is the SE rate of the same emitter embedded in bulk GaAs. The hypotheses are the following: point dipole source located inside the nanowire, on the maximum electrical field amplitude (i.e. on the wire axis), and with a dipole aligned with the electrical field. This generalized Purcell factor is a key figure of merit for the structure in the context of SE control.

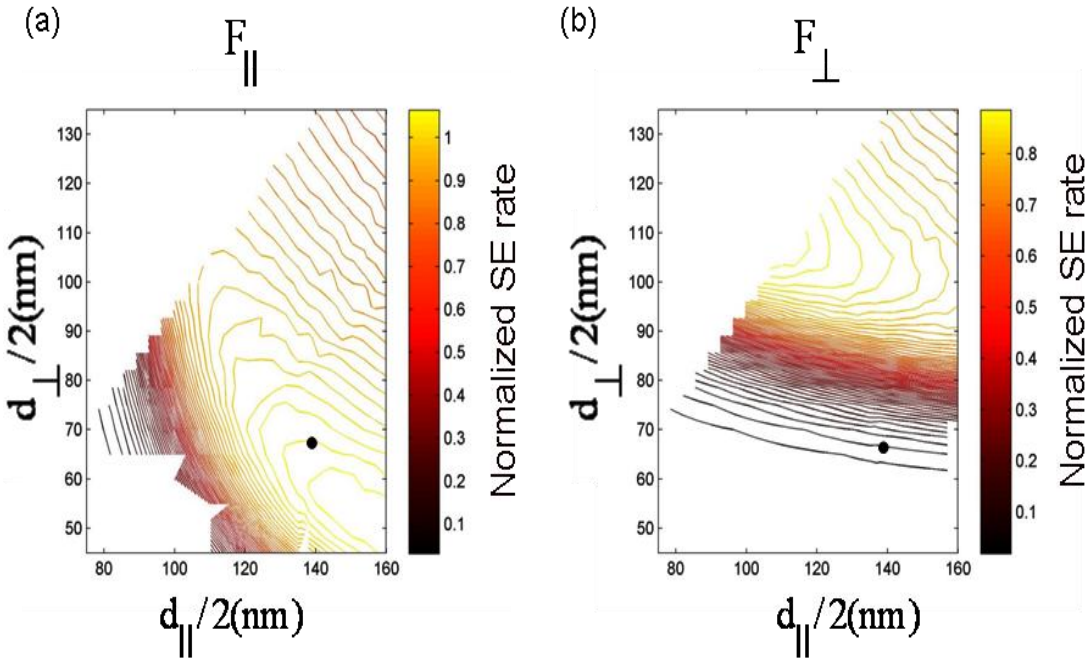

Figure 5.4: Generalized Purcell factors associated with $M_{\parallel}$ (a) and $M_{\perp}$ (b) as a function of the wire dimensions.

Figure 5.4(a) shows $F_{\parallel}$ as a function of the wire dimensions. For $270 < d_{\parallel} < 320$ and $120 < d_{\perp} < 140$, $F_{\parallel}$ is close to 1. This shows that $M_{\parallel}$ is well confined by the structure, leading to a good SE coupling. In fact, this value is

even larger than the optimal Purcell factor obtained in a cylindrical photonic wire (0.9, see chapter 2) which indicates that an elliptical section provides a better confinement of the guided mode. For the same size range, the generalized Purcell factor associated with mode $M_{\perp}$ is much smaller (see Figure 5.4 (b)). The black dot point represents the same nanowire dimensions as like Figure 5.3. Thus, a moderate shape anisotropy induces a huge anisotropy of the vacuum field fluctuations, with $F_{\parallel} / F_{\perp}$ greater than 100. Though these two modes are guided by the structure, the difference in the lateral confinement favours largely the one with a polarization aligned on the major axis of the ellipse.

5.2.3 SE control and β-factor

As we discussed in chapter 2, SE control in photonic nanowires also relies on a pronounced screening of the continuum so-called radiative modes along with the coupling to the guided modes. In order to optimize the geometry one has optimized all the effects of SE control. We here consider an emitter that features two orthogonal dipole components perpendicular to the wire axis. To ensure polarization control at the SE level, we further assume that each dipole components is simultaneously coupled to both modes $M_{\parallel}$ and $M_{\perp}$. In that case, the photons are emitted preferentially into $M_{\parallel}$, which will be the fastest decay channel. The fraction $\beta_{\parallel}$ of photons emitted in $M_{\parallel}$ reads

$$\beta_{\parallel} = \frac{\Gamma_{M_{\parallel,\parallel}} + \Gamma_{M_{\parallel,\perp}}}{\Gamma_{Tot,\parallel} + \Gamma_{Tot,\perp}} \quad , \tag{5.1}$$

where $\Gamma_{M_{\parallel}}$ is the SE rate into $M_{\parallel}$ (note that this rate can include a small contribution of a dipole oriented along (ll) for off-axis emitters), $\Gamma_{Tot,\parallel}$ and $\Gamma_{Tot,\perp}$ are the total SE rate (including SE rate into radiative modes) for a dipole oriented along (ll) and ($\perp$), respectively. We now consider the two different configurations:

On-axis emitter:

We first consider the ideal case when emitter is on the wire axis. The evolution of $\beta_{\parallel}$ as a function of anisotropic nanowire dimensions is shown in Figure 5.5 (a) (with λ = 950 nm). The black dot point represents the same nanowire dimensions as like Figure 5.3. This clearly demonstrates that for an on-

axis emitter β_{II} exceeds 93% over a broad diameter range, a first indication of the broadband operation of our device. The evolution of β_{II} as function of wavelength is shown in Figure 5.5 (b) and shows $\beta_{II} \approx 92\%$ (λ = 950 nm). Moreover $\beta_{II} > 90\%$ over the 900-990 nm wavelength range is obtained which is a key asset of this 1D photonic system.

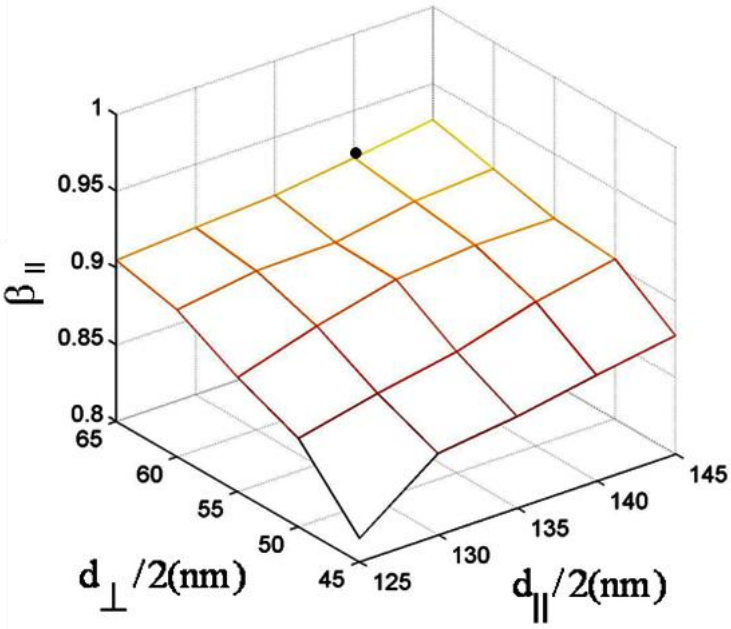

Figure 5.5 (a): Spontaneous emission control for an on-axis emitter: Evolution of β_{II} as a function of the nanowire dimensions.

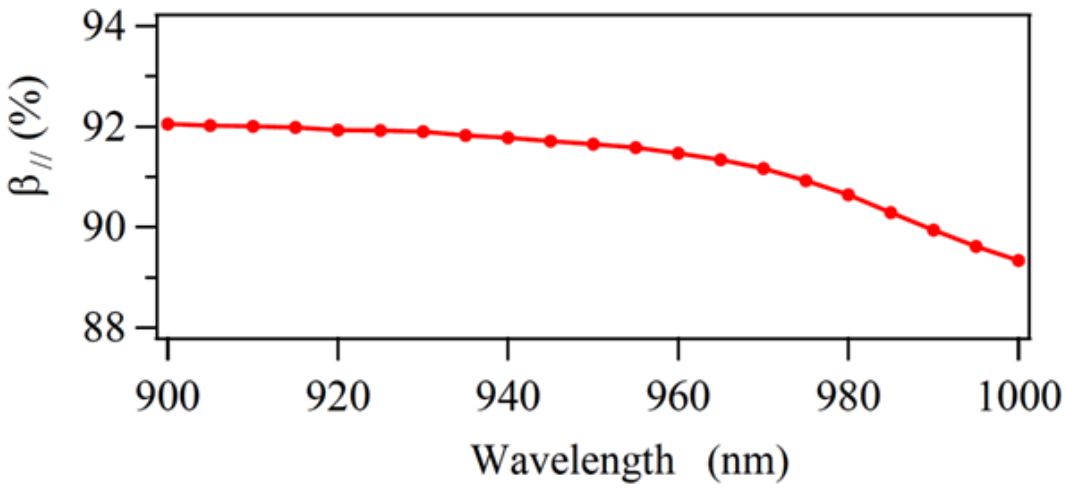

Figure 5.5 (b): Spontaneous emission control for an on-axis emitter: Evolution of β_{II} as a function of the free space operation wavelength λ.

Off-axis emitter:

Given our fabrication approach, the emitter can be off-axis in practice. The evolution of β_{II} as a function of the emitter position is shown in Figure 5.6 (λ = 950 nm, only one quarter of the elliptical section is presented). This figure clearly shows that in an infinite wire, 20% of a set of randomly positioned emitter displays β_{II}>85%. Such a tolerance is associated with the strong inhibition of the SE into the radiative modes.

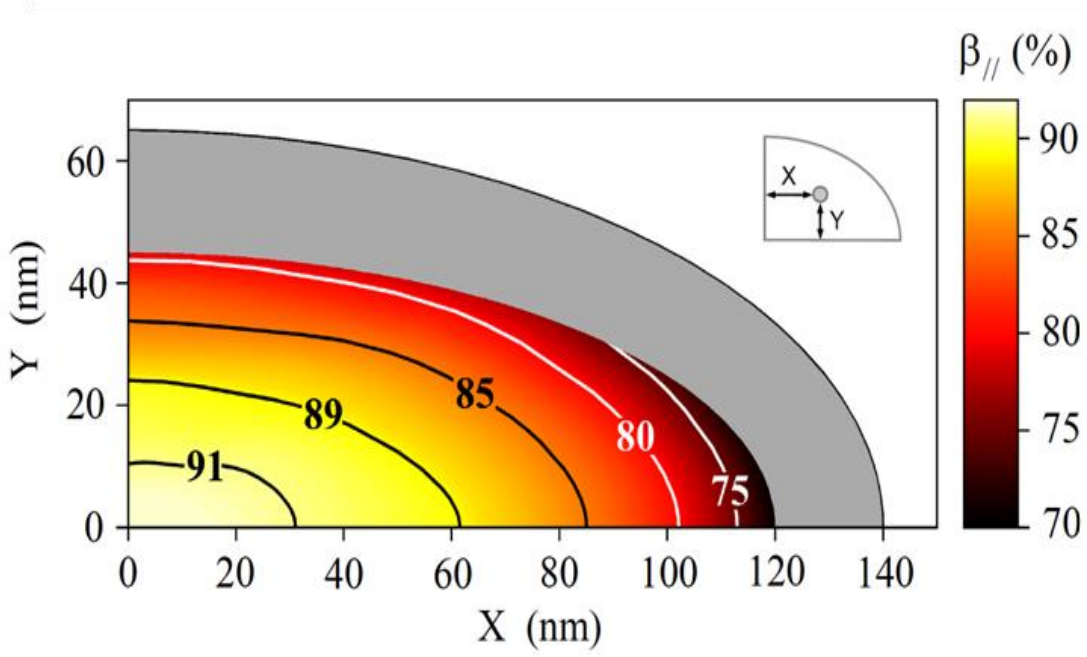

Figure 5.6: Spontaneous emission control for off-axis emitters, where the solid black line represents the boundary of the nanowire.

To summarize this theoretical analysis, an elliptical photonic nanowires strongly inhibit SE in all the electromagnetic modes, except the one of interest, for which a high coupling rate is preserved along with spatial and spectral tolerance.

5.3 Low energy excitonic complexes trapped in a QD

In the previous section, we have seen that it is possible to obtain single-mode emission with an emitter whose dipole components are simultaneously coupled to M_{II} and $M_{\perp}$. In this paragraph, we examine this condition for various low energy complexes that are trapped in a QD.

Charged exciton:

Usually self assembled InAs QDs have a tendency to be elongated along [110] direction (see Figure 5.7 (a)). This shape anisotropy does not influence the charged excitons (X^+ = 1 electron - 2 holes or X^- = 2 electrons - 1 hole). Each of these excitonic complexes presents doubly degenerate, optically active transitions with an isotropic dipole [17]. Thus charged excitons unconditionally fulfil the requirement of polarization at the SE level.

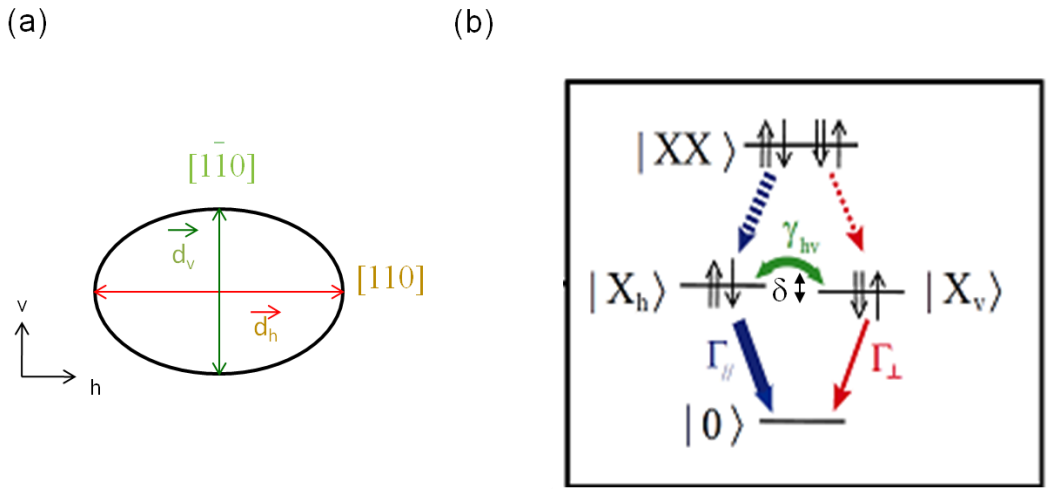

Figure 5.7: Anisotropic quantum dot, (a) Schematic two orthogonal components of bright exciton states, (b) Energy level diagram for different states.

Neutral exciton:

The case of the neutral exciton (X^0 = 1 electron – 1 hole) is different and more complex. For a symmetric QD, the neutral exciton features 2 families of states: 2 degenerate optically active state (the 'bright' exciton), and 2 degenerate non-optically active states (the 'dark' exciton). In self-assembled InAs/GaAs QDs, the dark excitons are located a few hundreds of μeV below the bright excitons. In the following, we concentrate on bright excitons. In fact, self-assembled InAs QDs are elongated along the [110] direction. The combined effects of the reduced shape symmetry and exchange interactions, lift the degeneracy of the two bright sates (energy splitting 'δ' on the order of few tens of μeV) (see Figure 5.7 (b)) [18, 19]. The new eigenstates are denoted as $|X_h\rangle$ and $|X_v\rangle$; the transitions toward the ground state of the QD (empty QD) have a linear dipole oriented along the crystallographic directions [110] and [1$\bar{1}$0] denoted as (h) and

(v) in Figure 5.7 (a). Under non-resonant pumping, we assume that $|X_h\rangle$ and $|X_v\rangle$ are pumped with the same rate.

The possibility to achieve polarization control then depends on the orientation of the photonic structure with respect to the crystallographic axis. If the photonic axis (ll) and ($\perp$) are oriented 45° off (h) and (v), then each dipole couples to M_{ll} and $M_{\perp}$: the two modes compete, leading to the desired SE control. On the contrary, if (ll) is aligned along (h) [or equivalently along (v)], each dipole sees only one mode, and the two dipoles decay independently. As in Ref. [20], this can be useful to probe an anisotropic density of modes with time-resolved and polarization-resolved measurements. However, this does not lead to a neat polarization under pulsed excitation. For each orientation, the transition emits 0.5 photon per excitation pulse (with different mean decay times); the number of emitted photon in each channel is thus equal (if the repetition rate is slow enough). Therefore, an additional coupling mechanism, like a fast spin-flip mediated conversion between the bright states is then required to funnel all the emission into mode M_{ll} [21].

Neutral bi-exciton:

The neutral bi-exciton is unconditionally coupled to the both modes M_{ll} and $M_{\perp}$, also leading to the desired SE control due to the photonic effect (see Figure 5.7 (b)).

5.4 Fabrication of elliptical photonic nanowires

In this section, we discuss the fabrication process of the elliptical photonic nanowires in brief. More details on the fabrication technologies can found in Chapter 3.

5.4.1 MBE sample

We start from a planar epitaxial structure, which is grown on a (001) GaAs wafer by molecular beam epitaxy (growth was performed by M. Ducruet at NPSC). The sample structure is shown in Figure 5.8. First a GaAs buffer layer is grown on the substrate. Afterward a 500 nm of $Al_{0.8}Ga_{0.2}As$ layer is grown: it will be used as an etching depth detection layer in the subsequent process. In the end of the growth, we grow a single array of self-assembled InAs QDs, buried

1μm below the top surface of a 2μm-thick GaAs layer. Nanowire will be defined in this 2 μm-thick GaAs in the later process. A rather low density of QDs (~ 200 μm^{-2}) is chosen in order to allow for single dot investigations.

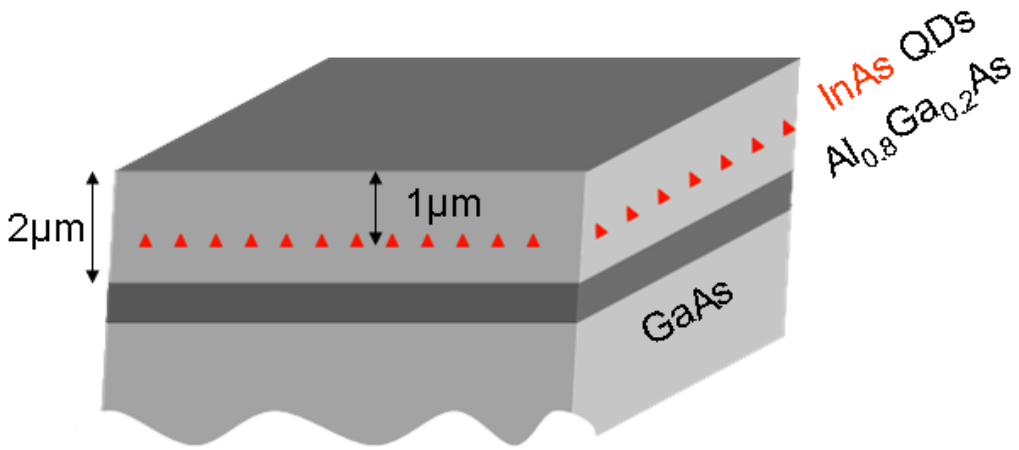

Figure 5.8: Schematic of the MBE sample for elliptical photonic wire.

5.4.2 Nanofabrication of photonic wire

The fabrication procedure of elliptical photonic nanowire consisted of patterning polymethyl-methaacrylate (PMMA) by electron-beam lithography and then transferring the pattern into the semiconductor by reactive ion etching (RIE). To produce the high polarization degree at a wavelength of around 950nm, where the QDs emit, the major and minor diameters 280 and 130 nm are required. In order to fabricate this anisotropic structure, the wall of the nanowire must be both straight and smooth. In this work, great efforts were put into finding the processing condition to produce high quality structures. Our efforts have been focused firstly on the search for a good etching mask, and secondly on the optimization of etching conditions. From the previous experience of the fabrication of cylindrical photonic nanowires, we know that reactive ion etching (RIE) can full fill the second requirement as it has the important property of achieving good anisotropy of the etched features. Therefore the main quest was to find the proper mask for this fabrication process. We used the two different hard mask for this study.

First approach: Silicon Nitride hard mask

In the first approach, we initially used silicon nitride (Si_3N_4) as a hard mask for etching. We used two steps anisotropic RIE process to fabricate the nanowires in this process. The nanofabrication process flow of this approach is

same as for regular taper structure which is described in the chapter 3. Therefore we first deposit 400 nm of Si_3N_4 on the epitaxial sample by PECVD as described in the chapter 3. To fabricate the device, first a 270nm thick layer of PMMA -4% resist is spun onto the wafer and baked at 180°C for 5 minutes. Then we defined the nanowire pattern which constitute of ellipses with various dimensions and aspect ratio (ratio of the major and minor axis) by using electron-beam lithography with optimized current dose as per different dimension requirements. In the laboratory frame, the crystal directions [110] and $[1\bar{1}0]$ are respectively horizontal (h) and vertical (v). The nanowire pattern was repeated for three different orientations θ of the ellipse major axis with respect to H: $\theta_{II} = 0°$, 45° and 90°.

After the development of the resist, a 60 nm of Al-metal was evaporated on the sample and the desired nanowire pattern transferred to this using lift-off process which leaves metal discs corresponding to the nanowire dimension; these discs served as a mask allowing the Si_3N_4 to be etched. In the first step of etching we used a SF_6 plasma based RIE process to transfer nanowire pattern into Si_3N_4 layer. As RIE is combination of chemical and physical etching therefore we used the high RF power to transfer the exact nanowire pattern into Si_3N_4 layer by making RIE process more physical. The etching parameters were 25 sccm of SF_6, 60 W of RF power with a 10 mTorr pressure in the chamber.

In the last step of process, a reactive ion etching process with $SiCl_4$ and Ar is used to transfer nanowire pattern into GaAs using the Si_3N_4 as an etching hard mask. Optimization of the RIE allows the realization of very smooth sidewalls. The gas flow was maintained as 75 sccm of Ar and 3 sccm of $SiCl_4$, which allows a good balance of physical sputtering and chemical etching components of RIE. The plasma was generated at the RF power of 80 W with a 15 mTorr chamber pressure. For these parameters, the RIE etch rate was estimated to be 125-150 nm/min. The samples are etched until the $Al_{0.8}Ga_{0.2}As$ layer is detected with laser interferometry.

A picture of the top of the structure is shown in Figure 5.9 (c). We know from the regular taper structure fabrication process (see chapter 3) that the Si_3N_4 hard mask is etched laterally and vertically during the SF_6-based RIE. We have used this to realize tapered nanowires, but in the present context, this effect prevents us to transfer correctly the shape of the mask (see Figure 5.9 (a)) into the GaAs. Due to the etching angle of the Si_3N_4 mask, the mask is partially destroyed when its lateral dimensions are too small (see Figure 5.10 (b)). Since this sample was designed to test SE control in structures with a well defined

section, we have developed a new hard mask, to allow for a good control over the shape of the wire cross-section.

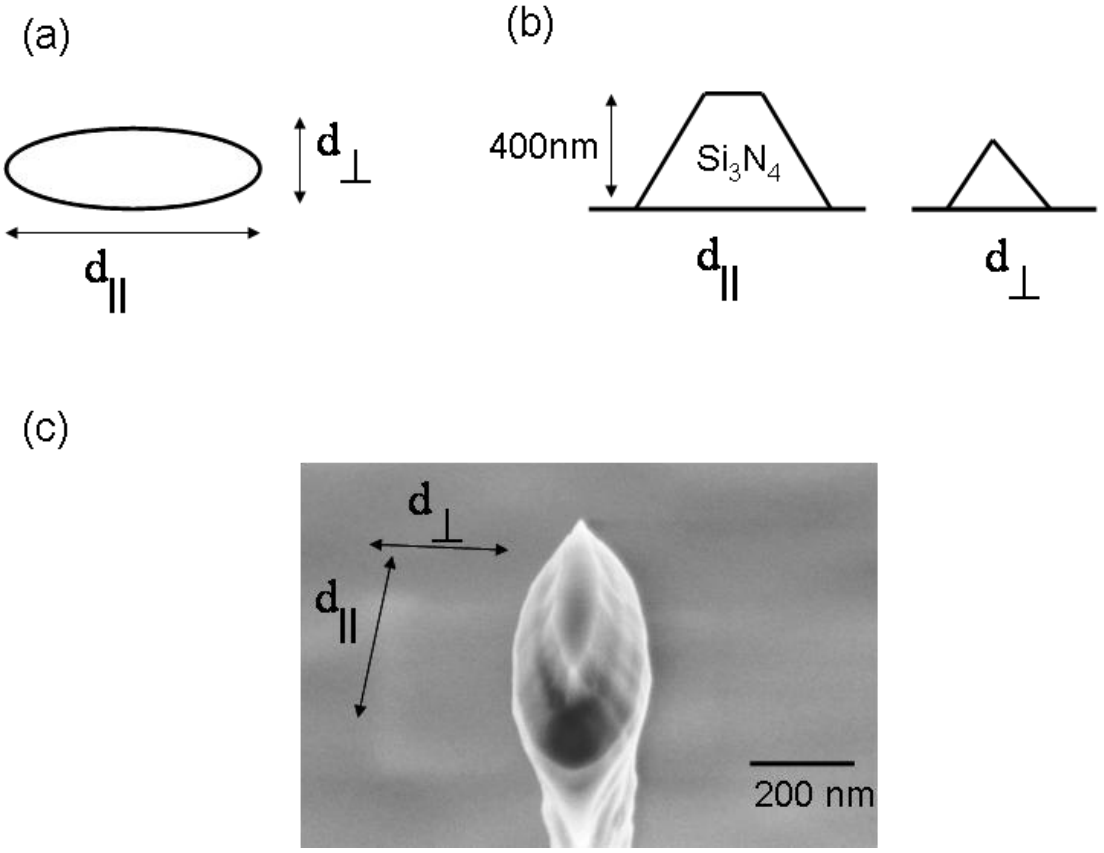

Figure 5.9: Limitation of Si_3N_4 etching hard mask, (a) Top view of the anisotropic etching mask, (b) highly anisotropic etching of the mask in two directions and (c) SEM image of the degradation of the etching mask.

Second (and successful) approach: Ni-metal hard mask

In order to remove the difficulty of Si_3N_4, we have used a harder etch mask made of Ni-metal. We already discussed the use of Ni-metal as a hard mask for the etching of '*Inverted taper'* structures in chapter 3 but Ni-metal mask was first introduced for the elliptical photonic nanowire fabrication. The requirements of the etching mask in this process, i.e. the high selectivity and less erosion of the side walls of the mask in Cl- based etching, are well fulfilled by the Ni metal mask. In this process we used a single step etching process. Figure 5.10 shows a schematic diagram of the process flow. The Ni later facilitates the etching of high

aspect ratio nanowires and inhibits the degradation of the side walls which would occur during the process of Si_3N_4 mask.

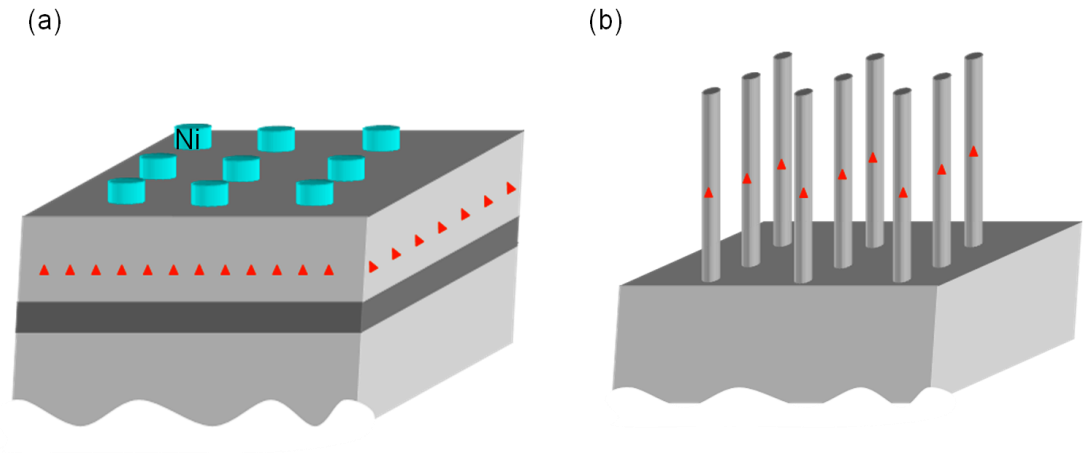

Figure 5.10: Schematic diagram of the process flow to fabricate elliptical photonic nanowire: (a) lift-off process leaves Ni-metal discs, which act as a mask for etching, and (b) Etching of the GaAs nanowire by $SiCl_4$/Ar based RIE.

In this process, we first spin coat the PMMA-4% resist on the epitaxial sample and after baking we performed electron beam lithography as in the first process, to define the desired nanowire pattern in PMMA. After the development of the expose resist, we evaporated 80 nm of Ni metal and a subsequent lift-off leaves the metal discs corresponding to the nanowire pattern. Then we performed $SiCl_4$/Ar based RIE etching to transfer the nanowire pattern into GaAs up to a 2-µm depth with the same etching parameter which we used in the last section. Figure 5.11 shows the SEM images of elliptical photonic wire fabricated by this process with major axis around 280 nm and minor axis around 130 nm where the dimensions of the structure have been precisely measured at the position of the QD.

SEM images revealed that the pattern transfer into the GaAs was very good, with smooth and straight side walls much improved over the first process, which clearly show the high quality of the etching and also indicates that a harder etch mask was useful to the RIE process. Furthermore undercutting was much reduced in comparison to the first process, which provides a highly anisotropic etching in both axes of the wire. In order to perform optics, we have to remove the Ni-metal mask from the top. We used chemical etching process with nitric acid 'HNO_3' (66%) diluted 5 times with D.I. water to remove the Ni. There is one

important advantage of the Ni-over the Si_3N_4 mask which is high selectivity in Cl-based RIE. Therefore one can use a very thin Ni-metal mask for the deep etching of GaAs which provides a way to etch very small feature size, even less than 100 nm. After the successful fabrication of the structure, the next step is optics experiments which we are describing in the next section.

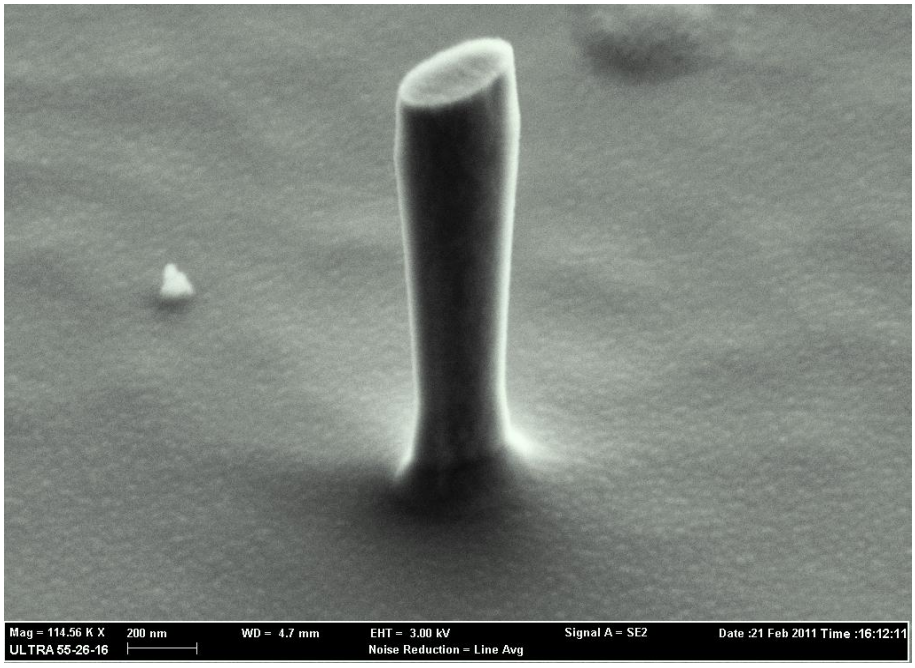

Figure 5.11: SEM image of elliptical GaAs -photonic nanowire fabricated by using Ni-metal hard mask.

5.5 Experimental results

In this section, we present the experimental results obtained on the elliptical photonic wire (measurements by Joël Bleuse and Mathieu Munsch).

5.5.1 Optical setup

In order to measure the photoluminescence (PL) from the photonic wire, we used the same micro-PL-setup which is described in the chapter 4, with some additional features for polarization analysis as shown in Figure 5.12.The PL light goes through combination of a rotating half-wave plate placed ahead of a fixed linear polarization in the detection arms of the setup, and of a monochromator equipped with a single-photon counter. The pulsed laser has the following characteristics: repetition rate: 76 MHz, wavelength 870 nm (excitation in the

wetting layer of the quantum dots). The residual polarization anisotropy of the setup was checked to be on the order of 1% above 900 nm. In addition; the luminescence of the ensemble of the QDs studied in this work, which peaks around 930 nm, does not exhibit any significant preferential polarization.

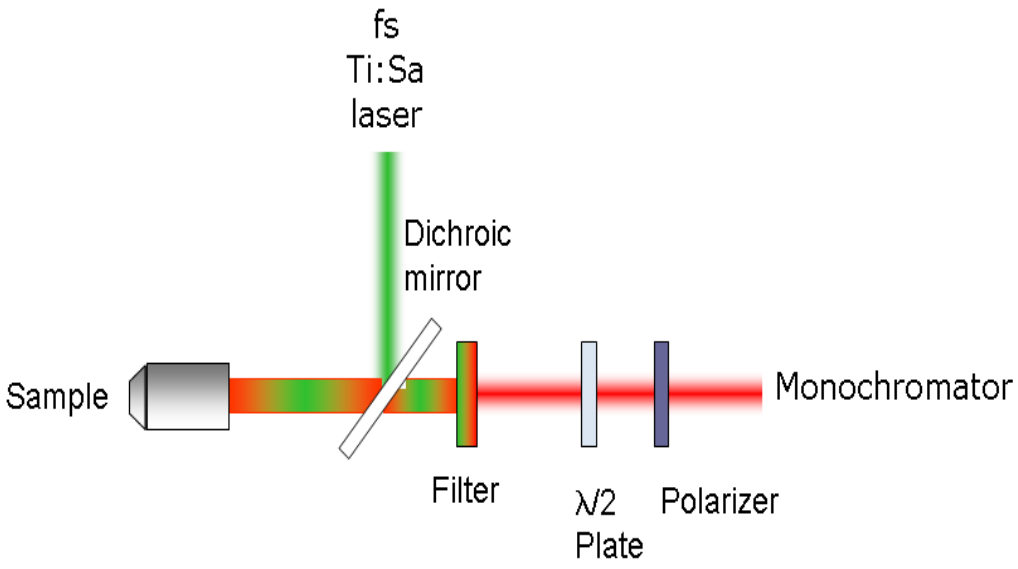

Figure 5.12: Schematic diagram of polarization resolved micro-PL step up

5.5.2 Polarization analysis

An example of micro-photoluminescence (μ-PL) spectrum measured at a temperature of 8 K on the elliptical wire PW_o for wavelength range 910 - 930 nm is shown in the Figure 2.13. The elliptical section of the wire is oriented along the (h) direction with dimensions d_{II} = 280 nm and $d_{\perp} = 0.46 \times d_{II}$. The spectrum features five well spectrally-resolved emission peaks due to the emission of the single quantum dots. The nature of these transitions has been determined using a combination of intensity dependence studies as a function of pumping power and decay time measurements. These peaks, originating from two different QDs named 'a' and 'b', have been identified as neutral exciton (X), biexciton (X_2), and a higher energy excitonic complex (X_n) transitions. The insets show the corresponding polarization analysis: The collected intensity I is plotted against the polarization angle θ [measured with respect to (h)]. It is clear from inserted figures that these five different lines exhibit a strong linear polarization, which is moreover closely aligned along the ellipse major axis.

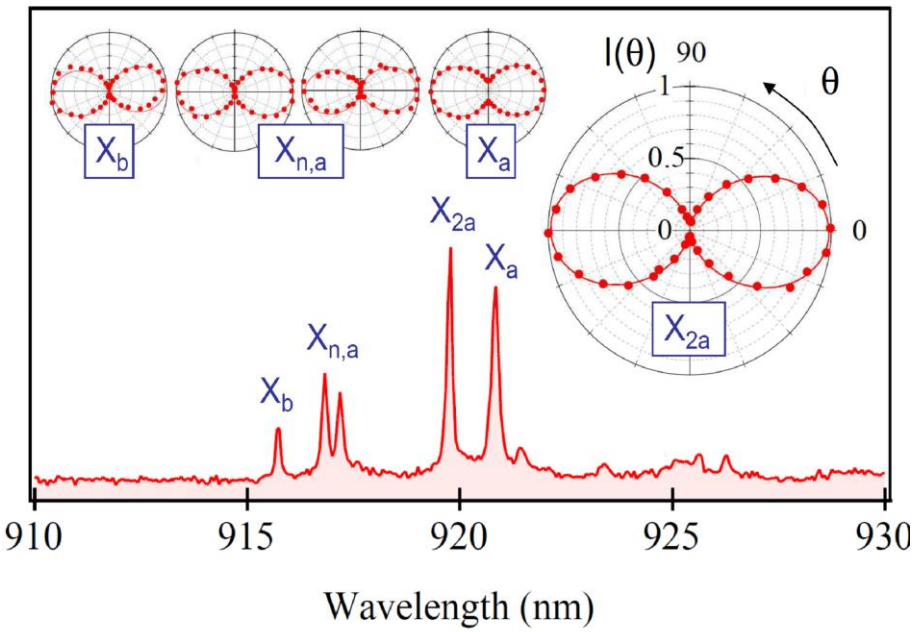

Figure 2.13: Polarization control in elliptical photonic nanowires: µ-PL spectra of InAs quantum dots embedded in wire named as PW_O, whose section major axis is oriented along (h). The polarization analysis associated with the 5 isolated spectral lines is shown in the insets.

For a quantitative analysis, the PL intensity variation with polarization angle θ is fit to the simple law:

$$I(\theta) = \frac{1}{2}(I_{\parallel} + I_{\perp}) + \frac{1}{2}(I_{\parallel} - I_{\perp})\cos(2\theta - 2\theta_O) + B. \qquad (5.2)$$

Here, $I_{\parallel}$ is the maximum intensity, obtained for $\theta = \theta_o$; $I_{\perp}$ is the minimum intensity and B represents a non-polarized, spectrally-flat background signal, which could be due to emission from the GaAs wafer. As a figure of merit of the polarization control, we introduce $C_{\parallel}$, the fraction of collected photons linearly polarized along θ_o:

$$C_{\parallel} = \frac{I_{\parallel}}{I_{\parallel} + I_{\perp}}, \qquad (5.3)$$

For the transition X_{2a}, $C_{\parallel}$ reaches 95 %. Moreover, $C_{\parallel}$ exceeds 90% on the 5 nm wavelength range spanned by the 5 transitions: this is a first experimental indication of the broadband SE control provided by elliptical photonic nanowires.

We also performed a polarization analysis on 9 elliptical photonic nanowires having same dimension as like PW_o but different major axis orientations: 0°, 45° and 90°. The corresponding polar plots for three different QDs embedded into 3 wires with major axis orientations: 0°, 45° and 90°

respectively, are shown in the Figure 2.14 (a). All of them show a strong linear polarization and the direction of the linearly polarized light follows the orientation of the far field linear polarization of the photonic structure, regardless on the orientation of the GaAs crystal. This demonstrates that the strongly polarized emission from the dot embedded into elliptical photonic wire is due to a photonic effect, and not due to the polarization of individual QDs. The complete set of total 20 measured polarization resolved spectra for various transitions studied in these 9 wires is shown in Figure 2.14 (b), which represents a polar plot of $C_{\parallel}$ versus θ_o. This figure clearly demonstrates that high $C_{\parallel}$ can be reproducibly obtained and the direction of the linearly polarized light always follows the direction of far field of the photonic structure whatever the excitonic complexes involved in the emission process.

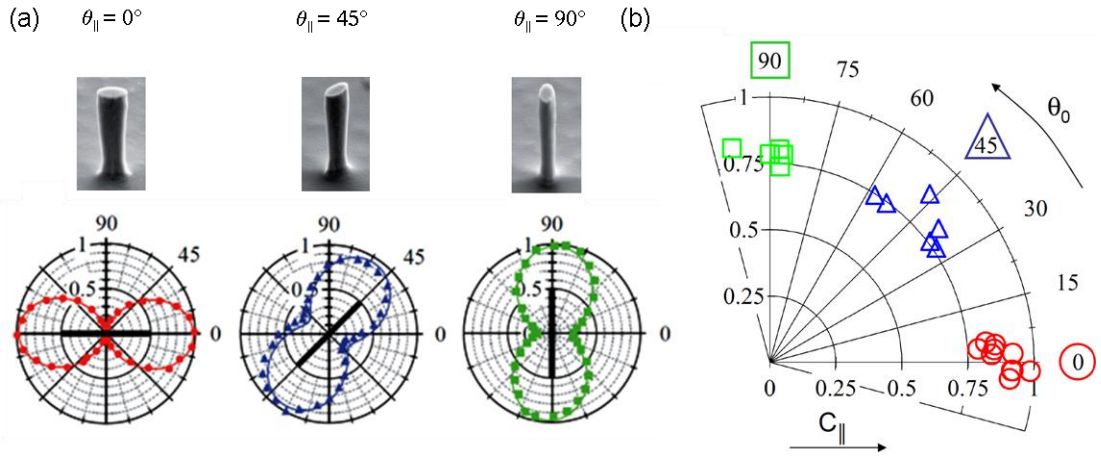

Figure 2.14: Proof of photon polarization control due to the photonic modes of the photonic structures, (a) Polarization analysis of the emitter embedded in photonic wires with the dimensions close to the one of PW_o, but various ellipse orientation $\theta_{\parallel}$ = 0°, 45° and 90° and (b) Degree of linear polarization plotted against the polarization angle for various emitters in these wires.

5.5.3 A complementary measurement: polarization-resolved time decay experiments

A high fraction of the collected photons with the desired linear polarization is clear indication of the funnelling of SE of an emitter into single guided mode of photonic wire. Besides this, we provide an additional evidence of single-mode emission by performing time resolved (TR) μ-PL measurements. We performed the TR-PL on the line X_b in the wire PW_0 [ll and ⊥ respectively aligned along (h)

and (v)]. Figure 2.15 shows the TR-PL measurements curve performed for the (ll) and (⊥) polarization on the neutral excitonic emission line X_b of PW_o (see Figure 2.13). Both decay curves show mono exponential behaviour with almost similar decay time 1.22 ns and 1.39 ns for (h) and (v) polarizations. We have observed a similar behaviour for all other transitions reported in this chapter. This analysis suggests a fast flip-flop mechanism between the bright components of the neutral exciton; it provides an indirect way for simultaneously coupling to both modes. A high spin-flip rate between the bright excitons was also observed in Ref. [21].

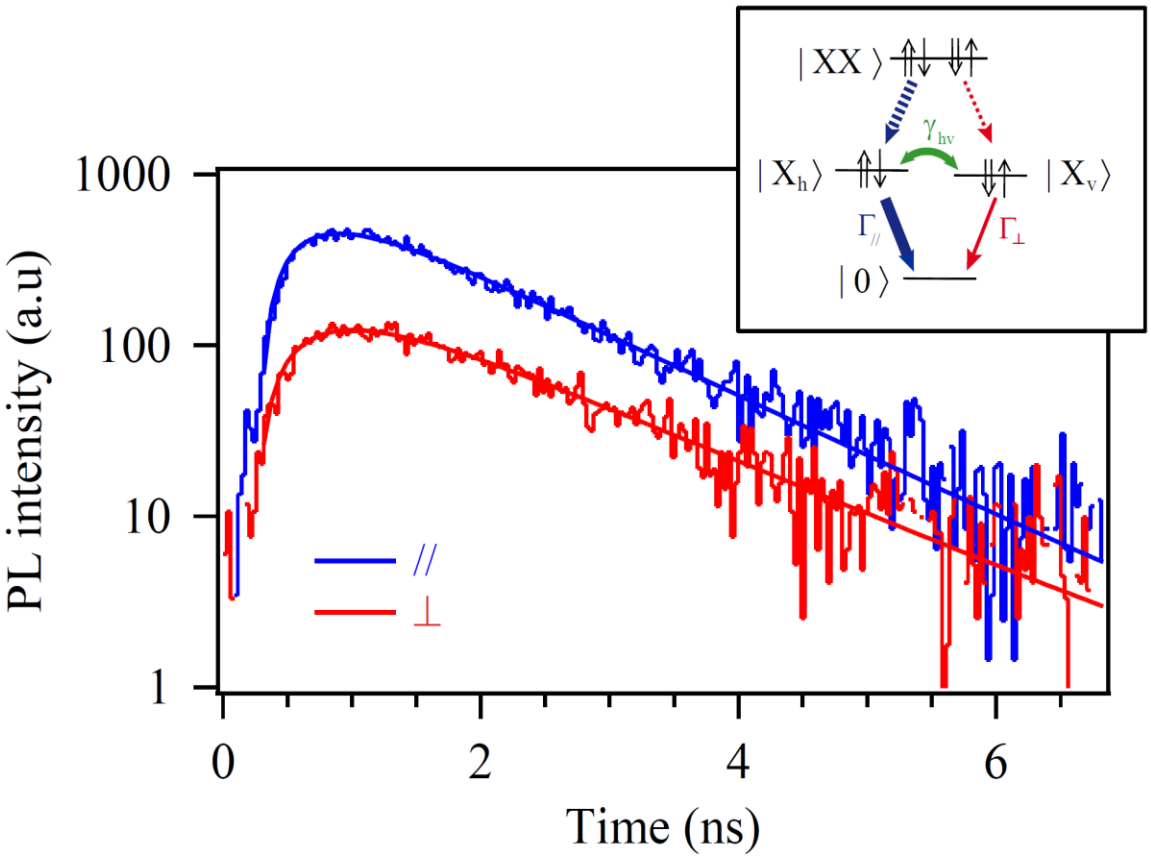

Figure 2.15: Controlling the polarization of the neutral exciton. Measurements are taken on the line X_b of sample PW_o, whose major axis'll' is aligned on (h). The main panel shows the time-resolved decay, collected for polarization oriented along'll' and '⊥ '(log-linear scale). The inset sketches the level structure and the associated radiative rates. In this anisotropic photonic structure, decay rate $\Gamma_{ll} >> \Gamma_{\perp}$. A fast spin flip-flop rate ($\gamma_{hv} >> \Gamma_{ll}$) can couple the bright exciton states $|X_h\rangle$ and $|X_v\rangle$, leading to the single decay rate.

5.6 Conclusion

In conclusion, we have theoretically shown that dielectric photonic nanowires with elliptical cross section offer an electromagnetic environments dominated by a single guided mode with well defined linear polarization. Thus, this structure can be used to funnel the SE of an emitter with isotropic, in-plane dipole components into a single optical mode. Moreover, this result is maintained over a broadband wavelength range, as expected for a 1D photonic structure.

We have completed our theoretical analysis by an experimental study. We have optimized the fabrication process of GaAs elliptical photonic nanowires with embedded InAs QDs; especially we have introduced a Ni hard mask to realize this structure. Polarization-resolved μPL experiments show that the fraction of collected photons with the desired polarization can be high as 95%. Among other perspectives, this work paves the way for the realization of high efficiency single-photon source with a well defined polarization. To do this, one could implement the same light collection optimization strategy (tapering of the wire and integrated mirror) as like cylindrical photonic wire which we have realized the chapter 2-4.

References

1. D. Kuksenkov and H. Temkin, "*Polarization Related Properties of Vertical-Cavity Lasers,*" Vertical-Cavity Surface-Emitting lasers: Design, Fabrication, Characterization, and Applications (Cambridge University Press) **Chap. 6**, 233 (1999).
2. D.V. Kuksenkov and H.Temkin, and S. Swirhun, "*Polarization instability and relative intensity noise in vertical-cavity surface-emitting lasers,"* Appl. Phys. Lett. , **67**, 2141 (1995).
3. B. Ellis, M. A. Mayer, G. Shambat, T. Sarmiento, J. Harris, E. E. Haller, and J. Vuckovic, "*Ultralow-threshold electrically pumped quantum dot photonic-crystal nanocavity laser*," Nature Photonics **5**, 297 (2011).
4. T. Jennewein, C. Simon, G. Weihs, H. Weinfurter and A. Zeilinger, "*Quantum Cryptography with Entangled Photons"* Phys. Rev. Lett. **84**, 4729 (2000).
5. E. Knill, R. Laflamme, and G. J. Milburn, "*A scheme for efficient quantum computation with linear optics*," Nature **409**, 46 (2001).
6. A. Shields, "*Semiconductor quantum light sources*," Nature Photonics **1**, 215 (2007).
7. Q. Turchette, R. Thompson, and H. Kimble, "*One dimensional atoms*" Appl. Phys. B 60, S1 (1995).
8. J.M. Gérard, D.Barrier, J.Y.Marzin, "*Quantum boxes as active probes for photonic microstructures: The pillar microcavity case,"* Appl. Phys. Lett, **69**, 449 (1996).

9. B. Gayral, “Controlling *spontaneous emission dynamics in semiconductor microcavities; an experimental approach*,” Ann. Phys. Fr **26**, N°2 (2001).
10. B. Gayral, J.M. Gérard, B. Legrand, E. Costard and V. Thierry-Mieg, “*Optical study of GaAs/AlAs pillar microcavities with elliptical cross section,*” Appl. Phys. Lett, **72**, 1421 (1998).
11. D. M. Whittaker, P. S. S. Guimaraes, D. Sanvitto, H. Vinck, S. Lam, A. Daraei, J. A. Timpson, A. M. Fox, M. S. Skolnick, Y.-L. D. Ho, J. G. Rarity, M. Hopkinson, and A. Tahraoui, “*High Q modes in elliptical micropillars*,” Appl. Phys. Lett, **90**, 161105 (2007).
12. A. Daraei, A. Tahraoui, D. Sanvitto, J. A. Timpson, P. W. Fry, M. Hopkinson, P. S. S. Guimarães, H. Vinck, D. M. Whittaker, M. S. Skolnick, and A. M. Fox , “*Control of polarized single quantum dot emission in high-quality- factor microcavity pillars*,” Appl. Phys. Lett, **88**, 051113 (2006).
13. E. Moreau, I. Robert, J. M. Gérard, I. Abram, L. Manin and V. Thieryy-Mieg, “*Single-mode solid-state single photon source based on isolated quantum dots*,” Appl. Phys. Lett, **79**, 2865 (2001).
14. R. Oulton, B.D. Jones, S. Lam, A.R.A. Chalcraft, D. Szymanski, D. O’Brien, T.F. Krauss, D. Sanvitto, A.M. Fox, D.M. Whittaker, M. Hopkinson, and M.S. Skolnick, “*Polarized quantum dot emission from photonic crystal nanocavities studied under mode-resonant enchance excitation,”* Opt. Exp. **15**, 17222 (2007).
15. E. Gallardo, L. J. Martínez, A. K. Nowak, H. P. van der Meulen, J. M. Calleja, C. Tejedor, I. Prieto, D. Granados, A. G. Taboada, J. M. García, and P. A. Postigo, “*Emission polarization control in semiconductor quantum dots coupled to a photonic crystal microcavity,”* Opt. Exp. **18**, 13301 (2010).
16. D. Englund, D. Fattal, E. Waks, G. Solomon, B. Zhang, T. Nakaoka, Y. Arakawa, Y. Yamamoto, and Jelena Vuc̆kovic´, “*Controlling the Spontaneous Emission Rate of Single Quantum Dots in a Two- Dimensional Photonic Crystal*,” Phys. Rev. Lett. **95**, 013904 (2005).
17. M. Bayer, G. Ortner, O. Stern, A. Kuther, A. A. Gorbunov, A. Forchel, P. Hawrylak, S. Fafard, K. Hinzer, T. L. Reinecke and S. N. Walck, “*Fine structure of neutral and charged excitons in self-assembled In(Ga)As/(Al)GaAs quantum dots*,” Phys. Rev. B **65**,195315 (2002).
18. D. Gammon, E. S. Snow, B. V. Shanabrook, D. S. Katzer and D. Park, “*Fine Structure Splitting in the Optical Spectra of Single GaAs quantum dots,*” Phys. Rev. Lett. **76**, 3005 (1996).
19. R. M. Stevenson, R. M. Thompson, A. J. Shields, “*Quantum dots as a photon source for passive quantum key encoding*,” Phys. Rev. B **66**, 081302 (2002).
20. Q. Wang, S. Stobbe, H. Thyrrestrup, H. Hofmann, M. Kamp, T. W. Schlereth, S. Höfling, and P. Lodahl, “*Highly anisotropic decay rates of single quantum dots in photonic crystal membranes,*” Opt. Lett. **35**, 2768 (2010).
21. I. Favero, G. Cassabois, C. Voisin, C. Delalande, P. Roussignol, R. Ferreira, C. Couteau, J. P. Poizat, and J.-M. Gérard, “*Fast exciton spin relaxation in single quantum dots*,” Phys. Rev. B 71,233304 (2005).

Chapter 6

Conlusion and perspectives

*A conclusion is the place where you get tired of thinking.-**A. Bloch***

6.1 Conclusion

Fiber-like photonic nanowires belong to the growing family of 1D photonic systems designed to control the SE of an embedded emitter. In this thesis, our major goal was to realize efficient single-photon sources using the family of III-As semiconductors. The emission from the source was collected in free space using a microscope objective. Importantly, the broad operation bandwidth inherent to a 1D photonic system allows for exploiting the very appealing properties of self-assembled QDs for single-photon emission with a high device yield, without resorting to complex nanofabrication processes.

SE control in fiber-like photonic nanowires is obtained thanks to the large refractive index contrast between the wire and its surroundings. It first allows confining tightly the fundamental guided mode in a GaAs wire having a diameter around 200 nm (operation wavelength of about 950 nm). Second, a pronounced dielectric screening effect cancels to a large extent the coupling to the 3D continuum of non-guided modes. Thus, nearly all the SE of an embedded InAs QD is funnelled into the fundamental guided mode. Providing that a proper engineering of the wire ends is conducted, a very efficient out-coupling to the far-field can be achieved. The full design of our single-photon source features a bottom integrated mirror and a top taper, mandatory to achieve a directive far-field emission pattern. When combined, these ingredients lead to global source efficiency close to unity.

During this PhD, I conducted a great effort for the nanofabrication of the devices. With regard to the process technology for making SPS's was developed almost from scratch and then carefully optimized to achieve various milestones along the way. Starting from a planar sample grown by molecular beam epitaxy, the fabrication implies in particular a flip-chip process (wafer bonding and removal of the growth wafer) and a carefully optimized etching step. This last step, conducted in a Reactive Ion Etching system, is crucial, since it defines the wire geometry, and thus the global performance of the device.

We have successfully fabricated three families of devices that have lead to new results. We have first realized photonic wires with a 'regular' taper (needle-like), relying on an integrated mirror. To this end, an original shape transfer process was developed. Under pulsed optical pumping, at cryogenic temperature, this single-photon source has shown remarkable performance, with a record source efficiency of 72%, combined with highly pure single-photon emission. This constitutes a great improvement in comparison to the state-of-art of cavity-based single-photon sources. In addition, this sample was also used for an experimental study of the SE control mechanisms in a photonic wire. Studying 'small' wires, for which the coupling to the guided mode can be neglected, a SE inhibition by a factor of 16 was achieved. Such a high value has only been achieved in the best photonic crystal membranes, which are much more complex structures. Moreover, studies conducted in wires ensuring an optimal confinement of the guided mode revealed a SE enhancement by a factor 1.5, close to the maximum theoretical value of 1.7. These results confirm the assets of photonic wires for an efficient and broadband SE control.

At present, the single-photon source efficiency is limited by the geometry of the taper (78% into N.A. = 0.75 for a tapering angle of 5°). Improving further the outcoupling efficiency with a needle-like taper might be difficult. Indeed, bringing the transmission of the taper to 97% requires a tapering angle as low as 2°. We believe such an ultra-sharp needle is difficult to realize with our etching approach, though it might be feasible using a direct growth method [1, 2]. We have thus chosen to develop an alternative tapering strategy, where the diameter of the wire is progressively increased. To this end, we developed a new process, which implies in particular a very robust Ni mask, and an etching recipe featuring a significant chemical component, to achieve a controlled undercut. A first sample has been realized (height 12 µm, bottom diameter of 200 nm, top facet

diameter of 1.5 µm). Theoretically, it should demonstrate efficiencies in excess of 85%, and preliminary results seem to be encouraging. Moreover, as discussed in the perspectives, this geometry is well adapted for the realization of an electrically pumped, single-photon LED.

The third class of devices was designed to achieve single-mode emission, in a mode featuring a controlled linear polarization. A photonic wire featuring an elliptical cross section with a moderate lateral aspect ratio (2) provides an electromagnetic environment dominated by a single guided mode with well defined linear polarization, oriented along the ellipse major axis. We have fabricated such a structure. Our main motivation was to demonstrate the polarization control in these structures. Thus, special care was taken to achieve a good control over the geometry of the wire cross section (using again the Ni mask), but the structure did neither feature bottom mirror nor tapering. Polarization-resolved micro-photoluminescence experiments show that the fraction of collected photons with the desired polarization can be high as 95%.

1.2 Perspectives

Research on photonic wires will continue in our group after my PhD. I present below a brief summary about some future work directions.

Electrically Pumped Single-Photon Source:

Electrical pumping is one of the major requirements for the practical application of single-photon sources. Three designs of single-photon LED in the photonic nanowire geometry are presented in Ref [3]. Among them, we believe that the trumpet-like tapers are the more adapted to reach this goal. We have already defined and optimized a suitable process flow for this device including 4 steps e-beam alignment and the n- and p- type contact recipes for GaAs. The first generation of devices (no bottom mirror) is almost ready for the experiments. To obtain a high-efficiency electrically pumped source, the next step is to integrate bottom mirror. Interestingly, the possibility to apply an electrical field along the quantum dots growth axis brings interesting tuning possibilities. Using this strategy, an optically-pumped, wavelength tuneable single-photon source could be realized. As discussed in the next paragraph, the possibility to apply electrical fields is also interesting to realize other sources of quantum light.

Source of Polarization-Entangled Photon Pairs:

It has been reported that by collecting the XX and X photons emitted by the biexciton cascade, a single dot can be used as a source of polarization-entangled photon pairs [4]. Thanks to its broadband behaviour, a photonic nanowire provides a natural platform to collect efficiently the radiative cascade of a single QD. In addition, due to achieved high single photon source efficiency 0.72 in photonic nanowire, it paves the way to realize a source of entangled photons with high potential efficiency (0.72 x 0.72 = 0.5) which would be a great improvement in comparison to state-of-art cavity based sources (0.34 x 0.34= 0.12) [5]. The major difficulty is then to work with a dot symmetric enough to exhibit a small fine structure splitting (energy separation between the two bright excitons). Usually, this is not the case of as-grown InAs QDs, which feature FSS of the order of a few tens of μeV. The FSS can be reduced by a post-growth, high temperature annealing [6]. Another control tool was demonstrated recently, using an electrical field applied along the growth axis [7]. In that case, quantum dots with a high vertical confinement are necessary, in order to prevent the tunnelling of the carriers out of the dot when the structure is strongly biased.

Source of indistinguishable single photons:

Advanced quantum information processing schemes often require the efficient emission of indistinguishable photons. Namely, the photons have to be emitted in the same optical mode (spatial structure, polarization and frequency). In addition, the photons must present identical temporal profiles: the lifetime T_1 of the QD excited state has to be smaller than the typical dephasing time T_2*. In this context, the polarization control achieved with anisotropic wires is a first step, which should be completed by the implementation of a mirror and a top taper. Regarding the constraint of an emission faster than dephasing processes, the moderate Purcell enhancement (x1.7) achievable in a photonic nanowire might be a limitation. Therefore, one could implement fast QDs such as the one formed by thickness fluctuations of the interfaces of a quantum well [8]. These emitters present a radiative lifetime much smaller than the one of standard InAs/GaAs QDs.

Quantum optics with a 1D atom, giant optical non-linearity:

Photonic wires are not only interesting for the realization of efficient sources of quantum light. They provide a very pure situation, where a single emitter is coupled to single electromagnetic mode. This situation, often referred

as a 1D atom [9], constitutes a model system for quantum optics experiments. As a first step, it can be used to demonstrate giant non-linearity (at the single-photon level). We have fabricated device for this project and experiments are under way (Inah Yeo, Gilles Nogues and Jean-Phillipe Poizat). For this resonant experiment, quantum dots must be spectrally stable. We have already resolved a problem of spectral instability due to the surface effect.

References

1. S. N. Dorenbos, H. Sasakura, M. P. van Kouwen, N. Akopian, S. Adachi, N. Namekata, M. Jo, J. Motohisa, Y. Kobayashi, K. Tomioka, T. Fukui, S. Inoue, H. Kumano, C. M. Natarajan, R. H. Hadfield, T. Zijlstra, T. M. Klapwijk, V. Zwiller, and I. Suemune, "*Position controlled nanowires for infrared single photon emission,"* Appl. Phys. Lett. **97**,171106 (2010).
2. J. Heinrich, A. Huggenberger, T. Heindel, S. Reitzenstein, S. Höfling, L. Worschech,and A. Forchel,"*Single photon emission from positioned GaAs/ AlGaAs Photonic nanowires*," Appl. Phys. Lett. **96**, 211117(2010).
3. N. Gregersen, T. R. Nielsen, J. Mørk, J. Claudon, and J.-M. Gérard, "*Designs for high-efficiency electrically pumped photonic nanowire single-photon sources*," Opt. Exp. **18**, 21204 (2010).
4. O. Benson, C. Santori, M. Pelton and Y. Yamamoto, "*Regulated and Entangled Photons from a Single Quantum Dot*," Phys. Rev. Lett. **84**, 2513 (2000).
5. A. Dousse, J. Suffczyn´ski, A. Beveratos, O. Krebs, A. Lemaıˆtre, I. Sagnes, J. Bloch, P. Voisin and P. Senellart, "*Ultrabright source of entangled photon pairs*," Nature **466**, 217 (2010).
6. D. J. P. Ellis, R. M. Stevenson, R. J. Young, A. J. Shields. P. Atkinson and D. A. Ritchie, "*Control of fine-structure splitting of individual InAs quantum dots by rapid thermal annealing*," Appl. Phys. Lett. **90**, 011907 (2007).
7. A. J. Bennett, M. A. Pooley, R. M. Stevenson, M. B. Ward, R. B. Patel, A. Boyer de la Giroday, N. Skold, I. Farrer, C. A. Nicoll, D. A. Ritchie and A. J. Shields, "*Electric-field-induced coherent coupling of the exciton states in a single quantum dot*," Nature. Phys. **6**, 947 (2010).
8. J. Hours, S. Varoutsis, M. Gallart, J. Bloch, I. Robert-Philip, A. Cavanna, I. Abram, F. Laruelle and J.-M. Gérard, "*Single photon emission from individual GaAs quantum dots*," Appl. Phys. Lett. **82**, 2206 (2003).
9. Q. Turchette, R. Thompson, and H. Kimble, "*One dimensional atoms*" Appl. Phys. B **60**, S1 (1995).

Appendix A

Depolarization Field in Thin Dielectric Cylinder

We consider an unpolarized thin dielectric cylinder of radius *r* at the origin and extending along the z-axis to infinity with dielectric constant ε. In case of $r << \lambda$, one can neglect the propagation of the field and treat problem as like electrostatics case. Suppose that the cylinder is illuminated by plane wave with uniform electric field $\mathbf{E} = E_o \hat{x}$ which is coming from infinity (like radiative modes) and it becomes polarized by polarization vector **P** which produce a depolarization electric field $\mathbf{E_{in}}$ inside the cylinder (see Figure A.1 (a)). In order to calculate this field, after the polarization of the cylinder we can consider the cylinder equal to the composition of two virtual cylinder separated by infinitesimal d along x-axis so that the cylinder 1 has a $-\rho$ volume density charge and cylinder 2 has a $+\rho$ volume density charge (see Figure A.1 (b)).

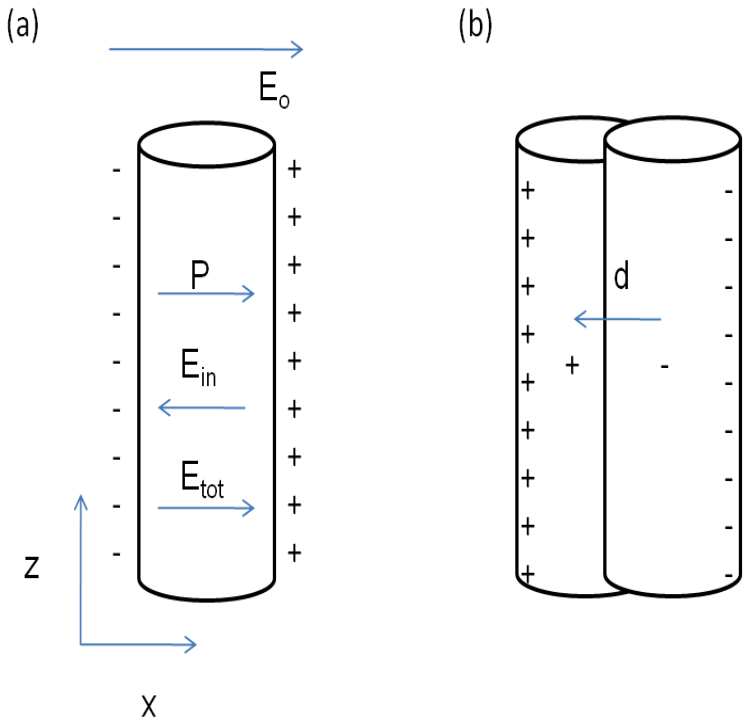

Figure A.1: (a) Schematic of a dielectric polarized cylinder placed in external electric field, (b) Schematics of the two virtual charged cylinder equivalents to the polarized cylinder.

By Gauss's law, the electric field of a uniformly charged cylinder with charge density ρ, at position **r** can be calculated as

$$\mathbf{E}(\mathrm{r}) = \frac{\rho}{2\varepsilon_o}\mathbf{r} \ , \tag{A.1}$$

Consider an arbitrary point in the overlap region of the two cylinders, the electric field at this point inside the superposed cylinder is equal to the vector sum of the electric field due to the positively and negatively charged cylinder, given by

$$\mathbf{E}_{\mathrm{in}}(\mathrm{r}) = \frac{\rho}{2\varepsilon_o}(\mathbf{r}_+ - \mathbf{r}_-), \tag{A.2}$$

where r_- and r_+ are the distance of this point from the centre of negatively and positively charged cylinder respectively . Therefore

$$\mathbf{d} = \mathbf{r}_- - \mathbf{r}_+, \tag{A.3}$$

Substituting the value of d from equation (A.3), we can rewrite equation (A.2) as

$$\mathbf{E}_{\mathrm{in}}(\mathrm{r}) = -\frac{\rho}{2\varepsilon_o}\mathbf{d}, \tag{A.4}$$

The polarization vector can be written as

$$\mathbf{P} = \rho.\mathbf{d}, \tag{A.5}$$

Hence the depolarization field inside the cylinder is given by

$$\mathbf{E}_{\mathrm{in}}(\mathrm{r}) = -\frac{\mathbf{P}}{2\varepsilon_o}, \tag{A.6}$$

It is clear from the equation (A.6), depolarization field is opposite to the polarization of the material due to the applied external field. The relation between the polarization vector and electric field is given by $\mathbf{P} = \varepsilon_0\chi_e\mathbf{E}$, where the electric field is given by the total electric field inside the dielectric sphere,

$$\mathbf{E} = \mathbf{E}_o + \mathbf{E}_{\mathrm{in}}, \tag{A.7}$$

After using the equations (A.6) and (A.7) with relation between **P** and **E**, we can deduce the depolarization electric field as a function of applied external field and written as

$$\mathbf{E}_{\mathrm{in}} = -\frac{(\varepsilon - \varepsilon_o)}{(\varepsilon + \varepsilon_o)}\mathbf{E}_o, \tag{A.8}$$

In the similar way one can calculate the depolarization electric field inside the thin dielectric slab and small dielectric sphere.

This thesis presents the realization of an efficient single-photon source based on an InAs quantum dot integrated in a photonic nanowire. A photonic nanowire is a monomode waveguide made of a high refractive index material (GaAs in our case). For an optimal wire diameter around 200 nm, nearly all the spontaneous emission of the embedded single-photon emitter (free space wavelength ~950 nm) is funnelled into the fundamental guided mode. In addition, the outcoupling efficiency of the guided photon to a microscope objective can be brought close to one with a proper engineering of the wire ends. The source thus features an integrated bottom mirror and a smooth tapering of the wire upper end. High performances are maintained over a broad wavelength range, a key asset of this 1D photonic structure. This thesis presents the physics which governs these structures, their realization, and their characterization. Under pulsed optical pumping, we demonstrate a single-photon source with a record efficiency of 0.72, combined with highly pure single-photon emission. We also discuss the possibility to obtain polarization control, using wire with an elliptical section.

Cette thèse présente la réalisation d'une source de photons uniques basée sur une boîte quantique InAs intégrée dans un fil photonique. Un fil photonique est un guide d'onde monomode constitué d'un matériau de fort indice de réfraction (GaAs dans notre cas). Pour un diamètre optimal voisin de 200 nm, pratiquement toute l'émission spontanée de l'émetteur (longueur d'onde dans le vide ~950 nm) est dirigée vers le mode guidé fondamental. Le couplage des photons guidés à un objectif de microscope est ensuite optimisé en travaillant la géométrie des extrémités du fil. Ce dernier repose ainsi sur un miroir intégré et présente une extrémité supérieure en forme de taper. Cette approche non résonante combine de très bonnes performances à une grande tolérance sur la longueur d'onde de l'émetteur intégré. Cette thèse discute la physique des fils photoniques, la réalisation des structures en salle blanche et les résultats obtenus lors de la caractérisation optique. En particulier, nous avons réalisé une source combinant une efficacité record (0.72, état de l'art à 0.4) et une émission de photons uniques très pure. Nous discutons également le contrôle de la polarisation obtenu dans des fils de section elliptique.